Universidad del País Vasco Euskal Herriko Unibertsitatea

NAZIOARTEKO BIKAINTASUN CAMPUSA
CAMPUS DE EXCELENCIA INTERNACIONAL

Myelin imaging and characterization by magnetic resonance imaging

Ander Egimendia Tolaretxipi

Supervised by Pedro Ramos Cabrer and David Otaegui Bichot

2019

Table of contents

List of Abbreviations

List of Abbreviations

a.u.	Arbitrary units
AD	Axial diffusivity
APP	Amyloid precursor protein
AU	Auditory cortex
Aβ	β-amyloid protein
BBB	Blood-brain barrier
BOLD	Blood oxygen level-dependent
C	Cortex
CC	Corpus callosum
CEST	Chemical shift exchange
Cg	Cingulate
CN	Cortical network
CNP	Cyclic nucleotide phosphodiesterase
CNR	Contrast to noise ratio
CNS	Central nervous system
CP	Cerebellar peduncles
CPu	Caudate putamen
Dg	Dentate gyrus
DMN	Default mode network
DTI	Diffusion tensor imaging
DWI	Diffusion-weighted imaging
EntC	Entorhinal cortex
EPI	Echo planar imaging
FA	Fractional anisotropy

FC	Functional connectivity
FOV	Field of view
genu-CC	Genu of the corpus callosum
gICA	Group ICA
gICA	Group Independent Component Analysis
GM	Grey matter
GP	Globus pallidus
Hc	Hippocampus
Hp	Hippocampus
Hyth	Hypothalamus
ICA	Independent component analysis
lat-CC	Lateral corpus callosum
LFB	Luxol fast blue
LPC	Lysophosphatidylcholine
M1	Primary motor cortex
M2	Secondary motor cortex
MBP	Myelin basic protein
MC	Motor cortex
MD	Mean diffusivity
med-CC	Medial corpus callosum
mFC	Mean functional connectivity
MR	Magnetic resonance
MRI	Magnetic resonance imaging
MS	Multiple sclerosis
MT	Magnetization transfer

MTR	Magnetization transfer ratio
MWF	Myelin water fraction
NFT	Neurofibrillary tangles
NgR1	Nogo receptor 1
NMR	Nuclear magnetic resonance
OD	Optical density
ON	Optic neuritis
OPCs	Oligodendrocyte precursor cell
OsO4	Osmium tetraoxide
PD	Proton density
PET	Positron emission tomography
Pir	Piriform cortex
PLP	Myelin proteolipid protein
PrL	Rostral dorsal prelimbic cortex
RD	Radial diffusivity
ROI	Region of interest
rs-fMRI	Resting-state functional MRI
RSG/RSD	Retrosplenial granular and dysgranular cortex
RSN	Resting-state network
S1	Primary motor cortex
S2	Secondary motor cortex
SCA	Seed based functional connectivity analysis
SCI	Spinal cord injury
SD	Standard deviation
SI	Signal intensity

SN	Subcortical network
SNR	Signal to noise ratio
SWI	Susceptibility weighted imaging
T	Tesla
T1w	T1-weighted
T2*w	T2*-weighted
T2w	T2-weighted
TBI	Traumatic brain injury
TE	Echo time
Tg	Transgenic
Th	Thalamus
TMEV	Theiler murine encephalomyelitis virus
TR	Repetition time
UTE	Ultra-short echo time
V	Volume
VC	Visual cortex
VEP	Visual evoked potential
W	Week
WM	White matter
Θ	Flip angle

Laburpena

Milioika pertsonek bizi kalitatea nabarmen kaltetzen dieten nerbio sistema zentraleko gaixotasunak pairatzen dituzte. Horien artean, garunean eragina duten gaixotasun neurodegeneratiboak daude, hala nola, Alzheimerra, esklerosi anizkoitza edo Parkinsona, zeintzuetan neurona galera jasaten den eta ondorioz, gaitasun kognitiboa murriztu eta autonomia galtzen den eguneroko bizitzan. Nerbio sistema zentralean, neuronekin batera, astrozitoak, mikrogliak eta oligodendrozitoak daude. Hauek ere funtsezko eginkizunak betetzen dituzte, hala nola neuronen beharrak asetu, immunitate sistemarekin bitartekaritza lanak egin eta neuronen axoiak mielinizatu. Hain zuzen, mielina da lan honen ardatz nagusia.

Neuronak, dendritez, axoiaz eta somaz osatuta daude. Pultsu elektrikoek neuronak zeharkatzen dituzte axoiatan zehar, axoiaren bi aldeetan ioien kontzentrazio aldaketa bortitzak eragindez. Pultsu elektrikoaren transmisio aproposa eman dadin, mielinak funtsezko zeregina du axoiak estaltzen, izan ere, geruza lipidiko honek bultzada elektrikoaren transmisio azkarra eta eraginkorra ahalbidetzen du. Oligodendrozitoak dira nerbio sistema zentralean mielina sintetizatu eta mantentzeaz arduratzen diren zelulak, baita neuronen behar energetikoa metabolitoen bidez (laktatoa eta pirubatoa esaterako) asetzen dutenak ere.

Mielina galtzeak edo desmielinizazioa delakoak axoien atrofia eta neuronen heriotza eragin dezake. Egoera hau bermielinizazioaren bidez ekidin daiteke, desmielinizazioaren ondoren oligodendrozitoek mielina geruza berri bat sortzen badute. Horretarako funtsezkoa da oligodendrozitoen zelula aitzindariek proliferatzea, lesio gunera migratzea eta oligodendrozito helduetan diferentziatzea, azken hauek mielina geruza berria eraiki dezaten. Hala ere, nahiz eta prozesu hau modu eraginkorrean eman, bermielinizazioan eraikitzen den mielina geruza berria aurrekoa baino meheagoa izaten da.

Jakina da desmielinizazio prozesuak hainbat patologiatan ematen direla, hala nola, iskemian, Alzheimerrean, garuneko lesio traumatikoetan edo esklerosi anizkoitzean, zeinetan desmielinizazioa patologia konplexu baten eragile nagusia den. Esklerosi anizkoitza gaixotasun autoimmune neurodegeneratiboa da, izan ere, immunitate sistemaren mielinari zuzendutako eraso latzek desmielinizazio plakak eragiten dituzte. Gaixotasun hau pairatzen duten pazienteek, bermielinizazio gaitasuna galtzen dute zahartzearen ondorioz eta immunitate sistemaren eraso ugariek eragiten duten mekanismoen higadurarengatik. Hori dela eta, ohikoa da gaixoak fase progresibo batetan sartzea, kalte neuronal eta funtzionala nabarmena eta atzeraezina jasanez.

Gaur egun arte, esklerosi anizkoitzera bideratu diren tratamenduak nerbio-sistema zentrala kaltetzen dituzten erasoak geldiaraztera bideratu dira, terapia immunosupresibo edo immunregulatzaileen bidez. Zalantza izpirik gabe tratamendu horien eraginkortasunak gaixoen bizi-kalitate hobea ahalbidetu du. Hala ere, jakina da immunitate sistemaren erasoen ondoren berreskuratzea ez dela erabatekoa eta denboran zehar izandako eraso errepikatuek gaitasun funtzionalen galtzea dakartela neurona heriotza dela eta. Egoera honek beste estrategia terapeutiko osagarriren garapena eskatzen du.

Azken urteetan, bermielinizazioa edo mielina konponketa indartzeko estrategiak garatzeko ikerketak burutu dira. Batik bat, oligodedrozitoen zelula aitzindarien diferentziazioa sustatzea ezarri da helburutzat, horrela mielina berria sintetizatzeko gai diren oligodendrozito helduak sortuz. Izan ere, esklerosi anizkoitzean eta desmielinizazioa ematen den beste gaixotasunetan egindako *post-mortem* ikerketetek adierazi dute oligodendrozitoek diferentziatzeko gaitasuna galtzen dutela. Baina bermielinizaziora bideratutako tratamenduen garapenak, lehenengo, desmielinizazio eta bermielinizazio prozesuen ezagutza sakona behar du. Aldi

berean, prozesu hauen azterketarako egokiak diren eredu esperimentalak definitzea eta tratamendu jakin baten eragina modu ez-inbasibo batean ebaluatzea ahalbidetzen duten teknikak garatzea ezinbestekoa da.

Desmielinizazioaren eta bermielinizazioaren azterketa *in vitro* ereduetan (oligodendrozito zelula aitzindarien kultiboetan), *ex vivo* ereduetan (kultibo organotipiko deritzen zerebelo xerra finetan), eta *in vivo* animali ereduetan egiten da, batez ere EAE eta kuprizona animali ereduetan. Horregatik, eredu hauetan desmielinizazioa eta bermielinizazioa, hau da, mielinaren kuantifikazioa, denboran zehar aztertzea ahalbidetzen duten teknika ez-inbasiboen garapena garrantzi handikoa da.

Zentzu horretan erresonantzia magnetikoaren bidezko irudigintzak (MRI, ingelesez) funtsezko eginkizuna izan dezake. Esklerosi anizkoitzean teknika honek plaka desmielinizanteak diagnostikatzeko duen sentikortasun aparta da. Testuinguru honetan, MRI teknikak aukera ugari eskaintzen ditu, kontraste anitzak dituzten kalitate handiko irudi anatomikoak lortzen baititu. Besteak beste, burmuineko eskualde desberdinen aktibazioa, garunean zehar urak duen difusioa (garunaren antolaketa eta egitura mailarekin erlazionatutakoak), edota garunaren ehunen arteko kontraste handia erakusten duten irudiak eraiki daitezke parametro desberdinak moldatuz. Hala ere, komunitate zientifikoak ez du oraindik adostu mielina kantitatea definitzeko MRI bidezko protokolo edota teknikarik, zenbait proposamen egin badira ere.

Lan honetan mielinaren edukia kuantifikatzeko eremu handiko erresonantzia magnetikoaren (11,7 Tesla) irudiak erabiltzeko eredu esperimentalak eta protokoloak garatu ditugu, lana 5 atal desberdinetan banatuta: 1) Kultibo organotipikoetan mielina kantitatea kuantifikatzeko protokoloen garapena.; 2)

Denbora luzean egindako erresonantzia magnetiko bidezko irudigintza multiparametriko ikerketa, mielinaren edukia kuantifikatzeko eta desmielinizazio eta bermielinizazio prozesuen jarraipena egiteko kuprizona sagu ereduan; 3) Erresonantzia magnetiko bidezko irudigintza multiparametrikoa Alzheimerreko bi animalia ereduetan, materia zuri eta grisaren aldaketak ikertzeko eta mielina kantitatearen neurketa burutzeko; 4) Atsedenean egindako erresonantzia magnetiko bidezko irudigintza funtzionalaren (rs-fMRI, ingelesez) ikerketa, garunaren funtzioan desmielinizazio eta bermielinizazio prozesuen eragina ebaluatzeko eta clemastina bermielinizazio terapia potentzialaren efektua aztertzeko anatomikoki eta garun-konektibitatean; 5) Zahartzeak garuneko konektibitatean duen eragina aztertu atsedenean egindako erresonantzia magnetiko bidezko irudigintza funtzionalaren bidez.

Aipatzekoa da Alzheimer eta zahartze ereduak lan honen helburu nagusien artean ez dauden arren, nolabaiteko mielina galera pairatu dezaketela, eta lan honetan ikertu izanak aukera eman digula esklerosi anizkoitzarekin lotutako desmielinizazioa aztertzeko garatutako metodologia esperimentalki balioztatzeko. Horrela, sendotasuna eta unibertsaltasuna eskainiz, nerbio sistema zentrala aztertzeko.

Lehenengo atala, hau da, kultibo organotipikoaren irudigintzarekin lotutakoa, erronka handia izan da eta horrek MRI teknika gaitasunak mugara eramatera behartu gaitu. Jaio ondoren 7-12 eguneko saguen zerebelo xerra kultiboak mielina ikertzeko egokitzat hartzen dira, lisolezitina detergentearen aplikazioak desmielinizazioa eragiten baitu kultiboetan, ondoren berehalako bermielinizazioa gertatuz. Testuinguru sinple batetik hasi nahian, kultibatu gabeko garun xerrak irudikatzen hasi gara (0,3-1 mm-ko lodiera), gero kultibo organotipiko lodietara (aurrekoak baino meheagoak eta egitura ahulagoarekin) jo dugu, azkenik, ohiko

kultibo organotipikoekin amaitzeko, askoz ere meheagoak direnak (<0,1 mm). Garun xerren eta kultibo organotipiko lodien irudigintza arrakastatsua izan da, seinale/zarata erlazio handiko irudiak eta materia zuria eta grisaren arteko kontraste ona lortuz. Hala ere, kultibo organotipiko finek (300-350 μm-koak jatorrian), 7 egunez kultibatu ondoren 100 μm baino gutxiagoko lodiera izaten dute, mehetuz baitoaz pixkanaka-pixkanaka, eta horrek asko zailtzen du kalitate oneko irudiak eskuratzea. Soinu/zarata erlazio ona duten irudiak lortu arren kultibo organotipiko finetan, ehunak ez du kontrasterik eskaini garunaren materia zuri eta grisaren artean. Honen ondorioz, nanoteknologia erabiltzen saiatu gara mielinarekiko espezifikoak diren partikulak sintetizatuz. Teknika honen potentziala erakusten duten kontzeptu frogak egin ditugu gure ikerketetan. Hala ere, mielinara zuzendutako liposoma funtzionalizatuek (gadolinio, fluoroforo eta mielinaren aurkako antigorputzarekin) ez dute esperotako espezifikotasuna erakutsi. Teknika molekularren garapena eta azterketak ikerketa sakona eskatzen duenez, eta tesi honen lehentasunen artean ez dagoenez, ez dugu ildo horretatik jarraitu.

Ex vivo ereduetatik *in vivo* ereduetara jotzeko, kuprizona eredu toxikoarekin lan egin dugu. Eredu honetan, kuprizona izeneko toxikoaren bidez garunaren materia txuri gune nagusiak kaltetu eta desmielinizatu egiten dira. Eredu honen ezaugarri eta abantaila nagusiak desmielinizazioa pixkanaka-pixkanaka gertatzen dela, eta ondoren, behin toxikoa dietatik kenduta, bermielinizazio espontaneoa ematen dela dira. Azterketa honetan, mielinaren edukia aurrekaririk gabeko bereizmen espazial eta tenporalarekin neurtu zen, esperimentuko 10 asteetan mielinaren berariazko irudi bateria eskuratuz. Osagarri gisa, *post-mortem,* mielinaren tindaketa espezifikoa egin da Luxol fast blue konposatuarekin. Honen bidez, desmielinizazio eta bermielinizazio prozesuak garbi identifikatu dira eta emaitza histopatologikoen eta erresonantzia magnetikoaren bidez lortutako seinaleareen arteko korrelazio zuzena

ahalbidetu du. Honela, ondorioztatu dugu T2 pisuez haztatutako irudi sekuentziak kontraste handiena eskaintzen duena dela, desmielinizazio, bermielinizazio eta egoera bereko subjektu osasuntsuekin alderatzeko sentsibilitate eta gaitasun handia izateaz gain. Aipatu beharra dago T2 pisuez haztatutako irudi sekuentzia mundu osoko laborategietan eta ospitaleetan erabiltzen dela egunerokoan, beste modalitate batzuk logistikoki konplexuagoak diren bitartean.

Lan honetan, toxikoaren esposizioaren ondorengo 2 asteetan hasi da patologia saguetan baina desmielinizazio eta bermielinizazio denbora patroi desberdinak identifikatu dira garuneko eskualde desberdinetan. Gainera, desmielinizazio kronikoaren ondorioak aztertu dira protokolo bera erabiliz toxikoarekiko esposizioaren ondorengo 6 hilabeteetan, eta oraindik ere sagu osasuntsuekin alde nabarmenak ikusi dira, erabateko bermielinizazioa eta sendatzea ematen ez direla adieraziz.

Lan honen hirugarren atalean, Alzheimer gaixotasunaren bi sagu ereduetan probatu da (amiloide plakak garatzen dituena alde batetik, eta tauopatia garatzen duena bestetik) kuprizona ereduan garatutako protokoloa. Honen interesa, sagu eredu desberdinek jasaten duten patologia desberdinean datza. Kuprizona ereduan aipatu da desmielinizazioa dela kaltearen eragile nagusia. Alzheimer ereduetan aldiz, patologiak garunaren materia txuri eta grisean kalte sakonak eragin ditzake modu konplexuan, axoien eta neuronen galtzea eraginez. Aipatzekoa da ikerketa honetan ez dugula aldaketa nabarmenik ikusi mielinari dagokionez bi Alzheimer ereduetan. Hala ere, amiloide plakak garatzen dituen ereduan, erresonantzia magnetikoaren bidezko irudigintzak garuneko materia zurian (ustez axoien kaltea dela eta) eta garuneko eskualde desberdinetan atrofia alterazioak agerian utzi ditu, tautopatia garatzen duen ereduan horrelakoak ikusi ez diren bitartean. Bi ereduetan alterazioak ikusi dira materia grisean, seguru asko, amiloide plakek edo tau

proteinek seinalean duten eragin zuzenaren edo sortzen duten kaltearen ondorioz. Ikerketa honen bidez, MRI multiparametrikoaren erabilgarritasuna frogatu, eta aztertutako parametro ugariek prozesu patologiko desberdinenganako sentikortasuna (eta mielinarekiko espezifikotasun eza zenbaitetan) dutela ikusi ahal izan dugu testuinguru desberdin batetan. Gainera, amiloide proteinek alde batetik eta tau proteinek bestetik, garunean eragiten duten kaltea deskribatu ahal izan dugu.

Orain arte ikusi dugun moduan, lan hau hein handi batetan irudi anatomikorako protokolo esperimentalak garatzera bideratu da, eta horrek patologia desberdinen garapenarekin erlazionatutako aldaketa aztertzea ahalbidetu du. Bestalde, lan honen beste atal garrantzitsu bat irudi funtzionalerako protokoloak garatzea izan da. Bermielinizazio eta desmielinizazio prozesuek garunean duten eragina aztertu da. Horrela, atseden egoeran egindako erresonantzia magnetiko irudigintza funtzionala (rs-fMRI) burutu da kuprizona ereduan modu longitunalean, patologiaren hasieran garuneko hiper-aktibitatearen fase bat dagoela antzemanez (Alzheimerra edo esklerosi anizkoitza bezalako patologietan ere gertatzen den bezala), eta ondoren, hipo-aktibitate edo konektibitate murriztuko fase bat ikusiz. Aldi berean, bermielinizazio prozesuan zehar, garunaren funtzioen berreskurapen progresiboa ikusi genuen. Prozesu horretan, beste sagu talde batetan, clemastina terapia bermielinizatzailea probatu zen eta konposatu honen izaera birsortzailea frogatu genuen, bai anatomikoki zein funtzionalki.

Irudi funtzionalen protokoloak oso eraginkorrak izan dira bermielinizazio eta desmielinizazio prozesuak deskribatzeko, neurona sare ezberdinek kaltetze eta berreskurapen patroi tenporalak erakusten dituztelarik. Emaitza honek terapia berrien garapenean lagundu dezake, ikuspuntu funtzionalaren arabera, tratamenduen administraziorako jarraibideak garatzea ahalbidetuz.

Nerbio sistema zentraleko gaixotasun asko kronikoki jasaten dira bizitzan zehar, garapen isilean hasiz, heldutasunean klinikoki agertuz eta zahartzaroan bere alderdirik erasokorrena erakutsiz. Garunaren bereizgarritasunetako bat bere plastikotasuna da, bere antolamenduak eta funtzionamenduak etengabe eboluzionatzen baitute bizitzan zehar. Hori dela eta uste dugu garrantzitsua dela indibiduo osasuntsuetan heltze eta zahartze prozesuak aztertzea, modu naturalean indibiduo osasuntsuetan ematen diren aldaketak eta gaixotasun desberdinei dagozkien alterazioak desberdintzeko. Hori ikertzeko, 2 hilabetetan hasi eta 13 hilabetera arte sagu osasuntsuetan konektibitate funtzionalaren bilakaera aztertzeko garatutako MRI protokolo funtzionalak erabili ditugu. Saguen biziraupenaren ikuspuntutik hau denbora luzea da, beraien batez besteko bizi itxaropena 25-27 hilabete ingurukoa da eta. Modu honetan, garun konektibitatea 2 eta 8-9 hilabetera arte progresiboki nola handitzen den ikusi ahal izan dugu, hortik aurrera progresiboki jaitsiz 13 hilabetera arte, sagu gazteetan ikusitakoaren antzeko balioak ikusiz azken puntu honetan. Emaitza hauek kontuan hartzekoak dira saguekin ikerketak egiterako orduan, bai esperimentu diseinu aldetik, baita emaitzen interpretazio aldera ere.

Laburbilduz, desmielinizazio eta bermielinizazioa, hots mielina, ikertzeko oinarrizko zutabe gisa balio izan duten neurodegenerazio eredu ugari erabili dira tesi honetan, mielinaren irudi sentikor eta espezifikoak egiteko oinarriak ezarri dira eta mielinaren kalte edo birsorkuntza maila anatomiko eta funtzionalean aztertu da. Hori dela eta, uste dugu lan honek eragin handia izango duela etorkizunean bermielinizazio terapia eraginkorrak garatzeko.

Resumen

Las enfermedades del sistema nervioso central afectan a millones de personas en el mundo, deteriorando de forma significativa su nivel de vida. Entre ellas están las enfermedades neurodegenerativas que afectan principalmente al cerebro, como el Alzheimer, la esclerosis múltiple o el Parkinson, que se caracterizan por la muerte paulatina de las neuronas con su consiguiente deterioro cognitivo y pérdida de autonomía en la vida diaria. Sin embargo, no solo de neuronas está compuesto el cerebro, ya que astrocitos, microglía y oligodendrocitos ejercen una función fundamental abasteciendo las necesidades de las primeras, estableciendo una comunicación directa con el sistema inmunológico o mielinizando los axones de las neuronas. Concretamente, la mielina, es el objeto de estudio de este trabajo.

Las neuronas, están formadas por dendritas, axones y el soma, donde encontramos el núcleo. El impulso eléctrico viaja a lo largo de las neuronas a través de los axones, permitido por la abrupta alteración en la concentración de iones a los dos lados del axón. En este contexto, la mielina juega un papel fundamental recubriendo los axones. Esta vaina lipídica posibilita una rápida y energéticamente eficiente transmisión del impulso eléctrico proporcionando aislamiento al axón neuronal. Los oligodendrocitos son los responsables de sintetizar y mantener la mielina en el sistema nervioso central, además de proveer de metabolitos (p.ej. lactato y piruvato) a las neuronas para poder hacer frente el elevado gasto energético de estas.

La pérdida de la mielina o desmielinización puede dar lugar a la atrofia axonal y muerte neuronal. Esta pérdida puede revertirse por medio de la remielinización, llevada a cabo por los oligodendrocitos. En este proceso reparador, las células precursoras de oligodendrocitos proliferan, migran al lugar de la lesión y se diferencian en oligodendrocitos mielinizantes, los cuales regeneran la vaina de mielina produciendo un característico recubrimiento de mielina más fino que el original.

Los procesos desmielinizantes han sido descritos en varias patologías como la isquemia, el Alzheimer, la lesión cerebral traumática o la esclerosis múltiple, donde la pérdida de mielina es la protagonista principal en una patología de gran complejidad. La esclerosis múltiple es una enfermedad autoinmune neurodegenerativa que se caracteriza por el ataque del sistema inmunológico a la vaina de mielina, causando placas desmielinizantes. En los primeros estadios de la enfermedad, la remielinización puede ser extensa y evitar el deterioro cognitivo. Sin embargo, los repetidos brotes a lo largo del tiempo junto con la pérdida de eficiencia regenerativa causada por el envejecimiento, hacen que este proceso pierda eficiencia. Así, los pacientes de esclerosis múltiple suelen entrar en una fase progresiva en la que la pérdida neuronal y la pérdida de funciones son sustanciales e irreversibles.

Hasta la fecha, los tratamientos en la esclerosis múltiple se han centrado en frenar los brotes que dañan el sistema nervioso central, mediante terapias inmunosupresoras o inmunoreguladoras. Puede afirmarse que la eficiencia de estos tratamientos ha posibilitado tener una mejor calidad de vida a los pacientes y ha reducido de forma abrumadora la frecuencia de estos brotes. A pesar de ello, la incompleta recuperación después de un brote y la acumulación del daño a lo largo del tiempo hacen que el paciente sufra un deterioro cognitivo por pérdida neuronal. Por este motivo, la remielinización ha sido objeto de estudio en los últimos años e impulsar este proceso mediante a tratamientos está en el foco de la investigación. Estos tratamientos se centran principalmente en promover la diferenciación de células precursoras de oligodendrocitos en oligodendrocitos maduros, proceso que se ha visto afectado en esta y otras patologías en estudios *post-mortem* realizados en humanos. El desarrollo de terapias remielinizantes exige un profundo entendimiento de los procesos de desmielinización y remielinización, la definición

de modelos experimentales adecuados para su estudio, y el desarrollo de técnicas que permitan evaluar de forman no invasiva el efecto de un determinado tratamiento.

El estudio de estos procesos se realiza principalmente en modelos *in vitro* con cultivos de células precursoras de oligodendrocitos, en modelos ex vivo con cultivos organotípicos (finos cortes de cerebelo cultivados) y en modelos *in vivo* con animales, principalmente en los modelos murinos EAE y cuprizona. Para el desarrollo de estudios longitudinales que permitan monitorizar los procesos de desmielinización y remielinización a lo largo del tiempo es imprescindible el desarrollo de técnicas no-invasivas, reproducibles, robustas y que permitan cuantificar de forma precisa la cantidad de mielina con la progresión de la enfermedad o en respuesta a un tratamiento.

En este sentido la imagen por resonancia magnética debe jugar un papel fundamental. Esta técnica se caracteriza por su carácter no invasivo, su alta resolución y su versatilidad, además de su magnífica sensibilidad para el diagnóstico de placas desmielinizantes en la esclerosis múltiple. La resonancia magnética ofrece un amplio abanico de posibilidades, ya que permite obtener imágenes anatómicas de alta calidad con múltiples contrastes, determinar la función y activación de diferentes regiones del cerebro u obtener imágenes de difusión del agua, las cuales ofrecen un gran contraste entre tejidos estructurados como la materia blanca (rica en mielina) y tejidos menos estructurados como la materia gris. A pesar de ello, hoy en día no existe ningún protocolo o técnica universalmente aceptada de imagen por resonancia magnética que ofrezca una medida (un parámetro medible) precisa del contenido de mielina en un tejido, a pesar de que varias técnicas hayan sido postuladas en la literatura como potenciales indicadoras del contenido de mielina.

En este trabajo hemos desarrollado modelos y protocolos experimentales para el uso de la resonancia magnética de alto campo (11.7 Teslas) para la cuantificación del contenido de mielina, y procesos asociados a ellos, dividiendo el trabajo en 5 apartados diferentes: 1) Desarrollo de protocolos de imagen por resonancia magnética para la cuantificación de mielina en cultivos organotípicos; 2) Estudio multiparamétrico longitudinal de imagen por resonancia magnética para la cuantificación del contenido de melina y monitorización de los procesos de desmielinización y remielinización en el modelo murino cuprizona; 3) Estudio multiparamétrico de imagen por resonancia magnética para la evaluación de alteraciones en la materia gris, y del contenido de mielina en dos modelos animales de Alzheimer; 4) Estudio de imagen por resonancia magnética funcional en estado de reposo para la evaluación del impacto de los procesos de desmielinización y remielinización, y de la aplicación de la potencial terapia remielinizante clemastina en la conectividad cerebral: 5) Estudio de imagen por resonancia magnética funcional en estado de reposo para estudiar el efecto del envejecimiento en la conectividad cerebral. Hay que mencionar que si bien los modelos de Alzheimer y de envejecimiento no son el objeto principal de este trabajo, pueden transcurrir con cierto grado de desmielinización. Su inclusión en el estudio nos ha permitido validar experimentalmente las metodología desarrolladas para estudiar la desmielinización asociada a la esclerosis múltiple, dotándolos así de robustez y universalidad para el estudio del sistema nervioso central.

El primer apartado, el relativo a la imagen de cultivos organotípicos, ha supuesto un reto mayúsculo que nos ha hecho llevar al límite las capacidades de la técnica experimental de imagen por RM. El cultivo de rodajas de cerebelo de ratones de 7-12 días es considerado un modelo *ex vivo* adecuado para el estudio de la mielina, ya que la aplicación del detergente lisolecitina provoca la desmielinización en el cultivo,

seguida de una remielinización espontanea. En una estrategia reduccionista, se ha comenzado por hacer imagen de rodajas de cerebro (0.3-1 mm de grosor), pasando después a cultivos organotípicos gruesos (más delgados que los anteriores y con una estructura más endeble), para finalizar con cultivos organotípicos convencionales, mucho más finos (<0.1 mm). La imagen de rodajas de cerebro y de cultivos organotípicos gruesos ha resultado exitosa, obteniendo imágenes de alta relación señal-ruido y un buen contraste entre materia blanca y gris. Sin embargo, los cultivos organotípicos finos (en origen de 300-350 μm), tras 7 días en cultivo pasan a tener un grosor de menos de 100 μm, que complica sobremanera la obtención de imágenes por resonancia magnética. A pesar de haber obtenido imágenes con buena relación señal-ruido, el tejido no ha mostrado contraste entre las zonas de materia blanca y gris. En una aproximación experimental avanzada hemos intentado hacer uso de la nanotecnología para desarrollar sondas de imagen molecular específicas de mielina, que permitirían paliar el inherente bajo contraste de la materia blanca en estos cultivos aumentando la sensibilidad de detección de la mielina mediante reconocimiento molecular. En nuestros estudios hemos hecho pruebas de concepto que demuestran el potencial de esta técnica. Sin embargo, nos hemos encontrado con que a pesar de haber intentado aumentar el contraste mediante liposomas funcionalizados específicos a la mielina, marcados con gadolinio y sondas fluorescentes, las uniones no-específicas de estas sondas con el tejido nos ha hecho ver que aún queda mucho trabajo que desarrollar en esta línea. Su desarrollo temporal va a traspasar el límite de este trabajo de tesis doctoral.

Para pasar de modelos *ex vivo* a *in vivo* se ha trabajado con el modelo murino cuprizona, en el que la intoxicación del ratón por dieta oral a través de este agente quelante de cobre produce una extensa desmielinización en los tractos de materia blanca cerebrales. La principal característica y ventaja de este modelo es que la

desmielinización se produce de forma progresiva alcanzando su máximo a las 5 semanas, seguida por una remielinización espontanea al cesar la administración del tóxico. En este estudio se ha realizado una monitorización del contenido de mielina con una resolución espacio-temporal sin precedentes, adquiriendo una batería de 9 imágenes potencialmente específicas a la mielina durante las 10 semanas del experimento. Como complemento, se han llevado a cabo estudios *post mortem* mediante la tinción específica de mielina Luxol fast blue, identificando claramente los procesos de desmielinización y remielinización y permitiendo establecer correlaciones directas entre los resultados histopatológicos con la señal obtenida por imagen por resonancia magnética. Así, hemos podido concluir que la imagen ponderada en T2 es la que mayor especificidad ofrece, además de una alta sensibilidad y capacidad de diferenciar los estados de desmielinización, remielinización y tejido sano. Cabe mencionar que la imagen ponderada en T2 se adquiere de forma rutinaria en laboratorios y hospitales de todo el mundo, al contrario de otras modalidades.

En este trabajo se han identificado también patrones temporales diferentes de desmielinización-remielinización en diferentes regiones del cerebro, comenzando a las 2 semanas tras la exposición al tóxico. Finalmente, se han estudiado las consecuencias de la desmielinización a nivel crónico, realizando el mismo procedimiento 6 meses después de la exposición al tóxico y pudiendo mostrar todavía diferencias notables entre ratones sanos e intoxicados.

A continuación, en un intento de validar la capacidad del protocolo experimental desarrollado para caracterizar los cambios en la mielina, hemos repetido nuestros estudios en dos modelos de ratón de Alzheimer, uno de ellos con sobreexpresión de la proteína precursora de amiloide (APP) y otro con sobreexpresión de la proteína tau. La gran ventaja de los modelos *in vivo* es que nos permiten segregar estos dos

procesos patológicos que tienen lugar en el Alzheimer, para estudiarlos por separado. Haciendo uso de técnicas histológicas, se ha medido el contenido de mielina en ambos modelos, no observando alteraciones sustanciales en este aspecto. Sin embargo, la imagen por resonancia magnética ha revelado alteraciones en la sustancia blanca (presumiblemente daño axonal) del cerebro y atrofia cerebral en diferentes regiones en el modelo de ratón que sobreexpresa proteína precursora de amiloide, mientras que estas anomalías no han sido detectadas en el modelo que sobreexpresa proteína tau. Es decir, en estas patologías puede haber daño axonal, pero no debido a una pérdida significativa de mielina, como ocurre en la esclerosis múltiple. Adicionalmente, hemos podido observar alteraciones en zonas de materia gris, probablemente debidas a la presencia de placas de β-amiloide u ovillos neurofibrilares (compuestos de proteína tau), o debidos a los procesos patológicos desencadenados por estos. Así pues hemos podido demostrar la utilidad de la realización de estudios de imagen por MRI multiparamétricos, que permiten distinguir los procesos de desmielinización de otros procesos patológicos en el cerebro.

Si bien gran parte de este trabajo se centra en el estudio de parámetros de imagen que nos permitan estudiar alteraciones patológicas asociadas a la mielina, otra gran parte se ha centrado en el desarrollo de protocolos experimentales de imagen funcional que nos permitiesen estudiar el impacto de los procesos de remielinización y desmielinización en la función cerebral. Así, se ha realizado un estudio longitudinal de imagen por resonancia magnética funcional en estado de reposo (rs-fMRI) durante los procesos de desmielinización y remielinización en el modelo de cuprizona, detectando que existe una fase de hiperactividad cerebral al inicio de la patología (como es conocido que ocurre también en patologías como el

Alzheimer o la esclerosis múltiple), para más adelante continuar con un estado de hipoactividad y disminución de la conectividad en las redes neuronales del cerebro.

En paralelo, durante los procesos de remielinización o regeneración, hemos sido capaces de detectar una recuperación paulatina de la función cerebral, proceso en el que el uso de un agente remielinizante como terapia, la clemastina, ha demostrado su carácter beneficioso, tanto a nivel anatómico como funcional. Los protocolos experimentales de imagen funcional se han mostrado muy eficaces a la hora de describir estos cambios, mostrando que diferentes redes neuronales muestran patrones temporales de deterioro y recuperación diferentes. Este resultado podría dar lugar a terapias más efectivas desde el punto de vista funcional, al permitir el desarrollo de pautas de administración de tratamientos con varios puntos temporales diferentes.

Muchas de las enfermedades del sistema nervioso central transcurren de forma crónica a lo largo de toda la vida del sujeto que las padece, comenzando de forma silente durante el desarrollo, mostrándose de forma clínica en la edad adulta, y mostrando su lado más agresivo durante el envejecimiento. Pero el cerebro es un sistema plástico, cuya organización y funcionamiento evoluciona constantemente a lo largo de la vida. Por ello creemos que es importante estudiar los procesos de maduración y envejecimiento en sujetos sanos, para poder distinguir cambios naturales de la función cerebral de aquellos cambios que son consecuencia de procesos patológicos o de terapias aplicadas frente a los mismos. Por ello, hemos utilizado los protocolos de imagen funcional en ratones sanos desde los 2 meses de edad hasta los 13 (un largo periodo de tiempo, teniendo en cuenta que la esperanza de vida media de un ratón es de unos 750-800 días para ratones de la cepa C57BL). De este modo hemos podido observar como la conectividad cerebral aumenta progresivamente desde los 2 hasta los 8-9 meses de edad para, a partir de ahí,

descender progresivamente hasta los 13 meses de edad, llegando a valores similares a los observados en ratones jóvenes de 2 meses de edad. Por lo tanto, hemos podido describir como el cerebro del ratón madura hasta los 8-9 meses y comienza a mostrar alteraciones en la conectividad cerebral a partir de este punto. De este modo es de esperar un declive de actividad cerebral en sujetos sanos usados como control en estudios con animales envejecidos, que deberá tenerse en cuenta en la interpretación de resultados cuando se comparen con sujetos patológicos.

En resumen, en esta tesis en la que se han utilizado varios modelos murinos de neurodegeneración como pilar fundamental para el estudio de la desmielinización y remielinización, se han sentado las bases para realizar una imagen sensible y específica de mielina y se ha estudiado el impacto a nivel anatómico y funcional de los procesos patológicos asociados esta, revelando importantes alteraciones que transcurren con diferente perfil temporal en diferentes zonas y redes del cerebro. Por ello consideramos que este trabajo tendrá un impacto considerable para el desarrollo de terapias remielinizantes efectivas en el futuro.

Introduction

Diseases of the Central Nervous System (CNS) include autoimmune diseases, cerebrovascular diseases, neurodegenerative and neurodevelopmental diseases, and traumatic injuries. Pathologies such as multiple sclerosis, Alzheimer's disease, traumatic brain injury or stroke, for instance, erode the well-being of countless people in the world. Meanwhile, the application of neuroprotective and neuroregenerative strategies raises hope for overcoming CNS diseases. Along with the development of new therapies, it is imperative to generate novel technologies to evaluate the progression of disease and the effectiveness of such therapies, not only in order to achieve a deep understanding of the mechanisms behind damage but also to reach a profound comprehension of the brain. Certainly, in a great extent due to implications of population aging, CNS diseases and understanding the complex function of the brain are among the major challenges for the XXI century for all humankind.

1. The central nervous system

The CNS is made of more than 100 billion cells composing the brain, spinal cord and retina. It is responsible for cognition, actions, senses and emotion and its energy consumption corresponds to the 20% of the total required energy in humans [1]. This system is protected by bones (skull and vertebrae) and by the blood-brain barrier (BBB) that confers a separation from the systemic blood circulation. Its isolation from the exterior makes the CNS less vulnerable to toxins or hazardous pathogens, but more difficult to reach by therapeutics when required, a situation aggravated by the limited self-repair capacity of the CNS.

Cell populations in the brain can be subdivided into glial cells and neurons, each group composed of approximately 85 billion cells [2]. Glial cells are encompassing astrocytes, oligodendrocytes and microglia. They have multiple functions, such as

supporting the neurons [3], regulating synaptic transmission [4], [5], myelinating of axons [6], maintaining and regulating the blood-brain barrier functionality [7] and being responsible for the cross-talk with the immune system [8]. It should not be surprising therefore that alterations in microglia could be underlying degenerative and inflammatory disorders in the CNS [9].

Neurons are responsible for receiving, storing and processing the information and are vulnerable to external damage. Their loss results in cognitive decline and loss of function. This is aggravated by the fact that mature neurons are post mitotic cells, unable to conduct division, adding difficulty to the regeneration of lost connections. Additionally, the complex network consisting of interactions between and within microglia and neurons is hard to understand, and challenging to restore, with currently available techniques and therapies.

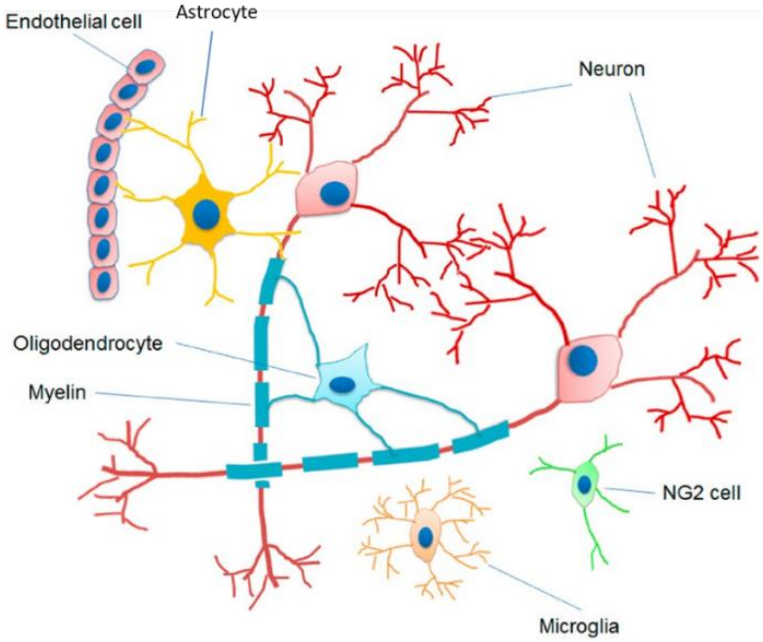

Figure 1. *Glial cells and neurons in the CNS. Adapted from* [10].

Basic understanding of the mechanisms of neuronal function and impulse transmission is required to better understand the implication of such functions in CNS diseases. Neurons are composed by the soma, or cell body, axons and dendrites. The transmission of the electrical signal through the axon lies in the generation of an unequal charge across the membrane of the neuron, by altering the ion concentrations between the inner and outer space of the cell (i.e. by establishing transmembrane ion concentration gradients) [11].

Briefly, at a resting state, and regulated by Na^+/K^+ pumps, high concentrations of sodium ions are kept at the outside of the neuron, with a lower concentration in the inside, establishing a potential of approximately -60 millivolts (lower in the inner space) between both sides of the membrane. Together with Na^+/K^+ pumps, the presence of gated channels sensitive to neurotransmitters enables an abrupt alteration of ion concentrations at both sides of the wall. With the advent of excitation produced by the neurotransmitters, in a phenomenon called depolarization, sodium channels located at the initial axonal segment of the neuron allow the massive entrance of sodium ions into the cell resulting in an inner positive charge, generating an action potential. This effect is propagated throughout the axon, soma and dendrites by voltage-gated sodium channels. Once the action potential reaches the dendrites, a release of neurotransmitters to the synaptic cleft of target neurons will be carried out depending on the strength and frequency of the action potentials. In this way, neurotransmitters release regulates the amplitude or strength of the next action potential [12].

Once the impulse has been transmitted, the repolarization of the cell membrane takes place, when K^+ channels compensate the charge by an accumulation of potassium ions into the extracellular space. Finally, the potential of the membrane goes back to normal [12].

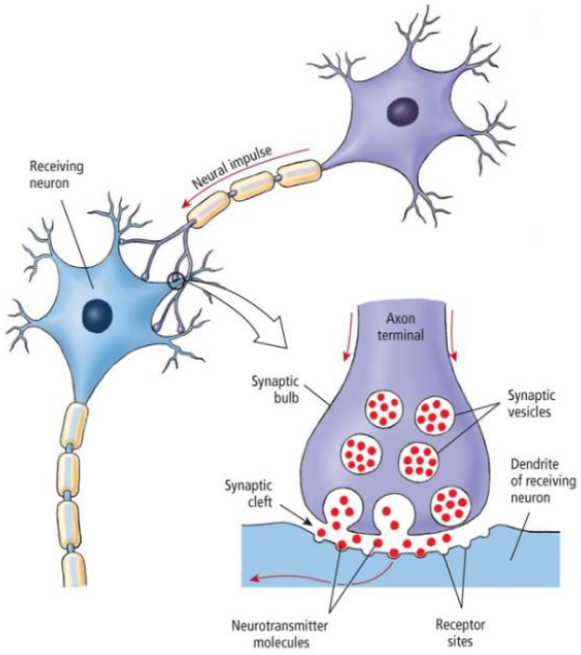

***Figure 2**. Neuronal synapse. Neurotransmitters are released into the synaptic cleft, which might trigger the generation of the action potential.*

Even though the propagation of action potentials takes place at high speed, the leaking of sodium ions towards the extracellular space makes the impulse progressively weak. In this context, myelin becomes a crucial player in the process of nerve impulse transmission. Myelin is a proteolipid membrane that wraps axons and provides insulation to them, preventing a high sodium ions leakage into the extracellular space and allowing a fast transmission of impulses. Hence, action potentials can travel at speeds up of 100 m/s, making possible a rapid response to a given stimulus [13].

2. Myelin

Myelin is a compact and highly organized multilamellar membrane that wraps axons of vertebrates, generated by oligodendrocytes in the CNS and by Schwann cells in the peripheral nervous system. Oligodendrocytes are metabolically very active and can generate around 5000-50000 mm^2 of myelin per cell per day, when myelination takes place [14]. The generated membrane is composed of spirally enwrapped units of double bilayers separated by an aqueous solution with a thickness of 3-4 nm [15]. In axons, the large myelinated region through which the electric impulse is transmitted is known as internode and is only interrupted with 1μm gaps named nodes of Ranvier, where a high concentration of Na^+ and K^+ channels allow the amplification of the impulse until the next node (Fig. 3).

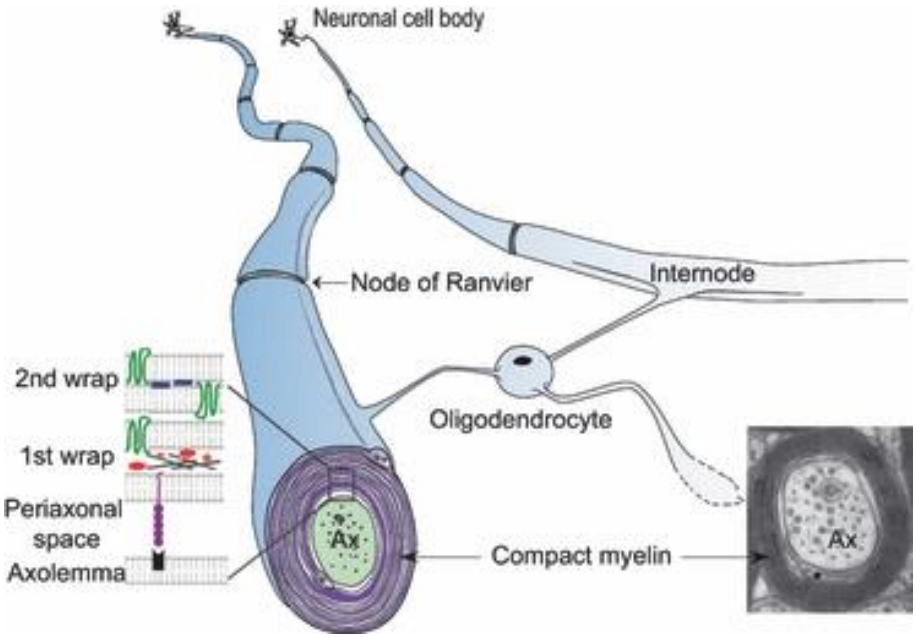

Figure 3. *Myelin sheath structure. The compact myelin membrane is extended all along the internode, closely interacting with oligodendrocytes* [16].

Myelin is approximately composed of 80% lipids and 20% proteins. The most abundant lipids are phospholipids and glycosphingolipids, which combine with cholesterol, while the most abundant proteins are myelin basic protein (MBP), proteolipid protein (PLP) and cyclic nucleotide phosphodiesterase (CNP). The importance of each of this components in function has been determined through transgenic mouse models, in which mice lacking myelin proteins such as CNP or PLP have shown axonal degeneration [17], [18].

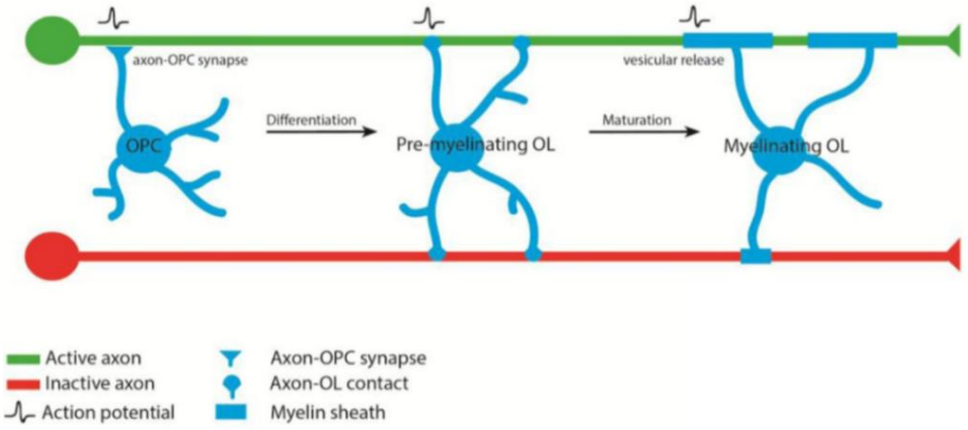

Figure 4. *Neural activity induces myelination by stimulating the differentiation of OPCs into myelinating oligodendrocytes (OL)* [19].

In the CNS, myelin comprises the 50% of the dry weight of white matter, where mainly myelinated axons are found, although myelinated fibres are also found in grey matter. As mentioned before, myelin provides electrical insulation to the neuronal axon, enabling a fast and energetically efficient transmission of action potentials. The speed of transmission is influenced by the ratio between the myelin sheath thickness and the axon diameter, named the g-ratio, which is around 0.7 in healthy axons [20]. The extent of myelination, and therefore the g-ratio, is regulated

by neural activity due to the cross-talk between oligodendrocytes (the producers of myelin) and neurons [21]. Interestingly, mice that have learnt to run on a complex running wheel have shown increased myelinating cell proliferation [22].

Additionally, myelin may provide trophic support to axons mediating axon-oligodendrocyte interaction [23], [24]. Lactate has been put forward as a candidate compound for meeting the high energetic axonal demand. In fact, it has been shown that axonal degeneration takes place when lactate release through the monocarboxylate transporter 1 (MCT1) is disrupted in oligodendrocytes [23]. The production of lactate in oligodendrocytes might be regulated by glutamate mediated axonal signal and released through the axo-myelinic synapse [24], [25].

3. Demyelination and remyelination.

Demyelination is the pathological process by which the myelin membrane is damaged. This can be caused by several reasons such as autoimmune reactions, infectious agents or trauma.

Regardless of the triggering cause and pathway, demyelination leads to a disruption of the signal conduction, as a consequence of the uneven distribution of Na^+ and K^+ channels along the axon, and in case an inflammatory response takes place, by the hazardous effects of extracellular compounds such as nitric oxide (NO), proteases, excitotoxins or chondroitin sulphate proteoglycans (CSPGs) [26], [27]. In this setting, denuded axons are prone to degenerate leading irreversibly to neuronal loss. Indeed, degeneration of chronically demyelinated axons is a major contributor to disability in MS patients and other pathologies.

This condition can be reverted through different ways including redistribution of Na^+ channels to restore the conduction of the electric impulse. This is enabled by the

migration of channels from the nodes of Ranvier all along the internode [28]. Nevertheless, this turns the conduction into a more demanding process in terms of energy. In case of such energy increment cannot be met, toxic levels of Ca^{2+} accumulate in the axons, leading to proteolytic enzyme mediated degeneration [29]. The absence of myelin might also make challenging the communication between axons and oligodendrocytes. Indeed, it has been described that axonal degeneration induces oligodendrocyte death, revealing the importance of the axon-oligodendrocyte cross-talk [17].

In order to prevent axonal degeneration, and in the end disability, remyelination is of utmost importance. This neuroprotective process consists in the restoration of myelin sheath, ensuring axonal viability. For the completion of remyelination, signalling molecules released by microglia and astrocytes, activate the proliferation of oligodendrocyte precursor cells (OPCs), existing in the subventricular zone. Next, OPCs recruitment at lesion site takes place. These cells have shown a high migrating capacity compared to neurons and other glial cells [30]. In embryonic mice, OPCs have shown to migrate by closely interacting and attaching with brain blood vessels, keeping their undifferentiated state until their arrival to demyelinated sites [31]. Certainly, endothelium in vascular vessels might play an important role in regulating the differentiating stage of OPCs [32].

OPCs differentiation starts with a substantial morphological change followed by attachment to the axon, expression of myelinating genes and the formation of myelin sheaths, boosted by growth factors, cytokines, chemokines, signalling molecules, transcription factors or mRNA, secreted by several cell types [33].

A characteristic feature of remyelinated axons is that they possess a thinner myelin membrane yielding in decreased g-ratios. In any case, still efficient conduction of

action potentials may be achieved, preventing axons from total degeneration. Efficient and accelerated remyelination in response to a demyelinating insult can avoid extensive axonal loss [34]. Of note, even though OPCs are the main source of mature oligodendrocytes, neural progenitor cells (NPCs) are also able to differentiate into myelinating oligodendrocytes.

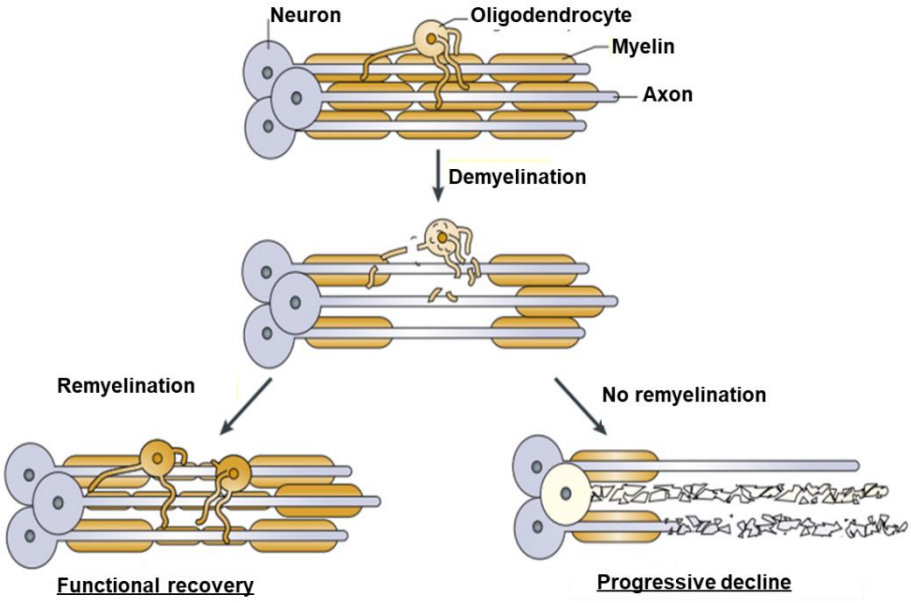

Figure 5. *Axonal fate after demyelinating insult. Myelin can be restored through remyelination, providing enough insulation to the axon to prevent its degeneration. Adapted from* [35].

However, remyelination very often fails after a demyelinating insult [36]. Unsuccessful completion of proliferation, migration and differentiation or even exhaustion of the pool of precursor cells might lie behind failed attempts of remyelination [37]. Certainly, many factors inhibit the recruitment or differentiation of OPCs during demyelination, including altered extracellular matrix, astrogliosis, presence of myelin debris, or downregulation of growth and trophic factors [38].

Post-mortem analysis conducted in multiple sclerosis patients has described undifferentiated OPCs populations around lesions [39], [40], which might be due to failed differentiation or to insufficient recruitment of OPCs, since cell density is crucial to accomplish differentiation. Nevertheless, the enhancement of OPC recruitment has not been effective in boosting remyelination by itself [41].

In this context remyelination therapies targeting differentiation could boost efficient and sharp remyelination by the implantation of exogenous cells that could promote this process, or by boosting endogenous remyelination by, for example suppressing the aforementioned inhibitory factors or by boosting the existing mechanism. Even though there is no approved therapy yet to promote remyelination, during the last years remyelination therapies are been addressed both in animal experimentation and human clinical trials.

4. Remyelination as an strategy for various neurodegenerative pathologies

Myelin is essential for the proper functioning of the nervous system. Myelination is a postnatal process that is completed during adulthood [42]. This has been confirmed by magnetic resonance imaging (MRI) measurements of fractional anisotropy (FA), which have shown that white matter content increases during the first three decades of life, peaking at middle age and decreasing thereafter. On the contrary, myelin regeneration takes place throughout the whole life, losing efficiency with aging. Constituent proteins and lipids of myelin are replaced with a half-life ranging from several weeks to months [43]. Alteration of the natural balance between the generation of new myelin versus the digestion of replaced sheaths leads to pathological processes that can be devastating for the patient, with significant alteration of basic functions and decline of cognitive capacities. The imbalance can

be triggered as a consequence of aging or by pathologies such as multiple sclerosis (MS), Alzheimer's disease, stroke, optic neuritis, etc.

Thus, the study of myelin composition and function and the understanding of its loss (demyelination) and restoration (remyelination) are needs of paramount importance for the development of efficient therapies against demyelinating diseases, and to facilitate a healthy and active aging. Along the next sections, the main causes of demyelination are briefly described.

4.1. Multiple sclerosis

Multiple sclerosis is an autoimmune disease of the central nervous which results in demyelination. In 85% of cases, the disease is not progressive but manifested in the form of relapsing-remitting periods, in which an abrupt attack of immune T-cells to myelin sheaths, enabled by the disruption of the blood-brain barrier, is followed by a remission of this process. As a consequence of inflammation, many other pathophysiological processes take place in the CNS detectable by MRI, such as oxidative stress, mitochondrial damage, glutamate mediated excitotoxicity, iron accumulation, sodium accumulation, demyelination and cellular and axonal loss [44]. In this condition, demyelinating lesions or plaques show up heterogeneously distributed throughout the CNS.

During the first stage of the disease, remyelination is extensive in a subset of patients, enabling the recovery of functional deficits [45]. However, this regenerative process progressively loses its efficiency, leading to a progressive phase in which the patient usually undergo cerebral atrophy, axonal degeneration and cognitive decline. This is thought to be caused by continuous demyelinating insults along with disease progression and aging [46]. Moreover, *post-mortem*

studies conducted in humans revealed the presence of undifferentiated OPCs around of chronically demyelinated plaques or the absence of OPCs [47], indicating that in this phase remyelination is not further taking place at significant levels [39].

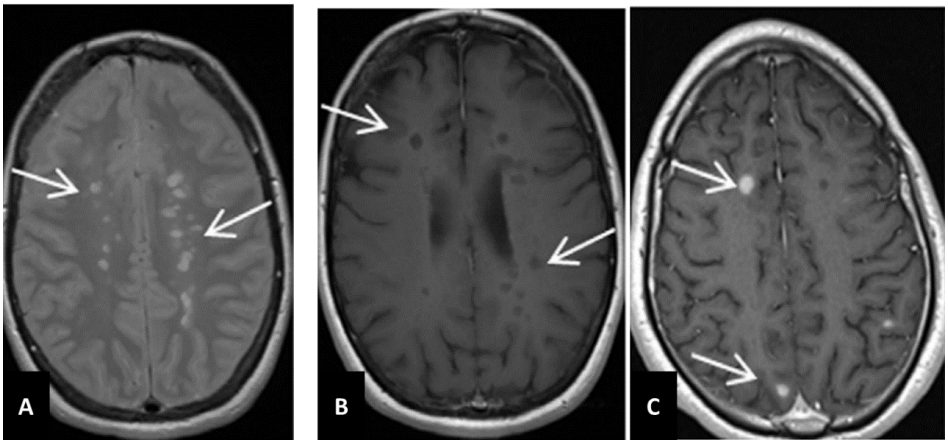

Figure 6. *Radiological signs of Multiple sclerosis with a typical distribution of lesions as observed in MRI. (A) T2-weighted, (B) T1-weighted, and (C) Gadolinium contrast enhanced T1-weighted MR images showing demyelinated plaques in multiple sclerosis patients* [48].

Currently approved therapies against MS target the modulation or suppression of the immune system. This has successfully led to an important reduction of relapses and a much slower progression of the disease [49]. However, therapies addressing remyelination or neuroprotection have not been approved yet. In consequence, patients are condemned to suffer the consequences of already happened degeneration, even in the absence of relapses [50].

During the last decades, research in MS has set focus on promoting remyelination. Several treatments have proved efficiency in preclinical models. However, all the therapies in this direction that have succeeded in animal studies finally failed in humans. At this moment the antihistamine Clemastine fumarate has shown to

reduce significantly the visual evoked potentials (VEP) in chronic demyelinating optic neuropathy by inducing remyelination [51]. According to previous studies, this improvement might be achieved by boosting OPCs differentiation into oligodendrocytes [34]. Finally, Temelinab, ((GNbAC1) an humanized antibody directed against the envelope protein (ENV) of multiple sclerosis associated retrovirus (MSRV)), has also shown remyelinating properties in clinical phase II [52], while the remyelinating potential of Fingolimod, a sphingosine 1-phosphate (S1P) receptor analogue and currently an MS approved drug as immunomodulator, is still inconclusive [53], [54].

4.1. Optic neuritis

Optic neuritis (ON) is the most common visual neuropathy [55], with an incidence of 1 per 100.000 people [56] and it is characterized by subacute visual loss. Usually, it is presented as a T cell-mediated inflammatory demyelinating disorder of the optic nerve [57], cursing with inflammation and oedema. Recovery starts approximately 1 week after the onset of the disease and, although patients usually recover almost completely their original visual capacities, consequences as impaired visual acuity, contrast sensitivity or colour vision remain [56].

Currently, steroids are generally used to slow down the attack but do not tackle nerve repair [58]. However numerous treatments are being tested in clinical trials at different stages targeting repair, all of them (except Anti-Lingo-1) were actually approved for other uses, such as simvastatin and erythropoietin alpha [56].

It has been described that optic nerve conduction velocity, measured as visual evoked potentials (VEP) tightly related to remyelination and ion channel reorganization, decrease during the first 2 years after the onset of the NO [59], [60],

indicating a (at least partial) restoration of signal conduction, and suggesting that function recovery might be achieved owing to remyelination processes. Unfortunately, no clinical improvements have been associated with a long-term decrease of VEP so far [59], [61], [62].

4.2. Leukodystrophies

Leukodystrophies are genetic disorders characterized by its heterogeneous manifestation and progressive nature, leading to alterations in white matter composition. They result from abnormalities in astrocytes, oligodendrocytes or other non-neuronal cell types [63]. These defects could affect lysosomal function, peroxisomal function, oligodendrocyte myelogenesis or astrocytes, preventing them from supporting remyelination in the CNS [35].

At the experimental level, the focus of researchers is set on genetic-based therapies through lentiviral adeno-associated virus vectors [64]–[66], and hematopoietic stem cells-based therapies [67], with promising results against adrenoleukodistrophies. Effects of stem cells go way beyond the replacement of abnormal cells, since they can improve the microenvironment, enabling glia maturation and white matter repair.

Leukodystrophies damage go way beyond myelin. The complexity of these disorders might call for multimodal therapies that can avoid axonopathy and vasculopathy [68]. Of note, growing scientific evidence confirms that axonal function does not only depend on myelin integrity, but also on the support provided by oligodendrocytes and astrocytes. Hence, remyelination therapies aimed only at differentiation, migration or proliferation of progenitor oligodendrocytic cells might fail in specific cases. Remyelination therapies together with gene or cell therapies in demyelinating leukodystrophies may be much more effective.

4.3. Aging

One of the most common causes of myelin loss is aging, defined as the time-dependent functional decline that affects most living organisms [69]. With aging, myelin digestion may become a challenging process for microglia, leading to the accumulation of lipofuscin granules in lysosomes in the elderly. Apart from the accumulation of these granules, myelin malformations are also characteristic of aging. Histological studies carried out in non-human primates have revealed the presence of myelin "balloons" [70], dense cytoplasm inclusions surrounded by myelin sheaths, and redundant myelin [71]. These abnormalities have been also seen in toxic demyelinating models and as a consequence of traumatic brain injury (TBI) [72]. Even though their cause is unknown, the presence of redundant myelin seems to decrease the conduction velocity, characteristic of elder subjects [73].

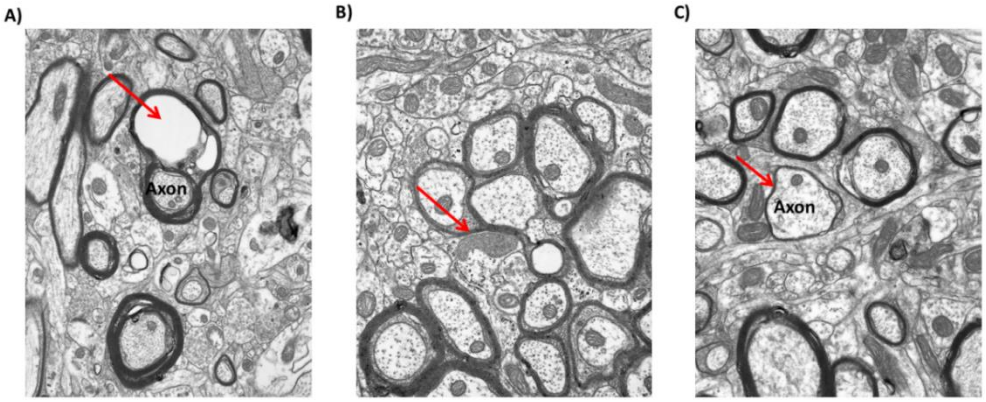

Figure 7. *Electron microscopy of aged non-human primate (rhesus monkey) brain. Myelin abnormalities are shown. Myelin balloons (A), redundant myelin (B) and remyelination (C) were observed in healthy rhesus monkeys* [73]. *http://www.bu.edu/agingbrain/*

Moreover, aging might be associated with white matter volume and weight loss [74]. Certainly, the weight of the brain was shown to be 11% lower in people aging 86

years or more, compared to young adults [75]. This value represents 150 g of tissue, assigned to cellular, myelin and fluid losses. In addition, *post-mortem* human histological studies revealed that demyelination in the periventricular and diffuse white matter might be associated to high Clinical Dementia Ratings (CDR) [76].

The increasing degeneration throughout life is not surprising, since regenerative processes lose their efficiency with age in most tissues [77]–[79]. Animal models have shown that remyelination after a demyelinating insult is completed within 4 weeks in young rats, while it takes up to 9 weeks in aged ones [80].

Environmental signals regulating remyelination, exhaustion of the pool of precursor cells, epigenetic changes [78], accumulation of myelin debris, failure in OPCs recruitment, or the incapability of OPCs to differentiate are among the main causes of the loss of efficiency in myelin regeneration processes [35], [81]. Both delayed recruitment of OPCs and a decrease in OPCs differentiation have been observed following the induction of demyelination in aged animals. Interestingly, heterochronic parabiosis (parabiotic pairing of two animals of different ages) where blood factors from young mates stimulate the differentiation of OPCs in the older mates, showed effective remyelination in aged models of spinal cord injury [82].

4.4. Stroke

Stroke is a leading cause of mortality and disability [83]. It is caused by a focal disruption of blood flow to the brain, mainly due to an artery occlusion (ischemic stroke) or rupture (hemorrhagic stroke). Stroke onset triggers a series of metabolic alterations in the brain that causes the death of cells of the neurovascular unit by apoptosis and necrosis [84]. The so-called ischemic core is the most affected area of brain tissue, with a rapid cellular loss. Conversely in the ischemic penumbra or peri-

infarct region, a reduced but not completely suppressed blood flow enables the eventual survival of cells. This makes the penumbra the major target for neuroprotective strategies [85].

For ischemic stroke (which accounts for the 80% of all strokes) restoration of blood flow in the first hours after an ischemic insult, either by surgical removal of the clot of by using recombined tissue plasminogen activator (rtpA), is the only currently approved treatment at the acute phase of the disease [86].

While preventing the extension of damage from the core to the peri-infarct region is important, the enhancement of reparative processes seems to be vital for functional recovery of the patients. The metabolic cascade after stroke results in oligodendrocyte death and subsequent demyelination, observed both in humans and rodents [87], [88]. Interestingly, diffusion MRI revealed that demyelination in the corpus callosum correlates with impaired motor function, after subcortical stroke in humans [89].

Microenvironment at the penumbra may represent a daunting challenge for tissue and function restoration. Increased levels of apoptosis, inflammation, free radicals, nitric oxide, glutamate or many other compounds resulting from the biochemical cascade triggered by the stroke, substantially hamper oligodendrogenesis [85]. Although OPCs proliferation has been reported, the differentiation into maturing oligodendrocytes frequently fails after stroke [90].

After the daunting cell loss, the organism enhances OPCs proliferation and inhibits differentiation into myelinating oligodendrocytes, in order to maintain a constant pool of precursor cells [91]. This has been reported to be performed by different signals, such as Wnt of Notch [92], [93]. Similarly, Nogo receptor 1 (NgR1) signalling pathway stimulates the differentiation of OPCs into astrocytes after stroke [94].

Hence, remyelinating potential therapies in stroke are focused on overcoming the inhibitory signals that avoid the differentiation of oligodendrocytes. For instance, the treatment with a Nogo receptor NgR1 antagonist [94], with Wnt-3a, the inhibition of phosphodiesterase III [95], or the cannabinoid antagonists WIN55, 212/2 [96] have all shown to promote remyelination.

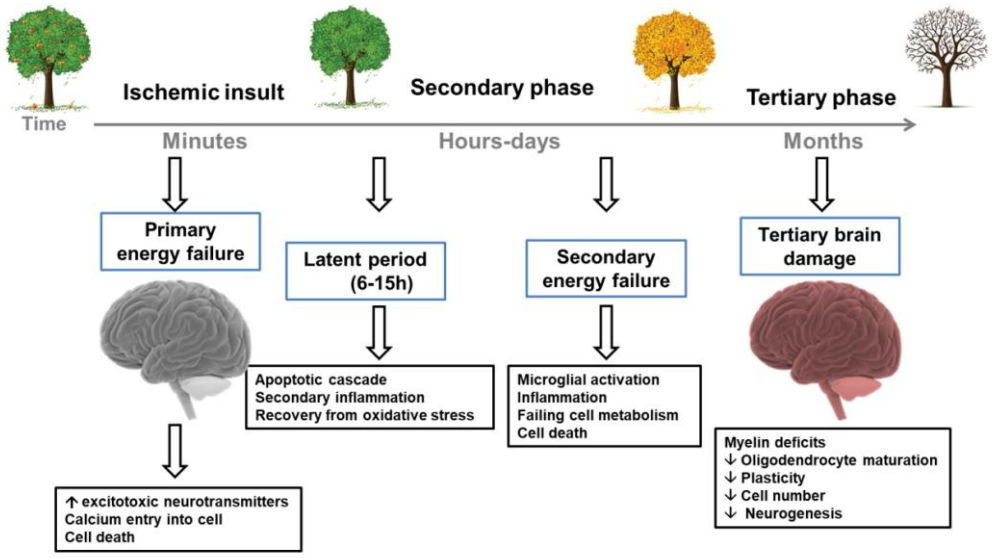

***Figure 8**. Biochemical cascade triggered by the ischemic insult. Adapted from* [97].

Similarly, bone marrow stromal cell mediated [98] or mesenchymal stem cell derived extracellular vesicles [99] [100] have shown effectiveness in promoting OPCs differentiation and subsequent remyelination [98].

4.5. Alzheimer

Alzheimer's disease is characterized by the accumulation of β-amyloid plaques (Aβ) and the formation of neurofibrillary tangles (NFT) in the brain, resulting in a decline

of cognitive function. However, how both Aβ and NFT influence the pathogenesis of Alzheimer's disease is not yet completely understood [101]. For a long time, Alzheimer's disease has been attributed in a great extent to Aβ plaques [102], but therapies aimed at lowering Aβ plaques have not been successful so far in human trials [103]. For this reason, the role of NFT and the damage to myelin are currently being considered crucial in the progression of the disease, instead of setting the focus only on Aβ [104], [105].

Post-mortem studies have shown an elevated concentration of degraded myelin basic protein complex in Alzheimer's disease human brains, as well as deposition of MBP at the margins of the Aβ plaques [106]. Furthermore, several myelin-related proteins have been associated with amyloid proteins [107]. Although the triggering factor has not yet been elucidated, myelin-related abnormalities have been observed prior to amyloid- and tau-associated pathology, in animal models [108].

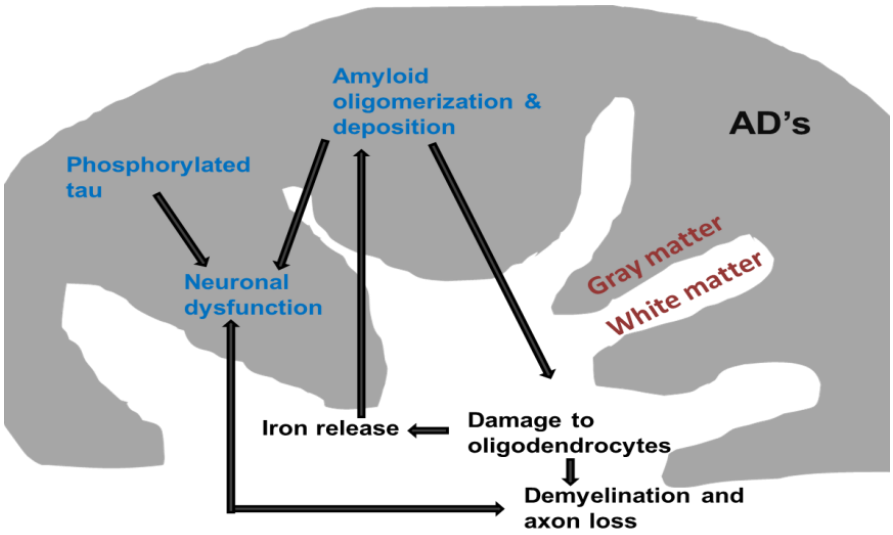

Figure 9. *Possible pathway for neurodegeneration and white matter damage in Alzheimer's disease Adapted from* [103].

It is believed that microenvironment in this disease might induce oligodendrocyte-linage cells death, as reduced populations of such cells have been found in areas with axonal damage and secondary myelin breakdown in patients [109], [110]. Moreover, *in vitro* studies have shown that beta amyloid peptides are not only toxic for mature oligodendrocytes but also for OPCs [111]–[113].

Current therapies in humans are focused on controlling Alzheimer's disease symptoms (such as deficit in episodic memory, language difficulties or global cognition impairment) and preventing the progression of the disease, rather than restoring the damage. Nevertheless, an approved drug for the treatment of the disease, Donepezil, has recently exhibited the capacity to enhance OPCs differentiation and promote remyelination *in vivo*, in the cuprizone mouse model [114]. Its contribution as a remyelinating therapy for Alzheimer's disease has not been elucidated yet.

Currently, the scientific community agrees on the importance of identifying pre-symptomatic markers of disease, before reaching hardly restorable levels of damage [115]. In this quest, the use of imaging technologies might be essential for detecting microstructural alterations, useful as early markers of disease [116], and enabling a prompt treatment. In this direction, a recent study has shown a positive effect of LINGO-1 antibody in early stages of the disease, when demyelination is detected in MRI, but Aβ deposition has not been observed yet [117]. Interestingly, LINGO-1 antibody has previously failed to succeed in clinical trials of MS but is still being considered for its remyelinating capacity exhibited in clinical trials [117], [118].

Whether or not the onset of Alzheimer's disease aggravates the natural decline of remyelination with age, whether or not this phenomenon is behind the severe cognitive decline associated with this pathology (aging is a risk factor for

Alzheimer's disease), and whether or not the use of remyelinating therapies could prevent the formation of new Aβ plaques, and promote the functional restoration of demyelinated neurons, are still unsolved questions in.

4.6. Traumatic brain injury

Impact, acceleration, deceleration, torsion or compression of the brain, mostly associated to motor vehicle accidents or sports and military actions, are the main causes of traumatic brain injury (TBI). Any of the aforementioned events yield different levels of cellular loss, haemorrhage, neuroinflammation, axon damage and demyelination, with a consequent functional or neurocognitive deficit [119]–[121]. Furthermore, the initial mechanical injury could trigger a series of reactions leading to additional damage [122]. Even though a pronounced traumatic axonal injury is the direct consequence of TBI, demyelination unrelated to axon degeneration is usually observed. In response to the insult, OPCs proliferate [95], [123] and new oligodendrocytes are generated. Importantly, experiments in animal models have shown that intact axons are demyelinated 3 days post mild TBI and remyelinated one week later [72].

Therapeutic approaches in TBI are mainly directed to contain associated secondary damages. Anti-inflammatory therapies have shown its efficacy in this context. Despite the role of acute inflammation in regeneration is not fully understood, it is believed that anti-inflammatory therapies might promote remyelination. The combined use of Minocycline and N-acetylcysteine has shown remyelination potential owing to their anti-inflammatory, anti-apoptotic and antioxidant capacity [124]. A similar observation has been made after treatment with Interleukin-1β antibody [125] or by the modulatory effect of immune cells by mesenchymal stem cells. The use of neural progenitor cells has also been effective in promoting

remyelination, restoring motor and cognitive deficiencies. Importantly, it has been seen that neural progenitor cells differentiate into oligodendrocytes, instead of astrocytes, neurons or microglia [126].

Together with anti-inflammatory approaches, intervention in the biochemical cascade caused by the impact can enhance remyelination. In a study conducted by Wu and colleagues, they observed that Vitamin B_{12} boosted remyelination after TBI apparently by avoiding stress-induced neuronal apoptosis [127].

4.7. Spinal cord injury

Spinal cord injury (SCI) affects substantially the patient's welfare, not only owing to a motor and neuronal dysfunction but also due to pain, spasticity, respiratory and cardiovascular alterations [128].

Like in TBI, the primary damage in SCI triggers a series of biochemical reactions leading to secondary damage, characterized by immune cell's activation, glutamate mediated excitotoxicity, haemorrhage, dysregulation of ion equilibrium, ischemia, or production of free radicals [129]. Demyelination takes place as a consequence of these events, being evident a decade after the injury [130]. Additionally, circa 50% of cells are estimated to die around the lesion epicentre [131], [132]

After the demyelinating insult, remyelination plays an important role in SCI [133]. The generation of myelinating oligodendrocytes has been observed even 3 months after SCI in mice [134]. However, the extent of remyelination is still controversial. Complete remyelination has been described in animal models [135], [136], as opposed to the presence of chronically demyelinated axons previously described after SCI [137]. In any case, the enhancement of remyelination through therapies might enable a functional recovery.

Several molecules have been proposed as remyelinating agents for the treatment of spinal cord injury, as extensively reviewed by Mekhail and colleagues [138]. The remyelinating effect of these compounds might lie in the protection of existing oligodendrocytes or in the promotion of OPCs proliferation and differentiation.

In addition, remyelination might be also facilitated by the use of biomaterials [139] or cell therapy. Several cell types such us, OPCs, Schwann cells, olfactory ensheathing cells, neuronal progenitor cells or neurotrophic factors secreting cells have been used to treat SCI, resulting in improved functional recovery in animal models [126], [140].

4.8. Towards multimodal therapies

As we have seen above, demyelination can be triggered by different pathways, such as genetic abnormalities, inflammatory attacks or oligodendrocyte death, resulting in neuronal death and cognitive decline. Demyelination is a common feature in many pathologies of the CNS and goes way beyond multiple sclerosis. Therefore, therapies aiming at remyelination, initially designed for the treatment of MS might actually be applied in other pathologies.

During the last years multiple potential remyelination therapies have been put forward. Such therapies can enhance both the recruitment and the differentiation of OPCs. Due to the common features of de- and remyelination, the development of remyelinating strategies is of great interest for application to different pathologies. A clear example is the antibody against the inhibitory Nogo-A protein. Nogo-A protein regulates axonal growth and internode length during myelin formation. After an injury, it has been shown that it restricts plasticity and neuronal growth. Inhibition of this protein has led to increased levels of plasticity, axonal regeneration

and remyelination in animal models of multiple sclerosis, stroke or spinal cord injury [141]–[143] leading to functional recovery. Similarly, the antihistaminic Clemastine has shown to enhance myelin repair in several mouse models such as the cuprizone and lysolecithin toxic models, a model of hypoxic brain injury and murine models of social isolation [144]–[147], among others.

All in all, brain injury very often involves demyelination together with further damage. In this context, cellular therapies might be helpful for the achievement of a regenerating atmosphere. The application of combined therapies focusing on different aspects of the pathology might have a synergic effect, as shown by the application of minocycline along with N-acetylcysteine after traumatic brain injury [148]. Moreover, in pathologies such as leukodystrophies, the application of only remyelination therapies might not be enough.

In this context, the growing evidence describing the reduced capacity of remyelination in aged individuals, the incompletely understood causes of demyelination, and the promising effectiveness of remyelinating therapies, support the need for effective experimental methodologies to study these phenomena.

5. Experimental models for the study of demyelination and remyelination

The study of how to prevent myelin damage and how to enhance its restoration requires suitable experimental models that allow the study of the underlying mechanisms of demyelination and remyelination. Current rodent models are based on features of MS, and the complexity of this disease makes difficult deciphering the contribution of single pathological events, hampering our deep understanding of the phenomena of demyelination and remyelination in their whole complexity.

Although none of the existing models presents the general features of MS, each one enhances a different aspect of the disease. Thus, these models can be considered complementary and can provide further insights about the effect of a therapy or the mechanism by which proliferation, differentiation and myelination take place. The use of a given model will, therefore, depend on the aim or target of a given study. Of note, as it will be explained later, although models for the study of demyelination and remyelination have been mainly developed to address multiple sclerosis, they share common characteristics with several other pathologies, enabling their use for the study of different diseases. In the following section we will analyze currently available *in vitro*, *ex vivo* and *in vivo* models for the study of demyelination and remyelination, highlighting the applications, strengths and weaknesses of each one.

5.1. In vitro models

5.1.1. OPC cultures

Myelination of neural axons requires the proliferation of oligodendrocyte precursor cells (OPCs), their migration toward the lesion site, and their differentiation into mature oligodendrocytes. Although OPCs migration has been studied using transwells, OPCs cultures are more commonly used to study of the proliferation and the differentiation steps [149].

Each differentiation step of OPCs is characterized by the expression of given proteins. Precursor cells express the platelet derived growth factor (PDGFR) and the neuron-glial antigen 2 (NG2). On the contrary, at the most advanced stages of differentiation, myelin proteolipid protein (PLP), myelin basic protein (MBP), myelin oligodendrocyte glycoprotein (MOG) or the myelin-associated glycoprotein (MAG) are expressed (Fig. 10). All cells belonging to the oligodendrocyte lineage

express the oligodendrocyte lineage transcription factor 2 (OLIG 2) [37]. Moreover, the markers 5-bromodeoxyuridine and caspase-3 can be used as markers of proliferation and cell death respectively. The use of fluorescence microscopy, cytometry or gene expression analysis can allow distinguishing the differentiation stage of cells [150], [151]. All in all, OPCs in culture is a simple and quite interpretable model. Potential therapies can be easily assessed in an environment with little interference before testing them in *ex vivo* or *in vivo* models.

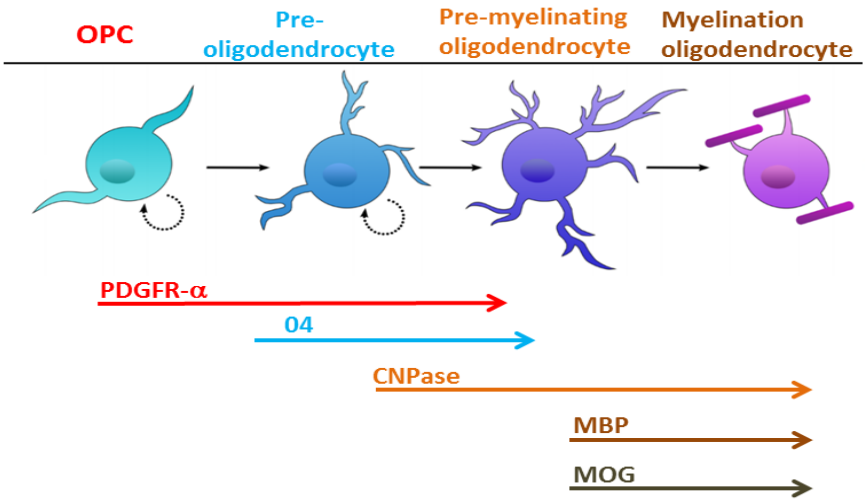

Figure 10. *Oligodendrocyte precursor cell maturation. At each maturational stage, different proteins are expressed by cells, allowing their specific characterization. PDGFR-α, O4, CNPase, MBP and MOG correspond to protein expression. Adapted from* [152].

5.1.2. Axon-based models

OPCs cultures allow monitoring of proliferation and differentiation of these cells but they do not tackle the study of myelination itself. This handicap can be overcome by the so-called axon-based models, in which axons derived from rats or mice

embryonic spinal cord explants, or synthetic axons, are used along with OPCs [153], [154]. The complexity of the spinal cord explants is higher as they include the presence of other cells of the CNS, while synthetic axons do not.

So far, *in vitro* models are mostly limited to these two options and they are designed to study very particular aspects of OPCs biology, or of the interaction of OPCs with axons. For the study of more complex aspects of myelination, more complex models are required.

5.2. *Ex vivo* models: Organotypic cultures

Brain organotypic slices kept in culture are a simple method to study myelin-related pathologies in their full complexity, since they preserve neural connections and cellular organization [155]. These cultures can be prepared from different regions of the brain, such as the hippocampus, brain stem, spinal cord or cerebellum with their original features, allowing to study the specific particularities of the process in different brain regions [156]. Hence, models for the study of Parkinson's disease, Huntington's disease and MS have been described in the literature [155].

Since the cerebellum of rodents contains an homogeneous axonal architecture, it has been put forward as an appropriate model for the study of remyelination and demyelination [156]. Briefly, cerebellum extracted from mice at post-natal date 7-12 is sliced in sections of 300-400 μm and cultured in semipermeable membranes. Next, brain slices have to be cultured for a period of at least 7 days in order to enable the cerebellum slice to adapt to the new medium and recover from the impact. At this point, the detergent lysophosphatidylcholine (lysolecithin) can be added to the medium to achieve extensive demyelination [157]. Following the demyelinating insult, remyelination is conducted spontaneously within the following days [158].

This process can be boosted by the use of remyelinating agents or by the implantation of exogenous cells. To achieve this aim, the use of cytosine arabinose is recommended to suppress the proliferation of endogenous cells [159].

Interestingly, cutting brain slices results in axotomy, which may result in neuronal loss. However, a reorganization of those axotomized neuronal axons is accomplished [160]. The most determinant sign of the survival of the culture is the observation of its thinning, becoming increasingly translucid. In addition, even though attempts have been conducted to thrive slices derived from older mice [158], [160] and with large slice thickness [161], the survival and regeneration capacity of such cultures is compromised.

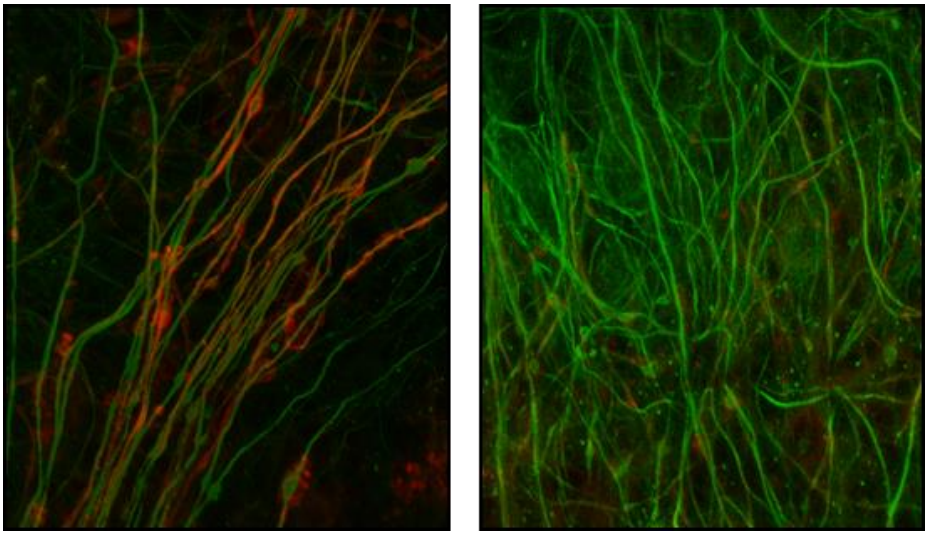

***Figure 11**. Organotypic culture immunofluorescence image acquired in a confocal microscope. Myelinated axons (left) and demyelinated axons (right) are shown. Myelin is shown in red. Axonal neurofilament in green. Image acquired by Iñaki Osorio-Querejeta.*

The monitoring of myelin can be performed by RT-PCR, western blot or immunofluorescence [162]. This last strategy consists in staining separately axons

and myelin. As such, co-localization of channels would reveal myelinated axons (Fig. 11). Long-term live imaging can be also performed with organotypic cultures transgenes expressed in mice [163].

5.3. *In vivo* models

5.3.1. Zebrafish

Zebrafish is a vertebrate model that should be outlined due to its rapid development and its transparency, that makes possible to directly visualize internal structures under the microscope [164]. Additionally, it is easy to manipulate genetically and it has shown to be an appropriate model in neuroscience research. Such features position the zebrafish as a suitable model for high-throughput screening of therapies and studies of genes related to myelin regulation [165]. Nevertheless, the therapeutic use of exogenous cells can be challenging in this model.

Interestingly, in this species oligodendrocytes wrap axons as seen in mammals [166]. The direct visualization of myelination and demyelination process is allowed by the use of genetically manipulated zebrafish, emerging as a very clarifying model for the study of intercellular interactions during these processes. However, it should be considered that myelin structure is not exactly the same for zebrafish as for mammals. While in the CNS of the zebrafish P0 protein is abundant, this only exists in the peripheral but not in the central nervous system of mammals [166].

So far, zebrafish has mainly been used for the study of remyelination and OPCs differentiation [167]. Demyelination can be induced by genetic cell ablation models through laser [168] or by toxic compounds such as lysolecithin. Moreover, even though the difference between zebrafish and mammals regarding their immune system is substantial, the development of a model that mimic human MS, despite its

limitations and particularities, is quite useful. The EAE zebrafish model, for instance, presents paralysis, reduced body weight and microglia activation [169].

The assessment of myelination can be done by several techniques such as *in vivo* fluorescent labelling, fluorescence transgenesis or whole-mount immunohistochemistry (IHC) [170]. The expression of a fluorescent protein by oligodendrocytes, for instance, allowed the monitoring of the myelination process by time-lapse *in vivo* microscopy [168].

5.3.2. Mammalian models

5.3.2.1. Toxicity-based models

These models are based on the use of a toxic compound to induce demyelination. The mechanism of administration and the pathway by which the damage is caused differ for the two most widely used models: the lysophosphatidylcholine (lysolecithin) and the cuprizone model will be analyzed.

5.3.2.1.1. Lysophosphatidylcholine (LPC)

Focal administration of lysophosphatidylcholine (LPC), to rodents white matter tracts produces extensive demyelination, similarly to what happens when LPC is administered in organotypic cultures. Interestingly, LPC is an endogenous lysophospholipid correlated with obesity [171], coronary artery disease [172] and aging [173]. The role of endogenous LPC in myelin damage, however, is still unclear.

The exogenous administration of LPC in the white matter leads to demyelination through cellular toxicity, leading to glial cell death. Plemel and colleagues hypothesized that LPC causes an increase in cellular membrane permeability at high concentrations due to its lipid disrupting properties [174]. Myelin could be also

directly altered through the same mechanism [175].

The induction of demyelination in rodent consists in the focal administration of LPC in the spinal cord or in brain regions such as the corpus callosum or the cerebellar peduncles by stereotaxic injection [176], [177]. Usually, an injection of 2 µl of 1% LPC is enough to induce noticeable damage [178].

Following demyelination, microglia and macrophages migrate toward the lesion site, astrogliosis takes place and axonal homeostasis is disrupted [179]. After the application of LPC in rodent spinal cord, myelin disturbance was observed as soon as 30 minutes, and remyelination was evident 7 days after injection, being completed at day 23 [178]. Immunochemistry [174] or MRI [180] have shown to be effective to assess myelin pathology in this model.

It should be mentioned that even though it is not reviewed in this work, ethidium bromide has also been used as a demyelinating agent in a similar fashion [181]. The toxicity of ethidium bromide lies behind its intercalating properties in the DNA structure, leading to an extensive astrocyte and oligodendrocyte death [182]. Nevertheless, it is not widely used as a demyelinating model, probably due to the carcinogenic nature of the compound.

5.3.2.2. Cuprizone mouse model

The cuprizone mouse model is the most widely used toxicity model of demyelination. Demyelination is achieved by administration of the copper chelator cuprizone (bis-cyclohexanone oxaldihydrazone) at 0.2-0.3% (w/w) through the diet for a period of 4-6 weeks. After the withdrawal of the toxic from the diet, robust remyelination is exhibited already after 4 days and is completed during the following weeks [183]. Certainly, the extent of demyelination and the severity of the

model depend on the strain of mice, age and the dose used [184]. The most common practice is to use mice of the C57BL6/j of eight weeks of age, feeding them with a 0.2% (w/w) cuprizone diet for 4-6 weeks. However, the administration of cuprizone for a period of 12 weeks is also used as a chronic model of demyelination, where extensive axonal loss and delayed remyelination is observed [185], [186].

The main strengths of this model are its simplicity, reproducibility and the extensive and progressive demyelination that mice undergo in several regions of the brain, such as the cerebellum or the corpus callosum. In addition, demyelination in grey matter regions has also been described [187]. Even though the integrity of the blood-brain barrier in this model is a matter of discussion [188], [189], immune T cells might not be involved in damage, contrarily to what happens in MS.

The intake of cuprizone results in an extensive selective oligodendrocyte loss. Growing evidence suggests that mitochondria are susceptible to cuprizone, causing cell loss and secondary demyelination. Even though the mechanism of action of cuprizone is inconclusive, it is suggested that its activity as copper chelator can interfere in the electron transport chain. Certainly, copper is present in several complexes of the mitochondria [190]. Chelation, therefore, might decrease adenosine triphosphate production and increase reactive oxygen species, triggering the damage. Electron microscopy analyses have revealed mitochondrial swelling after exposure to cuprizone [191]. Interestingly, OPCs are able to survive to cuprizone exposure due to their slower metabolism [192].

In response to the demyelinating insult, microgliosis and astrogliosis are prominent in the cuprizone mouse model after three weeks of administration of cuprizone [193]. While microglia takes care of the removal of myelin debris, astrocytes seem to interact with OPCs, mature oligodendrocytes and microglia, to support

remyelination [194]. One week after the withdrawal of cuprizone from the diet, when remyelination has already started, microgliosis is absent, while astrocytes are still active in the demyelinated regions [184]. Nevertheless, Manrique-Hoyos and colleagues observed that although remyelination causes a recovery of the behavioural deficits provoked as a consequence of a 5-week exposure to cuprizone, motor deficits were appreciable after 6 months of exposure to cuprizone [195].

The cuprizone model has emerged as a suitable model for the evaluation of remyelinating therapies. In this setting, MRI is becoming very useful for the longitudinal evaluation of remyelination in a non-invasive manner [196]–[199]. Additionally, Luxol fast blue staining [200], electron microscopy [201], immunohistochemistry [202] and immunofluorescence [203] are also used for the invasive evaluation of myelin.

5.3.2.3. EAE model

The EAE model is probably the most commonly used model in MS research due to their histopathological similarity with the human pathology. In this model the demyelinating insult is mediated by autoimmune inflammation. The attack of the immune system can be triggered through two main approaches: the first and the most common, consisting in the injection of a myelin protein such as PLP, MBP or brain emulsion with Freund's adjuvant and pertussis toxin. The second approach consists in transplanting active cells against myelin [164]. In addition, acute monophasic, relapsing-remitting and chronic progressive inflammation models can be induced depending on the type and dose of immunization agent used [204].

The EAE model exhibits blood-brain barrier disruption after the onset of the disease, resulting in infiltration of immune cells into the cortex, spinal cord and cerebellum

during the 50 days following induction [205]. Macrophages and T cells are the major infiltrated populations in the CNS in this model [206].

Owing to its similarity with MS, the EAE model has become a widely used model for testing therapies that might suppress or modulate the immune system. Nevertheless, this model is highly variable and, in contrast to toxin induced models, the extent and distribution of demyelination over time and space may be unpredictable. Hence, the evaluation of remyelinating agents is challenging in this model. The use of genetically modified lines can facilitate the evaluation of the model. In a study conducted by Mei and colleagues, genetically modified OPCs enabled the monitoring of newly generated mature oligodendrocyte lineage cells and allowed an easier evaluation of the effect of treatments [34].

The evaluation of a clinical score is a widely used method to assess the effect of a given therapy [207]. Moreover, electron microscopy, immunofluorescence, histochemistry and MRI are also essential techniques for the evaluation of myelin.

5.3.2.4. Viral infection models

The role that viruses could play in the aetiology of MS is controversial. A viral infection early in life, together with a specific genetic background, might cause the triggering of the disease [208]. However, further evidence is needed to support this hypothesis.

The inoculation of Theiler murine encephalomyelitis virus (TMEV) into rodents results in a progressive chronic demyelinating disease. The infection caused by TMEV leads to an autoimmune response that causes inflammatory demyelination. The main advantages of this model are its histopathological similarity with MS, the extensive demyelination undergone and the MS chronic progressive phenotype

exhibited by the mice [209]. Moreover, demyelinating lesions exhibited in MRI studies in the TMEV model have shown characteristics of humans MS: lesions found in spinal cord, brainstem and brain [210], T2 hyperintense spinal cord lesions [211], T1 hypointense in the cerebrum [212], deep grey matter damage [213] and brain and spinal cord atrophy correlated to disability [214]. This might be of utmost importance to develop specific imaging markers of myelin useful for myelin imaging in humans.

However, as in the EAE model, the lack of control of the temporal evolution of myelin damage and remyelination makes it difficult to evaluate the effectiveness of a given treatment. Additionally, the long incubation period required to symptoms manifestation, the high mortality rate and the technical difficulties related to safety issues are further disadvantages of using virus induced models [164].

5.4. Selection of the model

Models for the study of demyelination and remyelination can differ in their complexity and in their proximity to the human MS. The selection of the suitable model is crucial and depends on the objective of the study.

Organotypic cultures and OPC cultures represent valuable tools for the high-throughput screening of therapies due to their simplicity compared to *in vivo* models. Moreover, they allow a better understanding of the mechanism of action of a given therapy. Once the efficacy of a drug has been tested in those models, the use of a rodent model is highly advisable. Among these, the cuprizone model is probably the most simple and reproducible one, offering a clear time-pattern of demyelination of remyelination making it suitable for the evaluation of therapies. In contrast to toxic models, the EAE model and virus induced models can mimic better

the pathophysiology of MS. The application of treatments in these models is of great interest to confirm effective therapies in simpler models, albeit challenging.

6. Experimental techniques for the detection and quantification of myelin

In direct relation to the selection of a proper model, it is very important to consider the experimental methodologies of choice for the study of the evolution of the pathology, and the effectiveness of the novel diagnostic and therapeutic tools developed to treat myelin-related disorders. In this context, it is a priority to develop non-invasive techniques for the specific and sensitive detection and quantification of myelin content and status. In this section we first analyze invasive techniques for the characterization of myelin, mostly based in histopathological studies, considered the gold-standard to later focus on the use of magnetic resonance imaging, since it is our belief that MRI collects all the required advantages to become crucial technology to study of myelin in humans and rodents.

6.1. Invasive methods: histological techniques

Myelin is mainly found in the white matter (WM) of the central nervous system, accounting approximately for the 50% of its dry weight, and conferring the particular white colour of this tissue [215]. Even though it is found in smaller amounts, myelin is also supporting and insulating axons in grey matter tissue. This spirally wrapped membrane is composed of 80% lipids and 20% proteins, giving hydrophobic properties to the sheaths. Indeed, the chemical properties of proteolipids, lipoproteins and lipids constitutive of myelin are crucial for its staining in histological preparations.

Precisely, phospholipids (40% of the total lipids of myelin) are the main target of

most histochemical staining protocols. Briefly, lipoproteins are not extracted from the tissue by the use of organic solvents and hence, the protein-bound phospholipids can be stained due to its hydrophobic nature. Similarly, sphingolipids and unsaturated fatty acids associated with proteins can also be stained [216]. The amphiphilic nature of these molecules, together with the use of an amphiphilic dye, results in hydrophobic binding between both molecules in aqueous solution [217].

Luxol fast blue (LFB) [218] is probably the most widely used histochemical technique for myelin staining. Copper phthalocyanine is the key component of the staining. The blue colour characterizing this dye is the result of the electronic delocalization of the 18π electrons of this molecule. Interestingly, due to these features is widely used to synthesize pigments, catalysts and photoconductors [219].

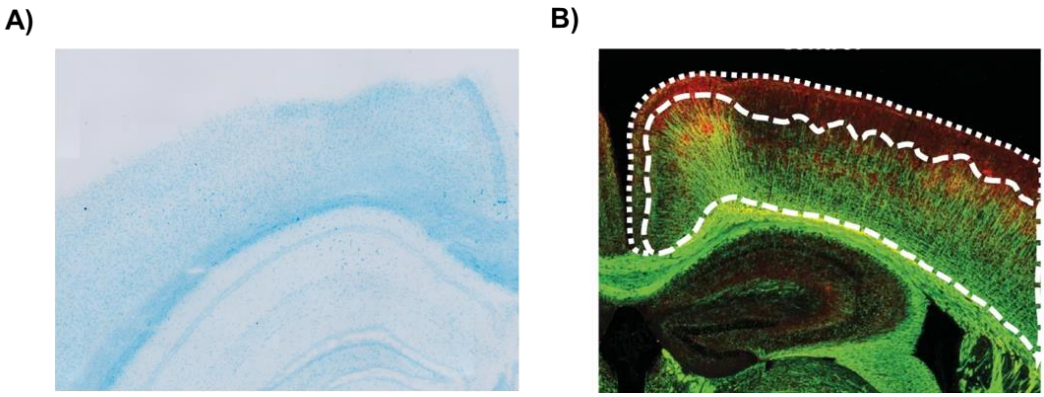

Figure 12. *Myelin staining. A) Luxol fast blue staining performed by us B) Anti-MBP immunofluorescent staining showing the myelin in green* [203].

The major disadvantage of this staining is that it does not enable single-axon staining, either detailed staining of peripheral nerves. LFB staining is usually accompanied by cresyl violet staining of cell nuclei based on a cationic dye. Carriel

and colleagues also put forward the MCOLL histochemical staining, combining LFB myelin staining and collagen fibre staining with the cationic silver red dye [220], [221]. In this way, a higher contrast between WM and GM was achieved, enabling the visualization of thinner myelinated nerve fibres.

The quantification of LFB staining can be addressed by differed approaches. The most widely used strategies are: 1) Scoring the samples from 0 (full demyelination) to 3 (normal appearing myelin) by three blinded observers [183], 2) Measurement of optical density (OD) [222], [223], and 3) Normalization of signal with a non-myelinated region [124]. Although LFB is the most widely used histological staining, alternative protocols have been described including Oil Red O, Sudan Black or Black Gold staining [224], [225].

In addition to histological staining, immunohistochemical or immunofluorescence techniques can provide a thorough view of myelin. These techniques are based on the specific binding of fluorescently labelled antibodies to myelin proteins, such as the myelin basic protein or the myelin proteolipid protein [226]. With this approach, it becomes possible to observe those proteins inside oligodendrocytes of Schwann cells, even before they are incorporated into the myelin membrane [227]. Immunofluorescence staining allows the evaluation of cortical myelination integrity in a highly accurate fashion [203]. The quantification of myelination can be performed by measuring the immunodensity, the stained area, the fibre length or the number of intersections.

A more detailed view of myelin can be achieved by the use of electron microscopy and light microscopy together with Osmium tetraoxide (OsO_4). This staining achieves a black staining of lipidic structures. The principle of this staining lies behind the oxidative capacity of OsO_4. This compound is reduced by the reaction

with the abundant unsaturated lipidic bounds composing myelin, causing the deposition of the blackish osmium in myelin [228]. Masson's trichrome can be used to counterstain collagen [221], [228]. One of the most common uses of electron microscopy is the measurement of myelin membrane thickness, very often expressed as the g-ratio, which measures the ratio between the myelin thickness and the axon diameter (diameter of axon/whole fibre diameter). This g-ratio in a healthy brain is around 0.6-0.7 [229]. Remyelinated axons are characterized for exhibiting thinner myelin sheath and a lower g-ratio. While this effect is pronounced in thick axons, such as those in the corpus callosum, in places of predominantly thinner axons is much difficult to distinguish remyelinated from healthy axons [230].

Finally, it is worth pointing out an alternative interesting approach was carried out by Aharoni and colleagues [231]. Choline is a phospholipid present in myelin. The analogue propargyl-choline has shown the capacity to incorporate in any kind of choline phospholipids without causing any detrimental consequence [232]. This compound can be visualized by attaching a labelled azide molecule. In their study propargyl-choline was intraperitoneally administered to the demyelinating mouse model EAE, and to control mice. Once the animals were sacrificed and the staining was performed, newly generated myelin was observed.

6.2. Non-invasive methods: magnetic resonance imaging

Magnetic resonance imaging (MRI) has emerged as a technique of great interest, both in preclinical models and humans, for diagnosis in multiple diseases, for the characterization of functional networks, and for the assessment of important functional biological systems like the blood-brain barrier or the immune system. MRI allows the visualization of biological tissues in a non-invasive manner, without

the use of ionizing radiation, which enables the conduction of repeated examinations for longitudinal studies. We strongly believe that MRI represents a unique tool for the non-invasive assessment of de- and remyelination processes and that advances achieved in preclinical research can be readily applied in the clinical setting, due to the high traslationality of this technique. In this section, the principles of nuclear magnetic resonance will be discussed, so we could better understand how it can be applied to assess myelin content and status, and its effects on functional and biological aspects such as the organization of functional brain networks during de- and remyelination processes.

6.2.1. Principles of nuclear magnetic resonance

After the pioneering work of Isidor Isaac Rabi (Columbia University, NY) in the 1930s (Rabi was the first person to use the concept “nuclear magnetic resonance” and won the Nobel Prize in 1944 for his discoveries), it is generally agreed that nuclear magnetic resonance (NMR) phenomenon in bulk materials, as we know it today, was first described simultaneously in 1946 by Edward Purcell, Torrey and Pound (Harvard University, MA), together with Block, Hansen and Packard (Sandford University, CA). Purcell and Block were awarded the Nobel Prize in Physics in 1952. NMR has found numerous applications in science and technology, including magnetic resonance imaging. However, until the seventies all experiments with NMR were focused on measuring the energy absorption and emission of solids, liquids and chemical compounds. In 1971 Raymoud Damadian observed different relaxation times of healthy tissue and tumours, triggering the medical application of NMR. The first steps towards magnetic resonance imaging (MRI) were made by Paul Lauterbur in the seventies, who obtained spatial information from a set of tubes by applying different gradients to excite protons. A few years later, Sir Peter Mansfield

developed the theoretical background for k-space and Fourier based image acquisition and processing and invented the first fast imaging technique called echo-planar imaging (EPI), enabling the development of the vast majority of current imaging methods in clinical MRI. Lauterbur and Mansfield shared the Nobel prize in medicine in 2003.

It is far beyond the scope of this work to describe the physical principles of the MRI technique. For that purpose, there are excellent manuals [233]–[235]. Instead, a basic concept of image contrast and relaxation of magnetization will be discussed since both are important for the understanding of the experimental section of this work.

In biomedical imaging, contrast is a term used to define the difference in signal intensity between two regions in the object under observation. Such difference is quantifiable, in computational terms, as the numerical difference between the intensities of pixels (or their three-dimensional equivalents, voxels) in an image, which, actually, may not be always appreciable by the naked eye.

For magnetic resonance imaging, in particular, image signal intensity, and therefore contrast, is the result of various contributing intrinsic (longitudinal and transverse relaxation times, proton density, diffusion coefficient, etc.) and extrinsic (type of acquisition schemes, timing parameters of pulse sequences, strength of magnetic field, etc.) parameters [236]. The contribution of all these parameters can be summarized in the following equation:

$$S = \rho \times F1 \times F2 \times F3 \quad (1)$$

where S represents the signal intensity for a given pixel (voxel) or region of interest (ROI). In conventional imaging application, MRI signal is due to protons (nuclei of hydrogen atoms), being generally assumed that those are mostly contained by water

and fat molecules in the body (other fractions of protons such those forming constitutive part of macromolecules have neglectable contribution to signal in conventional MRI applications). Thus, in equation (1), ρ represents the water and/or fat proton density in the pixel (voxel), and F1, F2 and F3 are three weighting factors ($0 \leq F1, F2, F3 \leq 1$) related to the aforementioned intrinsic and extrinsic parameters. F1 represents the so-called T1 weighting factor, F2 the T2 weighting factor and F3 the diffusion related weighting factor. In absence of significant contribution of molecular diffusion equation (1) simplifies and in general MRI images are referred as proton density weighted images (PD), T1-weighted images (T1w) and T2-weighted images (T2w) which can be also referred as T2 star weighted images (T2*w), as we will discuss later, depending of the most weighting factor in equation (1), although mixed or combined weightings are also not unusual. Thus, by understanding the intrinsic parameters of matter and their relation to the extrinsic parameters that control their influence on signal intensity, it is possible to control contrast on MR images, to enhance specific tissues or regions of interest (ROI).

As already mentioned, the intrinsic parameters depend on the physicochemical characteristics of the region of interest which, in the end, are a reflection of the biological characteristics of such region (water/fat content, presence of macromolecules, pH, temperature, presence of metals like iron, structural organization of tissues, intimately related to water diffusion characteristics, etc.). All these factors have a direct impact on signal intensity). On the other hand. MR scanners are operated by computers and software programs that are commonly referred as pulse sequences, which are nothing else than an execution program or image acquisition routine, to tell the different components of the MRI scanner how and when to operate to acquire an image. Each pulse sequence contains a series of extrinsic parameters that the user can tune on demand, to ponderate the weighting

factors expressed in equation (1), enhancing on this way the effect of particular intrinsic parameters in the areas under observation.

In summary, using different image sequences and tuning the different values of the extrinsic parameters that contain, one can modulate image contrast on demand, depending on the intrinsic parameters of the matter under observation. In the following paragraphs, we will describe all these concepts in an attempt to better understand signal contrast in MRI and its interpretation in biological terms.

As already mentioned, F1 in equation (1) represents the T1 weighting factor, which depends on the intrinsic parameter of the matter called longitudinal or spin-lattice relaxation time (T1), and basically two extrinsic parameters of the pulse sequence, the repetition time (TR) and the flip angle (θ). It is beyond our scope to provide a full description of these parameters (see [233] for full description). When F1 approaches to 1 there is no T1 weighting on the images and when T1 approaches to 0 the importance of this weighting factor is key on generation of signal and contrast.

On the other hand, F2 represents the T2 weighting factor (sometimes expressed as T2*, depending on the acquisition scheme or pulse sequence used for image acquisition). This factor depends on the transverse or spin-spin relaxation time (T2 or T2*, intrinsic parameters) and an extrinsic parameter of the pulse sequences called echo (or encoding) time (TE). Again, values of F2 close to 1 or to 0 define the importance of this weighting factor in the final signal observed in a region.

Finally, F3 is a diffusion related weighting factor (water molecules naturally diffuse within and among cells in tissues, influencing signal on MRI) which depends on the apparent diffusion coefficient of water protons (D, intrinsic parameter) and the amplitude, pulse duration and sequential timing of activation of the scanner diffusion gradients (G, δ, Δ, extrinsic parameters)

According to equation (1), depending on the different intrinsic parameters of the different regions under observation, we can modify the image contrast by playing around with multiple extrinsic parameters (pulse sequence dependent) such as the repetition and echo times, the flip angle or the use of diffusion gradients, to yield:

1) A Proton Density weighted image (F1 = F2 = F3 = 1, no influence of weighting parameters), achievable by using pulse sequences with short echo times and long repetition times, without using diffusion gradients.
2) A T1-weighted image (F1 < 1, F2 = F3 = 1), with high influence of the T1 parameter, achievable by using pulse sequences with short repetition times, low flip angles and short echo times, without using diffusion gradients.
3) A T2-weighted image (F2 < 1, F1 = F3 = 1), with high influence of the T2 parameter, achievable by using pulse sequences with long repetition times and long echo times, without using diffusion gradients.
4) A diffusion-weighted image, or DWI, (F3 < 1, F1 = F2 = 1), achievable when diffusion gradients are used during image acquisition, ideally with short echo times and long repetition times.
5) A combination of several or all the previous one, when various conditions are simultaneously satisfied.

Examples of all these different image weightings are presented in Fig. 13. As one can see in the figure, a good tissue contrast by tuning the imaging parameters one can enhance the contrast between tissues (such as white and grey matter) or regions of interest (such as the ischemic lesion) which are not straightforwardly differentiable for all image modalities. In other words, each feature to be studied requires the careful selection of the imaging sequence and the proper combination of the weighting factors (i.e. of the imaging parameters).

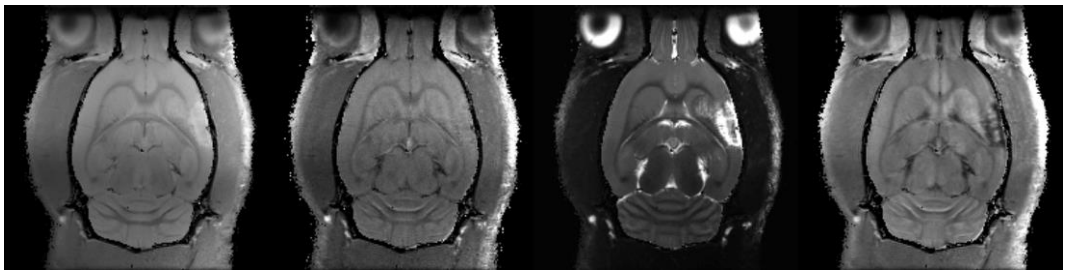

Figure 13. *MR images of a rat brain with an ischemic lesion obtained with different image contrast. a) Proton density image (F1~F2~F3~1), b) T1-weighted image (F1=0.125 ; F2~F3~1), c) T2-weighted image (F2=0.135 ; F1~F3~1), and d) Diffusion-weighted image.*

The interpretation of biomedical MR images, therefore, requires a thorough understanding of the corresponding signal contrast in relation to underlying pathophysiology behind it. A clearly defined ischemic lesion (like the one observed in the rat brain in Fig. 13c), may not be appreciable with inappropriate weighting factors (i.e. acquisition parameters), that may mask the contrast between different regions (lesion basically masked in T1w image in Fig. 13b).

On top of the acquisition schemes and parameters, other extrinsic factors like the main magnetic field, the hardware configuration (design and performance of RF coils, magnetic field gradients, shimming, local disturbances of the magnetic fields, etc.) have an influence on signal intensities and contrast on MR images, hampering the direct comparisons of images across different experimental setups, and keeping the evaluation of MR images qualitative and subjective, usually restricted to descriptions of relative contrast between different anatomical regions (the use of sentences like “presence of a hypo-, or a hyper-, intense signal in the region” are common in medical literature). In this cases, normalization of images may be necessary (against internal or external references) for image comparison, and the use of numerical variables such as signal to noise ratio (SNR) or contrast to noise

ratio (CNR) may be useful to establish such comparisons.

Having disclosed the influence of the most common contrast mechanisms in biomedical applications of MRI (i.e. T1, T2, PD and DWI), it is important to mention that there are other physical mechanisms, with their corresponding intrinsic and extrinsic parameters, that can be used to further modify contrast on MR images, such as susceptibility weighted imaging (SWI), magnetization transfer (MT), chemical shift exchange (CEST), etc., but whose principles and definitions are beyond the scope of this work (see reference [235], [237] or details about more specific contrast mechanisms such as magnetization transfer –MT-, T1ρ, chemical exchange saturation transfer, -CEST-, etc.).

6.2.2. Magnetic resonance imaging techniques for quantification of myelin content

As we have discussed earlier, along with its non-invasiveness, MRI technique has the great advantage of being multiparametric proportioning multiple types of contrast in relation with the microstructural environment of the regions (tissues) under observation. In this context, the definition of MR imaging biomarkers of myelin is a highly desirable goal pursued by researchers since those markers can provide important information to understand the dynamics of demyelination and remyelination in preclinical models, such markers can be translated to the clinical setting for the evaluation of myelin in humans, and can allow the evaluation of potential remyelination therapies in a longitudinal manner In this section we will review what it has been reported in literature in this field, with special focus on applications in the cuprizone model, increasingly used as a model for the evaluation of remyelination therapies, for reasons already mentioned, and because is the main model used in the experimental section of this work.

6.2.2.1. T1 and T2-weighted imaging

Myelination processes (in the early stages of life, for example) and abnormalities in myelin content can be thoroughly monitored by T1- and T2-weighted imaging. In regard to development of the brain, myelination is extensive during the first year of life in humans, and T1-weighted imaging is sensitive to the accumulation of cholesterol [238] and galactocerebroside [239] constitutive of new myelinated white matter. In further stages, a progressive reduction of T2-weighted signal is observed as the water content of myelin decreases [240], [241]. This pattern is also followed in mice, where normalized T2-weighted signal has been described to drop 8% throughout a period of 18 weeks, starting at 8 weeks [242].

In adulthood, for normal appearing white matter, the hydrophobic properties of myelin restrict molecular motion of protons, a scenario that is altered when WM is affected by pathological processes. It is important to considerer that T2 relaxation is affected by proton transfers, molecular exchange and water diffusion [240], and thus, white matter shows a lower T2 value than grey matter, generating contrast between both tissues in T2w imaging. Demyelination diminishes water diffusion restriction in WM and therefore is seen as an increase of signal for white matter on T2-weighted images. In the cuprizone model, for example, 5-6 weeks after exposure of animals to 0.2-0.3% (w/w) cuprizone containing diet, mice show an extensive demyelination in the corpus callosum, exhibited as the appearance of hyperintensity on T2-weighted images. In this mouse model, T2-weighted imaging has shown to be effective to evaluate in a semi-quantitative way the extent of demyelination between groups or throughout longitudinal studies. To address this aim, normalization of the signal between image sets is required (intra- and inter-individual differences exist). Thiessen and colleagues normalized MR signal in images with the CSF mean

intensity, observing a high correlation of normalized T2 signal with the number of myelinated axons measured by electron microscopy [198]. T2-weighted imaging also showed to be effective in assessing myelin content by estimating the grey matter/white matter ratio [196] and confirming a tight correlation with histology. Concerning grey matter, identification of demyelination calls for a very high resolution, since the number of fibres crossing the cortex is certainly reduced, compared to white matter tracts at the corpus callosum or cerebellum.

On the other hand, the use of T1-weighted imaging in this model has not been extensive. However, discriminant function analysis revealed that a combination of normalized T1-weighted imaging and normalized T2-weighted imaging resulted in a correct classification of 93.8% of cuprizone exposed and control mice [243].

In a clinical setting, both T1-weighted imaging and T2-weighted imaging play an important role as diagnostic tools. Recently generated inflammation is usually detected by gadolinium based T1-weighted imaging, and demyelinating plaques are detected by T2-weighted imaging. Nevertheless, in MS in the presence of oedema and inflammation, T1-weighted and T2-weighted imaging are not specific enough for myelin, as demonstrated by histopathological studies. Furthermore, this abnormal signal is not correlated with clinical disability, since there is no correlation between inflammation and disability. In other words, in absence of other effects, T1w and T2w imaging show a good degree of sensitivity and specificity for the detection of myelin, however other confounding concomitant effects that also alter T1w and T2w imaging signal (false positives) limit the applicability of this parameters by themselves. Certainly, this is the main reason why researches are still seeking for specific and sensitive sequences. [244], [245].

One of these attempts that is popular nowadays is the calculation of parametric

images showing the T1w/T2w ratio, instead of the individual parameters. This ratio has shown to be sensitive to detect cortical demyelination. Demyelination of cortical areas leads to hypointensities in T1w images and hyperintensities in T2w images. Hence, the ratio of both images results in increased contrast. *Post-mortem* studies revealed a statistical difference between myelinated and demyelinated cortices [246]. Also, WM alterations can be detected by the T1w/T2w ratio, as shown in schizophrenic patients. [247].This approach might be of high utility in the clinics, where T1 and T2-weighted images are routinely acquired.

6.2.2.2. Susceptibility weighted imaging

Susceptibility weighted imaging (SWI) is a modality that enhances the T2* effect (enhancing field inhomogeneities) and makes use of phase information, of great use for detecting paramagnetic compounds. Basically, SWI is based on the different magnetic susceptibility of the components comprising tissues. Under a magnetic field, some components are prone to magnetize, altering the magnetic field of the surroundings and substantially contributing to the so-called T2* effect. Of note, contrarily to T1 and pure T2 effects, magnetic susceptibility are noted at larger areas than the physical limits of the area where they are produced (there is a blooming effect that extends contrast in space). This effect is highly enhanced at high magnetic fields. SWI is highly sensitive to the detection of iron, deoxyhemoglobin and myelin. Additionally, since myelin is an anisotropically organized structure, its macroscopic geometry [248] and microstructural orientation [249] might introduce variability in this parameter.

Growing evidence has been added supporting the importance of myelin in the T2* effect in demyelinating models [250], [251]. Magnetic susceptibility of white matter is diamagnetic compared to grey matter. Growing evidence supports the fact that

myelin is behind this diamagnetic property [252]. For instance, in the shiverer mouse model of hypomyelination, magnetic susceptibility contrast is reduced by 96% in white matter [250], [253]. A similar conclusion was obtained for the cuprizone mouse model [250]. However, in the EAE mouse model, lesion detected with SWI were mainly indicating the presence of deoxyhemoglobin and in a lesser extent, demyelination, inflammation of parenchymal iron [251].

At the same time, iron accumulation and myelin damage are undergone by MS patients. Interestingly, T1-weighted and T2-weighted are not able to detect highly hypointense lesions which actually are revealed by SWI [254]. Observed hypointensities might arise from myelin loss, iron deposition or iron contained in oligodendrocytes [255], [256]. A study conducted by Deh and colleagues revealed that the magnetic susceptibility of myelin is increased when myelin breakdown takes place [257]. Once again, the presence of false positives is a limitation for the universal use of SWI as a specific biomarker of myelin content.

6.2.2.3. Magnetization transfer imaging

Magnetization transfer phenomenon is produced by the saturation of spins in macromolecules (non-aqueous tissue), which transfer their energy to the visible free water molecules, leading to a reduction of signal intensity from the former ones [258]. This phenomenon is strong in areas enriched on white matter. The measurement of the relative signal attenuation produced by the excitation pulse has been put forward as a semiquantitative measure of myelin density. The percentual change in the signal caused by the transfer of magnetization is reflected in a numerical parameter called magnetization transfer ratio (MTR).

In the toxic cuprizone and L-a-lysophosphatidylcholine stearoyl mouse models, MTR

has exhibited a decrease as a consequence of demyelination and, an increase after remyelination, in white matter rich regions, in agreement with immunohistochemistry staining validations [259], [260]. A decrease in MTR is also appreciated in the EAE model [261], [262] and in human studies [263] after white matter breakdown.

Nevertheless, the specificity of magnetization transfer imaging is currently under discussion, as it has been proved that is influenced by inflammation in the EAE model [264]. Additionally, in the cuprizone model MTR also showed a negative correlation with the GFAP marker of astrocytes, revealing an effect of astrogliosis in changes observed for this parameter [259].

The sensitivity of MTR may also be lower compared to conventional imaging [187]. Although abnormal values were found in the deep grey matter in the cuprizone model, no changes have been reported in the cortex or in the cerebellum, using magnetization transfer imaging [199].

6.2.2.4. Diffusion-weighted imaging

Diffusion-weighted imaging is based on the pattern of water molecules motion in tissues. Image contrast is achieved by the application of bipolar magnetic field gradient pulses. While in the normal appearing white matter, diffusion takes place mainly following the direction of white matter tracts (anisotropic diffusion), in the grey matter, the absence of barriers allows water motion in any direction of space (isotropic diffusion). Both conditions (anisotropic vs. isotropic diffusion) can be distinguishable by MRI, by applying diffusional gradients in multiple directions of the space (at least 6 directions). When DWI signal is similar irrespective of the direction of the gradients applied, water molecules are located in an isotropic

environment (grey matter) while predilected diffusion in particular directions of space indicates an anisotropic environment (white matter). The acquisition of DW images in multiple directions of space is generally referred as Diffusion Tensor Imaging, or DTI, and by image processing of these image data sets, directional vectors are mathematically synthesized in an ellipsoid or diffusion tensor, representing water motion in it. Combination of mathematical representation of these diffusion tensors (the so-called eigenvectors and eigenvalues) give rise to several imaging parameters, including:

- Fractional anisotropy (FA): a scalar value representing the degree to which diffusion is restricted to specific axes. A value of 0 represents pure isotropic diffusion and a value of 1 pure anisotropic diffusion
- Mean diffusivity (MD): the sum of diffusivity along the three axes.
- Axial diffusivity (AD): the diffusion coefficient along the principal axis of diffusion.
- Radial diffusivity (RD): the mean diffusivity orthogonal to the principal axis.

These four parameters give important information about the structure of tissues in relation to the diffusional behaviour of water on them. Thus, DTI is sensitive to many factors such as myelin thickness, axonal density, oedema, inflammation or cell swelling. In the human brain axial diffusivity describes the movement parallel to white matter tracts and radial diffusivity perpendicular to them. Pathologies altering the microstructure of both WM and GM can affect the diffusion of water molecules, and therefore the values of the MRI parameters obtained in DTI.

Table 1. *Schematic description of the main DTI parameters* [265]

	Unit of measure	Formula	Object measured
FA	Scalar value ranging between 0-1	$\sqrt{\frac{1}{2}}\frac{\sqrt{(\lambda_1-\lambda_2)^2+(\lambda_2-\lambda_3)^2+(\lambda_3-\lambda_1)^2}}{\sqrt{\lambda_1^2+\lambda_2^2+\lambda_3^2}}$	Fibers directionality/axonal loss
MD	mm^2/sec	$(\lambda_1+\lambda_2+\lambda_3)/3$	Amount of water diffusion/myelin loss
AD	mm^2/sec	λ_1	Diffusivity parallel to the fibers/myelin and axonal content
RD	mm^2/sec	$(\lambda_2+\lambda_3)/2$	Diffusivity perpendicular to the fibers/myelin content

FA: fractional anisotropy; MD: mean diffusivity; AD: axial diffusivity; RD: radial diffusivity; mm: millimeters; sec: second.

With the advent of demyelination, myelin barrier is disrupted and water diffusion is facilitated perpendicular to the axons. All in all, this causes an increase in radial diffusivity and a decrease of fractional anisotropy. Of note, abnormal FA values can be also shown due to several microstructural conditions such as inflammation, oedema or demyelination [266]. This has been proved in several studies conducted in the cuprizone mouse model, where radial diffusivity has shown to be an accurate marker of demyelination as confirmed by electron microscopy or histological studies [267]–[269]. These results have also been confirmed in the shiverer mice of hypomyelination [270].

In case axonal damage does not occur, axial diffusivity remains stable. A decrease of axial diffusivity is seen when axons suffer from atrophy or swelling [268], [271], as a consequence of hampered water diffusivity all along axons due to disordering of microtubule arrangement, filament aggregation or accumulation of myelin debris [272]. This was also confirmed in the EAE model, where a reduction of the axial diffusivity parameter was observed in the white matter of the EAE mice, tightly correlating with the staining of phosphorylated neurofilaments [273]. Moreover, in the optic nerve of EAE mice, an increase of radial diffusivity and a decrease of AD has been described [274]. DTI studies conducted in humans have confirmed the

increase of radial diffusivity as a consequence of demyelination, but show controversial data with respect to axial diffusivity [275], [276].

In agreement with the findings in multiple sclerosis mouse models, in a mouse model of retinal ischemia, a decrease in AD was observed after three days as a consequence of axonal damage with a posterior myelin degradation because of the biochemical cascade triggered by the ischemic insult [277]. Similarly, in an Alzheimer's disease model of β-amyloid deposition and in a model of Tau protein expression, decreased RD values have been found in the white matter [278], [279].

6.2.2.5. Water fraction imaging

Generally, mobile water protons in the human brain can be subdivided into three main groups according to their T2 relaxivities: 1) protons with very long T2 times (>2000 milliseconds, but this value depends on the applied magnetic field), corresponding to cerebrospinal fluid; 2) protons with intermediate T2 times (~80 milliseconds) corresponding to intracellular and extracellular water; and 3) protons with short T2 time (~20 milliseconds), corresponding to water within myelin spiral.

Focusing on white matter, two main pools of water can be identified: the first one can be attributed to the aforementioned water trapped between the myelin bilayers, and the second one to the intra-axonal and extra-axonal water [280], [281]. Apart from these, the signal arising from protons in myelin lipids and proteins exhibit very short T2 time, around 10-1000 microseconds. Hence the contribution of this last group would be negligible for the global signal. From the measurement of myelin contribution to the T2 relaxation time, the myelin water fraction (MWF) is estimated as the ratio between the area of the curve corresponding to myelin water and the area of the curve of the total water [282].

Myelin pathologies might lead to an increase of the T2 time of water trapped in the myelin membrane, as a consequence of water liberation. This has been proved in MS patients [280], [283]. An study in guinea pigs at 4T demonstrated the specificity of myelin water imaging [264]. Nevertheless, iron has shown to contribute to signal detected in myelin water imaging. In histopathological studies removal of iron from tissue resulted in an MRI signal drop of 26% in white matter [284]. Further studies are needed to prove the specificity of myelin water fraction imaging.

It should be kept in mind that at high-fields, like the ones used in preclinical imaging, the T2 relaxation time is much lower than at clinical fields. At 11.7T relaxation time of white matter regions vary between 24 and 31 ms [187], on the contrary in a human 3T scanner white matter relaxation time is about 47 ms, approximately [285]. Therefore, the sharp T2 time decay at high fields hampers the acquisition of data from water trapped in the myelin membrane. Studies performed at 7T in the cuprizone mouse model didn't found myelin associated components in the T2 decay [198]. On the contrary, at 1.5T, demyelination and remyelination processes were specifically monitored with this technique in a rat model [286]. This example shows the disadvantages of using high fields, where the reduced T2 times do not enable the identification of multiexponential curves.

6.2.2.6. Ultra-short echo time

Myelin water content is about 40% [287]. Unlike the aforementioned approaches, ultra-short echo time (UTE) targets the non-aqueous components of myelin, from which conventional MRI does not get any direct signal. That is, it targets at protons in lipids and proteins. The decay time of these components is around 10-1000 microseconds in human scanners and therefore virtually undetectable with conventional imaging modalities. Moreover, selective visualization of myelin might

be hindered by the signal coming from water pools.

The use of an adiabatic inversion recovery pulses and UTE pulse sequence has shown to be effective in detecting demyelination [288], [289] in humans (minimum TE of 8 μs) and rat spinal cord [290]. So far, few studies have been conducted with UTE in humans and further validation of this technique is required. Furthermore, this technique is highly demanding for the MRI hardware and is not universally available as the previously discussed techniques.

In summary, multiple MR imaging modalities have been proposed to characterize myelin content in the brain and to study demyelination and remyelination processes. Despite showing enough sensitivity of detection the specificity of the defined parameters, MRI is limited to specific experimental conditions or particularities of the model applied or disease studied. False positives are not unusual at all, and thus, no convention or universal agreement has been reached yet for any of the aforementioned imaging modalities and imaging parameters, or even for other more exotic like T1ρ and other not reviewed here, as a truly specific indicator of myelin content, for which further research in this field is totally justified.

6.2.3. Other Imaging modalities

As an alternative to MRI, other non-invasive or minimally invasive imaging modalities have been described for the study of myelin. Positron emission tomography (PET) is a useful tool for imaging the CNS at a molecular level and has also been used for the evaluation of myelin content. Several tracers has been postulated as potential myelin markers, such as [11C]BMB [291], [11C]PIB [292], [11C]CIC [293] and [11C] MeDAS [294]. Among them, [11C]PIB has shown to be a promising tracer, since it is able to assess the remyelinating capacity of different

individuals [295]. Its function might lie both in its capacity to get trapped in the structure of myelin and in its solubility in the myelin bilayer. Nevertheless, the lipophilic nature of the tracers can result in nonspecific binding [296]. Furthermore, current PET tracers are not able to detect small demyelinating lesions (0.5 mm or less), owing to the intense signal arising from the surrounding myelin. [297]. In addition, Zhang and colleagues have recently concluded that the [11C]PIB tracer was not sensitive enough for the evaluation of myelin in the LPC rat model, due to the side effect caused by the procedure [298]

Even though currently there is not any robust tracer for myelin, in future PET might become a technique of interest for the evaluation of remyelinating therapies. However, contrary to magnetic resonance scanners, PET imaging is not widely available in clinical sites and it requires the injection of a radioactive tracer.

On the other hand, visual evoked potential measurement is a non-invasive tool for the evaluation of the visual system. This can be applied in optical neuritis which usually manifested in the first stage of MS. Roughly speaking, the amplitude of VEPs is thought to be correlated with the number of functional nerve fibres. The prolongation of VEP latency after the lesion has been put forward to describe demyelination, while a reduction of the VEP latency has been attributed to remyelination [26]. This technique has been used for the assessment of therapies in clinical trials [51], but the use of this indirect measurement is just limited to the visual pathway.

7. Resting-state functional MRI

To finish this introductory section, the principles and use of functional MRI will be reviewed. Indeed magnetic resonance does not only provide anatomical imaging but

offers the possibility to assess the connectivity patterns in a functioning brain, depicting the organization of neuronal networks and how these change in terms of changes on organization and strength of connectivity. Certainly, brain function can be altered as a consequence of natural processes such as maturation, aging or learning, or in response to pathological and healing processes.

In particular, resting-state functional MRI (rs-fMRI) has emerged as a very useful tool for the evaluation of brain function and connectivity, revealing substantial abnormalities in neurodegenerative diseases. Importantly, during the last decade an extensive characterization of rodent brain connectivity has been performed. Nevertheless, still further gaps in knowledge have to be addressed regarding brain connectivity. In this work implications of both remyelination and demyelination in brain function and connectivity will be addressed, taking into account that they take place in the context of aging, which also has an impact on functional changes. But first, the principles of rs-fMRI, data acquisition and analysis approaches and the importance of the anaesthetic protocols for preclinical imaging will be reviewed.

7.1. Principles of resting-state functional MRI

The brain enables us to perform countless functions. Even though the brain is composed of several specialized brain regions, a constant interaction between them endows us with the capacity to perform a multitude of tasks. The complexity of the brain is still beyond our comprehension and still, a heap of questions are unresolved. Nevertheless, brain imaging has undergone great development during the last decades, providing deep knowledge. Since its discovery in the early nineties, resting-state functional MRI has become a crucial tool for the understanding of brain functions.

Neurons are energetically highly demanding cells, which lead to a high oxygen and glucose requirement. When performing a given task, the supply of oxygen and the cerebral blood flow are increased regionally, this is called hemodynamic response [299]. As a consequence, with the advent of function, deoxyhemoglobin will be partially substituted by oxyhemoglobin.

The different magnetic susceptibility of oxyhemoglobin and deoxyhemoglobin alters the local magnetic field and therefore affects the magnetic resonance signal. While oxyhemoglobin has diamagnetic properties, deoxyhemoglobin is paramagnetic. Hence, deoxyhemoglobin can lead to a reduced T2* relaxation time, comparing to oxyhemoglobin, producing a blood oxygen level-dependent (BOLD) signal changes in MRI [300]. Identification of active regions can be carried out by detection low frequency (0.01-0.1 Hz) fluctuations in the signal.

Until 1995, functional MRI studies were task or stimuli based. These experiments seek for regional activity under a given task, compared to a non-stimulated control status. In 1995, Biswal and colleagues were performing one of those experiments, recording BOLD response while performing a finger-tapping activity. In the meantime of tapping activity, they found a tight correlation between the homologous regions of the motor cortex in both hemispheres of the brain corresponding to neural activity [301]. They postulated that a deep analysis of MRI signals from the brain in the absence of any stimulus (resting.state) could actually provide the information required to build up connectivity maps of the different neuronal networks. From that time on, rsfMRI has become a valuable tool for the understanding of the brain and neurologic pathologies, focusing on low frequency brain fluctuation of the BOLD signal. Interestingly, Ma and colleagues confirmed the tight correlation between rsfMRI and neural activity by recording neuronal activity with optical imaging of calcium-sensitive fluorophore GCaMP together with rsfMRI

[302]. Compared to task-evoked fMRI, rsfMRI can have a detailed view of brain networks that are not accessible by sensory stimulation and depict multiple networks simultaneously.

Certainly, rs-fMRI has allowed the identification of several neuronal networks. The default mode network (DMN), is a highly consistent network between different individuals and across time [303]. Additionally, it has been demonstrated its conservation in different species [304], [305]. Further studies in optical imaging [306] and PET have confirmed the existence of this network, involving many regions of the brain [307]. Moreover, the importance of this network also relies on its implication in several neurodegenerative pathologies [308]–[310].

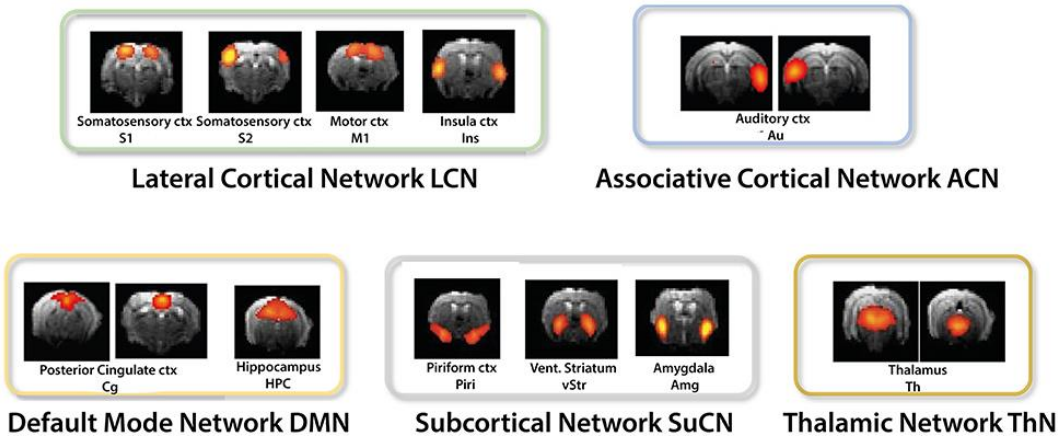

Figure 14. *Group independent component analysis (ICA) identification of functional hubs in the mouse brain (Bukhari, Schroeter, Cole, & Rudin, 2017).*

During the last years, substantial progress has been made in rodent resting-state fMRI. This has been possible due to the increasing interest in identifying imaging biomarkers of neurodegenerative diseases. In this setting, rodent models provide the possibility to perform longitudinal studies and manipulate experimental

variables. Furthermore, the development of transgenic rodent models permits a detailed study of a particular component. For instance, in Alzheimer's disease, a mouse model β-amyloid deposition [311], a mouse model of tau protein overexpression [278], [312] and a mouse model overexpressing both β-amyloid and Tau-protein have been developed [108]. In this way, the implications of each given marker of the pathology can be revealed. Additionally, better development of experimental protocols for rodent resting state [313], [314] has further facilitated a large characterization of resting-state networks in rodents [315], [316]. The importance of studies conducted in rodents it is increasing by the fact that resting-state cortical and subcortical networks have been found analogous to those in humans in both rats [317], [318] and mice [315], [319].

7.2. Data acquisition and analysis

The analysis of resting-state data is of utmost importance. Signal fluctuation in fMRI is highly contaminated by confounding effects that should be filtered out. In fact, data from the human connectome project reveals that signal related to neural activity was observed to correspond to the 4% of the variance of the total signal [320]. The rest of the signal corresponds to physiological noise (heart-rate, respiration), motion artefacts and artefacts arising from the scanner electronics and vibrations. However, many of these effects, such as respiration and cardiac pulse, take place at higher frequencies than neuronal activity related to BOLD signal fluctuations and can be filtered by signal processing techniques [315].

Thus, it is crucial to perform noise removal that could hide fluctuations arising from BOLD. A preprocessing pipeline usually includes motion correction, spatial smoothing, removal of the first 10-20 time points, normalization, high-pass filtering and registration to a common space [321]. Murphy et colleagues provided a detailed

review of data cleaning approaches [322].

In practice, two main approaches are followed for rs-fMRI data acquisition and processing. The first approach consists in the monitorization and recording of physiological parameters during data acquisition. After the recording, linear regression can be performed to remove the confounding effect. Kalthoff and colleagues [314] observed that linear regression of motion reduced the variance of data by 15% to 35%. Additionally, respiration regression reduced the variance approximately 5%, while the main magnetic field drift and cardiac pulse regression lead to a reduction of 1% in rats. Even though this might be an effective strategy, physiological monitoring data is not always straightforward or available (MR compatible devices are required for monitoring). Additionally, many artefacts arising from the MRI hardware are not removed by this approach alone. These artefacts are show complex patterns and could be challenging to remove [323].

The second approach is a data-driven procedure consisting of accomplishing a decomposition of signal through independent component analysis (ICA) [324] with a posterior removal of noise-related components. ICA decomposes fMRI data into several components, each of them represented by a 3D spatial map and a time course. Some of these components will correspond to neuronal activity related signal components and the rest of them to artefacts or noise, which can be regressed out to reduce the negative effect on posterior analysis. The correct classification of these components is crucial. To address this aim, some automatic approaches have been developed. This will call for visual inspection of components for posterior training. The spatial and temporal behaviour of signal and noise components are extensively described in the literature [323], [325], [326]. The correct interpretation of the ICA spatial map, the power spectral density and the associated time series are essential for a proper evaluation. The following ones are the main features of signal

components regarding the spatial map [327]:

- Low number of large clusters.
- Activity should be found in grey matter and not in white matter.
- Activity should not be overlapped with the boundaries of the brain.
- Activity should not be found close to regions prone to have susceptibility artefacts.
- Activity should not contain artefacts related to the MRI sequence, such as banding patterns or streaks.

Concerning the interpretation of the time series, signal related components exhibit an oscillatory time course. For instance, components arising from motion can show a pronounced peak in the time series.

Manual classification might be time consuming and with big sample size, it could become tedious. In order to facilitate data analysis, automatic artefact component classification and data cleaning can be conducted with FIX [328] which is based on the hierarchical fusion of classifiers (http://fsl.fmrib.ox.ac.uk/fsl/fslwiki/FIX). The use of FIX requires previous training with high-quality data. This approach has shown to be effective both in humans [329] and rodents [330].

7.3. Analytic approach

After data cleaning, group analysis is performed. There are two main approaches for the interpretation of resting-state data: temporal association and temporal integration [331], [332]. The first one is focused on regional activity and is used for mapping of active areas. The second one looks for connectivity between different regions by looking at the temporal correlation of the time series over time. ICA

(temporal association) and Seed-based correlation analysis (temporal integration) are the two main approaches

7.3.1. Seed Based Functional Connectivity Analysis

Seed based functional connectivity analysis (SCA) is a widely used approach for the study of brain connectivity. The aim of SCA is to assess the temporal correlation between the mean time series of different regions. The selection of the ROIs can be done in a hypothesis-driven way or after a previous analysis, such as ICA. Hence, regions with a high temporal correlation are suggested to be connected and participate in the performance of the same task. After the measurement of the partial or full correlation between different regions of interest, a matrix plotting the strength of each interaction is often built with a colour-coded fashion.

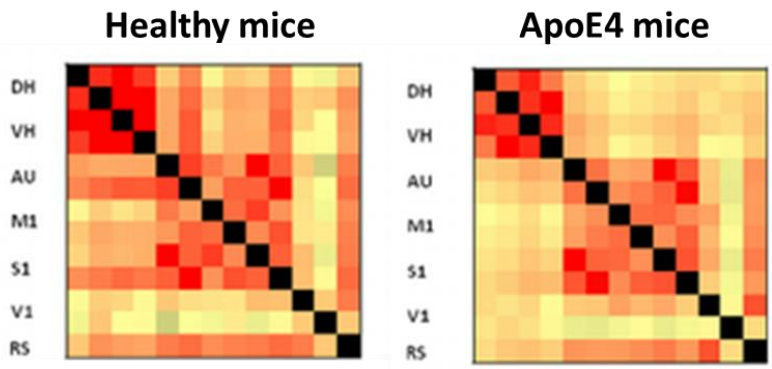

Figure 15. *Cross-correlation matrices of healthy mice and ApoE4 knock-out mice. Adapted from* [333].

The use of this analysis has been widely used and has been sensitive to the identification of altered connectivity in pathological conditions [186], [334], [335]. Indeed, the main advantage of this analysis is its interpretability and simplicity.

However, the reached conclusions might depend on the ROIs selection.

7.3.2. Independent component analysis

Independent component analysis (ICA) can be carried out for the cleaning of data and also for the identification of resting-state networks group-wise. This is not hypothesis-driven and enables the identification of independent spatiotemporal components that correspond to functional networks.

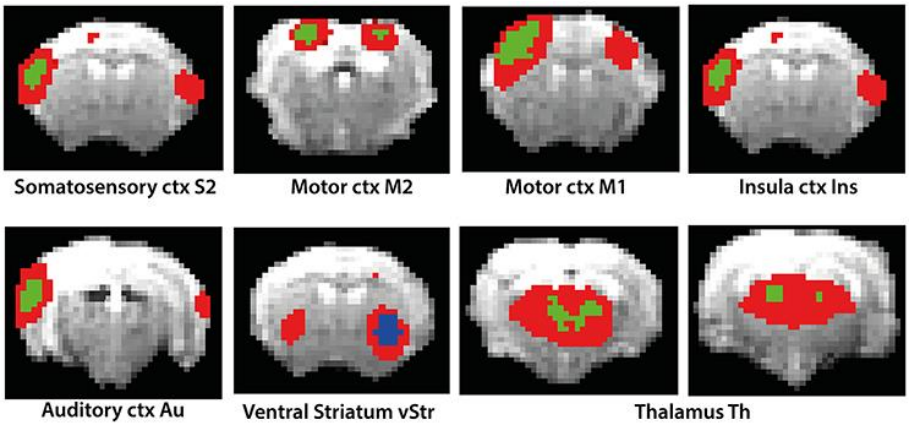

Figure 16. *Results of Dual Regression analysis for eight components derived from ICA for isoflurane-anaesthetized mice compared to medetomidine-anaesthetized mice (green higher, blue lower).* [336].

This is achieved by decomposition of 4D fMRI data into independent components. It is performed in two steps: first, 4D fMRI data is ordered in a 2D space by arranging all voxels for each given time point into a single row. Second, this matrix is decomposed into two additional matrices, one containing the time course of each component in each column and the second one containing the spatial map of each component in each row. In this way, networks consistent within a given group can

be detected, while signal arising from confounding sources in each individual is removed by averaging. Contrary to SCA, this approach enables the identification of all active regions in the brain.

7.4. Anaesthetic protocol

A final aspect that should be tackled is the key influence on the use of anaesthetics, in the case of animal experiments. Unless extensive and complicated training is performed, research animal, conversely to humans, does not show a cooperative attitude when performing fMRI experiments. Thus, confounding effects such as anxiety and fear, as well as strong movement artefacts would be present in non-sedated or anaesthetized animals. This calls for the use of anaesthesia protocols that for sure have some influence on neural activity and thus, anaesthesia protocols become a crucial part of fMRI studies in rodents, with critical influence in the results obtained [337].

Ideally, the anaesthetic protocol should avoid the motion of the animal while achieving a brain state resembling the wake-up activity. The use of anaesthesia can have several implications in brain function and may interfere with the resting-state networks. In a study performed by Grandjean and colleagues [338], it was described that in mice under isoflurane cortical activity is observed, while subcortical networks are attenuated. With medetomidine anaesthesia, on the other hand, subcortical activity was displayed. The combination of both anaesthetics at low dose resulted in a superposition of the effect of both anaesthetics, exhibiting extended activity in both cortical and subcortical regions. A lot of work has been published in relation to the influence of anaesthesia, and multiple protocols have been described in the literature. However, the experimental protocol based on the use of these two anaesthetics, as described elsewhere (Egimendia et al, 2019) is widely accepted by

the scientific community and it will be used in the experimental sections of this works.

So far the theoretical background and a comprehensive review of the state of the art has been provided in relation to myelin, myelin-related pathologies, therapies and the existing experimental techniques for the study, both at the anatomical and functional level. Thus, the information provided here is sufficient to facilitate the full comprehension of the experimental sections of this work that will follow this introductory section.

Justification

Demographic changes in our society, reflected in progressive aging of the population in industrialized countries, has a direct impact on the incidence of neurological disorders, with the corresponding burden for society at welfare and economic levels. Loss of autonomy and dependency of individuals associated with aging and neurological disorders is one of the most worrying threats for healthcare systems. The understanding of the mechanisms underlying functional deficits and/or cognitive decline associated and the development of strategies to ameliorate their impact or simply to promote healthy and active aging, are among the most ambitious framework policies of the authorities and supra-governmental organizations such as the EU or the WHO.

It is well established that myelin is an essential element for neuronal transmission and that alterations in myelin content and structure are implicated in the cognitive decline suffered during the progression of multiple sclerosis and other demyelinating pathologies. In this context, remyelination has emerged as a promising neuroprotective approach, putting forward several potential therapeutic approaches to facilitate this process. In consequence, the development of models and tools that allow us to fully characterize the process of demyelination and remyelination, from both an anatomical and a functional point of view, is of paramount importance for the development of novel therapeutic approaches to treat myelin-related diseases. Despite the efforts done in this direction, no single experimental model or experimental techniques have managed to become gold-standards for such purpose, and studies aiming at the establishment of robust experimental models and protocols for the study of myelin are justified.

In this work, started three years ago we described our efforts to establish robust experimental models where demyelination and remyelination processes take place, both at in vitro and *in vivo* settings, and to develop non-invasive methodologies that

will allow us to perform non-invasive and longitudinal studies of the progression of these processes and evaluate the effectiveness of therapeutic approaches for remyelination. In particular, we have focused our attention on the use of magnetic resonance imaging, an experimental technique that presents high versatility and no invasiveness. Additionally, it provides both anatomical and functional information and is readily translatable to the clinical setting, since is one of the most powerful and used medical imaging techniques in this context.

Our final aim was to 1) contribute to de field by providing robust experimental models and techniques to study myelin in a non-invasive manner, 2) to use them to study the processes of demyelination and remyelination both at anatomical and functional level, highlighting the strengths and pitfalls of the proposed methodologies and 3) to test them in terms of sensitivity to describe the advantages of a remyelinating therapy, in order to highlight their potential as fundamental tools to enable the development of novel and more effective therapies against demyelination.

Hypotheses

The present work has been developed based on the following working hypotheses:

1) In vitro models of demyelination and myelination are fundamental tools for the study of these processes. However, quantification of myelin in such models remains a challenge for the current state of the art. Thus,

- We hypothesize that magnetic resonance imaging could become a valuable tool to determine the myelin content in *in vitro* models of demyelination.

2) Non-invasive assessment of myelin content and status in *in vivo* models of demyelination and remyelination is a key aspect for the study of these processes. Despite several magnetic resonance imaging parameters have been postulated as potential imaging biomarkers of myelin, certain controversy remains in the current state of the art about their sensitivity and specificity, and none of them has achieved the status of gold-standard.

- We hypothesize that it is possible to define an MRI parameter, or series of parameters, which used in conjunction with histological validations, can describe with sufficient sensitivity and specificity, the processes of demyelination and remyelination in a non-invasive and longitudinal manner.

- We further hypothesize that the experimental conditions such as the timing of the experiments, the magnetic field of the MRI system, the spatial resolution and other experimental conditions can influence the potential universality of use of those parameters.

- Finally, we hypothesize that the animal model used for the study also plays a key role in the potential universality of MRI-based parameters as imaging

biomarkers of myelin since most of them are altered in different manner and by different pathophysiological processes. Thus, specific imaging biomarkers established using the cuprizone mouse model might lose specificity to detect myelin-related phenomena in models of other diseases, such as Alzheimer's disease.

3) Alterations of brain connectivity and functional networks concomitant with pathological and or therapeutic processes, in the context of demyelinating diseases, remain not completely elucidated in the current state of the art.

- We hypothesize that resting-state functional MRI methodology is sensitive enough to detect functional decline and reinstitution associated to the demyelination and remyelination processes present at the murine cuprizone model of multiple sclerosis, and that the performance of a longitudinal functional study in the cuprizone murine model may provide invaluable information to understand the underlying mechanisms of both processes.

- We further hypothesize that resting-state fMRI is sensitive enough to detect differences between spontaneous (naturally occurring) vs. therapeutically induced functional recovery from a demyelinating insult, reinforcing the importance of this technique for the development of therapies for the treatment of multiple sclerosis and other demyelinating diseases.

Objectives

Based on the aforementioned hypotheses, these have been the objectives of the current work:

- To develop an experimental setup that allows the use of magnetic resonance imaging for the non-invasive and longitudinal assessment of myelin content in an *ex vivo* model (organotypic cultures) for demyelination-remyelination.
- To find an MRI parameter, or series or parameters, that can be used as a sensitive and specific imaging marker of myelin content in the *in vivo* cuprizone murine model of demyelination-remyelination, with the corresponding histological validation.
- To use the developed imaging protocols to provide a high temporal and high spatial resolution longitudinal description of myelin content in the brain of mice, both during the demyelinating insult induced by cuprizone and the spontaneous remyelination that follows, including the acute and chronic stages of the pathology.
- To test the specificity and universality of the developed imaging protocols in the mouse model of β-amyloid deposition and in a mouse model of tauopathy, representative of events related to Alzheimer's disease.
- Use of the aforementioned MR imaging protocols to establish if the development of β-amyloid deposits or neurofibrillary tangles has associated alterations on myelin, in two animal models of Alzheimer's disease.
- To develop experimental protocols for functional MR imaging that allow the description of functional connections in the brain, as well as the quantification of their strength, and use these techniques to analyse the impact of demyelination and remyelination at functional brain connectivity

level in the brain using the cuprizone murine model.

- To use the aforementioned functional methods to compare spontaneous versus therapeutically enhanced remyelination processes from a functional and anatomical point of view, treating cuprizone intoxicated animals with clemastine.
- To investigate the functional changes associated with the processes of maturation and aging in healthy subjects as potential confounding effects on the long-term functional studies of demyelination and remyelination processes.

Experimental Section

Chapter 1

Magnetic resonance imaging as a tool for the study of cerebellar organotypic cultures

1. Foreword

Organotypic cultures represent an advanced in vitro model of added value for the study of pathologies of the central nervous system, such as demyelinating diseases. Several reports in the literature have shown the goodness of these cultures for the study of demyelination and remyelination processes. We believe that it is possible to develop a protocol for the quantification of myelin in organotypic cultures by non-invasive means, in particular by magnetic resonance imaging, enabling the study of such cultures in a longitudinal way, with the advantages that such feature represents. Thus, the first experimental chapter of this thesis is devoted to the efforts carried out to develop experimental protocols of preparation and managing of organotypic cultures from mouse brain and to develop MRI based imaging protocols to quantify myelin content on those cultures.

Being aware of the difficulties that involve exploring unknown terrain and of the limitations that magnetic resonance imaging could have for culture imaging, we have carried out a reductionist approach to tackle this issue, as we report in this chapter.

2. Introduction

In vitro models can provide very important information on particular biological aspects or events, helping to a better understanding of mechanisms of disease or healing in shorter time than *in vivo* models, by isolating the target subject of study from confounding effects present in the complexity of an *in vivo* setting. In general, *in vitro* models may represent different levels of simplification. For the particular case of the central nervous system, the neurovascular unit is a quite complex system with strong interaction among its components and thus, unlike *in vitro* cell cultures, *ex vivo* organotypic brain cultures may provide a more realistic setting in which glia closely interact with neuronal axons in three-dimensional space [160]. Organotypic brain cultures have become a simplified way to study demyelination and remyelination processes and are considered a suitable tool for the evaluation of therapies, based on drugs or by genetically manipulated cells [158] (Fig. 1.1). One of the biggest advantages of using this model is the possibility to run multiple studies in parallel, with virtually the same conditions for all *in vitro* samples. In this way, several treatments can be evaluated in a short period of time compared to *in vivo* studies, enabling rapid screening of high-throughput therapies.

Different brain regions have been typically cultured, however, since the cerebellum contains a homogeneous axonal architecture, it has been put forward as an appropriate model for the study of myelin [156]. Briefly, cerebellum extracted from mice at post-natal day 7-12 can be sliced in sections of 300-350 μm of thickness, and cultured on semipermeable membranes immersed in culture media. Tissue sections have to be cultured for a period of at least 7 days in order to enable the cerebellum slice to adapt and recover from the impact of processing. At this point, lysolecithin can be added to the medium to achieve extensive demyelination [157]. Following

the demyelinating insult, remyelination is conducted spontaneously within the following days [158], which can be further stimulated through therapies.

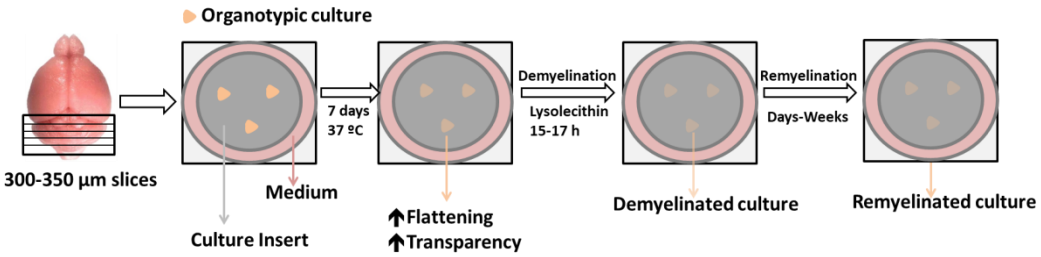

Figure 1.1. *Preparation of cerebellar organotypic brain cultures for the study of myelin pathology. A mouse brain is extracted from post-natal mice (7-12 days) and sliced in 300-350 µm. Slices are cultured for one week and lysolecithin is applied to induce demyelination. Finally, remyelination takes place spontaneously, which can be boosted by therapies.*

Myelin content on those cultures has been traditionally characterized by invasive methods like RT-PCR, western blot or immunofluorescence [162]. However, each of those has disadvantages: 1) RT-PCR quantifies myelin related genes but does not provide a direct measure of myelin content. 2) Western blot can provide a semiquantitative measure of myelin content, but it is not sensitive enough to detect the myelin content of a single slice. 3) Immunofluorescence is based on the staining of axons and myelin separately. As such, co-localization of channels would correspond to myelinated axons. Although information of great interest can be obtained, it is challenging to have a quantitative and reliable measure of myelin content.

Additionally, long-term live imaging can be also performed with organotypic cultures transgenes expressed in mice [163]. Nevertheless, so far, any technique has shown the simplicity and accuracy to assess myelin content in a robust way.

In this context, we postulate that magnetic resonance imaging could provide a

quantitative or semi-quantitative estimation of myelin content in cultures, with the huge advantage of non-invasiveness, and therefore enabling longitudinal studies in the same cultures. MRI has been widely used for quantification of myelin humans and preclinical models and many parameters have been tightly correlated to myelin content, such us, T2-weighted signal or radial diffusivity (for more information refer to Chapter 2) [215]. However, imaging of organotypic cultures represents a great challenge due to several factors. During thriving, brain slices lose stiffness, spreading on the surface of the supporting membrane where they lean on, becoming increasingly thinner, reaching a thickness below 100 μm [339]. In this work, we describe our attempts to achieve an experimental protocol for the MRI based non-invasive quantification of myelin content in organotypic cultures from mouse cerebellum, including molecular imaging approaches that require the design of myelin-specific imaging probes. This challenge has been arduous, considering that organotypic culture imaging is far from being a simple and reliable method, due to the various obstacles found on the way. In fact, to our knowledge, there are less than 10 publications on this issue, and most of them actually use tissue slices, with their characteristic thickness and structures, but not purely thin organotypic cultures.

In a reductionist approach, we have conducted this research in four steps of increasing difficulty. First, we have studied the possibility of using MRI to image slices of tissue directly excised from the cerebellum of mice and immediately fixed in paraformaldehyde (herein referred as brain tissue sections). The purpose of this study was to set up imaging protocols, the logistics of placing tissues in the magnet and adapt the MR hardware for proper imaging of these experimental setups. Additionally, we also tested the sensitivity of detection, the limits of spatial resolution and the Signal-to-Noise ratio and Contrast-to-Noise ratio achievable, using consistent and stiff pieces of biological material of well-defined tissue limits

and internal structures. Secondly, we continued our research with proper organotypic tissue cultures of large thickness sections (herein referred as thick organotypic cultures), cultured for one week, that somehow resemble the brain tissue sections but with more diffused boundaries and internal structures. Next step on our research consisted on the use of thinner organotypic tissue cultures (herein referred as thin organotypic cultures) where is practically impossible to distinguish any internal structure by visual inspection and basically resemble thin amorphous masses of tissue. Finally, we have constructed imaging probes that specifically target myelin for a molecular recognition approach, in an attempt to increase the sensitivity of detection of myelin in the tissue cultures. Somehow with this approach we have used a relatively simple starting point and we progressively advanced towards the real, more complex, *in vitro* model that we desired to develop.

3. Materials and methods

3.1. Brain tissue sections

C57BL6/6 mice at postnatal day 7-12 were sacrificed, brain cerebellum were sliced at a different thickness (1.9 mm, 0.8 mm, 0.5 mm, 0.3 mm, 0.1 mm) and fixed in paraformaldehyde (10%) for 40 minutes. Next, brain sections were washed with PBS 2 x 10 minutes and imbibed in 2% low melting point agarose (A9539; Sigma) in a 50 ml Falcon tube for imaging. The possibility of performing multi-planar imaging allowed us to scan sets of several tissue sections in each experiment, by piling the sections inside the agar gels.

MRI studies were conducted at 7 and 11.7 T Bruker Biospec MRI systems. Image of different brain tissue slices and organotypic cultures were acquired with spatial resolutions ranging from 25x25x25 μm3 to 100x100x500 μm3. Different T2-

weighted imaging modalities have been tested (turboRARE, MSME) with echo-times ranging from 30 to 50 ms and repetition times ranging from 2000 to 5000 ms. Thick organotypic slices have been acquired with a turboRARE sequence with a TR=2000 ms; RARE = 10; effective echo time TE=70 ms; FOV =10 mm x 10 mm; Image matrix 400 x 400; 24 slices with a thickness of 0.3 mm without a gap.

Moreover, imaging of thin organotypic cultures was also conducted with a spin-echo diffusion technique with a b-value of 1500 s/mm^2, gradient pulse duration of δ =6 ms, gradient pulse spacing of Δ=14ms, TR=2820 ms, slice thickness 0.250 um.

For the analysis of the images the Signal-to-Noise Ratio (SNR) was calculated for white and for grey matter, at the different tissue thickness and for both spatial resolutions (Table 1). SNR was defined as the mean signal intensity in a region of interest (ROI) of the tissue, divided by the standard deviation of the noise obtained from a ROI at the background, outside of the object of interest (SNR= $mean_{tissue}/SD_{background}$). The Contrast -to-Noise Ratio (CNR) between grey and white matter was obtained as the difference of the mean of each tissue divided by the standard deviation of the background (CNR= [$mean_{GM}$ - $mean_{WM}$] / $SD_{background}$).

3.2. Thick organotypic cultures

C57BL6/6 mice were sacrificed at post-natal day 10-12. The cerebellum immediately extracted and placed in organotypic culture medium, with BME 24 ml (41010, Thermo Fisher); 24% HBSS (24020091, Thermo Fisher); 24 % Horse Serum (26050088, Thermo Fisher); 0.125% Glutamine (25030024; Invitrogen); 1% antimycotic and antibiotic (A5955, Sigma); 3.5% Glucose (A1422, Panreac) for every 50 mL.

Following this procedure organotypic brain slices of 750 µm thicknesses were

cultured. Sagittal sections of the cerebellum were taken using a McIlwain tissue chopper (McIlwain). Sections were separated and placed on a Millicel Cell Culture Insert membrane (PCIM ORG 50, Millipore) on a P6 plate and incubated in organotypic culture media at 37 °C and 5% CO_2. Next, cultures were fixated with 4% paraformaldehyde for 40 minutes and kept in PBS (0.05% sodium azide) at 4ºC until scanning session. Organotypic cultures were embedded in 2% agarose before MRI scanning. For this aim, the membrane of the cell culture insert was gently cut around the tissue with a scalpel.

The MRI sequences and parameters used for imaging these agar gels with imbibed cultures was based on the previously optimized sequences for tissue sections, and parameters were used in the same ranges as defined before.

3.3. Thin organotypic cultures

Thin organotypic culture samples were prepared as described in the previous section, but with a thickness of 350 μm, which represent the desired target for our experimental *in vitro* assay (see discussion section).

Demyelination was always induced after one week of culturing by exposing organotypic cultures to 0.5 mg/mL lysolecithin (L4129, Sigma) containing medium for 15-17 hours.

3.4. Myelin specific functionalized liposome synthesis and staining.

Myelin-targeting liposomes were prepared by the lipid film hydration and extrusion method [340] using a mixture of lipids composed by 1,2-distearoyl-sn-glycero-3-phosphocholine (DSPC: x= 0.6), 1,2-distearoyl-sn-glycero-3-phosphoethanolamine-N-[maleimide(polyethylene glycol)-2000] (ammonium salt) (PEG-DSPE: x= 0.025),

DTPA-bis(stearylamide) (gadolinium salt) (Gd-BSA: x=0.017), Cholesterol (Cholesterol : x=0.333). All lipids (from Avanti Polar Lipids, AL, USA) were dissolved in chloroform:methanol (6:1) mixture. Films were formed by the evaporation of chloroform:methanol (6:1) solution on a rotavapor (high vacuum at 30°C), dried under nitrogen flow for 2 h and rehydrated with 7 mL of water at 65°C. Rehydrated liposomes were extruded 14 times at 65°C through polycarbonate membrane filters (Whatman, Renfort, UK) using consecutive decreasing pore sizes of 400 nm (x2), 200 nm (x4) and 80 nm (x8). Once the liposomes were obtained, their lipid content quantification was done by Rouser method [341].

Gadolinium ions (Gd^{3+}) responsible for the generation of T1 MRI contrast were complexed with the lipid Gd-BSA, which is a constitutive element of the liposome membrane. It was possible to tailor the magnetic properties of liposomes to get the best performance in MRI by modifying the DTPA-BSA percentage during the lipid film formation. Four different Gd-BSA concentrations were assayed in order to achieve the highest T1 effect (represented as R1 (1/T1) in Fig. 1.5B). The fluorescent die 3,3'-Dioctadecyloxacarbocyanine Perchlorate (DiOC18) (Life Technologies, NY, USA) was added to the formulation into the organic phase before lipid film was formed.

Liposomes were conjugated with the anti-myelin basic protein antibody (Ab62631, Abcam) or anti-IgG protein as a control antibody (referred to as control liposomes) (Ab18447, Abcam). To address this aim, the antibody was activated by mixing it in SATA solution (1:80 mol/mol). Afterwards, the SATA-antibody solution was added to the liposome solution in a vial (50 μg of protein per 1 μmol of lipids) and kept it overnight at 4°C under N2 atmosphere. Uncoupled protein was removed by centrifugation (65000 rpm, 45 min) and the pellet containing the liposomes was resuspended in HBS until use.

Cell culture inserts were prepared, each of them with 3 thin organotypic slices. After one week, cultures were demyelinated as mentioned before. Control cultures were not exposed to lysolecithin. Next, cultures were fixated with 4% paraformaldehyde for 40 minutes and washed with DPBS. Tissue was blocked with a solution composed of DPBS, 0.5% Triton (T8787, Sigma) and 10% goat serum (G9023, Sigma) for one hour at room temperature. A volume of 350 µL of liposomes was added and samples were incubated overnight at 4°C. Then, samples were washed with 0.1% Triton in DPBS and stained with Hoechst (B2261, Sigma) 10% in DPBS for 10 minutes. Images were acquired using a Nikon Eclipse 80i digital microscope (Nikon) and analyzed using NIS elements AR 3.2 software (Nikon).

4. Results and Discussion

The development of remyelination therapies during the last decade calls for the development of new techniques for the evaluation of the effect of a given therapy. This should be accomplished both in *in vivo* models and in simpler models, such as the organotypic culture, in which remyelination therapies could be tested [156]. In this study, we have looked for a reliable, robust and reproducible imaging technique for the quantification of myelin in organotypic cultures for high-throughput therapies. Magnetic resonance imaging stands out for its high resolution that together with an ultra-high field MRI could tackle this issue.

To evaluate image quality we have made use of the Signal-to-Noise ratio metric [342]. High resolution imaging of brain tissue slices of different thickness enabled obtaining 2D MR images with high SNR (Fig. 1.2 and Table 1.1), and a good contrast between white matter and grey matter regions of the brain. Sagittal 2D images were acquired to locate the tissue sections within the agarose gels (Fig. 1.2A), and then 300 µm thick 2D coronal sections were acquired through the middle section of the

tissues, irrespective of the thickness of the tissue slice (Fig. 1.2B). Moreover, no artefacts arising from sample manipulation were detected.

As shown in Table 1.1, higher SNRs are obtained at higher spatial resolution in all the slices, with no substantial differences at different tissue section thickness (logical if we consider that imaging slices are all acquired at 300 μm thickness, irrespective of the thickness of the tissue section). CNRs also showed similar orders of magnitude for all tissue sections and spatial resolutions.

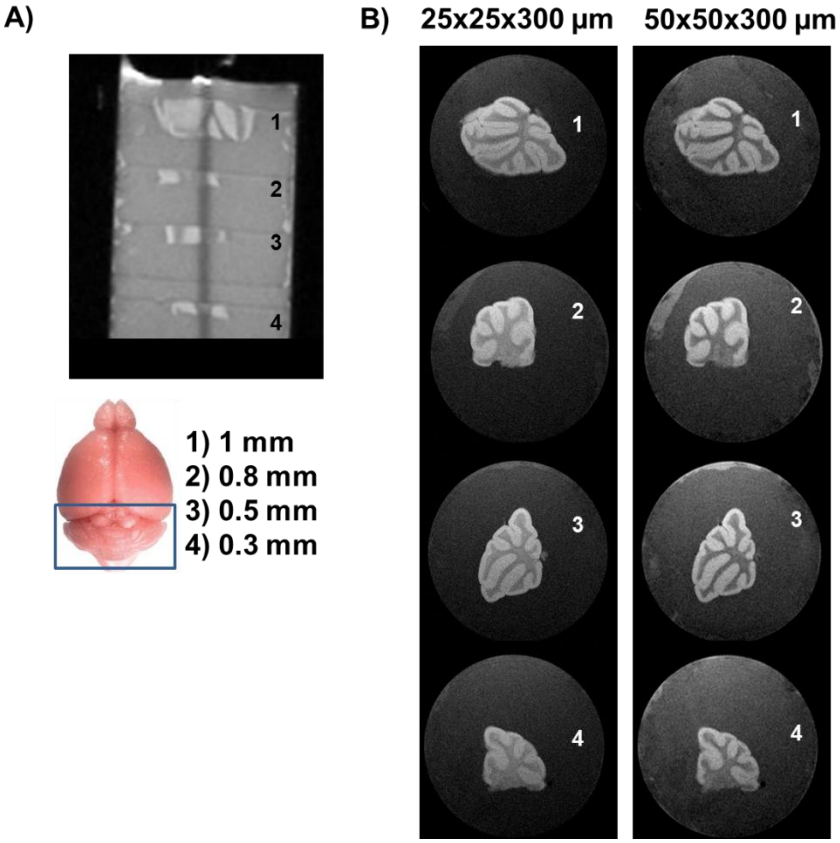

***Figure 1.2**. Imaging at 7 T of cerebellum of mice at postnatal day 7-12, sliced at various thicknesses (1 mm, 0.8 mm, 0.5 mm, 0.3 mm approximately) and fixed in 2% agar. A) Sagittal MRI image showing piled cerebellum tissue sections of different thickness imbibed. B) Coronal images of the different tissue sections at different spatial resolutions.*

Table 1.1 *SNR and CNR of T2-weighted images of brain slices.*

Tissue thickness (mm)	Ultra Hi-Res (25x25 µm)			Hi-Res (50x50 µm)		
	SNR_{GM}	SNR_{WM}	CNR_{GM-WM}	SNR_{GM}	SNR_{WM}	CNR_{GM-WM}
1.0	39.3	26.0	13.4	17.7	11.2	6.5
0.8	37.1	25.6	11.5	33.7	18.2	15.5
0.5	32.8	22.9	9.9	25.6	14.8	10.8
0.3	28.5	22.7	5.8	25.4	16.3	9.0

What this study demonstrates is that when tissue sections present internal structures and tissue boundaries that are well preserved, MRI is capable to distinguish white matter from grey matter with a good SNR, and showing good contrast between white and grey matter, within a wide range of experimental conditions. However, the practical applicability of imaging these brain slices is limited, since MRI enables the non-invasive acquisition of *in vivo* images of the whole brain without the need of slicing the brain. In this case, we pursued the use of an easy-to-handle experimental setup that resembles the final target tissues, for optimization of imaging protocols. Once this goal was achieved, a more ambitious objective was targeted by imaging thick organotypic brain slices.

We have already pointed out that typical organotypic cultures are prepared from tissue sections of 300-350 µm thickness when excised from the brain. However, before we attempted to image such cultures, we prepared cultures of double thickness, to further optimize experimental protocols with reasonably manageable samples. In tissues of such thickness maintained in culture, the permeability of nutrients and oxygen to the inner parts of the tissues is compromised, usually leading to cell loss and tissue necrosis [160]. Even though attempts have been carried out for culturing organotypic thick slices [161], their suitability as a model

for studying demyelination and remyelination processes is remote. Thus, we consider this sort of material as a further step towards our final goal, but not a valid model for future studies.

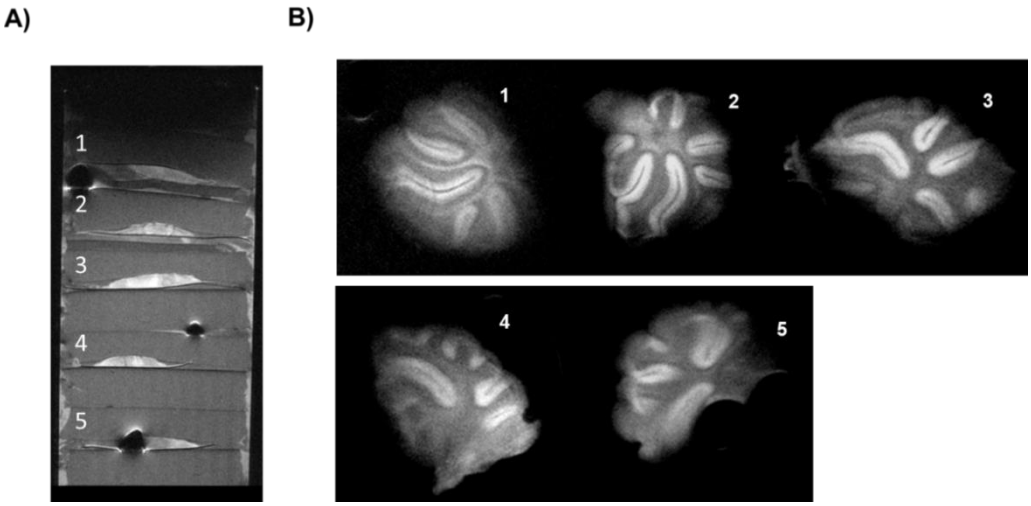

Figure 1.3. *A) Sagittal view of piled thick organotypic cultures imbibed in agar gel. Air pockets are visible as large susceptibility artefacts (signal voids). B) Coronal 2D MRI images of the cultures derived from mouse cerebellum at postnatal day 7-12 and cultivated for 7 days.*

A set of 5 organotypic cultures of 750 μm thickness at the beginning of the culture (slices start to collapse with time so the final thickness is reduced) is presented in Fig. 1.3. Only results for the optimized MR imaging sequence and target spatial resolution are presented here. The mean calculated SNR for this cultured tissues resulted in 62.7 for grey matter and 38.9 for white matter, with a CNR of 31.9 between both tissues. With these results, we can conclude that actually good quality images can be obtained from these cultured tissues where the white matter is still clearly identifiable. However, lines defining the limit between white and grey matter, as well as external limits of the culture sections are starting to look blurry

and less defined, compared to those observed in the prior study with tissue sections.

After establishing a point of departure with brain slices and thick organotypic cultures we aimed at thin (350 μm at the beginning of the culture but <100 μm at the imaging experiment) organotypic cultures in a non-invasive way. It should be born in mind that flattening and increased transparency of the tissue sections with time is actually an indicator of tissue health and survival [160]. In this sense, using mice at post-natal day 12 resulted in a more firm structure compared to younger cultures, facilitating MRI and, at the same time, enabling tissue survival. Nevertheless, many problems were encountered when imaging these cultures. In the first place, it resulted more difficult to handle the thin tissues and position them in the agar gels, observing the appearance of air bubbles within the agarose gel, leading to susceptibility artefacts in MRI images (signal voids), as seen in Fig. 1.4C. In the second place, the porous film supporting the culture was hardly kept flat and resulted highly complicated to position the 2D transverse imaging plane crossing through the whole organotypic section (blended tissues). In the third place, it was virtually impossible to distinguish the tissues from the agar on T1, T2 and T2* images, since contrast between tissue and background agar was almost absent in most images due to partial volume effects, caused by the very small thickness of the tissues at the moment of imaging (tissues spread on the surface of the membrane from the original 350 μm to < 100 μm at the imaging stage). In some cases, it was possible to minimize all these effects and obtain images from the tissue (Fig. 1.4B.) but with very low SNR (actually dark contrast) and virtually no distinction of white and grey matter.

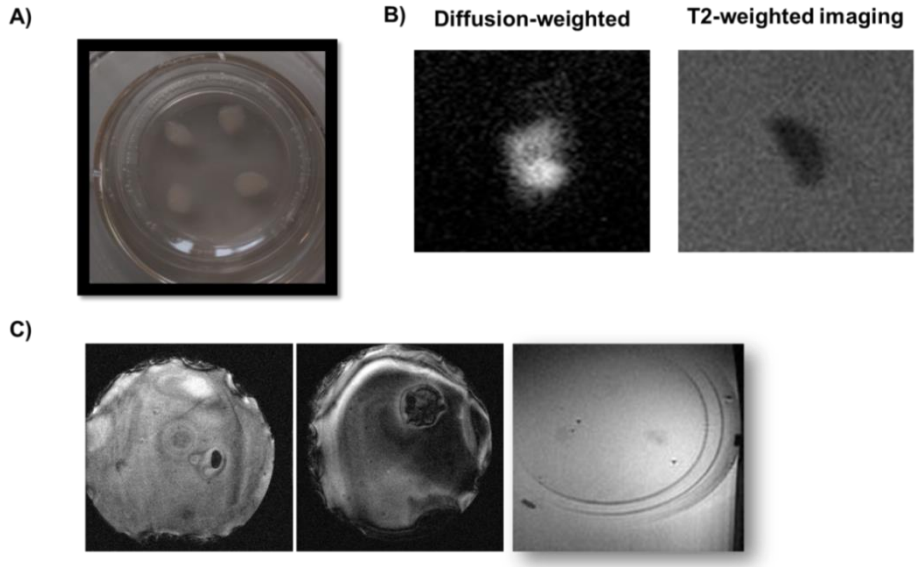

Figure 1.4. *Thin organotypic cultures showing, A) optical picture. B) MRI images of organotypic cultures. Diffusion-weighted imaging on the left and T2-weighted imaging right. C) Representative images of common problems arising from organotypic culture imaging: left, air bubble above the organotypic culture; Center, wrong alignment of imaging plane with culture's plane; Right, poor signal due to the thinness of the culture.*

In view of these results, we attempted a different approach by conducting diffusion-weighted imaging (Fig. 1.4B). In this case, SNR of the culture was increased to high levels, (>45) but no contrast was observed for the different components of the tissue, being useless to follow up differences on myelin content, which was our final goal. We have reached a bottle-neck that we have not been able to solve, at this point.

Thus a different final experimental approach was attempted, involving the use of myelin-targeting liposomes, for its detection based on a molecular imaging approach (Fig. 1.5A).

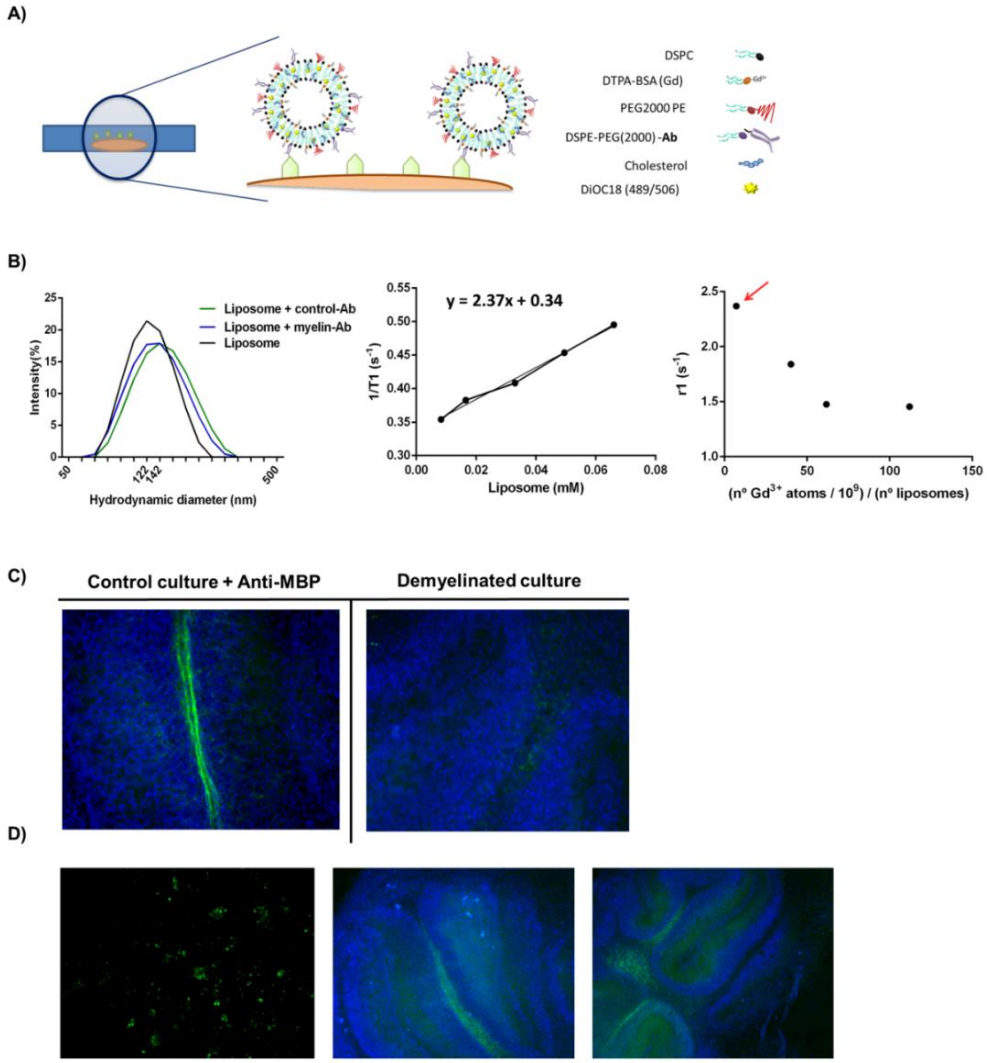

Figure 1.5. *Molecular recognition of myelin. A) Functionalized liposomes with gadolinium and fluorophore (DIOC18) that recognize myelin on cultures. B) Left: hydrodynamic diameter measured before and after antibody binding to the liposomes; centre: relaxation rate of the synthesized liposomes; right: relaxivities of the different synthesized liposomes. Red row indicates the optimized liposomes, which were used for the staining. C) Staining of organotypic cultures with liposomes functionalized with anti-MBP and anti-IgG (control) after fixation in healthy and demyelinated cultures. Cell nuclei are shown in blue and myelin in green. D) Common problems found after staining: liposome aggregates (left), non-specific binding of control liposomes (centre), non-specific binding of anti-myelin liposome (right).*

Myelin specific liposomes that target at myelin basic protein were designed including the anti-MBP (myelin basic protein) antibody in their surface. For control, similar liposomes were prepared using the unspecific anti-IgG protein. Liposomes were prepared with a hydrodynamic diameter of 124±1.47 (SD) nm that after conjugation with the antibodies resulted in 133.88±1.50 (SD) for the anti-IgG antibody and 124.7±1.47I nm for the anti-MBP antibody, as corroborated by dynamic light scattering (DLS) measurements (Fig 1.5B).

Liposomes were constructed including imaging probes for their detection. In a multimodal approach, we have included gadolinium chelates, for MRI detection and a fluorophore for fluorescence microscopy. One important aspect of this labelling is the optimization of the gadolinium content per liposome, since it has been demonstrated that an excessive load of this ion could quench the T1 effect and reduce the sensitivity of detection and image contrast [343]. Thus, several formulations were prepared at different concentrations of gadolinium and the magnetic relaxivity of each one was determined by MRI (Figure 1.5B). For this purpose, a series of solutions of different concentration were prepared for each liposome formulation and the relaxation rates R1, which correspond to the reciprocal of the T1 relaxation times (R1=1/T1) were measured (Fig. 1.5B). Magnetic relaxivities r1 ($mM^{-1}s^{-1}$) of each formulation were obtained as the slope of the plots of R1 vs. concentration of gadolinium in the liposomes (determined by mass spectrometry), as it is shown in Fig. 1.5B. The experimental procedures and detailed data analysis were the same as described elsewhere [343]. From our studies, we concluded that the optimal load of gadolinium for these liposomes resulted in 7.1 x 10^9 units per liposome and an r1 value of 2.17 $mM^{-1}s^{-1}$.

Next, liposomes were tested for their capacity to selectively bind to myelin sheaths, in tissue sections. For this purpose, we started our study by using fluorescence

microscopy, due to the high sensitivity of detection of this technique compared to MRI and to the more simple logistics to prepare samples and measure them.

Imaging studies showed that green-fluorescent MBP-targeting liposomes can specifically bind to myelin in healthy organotypic cultures, while no visible attachment was observed when demyelinated cultures were cultured with the liposomes (Fig. 1.5C), providing proof-of-concept that this novel approach can actually recognize myelin in cultures. Nevertheless, when performing replicas of this procedure, non-specific binding of both MBP-specific and IgG unspecific liposomes has been frequently observed together with the formation of liposome aggregates (Fig. 1.5D). Certainly, this is a known problem when using liposomes with tissue sections, since it has been described that liposomes have shown to bind to biological tissue by electrostatic forces or by non-specific hydrophobic forces [344]. The fact that specific biding to myelin sheaths has been achieved but not in a reproducible manner and at this moment, somehow randomly in our experiments, makes our protocol unreliable and poorly robust, requiring of further refinement.

The staining protocol for fluorescence imaging includes a series of steps such as fixation and incubation periods, which substantially degraded the tissue structure. Owing to this fact, MRI of these liposome-labelled cultures was not possible. Due to the lack of specificity observed in fluorescence studies, the performance of MRI studies in non-fixated tissue sections was set on hold, until we could solve the conditions for a truly myelin-nanomaterial molecular recognition. Since we cannot even assure that liposomes will be the nanosystems finally used for this purpose, seems reasonable not to lose time on optimizing MRI experiments with non-working nanomaterials. Currently, we are working on the development of such alternate nanomaterials, but this represents a whole research line *per se,* that will run in parallel to the further development of this doctoral thesis. We have provided proof-

of-concept for the specific detection of myelin cultures, we have identified the problems that represent a bottleneck, and we are working on effective solutions to solve them, but at this point, resources must be allocated for the study of the *in vivo* models.

5. Conclusions

The development of experimental protocols for the non-invasive *in vitro* characterization of myelin in cultures may represent a breakthrough for the performance of high throughput studies of treatments in highly reproducible experimental conditions. MRI of thick brain slices of thick organotypic cultures have been possible with high SNR and CNR, demonstrating the potential of the technique for quantification of myelin. Nevertheless, such systems result inadequate as *ex vivo* models since the preservation of cells at the interior of thick sections in culture is highly compromised. On the other hand, thin organotypic cultures present an inherent problematic that makes not possible, at this moment, to obtain useful protocols for quantification of myelin by MRI. Molecular recognition processes with myelin-specific nanomaterials detectable by MRI can provide a valuable solution to those problems, but we have not succeeded yet to find a suitable nanosystem to assure the required level of specificity and reproducibility. Ongoing research in this line will tell us if this is a good approach for the obtaining of experimental *ex vivo* tools for the study of demyelination and remyelination.

Chapter 2

Profiling of acute and chronic demyelination and remyelination in the cuprizone murine model of multiple sclerosis: a histological and multiparametric MRI study at high spatial resolution

A. Egimendia *et al.* (Submitted)

1. Foreword

Once we have established the potential and the limitations of MRI for the study of *ex vivo* models of demyelination, in this chapter we have advanced towards the applications of this imaging technique in *in vivo* models, in particular, to the cuprizone murine model. This model is one of the most broadly used experimentally for the study of myelin pathology for several reasons, that include; robustness and reproducibility, simplicity, the presence of progressive demyelination and spontaneous remyelination phases in the same subject and, specially, mild alteration of animal health and welfare. Owing to these features, this model has been widely used for the evaluation of therapies targeting multiple sclerosis.

In this chapter, we have undertaken the challenge for establishing the base for the evaluation of myelin content and provide a deeper insight into the cuprizone mouse model by running a multiparametric magnetic resonance imaging protocol.

2. Introduction

Multiple sclerosis (MS) is an autoimmune disease of the central nervous system characterized by demyelination, resulting in cognitive decline and loss of autonomy. Damage can be partially ameliorated by means of remyelination, or restoration of the myelin sheath before the axon degenerates. However, inhibitory signalling, lack of growth factors, deficient oligodendrogenesis and cell death make this process frequently unsuccessful in MS patients [38]. Consequently, the possibility of applying neuroprotective therapies that promote remyelination has been in the limelight of scientific research during the last years [26].

In the task of understanding the disease and developing novel therapies against it, the use of animal models plays a pivotal role. The cuprizone mouse model is probably the most widely used *in vivo* model for the evaluation of remyelination therapies. This is one of the called toxic models of MS, where a toxicant is used to induce demyelination, presenting spontaneous remyelination after stopping the demyelinating insult. Thus, mice exposed to 0.2-0.3% (w/w) cuprizone in the diet undergo an increasingly pronounced demyelination peaking at week 5 of administration of the toxicant [345]. In this model, the corpus callosum of the mice is the most affected region of the brain. After the withdrawal of cuprizone, remyelination can be observed already after 4 days, reaching its maximum during the following weeks [183].

For the precise evaluation of novel therapies, it is necessary to define specific and sensitive markers of myelin content, ideally using non-invasive techniques. In this context, MRI stands out among most imaging techniques because of its non-invasiveness, high spatial resolution, and multiparametric and versatile nature. In the particular case of the cuprizone model, there is a relevant body of evidence in

literature tackling the use of MRI to quantify myelin in the brain. Among other approaches, myelin visualization has been attempted through its water content. Indeed, the direct visualization of myelin is very challenging due to the rapid decay of its signal (few microseconds) [346]. However, those very short relaxation times have led to define other alternatives aiming at imaging myelin water in an indirect manner, using one of the multiple parameters measurable by MRI, such as the use of T1-weighted (T1w) and T2-weighted (T2w) imaging [196] or a combination of both parameters [347], spectroscopy [348], diffusion tensor imaging (DTI) [272], magnetization transfer imaging [349], susceptibility weighted imaging (SWI) or a multi-exponential determination of T2 relaxation times [350].

No consensus has been reached in this issue so far, and no single MRI parameter or protocol has been adopted as the gold standard for the evaluation of myelin content in the cuprizone model, showing all pros and cons that are beneath of the ongoing discussion. An additional fact that makes difficult to compare the performance of different parameters for myelin content, is that studies are performed at different magnetic fields, using different sequences, different reference methods (gold-standards), different amount of toxic, as well as different exposure times to cuprizone (acute vs. chronic), etc. To further deep in this issue and attempt to clarify if it is possible to define a robust and reproducible manner to study myelin by MRI that can be universally accepted, the evaluation of multiple parameters acquired simultaneously in the same imaging protocol for the same experimental conditions might be of utmost importance.

Furthermore, temporal and spatial resolutions at which MR parameters are acquired are not minor issues. Myelin is basically present in the white matter tracts of rodents. Due to the small size of anatomic structures in the mouse brain, the presence of partial volume effects may be quite significant, contributing to

confounding effects when spatial resolution is not particularly high. Thus, the use of high magnetic fields and magnetic gradient strengths represent an important advantage for the mapping of MRI parameters at very high spatial resolution, to minimize partial volume effects and increase sensitivity.

In this study, we have used a multiparametric MR imaging acquisition protocol at ultra-high field (11.7T) to achieve high spatial resolution (up to 75 μm/pixel). In this way acute demyelination and remyelination processes of the cuprizone murine model have been characterized, with a temporal resolution of 1 week during 10 weeks of evolution, studying as well the long-lasting effects of the toxic compound at 6 months after the demyelinating insult. Achieving such spatial resolution represents an important challenge when adding the constraint of acquiring the maximal number of MRI parameters in an experimental protocol of <3h, a time constraint imposed for animal welfare reasons. We have been able to include in our protocol most of the used parameters described in literature (i.e. T1w imaging, T2w imaging, with T1w/T2w ratio, SWI, MTR and DTI imaging), which has allowed us to directly compare their capacity to depict changes in myelin at the very same experimental conditions with direct registration of parametric images. In addition, we include a parallel histological study with Luxol fast blue (LFB), considered a gold standard for myelin staining, which has been used to establish the sensitivity and specificity of the aforementioned MRI parameters to detect myelin in the cuprizone murine model of multiple sclerosis. Our results may bring light to the lasting controversy of which MRI-derived parameter, if any, describes best the myelin content of the cuprizone mouse model.

3. Materials and methods

3.1. Animals and experimental protocol

Animal experiments were performed in our SPF facilities under a full accreditation from the Association for the Assessment and Accreditation of Laboratory Animal Care International (AAALAC). All animal procedures were approved by our Institutional animal care and use committee (IACUC) and local authorities (License PRO-AE-SS-089, Diputación Foral de Gipuzkoa, Spain).

Ad libitum access to food and water was provided to the animals under controlled light environment (12h light/dark). Fifteen mice were exposed to 0.2% (w/w) cuprizone diet (Envigo TD.140800) for a period of 5 weeks. Six mice (n = 6) were scanned at 11.7T on a weekly basis from week 0 to week 10 (11 scanning sessions) sacrificing them after the last imaging session for histological analysis. In addition, other 6 mice (n=6) from a total of 15 were sacrificed at week 5 for the histological analysis. Three of the total of 15 (n=3) were scanned 6 months after being exposed to cuprizone. Cuprizone containing pellets were renewed every 3 days. The same approach was conducted with n=15 animals fed with regular diet as the control group (n=6 mice sacrificed at week 5, n=6 sacrificed at week 10 and n=3 animals sacrificed at month 6, all scanned by MRI on a weekly basis and finally submitted to histology). No single animal was lost during the performance of this study.

3.2. MRI

MRI measurements were performed on an 11.7 Tesla (T) horizontal bore Biospec 117/16 scanner (Bruker Biospin, Ettlingen, Germany) with a mouse brain surface coil for the reception and a volumetric coil for transmission. Anaesthesia was induced with 4% isoflurane and kept at 1.5-2% during scanning. Respiration rate

and rectal temperature of the animals was continuously monitored inside the magnet with an MR compatible device (Model 1030, SAII, Stony Brook, NY, USA). After manual tuning and matching of RF-coils and automatic setup of the system (i.e., pulse power calibration, shimming, and setting on resonance frequency), 3 scout images were acquired in axial, coronal and sagittal directions using a Flash sequence, as reference for the rest of the study, composed by a series of MR images of different contrast, acquired by different pulse sequences (Fig. 2.1):

1) Susceptibility weighted imaging (SWI) was achieved with a gradient echo sequence with TR/TE=1200/6 ms, FOV 12.75 mm x 12.75 mm, matrix size 170x170 (75 μm in-plane resolution), flip angle of 60º, Nav= 3 averages and 24 consecutive slices of 500 μm thickness (covering the whole brain in a 12 mm field of view along z axis).

2) Magnetization transfer imaging was achieved acquiring 2 sets of 2 images (with different MT pulse strengths each image) using a FLASH (fast low angle single shot) pulse sequence using TR/TE=400/3 ms, FOV 25.6 mm x 25.6 mm, matrix size 256x256 (100μm in-plane resolution), a flip angle of 40º, Nav=6 averages and 2 sets of 12 consecutive slices of 500 μm thickness (covering the whole brain in a 2x6 mm field of view along z axis). MT contrast was generated by a pulse at irradiation offset of 4000 Hz, amplitude 7.8 μT and length 20ms (Msat) acquiring for reference a second image (M0) with identical parameters except for the irradiation offset of 30000 Hz.

3) T1-weighted images were acquired with a TurboRARE image sequence using a RARE factor of 2, TR/TE_{eff}=1200/6.0 ms, a FOV 12.75 mm x 12.75 mm and matrix size 170x170, giving an in-plane resolution of 75 μm, a flip angle 90º, Nav= 6 averages and 24 consecutive slices of 500 μm thickness (covering the

whole brain in a 12 mm field of view along z axis).

4) T2-weighted images were achieved with a TurboRARE image sequence using a RARE factor of 8, TR/TE_{eff}=4938/40 ms, a FOV 12.75 mm x 12.75 mm and matrix size 170x170, giving an in-plane resolution of 75 μm, a flip angle 90º, Nav= 8 averages and 24 consecutive slices of 500 μm thickness (covering the whole brain in a 12 mm field of view along z axis).

5) Diffusion parameters were obtained with a spin-echo-DTI pulse sequence acquired using TR/TE=1410/20 ms, FOV 12.8 mm x 9.6 mm and matrix size 128x96, giving an in-plane resolution of 100 μm, a flip angle of 90º, a b-value of 1000 $mm^{-2}s$ (using δ= 4 ms and Δ= 11 ms), 40 gradient directions, 5 b0 images and Nav=1 average. 24 consecutive slices of 500 μm thickness were acquired to cover the whole brain in a 12 mm field of view along z axis).

Thus, total scanning time of the complete imaging protocol resulted in 2h 24m (5' for 3 scout images + 30'40'' MTR + 10'12'' SWI + 12'34'' for T2w + 9'21'' for T1w + 76' for DTI), not considering time required for adjustments and animal positioning.

3.1. Image analysis

Image analysis was performed automatically using in-house routines implemented in Linux and manually inspected after completion. First, some preprocessing was performed for each image. Voxel dimension units were multiplied by 10, to improve the processing performance of FSL [FMRIB (Oxford Centre for Functional MRI of the Brain) Software Library; http://www.fmrib.ox.ac.uk/fsl, (Jenkinson et al., 2002; Smith, 2002)], taking into account the reduced dimensions of the rodent brain compared to human brain. Additionally, diffusion images were denoised using local PCA-based algorithm [351] implemented in Dipy library [352] for python.

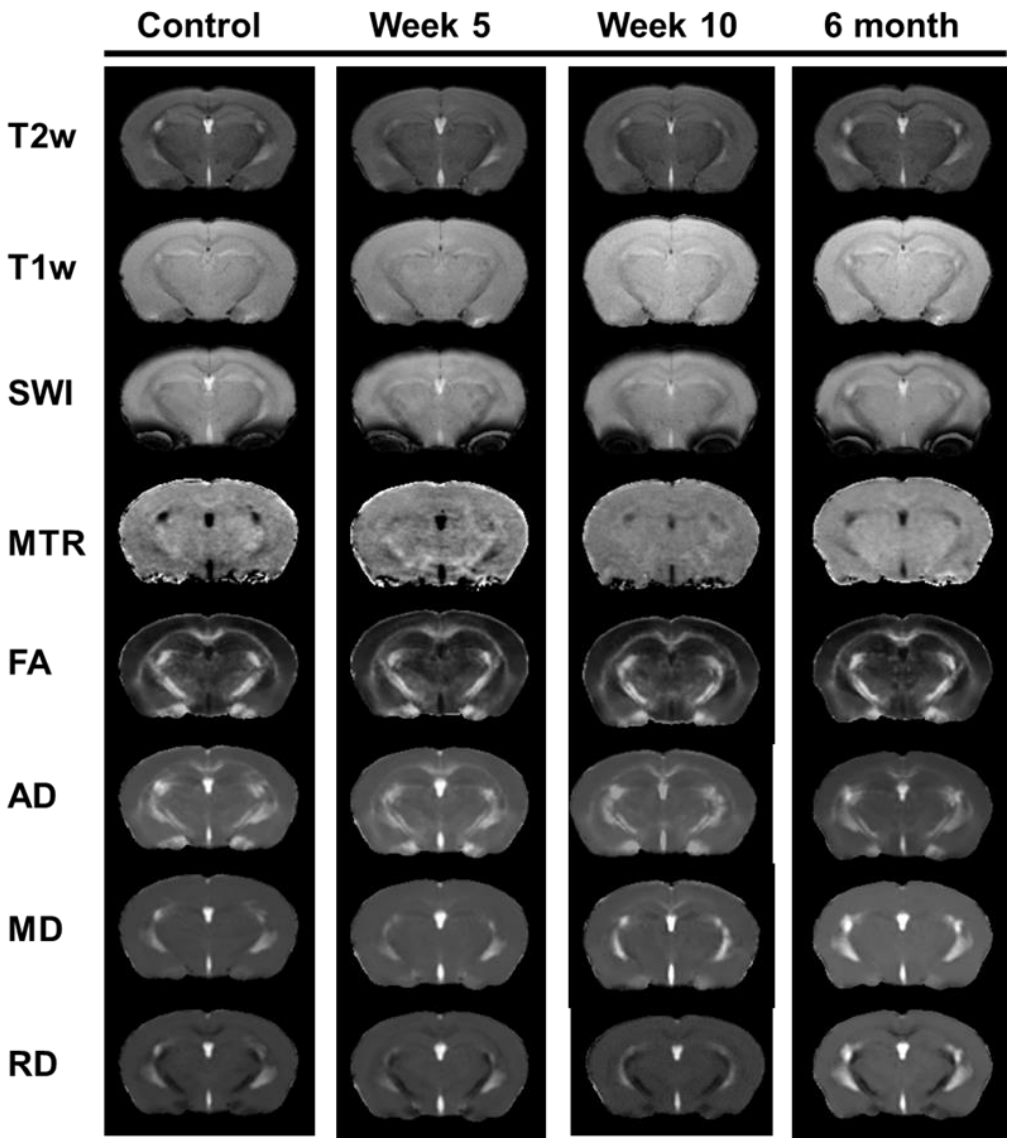

Figure 2.1. *Imaging protocol. T2-weighted (T2-w), T1-weighted (T1-w), T1-w/T2-w ratio (T1w/T2w), susceptibility weighted imaging (SWI) magnetization transfer ratio (MTR), fractional anisotropy (FA), axial diffusivity (AD), radial diffusivity (RD) and mean diffusivity (MD) images are shown. In the first column, images corresponding to the control group, the other columns correspond to cuprizone exposed mice for 5 weeks, and scanned at weeks 5 and 10, and 6 months from the beginning of exposure*

Next, all images were placed in the same space as a downsampled in-house template of the mouse brain. The high resolution T2w image was used for achieving optimal brain extraction and registration by skull stripped and bias correction using FSL, followed by registration to the in-house template. For each image session, the rest of images acquired with different MR modalities underwent the same brain extraction and registration transformation as the one performed in the T2w image (all images acquired per session have the same origin of coordinates and image orientation). Simultaneously, the publicly available AMBMC (Australian Mouse Brain Mapping Consortium, http://www.imaging.org.au/ AMBMC/) C57BL/6J mouse atlas was registered to the template for later automatic selection of ROIs.

Once the images were placed in the same space T1w and T2w images were divided (to create parametric images for T1w/T2w ratio) and MTR parametric images were calculated with the following formula: MTR = [(M0-Msat)/M0]x100, were M0 and Msat are the images acquired with 30 kHz and 4 kHz off-resonance pulses, respectively. Additionally, the mean signal of T1w, T2w and SWI images were normalized (whole brain signal = 10000), to enable inter- and intra-individual comparison of images all along the study.

A series of regions of interest (ROIs) were selected and extracted using the AMBMC anatomical atlas for their definition, covering both grey matter and white matter regions. These regions include: the corpus callosum (CC), the cerebellar peduncles (CP), the hippocampus (Hc), the thalamus (Th), the caudate putamen (CPu), the hypothalamus (Hyth), the motor cortex (MC) and the cortex (C) (comprising de somatosensory cortex and auditory cortex). The CC was subdivided in the medial corpus callosum (med-CC), the genu of the corpus callosum (genu-CC) (ROI of the genu-CC was manually drawn after visualization of abnormalities in this regions)

and the lateral corpus callosum (lat-CC) as might exhibit a different demyelination temporal pattern. Finally, the mean intensity of each ROI was calculated for every image. Calculated values were averaged group-wise and the standard deviation (SD) was calculated for each ROI and parameter. In this way, a mean±SD was obtained for each region and parameter for every single week of study.

3.2. Histology

At weeks 5, 10 and at 6 months of study animals allocated for histology were perfused and tissues processed for LFB staining. Briefly, animals were deeply anaesthetized and transcardially infused with 20 mL of heparin-saline (20 units per mL of saline), followed by 20 mL of 10% formalin. Brains were dissected and fixed in 10% formalin at 4°C for 24 h, followed by 20% sucrose in PBS until they sank. Brains were frozen in dry ice cooled isopentane, and stored at -80ºC until processed. Twenty-five micrometre thick sections were cut on a cryostat (Leica CM3050S, Leica Microsystems, Germany) and stored at -20ºC until stained. Samples were stained with Luxol fast blue (LFB) (Sigma, S3382) and cresyl violet (Sigma, C5042) and analyzed on a cell observer microscope (Axio Observer, Carl Zeiss, Germany).

ImageJ software [353] was used for image displaying purposes and manual analysis. Blue (LFB, myelin) and purple (cresyl violet, cell nuclei) channels were split using customized Color Deconvolution plugin of ImageJ. Pixel intensity values in images were converted to optical density (OD) for myelin quantification. For the evaluation of imaging markers for myelin, medial corpus callosum (med-CC), lateral corpus callosum (lat-CC), the cerebellar peduncles (CP) and the cortex were manually selected for both histological samples and MRI images, used for correlation analysis (parametric MRI analysis was performed with automatic ROI selection). Control samples from week 5 and week 10 were grouped.

3.3. Statistical analysis

Graphpad/Prism software was used for statistical analyses. Normality assessment was performed with quantile-quantile (Q-Q) plot [354]. For normally distributed data the statistical significance of the difference between groups was determined by a two-way analysis of variance (ANOVA). Afterwards, unpaired t-test was applied. If the sample did not follow normal distribution a Mann-Whitney test was applied. Statistical significances were set at $p>0.05$ (*).

Afterwards, linear regression was performed with the data collected in MRI and LFB and the Pearson's correlation coefficient (r) and r^2 were estimated for evaluation of the specificity of each parameter. Statistical significances were set at $p>0.05$ (*).

4. Results

4.1. Variations on MRI parameters with demyelination and remyelination processes

It has been reported that mice exposed to 0.2% cuprizone in diet suffer progressive signs of demyelination for 5 weeks, mostly in the CC [345]. Afterwards, mice present spontaneous remyelination during the following weeks, being completed at week 10. This pattern has been confirmed in our studies, and in Fig. 2.2 we present the values obtained for the measured MRI parameters at these time-points for cuprizone vs. control animals, together with the long-lasting effects caused by cuprizone at the chronic stage of 6 months from the demyelinating insult. To our knowledge, no data at such long period of time is available in the literature, although a stage of so-called "chronic" demyelination has been reported for animals submitted for 12 weeks to cuprizone diet [355].

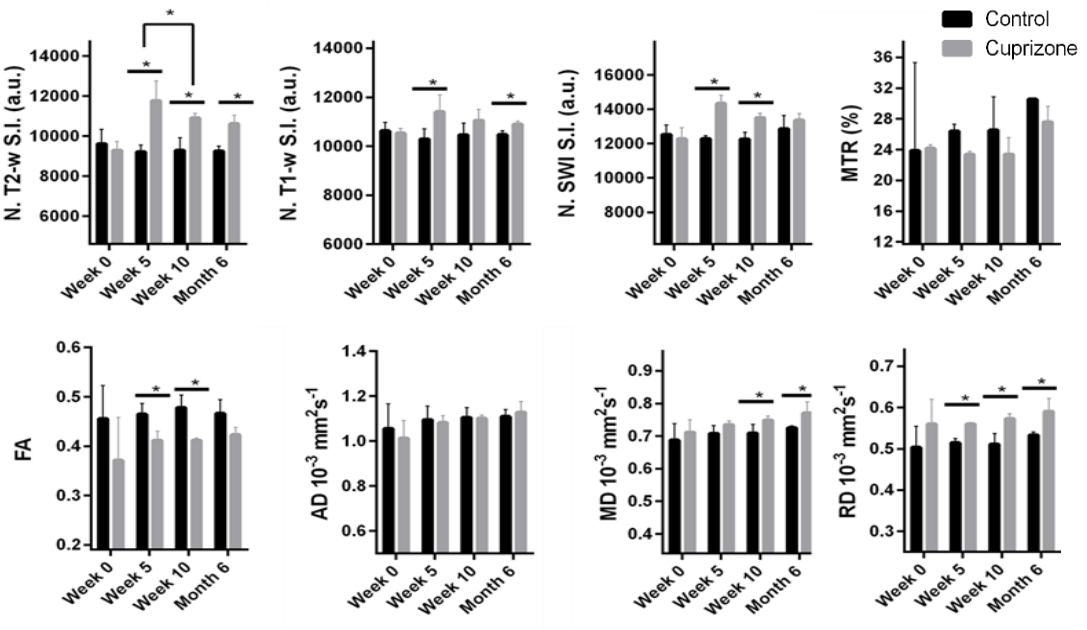

***Figure 2.2**. Plots representing parametric values obtained with the different sequences at the med-CC of cuprizone exposed (grey bars) vs. control (black bars) mice. Normalized T2w and T1w signal intensities, normalized SWI signal intensity, magnetization transfer ratio (MTR), fractional anisotropy (FA), axial diffusivity (AD), radial diffusivity (RD) and mean diffusivity (MD) values are plotted at week 0, 5, 10 and month 6 after starting cuprizone administration*.

In order to assess the capacity (sensitivity) of the studied parameters to depict alterations in myelin content we used the med-CC region of interest, where extensive demyelination takes place. In this region, at week 5, demyelination leads to increased values of T2w, T1w and SWI normalized signal intensities, as well as in RD in the cuprizone group respect to controls, while the parameters T1w/T2w ratio, MTR and FA showed decreased values in the cuprizone group, respect to controls. No significant differences were observed for axial and mean diffusivities at this time-point. In terms of magnitude, the MRI parameter that shows the largest difference between cuprizone treated animals and controls was the normalized T2w signal intensity, which was a 28.3% higher for the cuprizone treated group (Control

= (9.2±0.4)x10^3 a.u. vs Cuprizone = (11.8±1.0)x10^3 a.u., ΔT2w = 28.3% , p<0.001). Following, by order of difference, normalized SWI signal intensity (Control = (12.3±0.2)x10^3 a.u. vs. Cuprizone = (14.3±0.5)x10^3 a.u., ΔSWI = 16.3%, p<0.01), MTR (Control = 26.4±0.9% vs. Cuprizone = 23.4±0.4%, ΔMTR= -12.8%; p<0.01), FA (Control = 0.46±0.02 vs. Cuprizone = 0.41±0.02, ΔFA= -12.2%, p<0.05), normalized T1w signal intensity (Control = (10.3±0.4)x10^3 a.u. vs. Cuprizone = (11.4±0.7)x10^3 a.u., ΔT1w = 10.7%, p<0.001), and RD (Control = (0.51±0.01)x10^{-3} mm^2s^{-1} vs. Cuprizone = (0.56±0.00) x10^{-3} mm^2s^{-1}, ΔRD=9.8%, p<0.01).

It has been described that once cuprizone is withdrawn from diet remyelination leads to the restoration of myelin sheaths [355]. If we set our attention to week 10, five weeks after withdrawal of cuprizone, when spontaneous remyelination has taken place, some of the parameters still show significant differences between controls and cuprizone treated animals, although differences are reduced respect to those observed for week 5. In particular T2w normalized signal intensity (Control = (9.4±0.4)x10^3 a.u. vs. Cuprizone = (10.9±0.2)x10^3 a.u., ΔT2w = 5.34% p<0.001), SWI (Control = (12.3±0.4)x10^3 a.u. vs. Cuprizone = (13.5±0.3)x10^3 a.u., ΔSWI = 9.8%, p<0.01) and for FA (Control = 0.48±0.02 vs. Cuprizone = 0.41±0.00, ΔFA = -17.1%, p<0.05). For Radial diffusivity, the difference between controls and cuprizone treated animals actually increases from week 5 to week 10 (Control = (0.51±0.03) x10^{-3} mm^2s^{-1} vs. Cuprizone = (0.57±0.01)x10^{-3} mm^2s^{-1}, ΔRD= 11.8% p<0.05). Finally, differences in T1 and MTR diminish, so the mean values of these two parameters become not significantly different between controls and cuprizone treated animals, at week 10. When evaluating remyelination, which might be reflected in a signal change comparing the peak of demyelination (week 5) and the remyelinated condition (week 10) T2w imaging is the only one exhibiting a significant difference (ΔT2w =7.8%, p<0.05).

If we analyze data obtained at month 6 after the demyelinating insult, only normalized T2-weighted signal intensity (Control = (9.2±0.2)x10^3 a.u. vs. Cuprizone = (10.6±1.0)x10^3 a.u., ΔT2w = 15.2% , $p<0.05$), normalized T1-weighted signal intensity (Control = (10.5±0.2)x10^3 a.u. vs. Cuprizone = (10.9±1.0)x10^3 a.u., ΔT2w = 3.8% , $p<0.05$), MD (Control = (0.73±0.01)x10^{-3} mm^2s^{-1} vs. Cuprizone = (0.77±0.03) x10^{-3} mm^2s^{-1}, ΔMD=5.2%, $p<0.05$) and RD (Control = (0.53±0.01)x10^{-3} mm^2s^{-1} vs. Cuprizone = (0.59±0.03)x10^{-3} mm^2s^{-1}, ΔRD=11.38%, $p<0.05$) showed significant differences between controls and cuprizone treated groups, while MTR, SWI, FA and AD showed not significant differences for these two groups in the med-CC ROI.

In this setting, the sensitivity of several parameters to myelin pathology has been observed. MD and AD did not show any difference at the peak of maximum demyelination (week 5). Due to this factor, the MD and AD metrics have been discarded for the histological validation and characterization of the model. A similar analysis was performed for other brain regions, automatically selected by co-registration of the data to a segmented atlas of the brain. The temporal evolution of relevant parameters will be discussed later in this work.

4.2. Luxol fast blue quantitation of myelin content

Optical density measurements of Luxol fast blue staining (LFB-OD) in histological sections of brain tissue revealed significant demyelination in the cuprizone mouse model (Fig. 2.3). After 5 weeks of exposure to the toxicant, OD was 118% higher in the med-CC of control mice compared to cuprizone treated mice (Control = 0.24±0.05 vs. Cuprizone = 0.11±0.04, $p<0.05$), 69% higher in the lat-CC, (Control = 0.27±0.05 vs. Cuprizone = 0.16±0.06, $p<0.05$) and 110% higher in the CP (Control = 0.21±0.04 vs. Cuprizone = 0.10±0.08, $p<0.05$). As expected, these values were reduced at week 10 due to remyelination phenomena: OD was 14% higher in the

med-CC (Cuprizone = 0.21±0.02, not significantly), 50% higher in the lat-CC (Cuprizone = 0.18±0.04, $p<0.05$) and 40% higher in the CP (Cuprizone = 0.15±0.04, $p<0.05$) compared to the values reported for the control group. The med-CC was the only ROI showing a significant difference ($p<0.05$) when comparing values obtained at w5 vs. w10 for the cuprizone group, not finding any differences for the control group. No significant difference was found in the cortex.

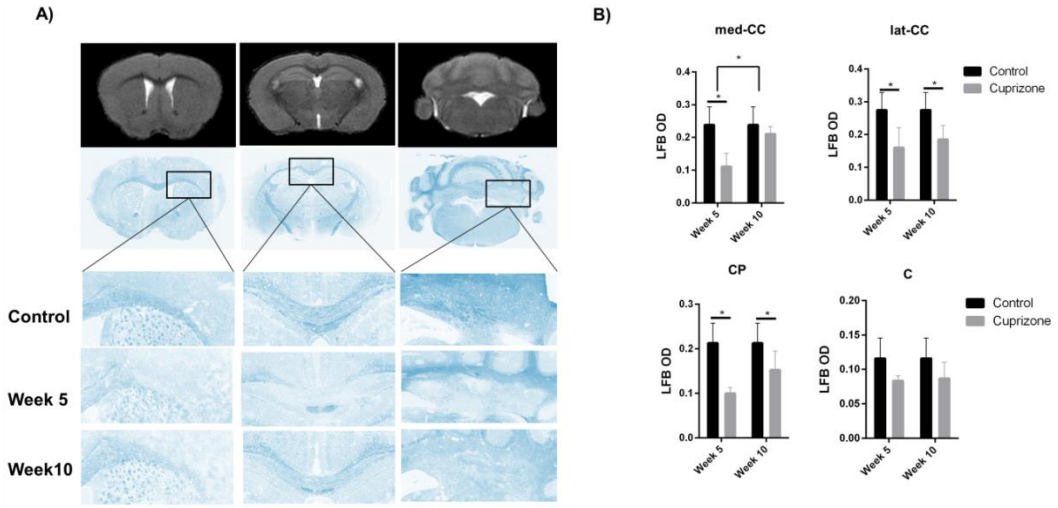

Figure 2.3. *Luxol fast blue (LFB) staining of myelin for cuprizone treated and control mice. A) Images showing demyelination and remyelination in the lat-CC, med-CC and CP in control mice, after 5 weeks of exposure to cuprizone and at week 10 of the experiment. B) Optical density (OD) measures of LFB staining in the med-CC, lat-CC, CP and C in manually drawn ROIs.*

Plots of LFB-OD versus the different MRI parameters were constructed, using data from different ROIs of the brain and linear regressions were calculated, together with Pearson's correlation coefficients (r) and r^2, in order to evaluate the specificity of each parameter as an imaging biomarker for myelin (Fig. 2.4).

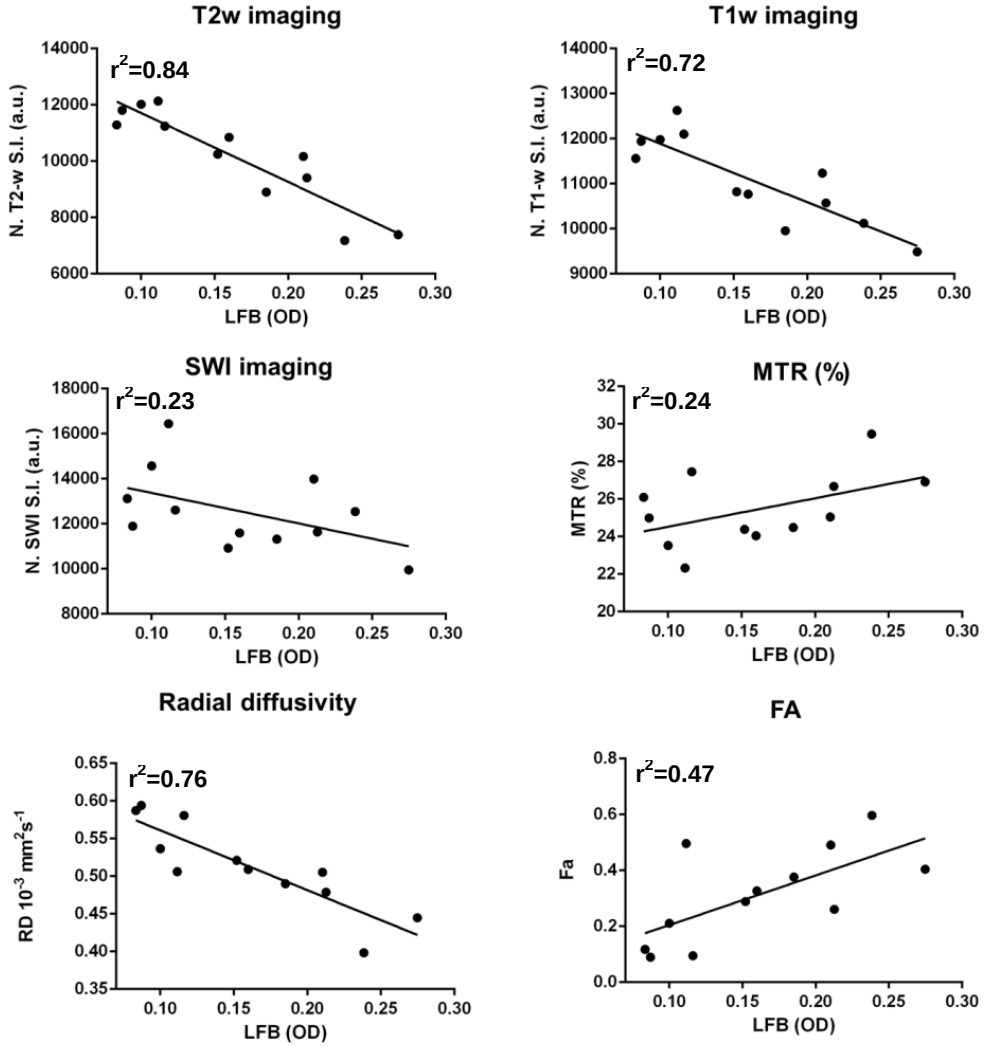

Figure 2.4. *Linear regression of relevant parameters obtained by MRI vs. LFB Optical densities. Data presented includes values from the region of interest medial corpus callosum, lateral corpus callosum, cerebellar peduncles and cortex.*

The normalized signal intensity of T2w images showed the highest correlation with LFB-OD values (r^2 = 0.84, $p<0.001$), with a negative slope indicating that the higher the content in myelin the lower the T2w signal. The correlation between LFB-OD

and RD (r^2 = 0.76, p<0.001), normalized T1w signal intensity (r^2 0.72, p<0.001) and FA (r^2 0.47, p<0.05), also showed significant correlations with LFB-OD values. No significant correlation was observed for MTR and SWI. The low degree of correlation observed for some of the measured MRI parameters indicate that changes observed may include other confounding effects (false positives) apart from changes on myelin content, compromising their specificity.

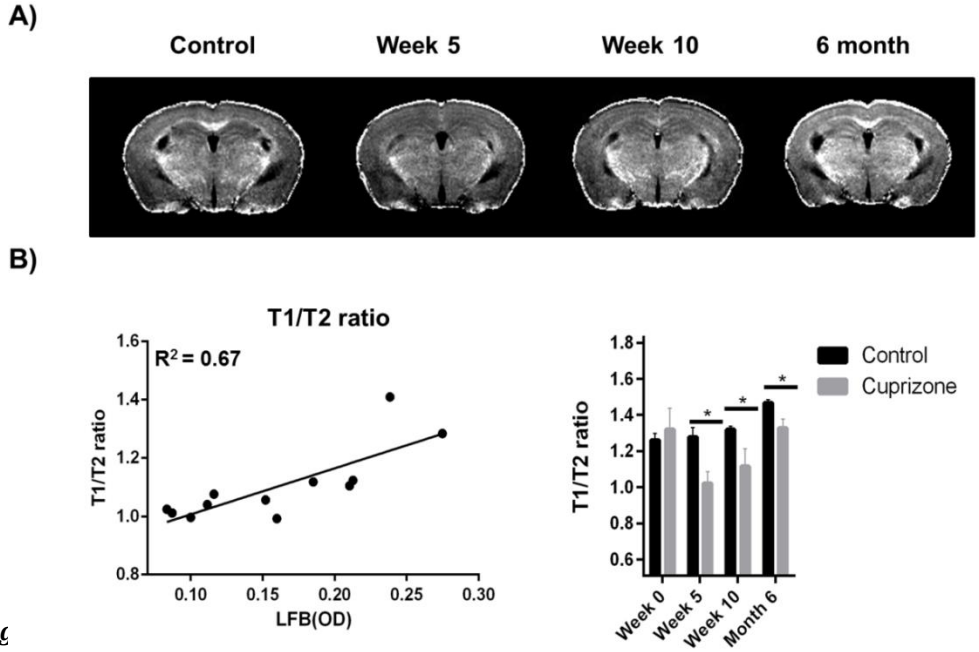

Fig *T1-weighted and T2-weighted images. A) T1w/T2w ratio for control, week 5, week 10 and 6 months. B) linear regression of T1w/T2w ratio vs. LFB optical density (left) and temporal pattern shown for the whole study compared to control.*

Combination of different measured MRI parameters was conducted, and we could observe that the ratio T1w/T2w shows a good contrast between gray and white matter (Fig. 2.5A), with good sensitivity to myelin damage at week 5 (Control =

1.28±0.05 vs. Cuprizone = 1.02±0.06, ΔT1w/T2w= -25.5%, p<0.001) and a reduced difference between cuprizone exposed and control group at week 10 of study (Control =1.32±0.02 vs. Cuprizone = 1.17±0.10, ΔT1w/T2w = -12.8%, p<0.05) and after 6 months of exposure to cuprizone (Control =1.47±0.02 vs. Cuprizone = 1.33±0.05, ΔT1w/T2w = -10.5%, p<0.01). However T1w/T2w ratio exhibited a slightly worse correlation with LFB staining than T1w or T2w by themselves (r^2 = 0.67). In parallel to correlation studies, a deeper analysis of histological images revealed areas of accumulated myelin debris near the medial section of the corpus callosum at week 5 (arrows in Fig 2.6A).

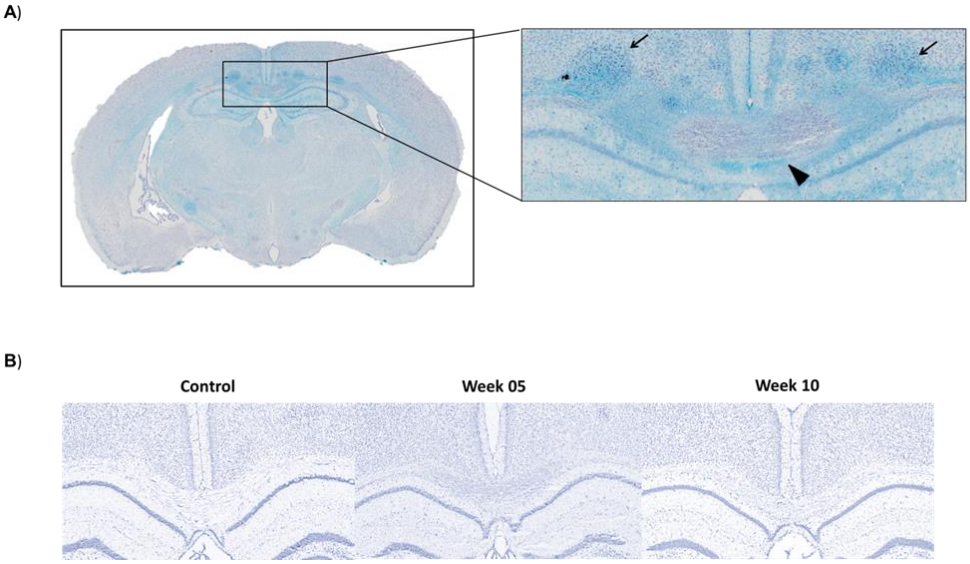

Figure 2.6. *LFB-cresyl violet staining of a cuprizone treated animal. A) Representative cresyl violet staining after 5 weeks under cuprizone. Corpus callosum is magnified. Arrows indicate myelin debris, probably phagocyted by microglia. Arrowhead points a high cell density (most likely microglia) colocalized with a region of high demyelination B) Representative cresyl violet staining of the corpus callosum in control, in demyelinated (W5) and remyelinated (W10) mice. Cell density peaks at week 5 and is reduced again at week 10 in the corpus callosum.*

Co-staining of these sections with cresyl violet showed that the highly demyelinated region at the centre of the med-CC (lack of LFB staining) is actually a region of high

density of cresyl violet positive cells, at higher density than control animals before cuprizone treatment. At week 10, after remyelination, cell density in this area is reduced again to quasi-normal levels (a slight increase on cell density is still observable at this time point) (arrowhead in Fig 2.6A and Fig 2.6B). These results may reflect the activity or reactive microglia in this animal model

4.3. Profiling of the temporal evolution of MRI parameters in the cuprizone model

A follow up of the values of the MRI parameters have been performed for 10 weeks, with a temporal resolution of 1 week, including a final exploration of animals 6 months after the demyelinating insult. In this way, acute demyelination (weeks 0-5) and spontaneous remyelination (weeks 5-10), as well as chronic state (month 6) periods of the model were studied by multiparametric MRI.

From data reported in the previous two sections we can conclude that in our experimental setup T2w, T1w and radial diffusivity show a highest correlation to Luxol fast blue staining together with sensitivity to demyelination. For this reason, the temporal evolution of these parameters have been studied.

The use of high-resolution imaging (minimizing partial volume effects) and image analysis in a common space for all images allowed us to determine that in this model there are different temporal profiles of evolution of MRI parameters, depending on the region of interest analyzed. In other words, it seems that demyelination and remyelination take place at a different pace for different regions of the brain (Fig. 2.7 and Fig. 2.8).

Focusing on T2w imaging, the most sensitive and specific parameter according to previous data, the med-CC in the cuprizone group showed a slight increase between

weeks 0 and 2, and from that point an abrupt increase is observed (ΔT2w SI $_{w2\text{-}w3}$= 20%), peaking at week 5 (ΔT2w SI$_{w0\text{-}w5}$= 30%).

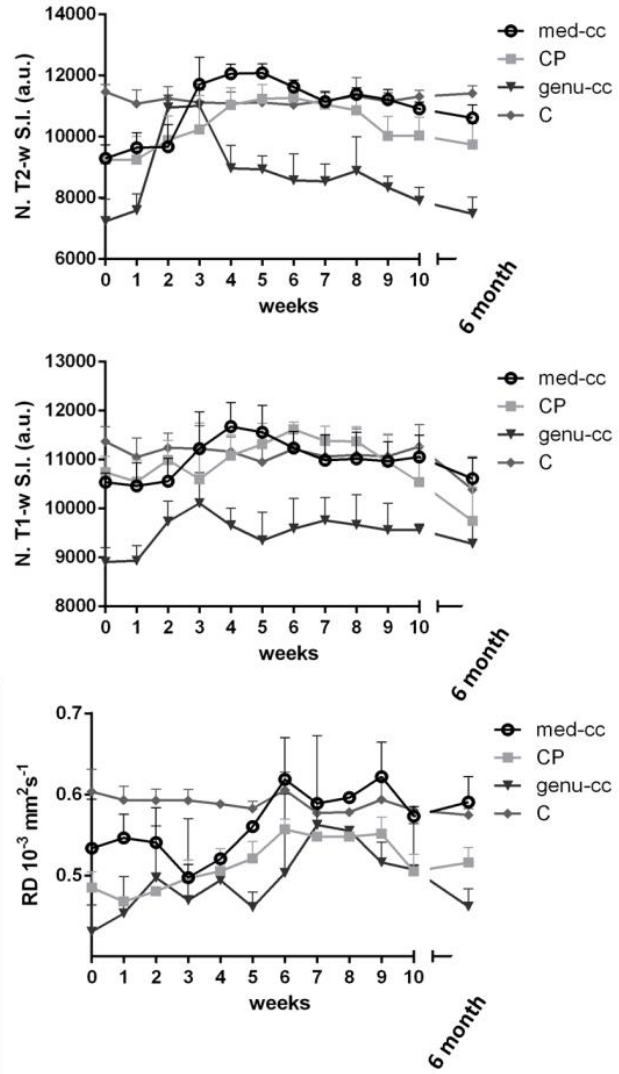

Figure 2.7. *Temporal patterns of demyelination and remyelination in the medial region of the corpus callosum (med-CC), the cerebellar peduncles (CP), the genu of the corpus callosum (genu-CC) and the cortex (C) of the mice exposed to cuprizone (0.2%, weeks 0-5) measured with normalized T2-weighted and t1-weighted signal intensity and radial diffusivity (RD).*

From that point, values remain higher for cuprizone exposed animals, with a slow reduction between weeks 5 and 10 (ΔT2w $SI_{w5\text{-}w10}$= -10.72%). This tendency is continued until 6 months when T2w signal intensity values were 14% higher than those observed at the beginning of the experiment for cuprizone treated animals.

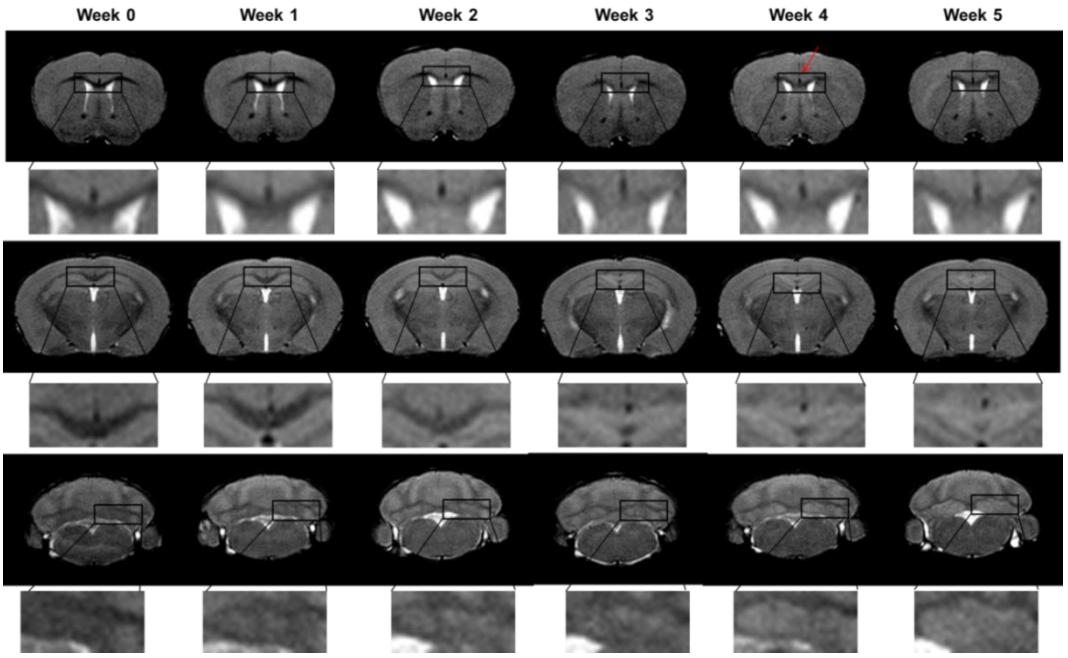

Figure 2.8. *T2-weighted images of mice during their exposure to cuprizone (0.2%). Cuprizone induces demyelination with a different temporal pattern in cuprizone exposed mice in the genu-CC, med-CC and CP. Red arrow indicates the central genu of the mice, which is highly demyelinated at week 2 and remyelinated at week 4.*

A different pattern was observed for the CP, that shows a progressive increase already from the first week after exposure, peaking at week 4 (ΔT2w $SI_{w0\text{-}w4}$=19% for cuprizone group). Then differences in T2w signal remained invariable until week 8 when there is a sudden decay to the final values, almost constant from week 9 to

month 6 at values 10% higher than those observed at week 0 for cuprizone animals.

A third different pattern was observed for the genu-CC, where an abrupt increase of T2w signal intensity values was observed for the cuprizone group between week 1 and week 2 (ΔT2w $SI_{w1\text{-}w2}$= 51%), still increasing until week 3. At this point, values suddenly drop (ΔT2w $SI_{w3\text{-}w4}$= -21%, ΔT2w $SI_{w0\text{-}w4}$= 24%), remaining invariant until week 8, when values start to progressively decay to those observed at the beginning of the study at month 6 (ΔT2w $SI_{w8\text{-}m6}$= -19%, ΔT2w $SI_{w0\text{-}m6}$= 3.3%).

No significant differences on T2w signal intensity were observed for ROIs including Hp, Th, CPu, Hyth, C and MC all along the study, as can be appreciated in Fig. 2.8.

T1w imaging reproduces pretty accurately the pattern followed by T2w image, even though showing a less pronounced effect. Changes on radial diffusivity are more complex to analyze. First, DTI images have been acquired at lower spatial resolution than T2w images (3µl vs. 1.7 µl per voxel) due to hardware-and scanning time related constrictions. Thus, partial volume effects gain importance, which may have capital importance on the measured values, especially relevant for small ROIs, and considering the small difference observed for the mean RD values, respect to their standard deviations (see plots in Fig. 2.7). Thus, although RD is sensitive enough to detect the difference between controls and cuprizone treated animals at points of maximal demyelination and remyelination, this parameter may be not sensitive enough to depict changes with a temporal resolution of 1 week in this model. A look at plots presented in Fig. 2.7, however, reveals that RD predicts delayed loss of myelin in comparison to T2w imaging which would start from week 3-4, and peaking between weeks 6 and 9, depending on the region of interest analyzed. Further decline of values during remyelination and at chronic phases are mild, except for the genu-CC where the drop is significant from week 9 to month 6. The

fact that axonal damage, irrespective of loss of myelin or not, affects RD values (see discussion) may be an important factor to consider when analyzing RD results.

5. Discussion

5.1. MRI based imaging biomarkers sensitive and specific for myelin

The establishment of robust parameters for the accurate evaluation of myelin pathology and a deeper understanding of demyelination and remyelination dynamics is a task of utmost importance for the assessment of remyelination therapies. So far, many studies have been conducted in this direction using the cuprizone mouse model [187], [198], [202], [250], [267], [356], [357], nevertheless, these works leave room for a series of improvements that we have tried to fill with this work. In particular, 1) we have tackled a complete multiparametric approach, allowing the comparison of different MRI parameters in exactly the same experimental conditions, 2) we have used high spatial resolution (100-75 μm per pixel at slice thickness of 500 μm) to minimize the influence of partial volume effects, 3) we have performed a correlation between MRI parameters with the histological gold standard for myelin (LFB) and finally, 4) we have studied the dynamic changes of multiple parameters at multiple brain regions during the acute demyelination and remyelination, as well as chronic stage of the cuprizone model, being able to establish the existence of different temporal profiles at different areas of the brain. Most of the published works tackle these aspects only in part, giving a partial view of the whole picture. To our knowledge this is the first work that considers all these issues simultaneously, for a more global analysis, being able to report some interesting findings not described before. All in all, we believe that data reported here is a contribution that deserves to be considered for the tasks of

defining MRI-based imaging biomarkers of myelin in the cuprizone model.

The first aim of this study has been to evaluate the degree of effectiveness of different MRI parameters to quantify myelin content in the cuprizone mouse model, for which measurements were conducted in the area of more extensive demyelination in this model, the medial section of the corpus callosum (med-CC). In order to be considered a good biomarker of myelin, an MRI parameter should be sensitive enough to depict demyelination observed in this region. In this sense, all analyzed parameters except MD and AD have been able to show significant differences of demyelinated mice (week 5) compared to healthy mice. These results are in line with previously reported findings [268], [358]. The parameter that showed a higher sensitivity of all was T2w signal intensity, in agreement with previously reported works [186], [187], [196], [198]. In addition to extensive changes observed at week 5 upon cuprizone diet in the med-CC, this parameter has been the only one describing the remyelination process significantly, taking place for 5 weeks after discontinuing the poisoning with cuprizone. In addition, in a previous study, this parameter has been shown to be sensitive to even detect cortical demyelination in a model of chronic demyelination (12 weeks non-interrupted cuprizone diet) [187], which is not described for the acute demyelination model (5 weeks on cuprizone diet).

Histological studies actually confirm the great correlation (r^2 = 0.84) existing between T2w signal intensity and optical density in Luxol fast blue staining (a gold standard for myelin), demonstrating the good specificity of this MRI parameter for the cuprizone model, a result that is in agreement with previous literature [223].

The use of T2w signal intensity as imaging biomarker of myelin has further advantages beyond its sensitivity and specificity. Conversely to other imaging

modalities such as MTR or DTI, T2w imaging is straightforward with lesser demand on the MRI hardware, is less prone to image artefacts than, for example, SWI, and allows higher spatial resolutions in relatively short times because of its high SNR, compared to other sequences. However, it should be mentioned that T2w imaging is not only sensitive to myelin demyelination but also to other processes such as inflammation, oedema, axon loss [359], micro-bleedings, iron accumulation, protein aggregation, etc. Those processes may act as confounding effects and lead to false positives, overestimating (or masking, depending on the process) changes in myelin content. This is one of the advantages of the use of the cuprizone model, since barely any of the aforementioned processes with influence on T2 are present in an extensive manner, allowing the direct correlation of T2w signal with myelin content. It should be mentioned that axon loss has been reported with higher administration of cuprizone [360], where white matter damage is more extensive.

However, results and conclusions extracted here may not be extrapolated to other animal models or experimental contexts beyond the features of the cuprizone mouse model. In this sense, it is important to bear in mind that research in multiple sclerosis requires parameters sensitive to demyelinating plaques that can accurately correlate with the lesion burden in patients. In this context, T2w imaging has limitations probably due to the deep pathological processes that take place in demyelinating plaques, which go far beyond the change on myelin content. Nevertheless, it might be suitable to detect remyelinating events and assess the effectiveness of a given treatment in clinical studies [361].

In this sense we can consider the fact that other studied imaging parameters have shown enough sensitivity and specificity to myelin, such as radial diffusivity and T1w imaging. Thus we postulate that a multimodal approach that includes the measurement of several parameters will always be better than measuring just one,

to help to avoid confounding effects, an issue that we will discuss later in this work.

Interestingly, the use of combined T1w and T2w imaging through the T1w/T2w ratio has been proposed in the literature for increasing the sensitivity of MRI to detect myelin in the brain, mainly in cortical regions [246], [347]. In our work, we have not found that this ratio improves the sensitivity achieved by T2w signal intensity itself. On the contrary, the reduced degree of sensitivity and specificity observed for T1w, compared with those observed for T2w, resulted in a worse performance of the T1w/T2w ratio than T2w. An explanation for the apparent discrepancy of our findings and previous literature may be found on the difference on the used magnetic field (11.7T in our study,) in comparison with published works, mostly in clinical scanners at 1.5T or 3T (T1 and T2 values and relationship are quite different at ultra-high fields, respect to clinical ones). In fact, T2 values at high or ultra-high field are very low, compared with clinical fields, which makes much more difficult to avoid any trace of T2 weighting on T1w images (a minimal echo time TE>0 is something that we cannot avoid when acquiring T1 images, and when T2 values are low, T2w contamination on T1w images is higher). On the other hand, partial volume effects may also have some impact in relation to this discrepancy. Thus, resulting equally valid for the study of myelin content, the better performance of the T1w/T2w ratio respect to T2w alone, as a marker of myelin, may be dependent on the experimental conditions.

In this sense, radial diffusivity represents an interesting contribution that should be considered. Indeed there are reports in the literature on the capacity of RD to monitor both demyelination and remyelination in the cuprizone model, and this parameter has been suggested as a promising biomarker of myelin in MS [362]–[364]. We have observed that RD is specific and sensitive to demyelination, but not sensitive enough to monitor remyelination, at least in the extension achieved in our

experimental conditions. Interestingly, the same pattern is observed in MD parameter during remyelination.

In respect to other diffusion related parameters, FA has shown high sensitivity but very low specificity for myelin content, while MD and AD were not sensitive for myelin. These findings are in line with previously reported results [365]. The same conclusion as extracted for FA can be extended for MTR and SWI imaging, which have shown sensitivity but not specificity for myelin. In this sense, we do not reach a consensus with previously reported works and thus, Thiessen and colleagues defend a strong correlation between MTR values and the myelinated axons fraction, measured in electron microscopy images of the corpus callosum of cuprizone exposed mice [198]. However, those authors studied only the demyelinating process (MR imaging during 6 weeks at which cuprizone was continuously administered) and did not include remyelination periods. It is a general observation in our study that while most of the measure MRI parameters where sensitive to detect demyelination, they lose sensitivity when detecting remyelination, which is much subtle in this model than demyelination. Here may lay an explanation for the observed discrepancies. Regarding SWI, although myelin is considered to be an important contributor to the T2* effect characterizing SWI imaging, further processes related to iron deposition might influence signal [250] and resulted less useful than T2w signal in our study (also susceptibility effects observed at 11.7T are very high, limiting the use of SWI images).

Altogether our results suggest that normalization of T2w imaging might be considered a robust and straightforward approach for evaluation of myelin content in the cuprizone mouse model at high or very-high magnetic fields. Moreover, the short acquisition time of T2w imaging respect to other imaging modalities permits the scanning of a higher number of animals per day, substantially improving the

logistics of the study. Results would be further supported by the acquisition of T1w imaging and RD, which have also shown a good performance throughout the study.

5.2. Temporal patterns of demyelination-remyelination processes in the cuprizone mouse brain

After having defined three useful parameters for the quantification of myelin changes in the cuprizone mouse brain, we proceeded to study myelin evolution with time during the acute phase of demyelination (weeks 0-5 during cuprizone diet) and remyelination (weeks 5-10, back to toxicant-free diet), as well as a very chronic stage of demyelination (6 months after the demyelinating insult). This pattern has been thoroughly followed and deciphered by T2w imaging in different regions of the brain, as discussed in the following lines.

As previously reported the region of med-CC showed progressive demyelination from the beginning of the administration of cuprizone until week 5 of the study (Fig. 2.7). At this point cresyl violet staining has revealed high cell density in the med-CC, probably indicating phagocytosis conducted by microglia [189], [366]. This is supported by the myelin debris found around de corpus callosum together with a high cell density at this stage.

A slightly different temporal pattern was observed in the CP, were demyelination is evident at week 4 of experiment and remaining stable from that point to week 8, despite having interrupted cuprizone administration at week 5. Furthermore, our data indicate that demyelination in the central part of the genu of the corpus callosum is extensive already at week 2. This condition is reversed at week 4 of experiment and animals present remyelination in this region, despite still being under the cuprizone diet. Other authors have reported demyelination onset at week

3 of cuprizone diet [184], but demyelination at week 2 of exposure to 0.2 % of cuprizone has only been described in juvenile mice of 3 weeks of age [367]. Thus, our multi-regional analysis in high-resolution MR imaging (reduced partial volume effects) reveal unusually reported demyelination already starting 2 weeks after cuprizone administration and signs of remyelination at week 4, when animals are still under cuprizone diet. The *retrogenesis* hypothesis might be considered to explain the early demyelination genu of the CC. This contends that late-myelinated axons during brain development, such as the ones in the genu are more susceptible to degenerate than those myelinated in later stages of life, such as the splenium. White matter degeneration in Alzheimer's disease or during aging, for instance, is correlated with myelogenesis pattern in life [368], [369].

Even though mice underwent demyelination in the genu-CC at an early stage of the experiment, the prompt regeneration conducted in the genu of the CC might be crucial for axonal protection, since remyelination protects axons from degeneration [27]. In a similar fashion in the "chronic cuprizone model", where cuprizone is administered for 12 weeks, an unsuccessful attempt to remyelinate is conducted at the late stages (week 6) of acute demyelination [370], [371].

The clear temporal patterns described by T2w imaging are also revealed by T1w imaging, but in a less pronounced fashion. Nevertheless, even though RD revealed demyelination in a delayed way in the regions analysed, failed to monitor remyelination during the following weeks.

In general, our study demonstrates that the generally accepted paradigm of loss of myelin starting 3 weeks after cuprizone treatment and peaking at week 5, with posterior progressive remyelination until week 10 (if cuprizone is discontinued), is basically sustained for the med-CC, but when other regions of the brain are analyzed

at high spatial resolution, different patterns of evolution with time can be described.

5.3. Chronic effects at 6 months of a demyelination insult

Finally, the long-lasting effects of demyelination have been analyzed in this model on which remyelination takes place (at least partially) after the withdrawal of cuprizone from the diet. Although the extensive demyelination achieved at week 5 in the med-CC and CP is partially reversed during the following weeks following the withdrawal of cuprizone, the normalized T2w signal still exhibits a higher signal in the cuprizone treated mice compared to control at week 10 of the experiment. This might be explained by the formation of a thinner but already functional myelin membrane, characteristic of remyelination. In this way, Optical density values in LFB staining are smaller (T2w values higher) at week 10 compared with week 0, although axons seem to be functional at this point [35].

Importantly, after 6 months of exposure to cuprizone, the difference in some of the measured MR parameters between cuprizone treated animals and controls is still evident. Normalized T2w and T1w signal intensities, RD, FA, MD and T1w/T2w ratio still show differences in the corpus callosum. Of note, as shown in Fig. 2.2, recovery after demyelinating insult does not seem to be completed at week 10, since most parameters show a reduced difference with the control group at month 6. Results indicate that despite the partial reversion of demyelination after a brief period of time (5 weeks on the whole life of an animal) long-lasting effects remain, even 6 months later (which correspond to nearly ¼ of the lifespan of a mouse). In agreement with previous reports, Manrique and colleagues described locomotor abnormalities and axonal damage approximately 6 months after a cuprizone insult [195]. Thus, cuprizone might cause long-lasting and irreversible effects in the mouse brain, which might be indicative of a remyelination in which axons are recovered by

sheaths thinner than the originally present, before the insult, rather than axonal loss. In this sense treatments aimed to enhance the remyelination of affected axons may represent a new hope for the treatment of demyelinating diseases.

6. Conclusions

Our studies on the use of MRI to for the study of myelin content in the cuprizone mouse model have led us to important conclusions that will help us to develop more effective therapies against demyelinating diseases in the future. In particular: 1) An MRI protocol that includes the acquisition of high resolution T2-weighted, T1-weighted and RD images is the most suitable one for the full characterization of multiple aspects of myelin content in the mouse cuprizone model at high or ultra-high magnetic field. 2) The use of normalized T2w signal intensity or the combination of this parameter with RD and T1w are the most sensitive and specific way to follow myelin changes in the brain of the mouse, but other imaging parameters are important to discard T2w changes caused by other processes different than changes in myelin content. 3) Multi-regional analysis (multiple ROIs selection) is required in the mouse cuprizone model since up to 3 different temporal evolution patterns have been distinguished for the demyelination-remyelination processes in the cuprizone mouse model. This is an important issue when developing novel therapies against demyelination since alterations star as early as 1 week after cuprizone, and continue to week 9, even when cuprizone is discontinued 4 weeks earlier, depending on the region of the brain considered. And finally, 4) demyelination leaves long-lasting effects visible up to 6 months after the demyelinating insult, despite spontaneous remyelination is allowed to take place. Altogether, these results highlight the importance of developing effective remyelinating therapies for the treatment of demyelinating disorders.

7. Supplementary data

Supplementary Table 2.1. Manually measured MRI and LFB-OD values used for linear regression (Fig. 2.4) analysis in the cuprizone mouse model.

Region	Group	T2-W mean ±SD	T1-w mean± SD	$T1_w/T2_w$ mean± SD	SWI mean ±SD	MTR mean± SD	FA mean± SD	RD mean± SD	LFB mean± SD
Med-CC	**Control**	7182.54± 479.83	10124.75 ± 349.38	1.54± 0.08	12544.11± 342.73	29.46± 2.07	0.60± 0.06	0.40± 0.03	0.24± 0.05
	Week 5	12135.48± 680.35	12625.44 ± 431.32	1.10± 0.09	16442.75± 300.13	22.33± 0.57	0.50± 0.02	0.51± 0.03	0.11± 0.04
	Week 10	10170.02± 1157.39	11235.96 ± 497.21	1.19± 0.16	13984.06± 229.01	25.04± 1.80	0.49± 0.05	0.51± 0.02	0.21± 0.02
Lat-CC	**Control**	7386.72± 626.84	9488.82± 380.02	1.41± 0.06	9953.71 ± 156.46	26.91± 1.88	0.40± 0.04	0.44± 0.02	0.27± 0.05
	Week 5	10849.72± 623.58	10768.73 ± 355.97	1.05± 0.11	11592.43± 462.29	24.04± 0.73	0.33± 0.02	0.51± 0.01	0.16± 0.06
	Week 10	8904.70± 754.04	9955.47± 477.31	1.21± 0.18	11322.30± 298.33	24.49± 1.61	0.38± 0.02	0.49± 0.02	0.19± 0.04
CP	**Control**	9406.90± 252.54	10571.57 ± 277.19	1.19± 0.04	11633.55± 368.15	26.68± 3.72	0.26± 0.04	0.48± 0.02	0.21± 0.04
	Week 5	12024.99± 587.54	11980.65 ± 525.95	1.05± 0.06	14569.04± 380.10	23.53± 1.46	0.21± 0.09	0.54± 0.04	0.10± 0.01
	Week 10	10250.06± 896.58	10824.40 ± 1102.97	1.12± 0.12	10922.32± 1930.35	24.39± 0.61	0.29± 0.04	0.52± 0.03	0.15± 0.04
C	**Control**	11241.77± 396.38	12100.35 ± 239.37	1.14± 0.04	12612.49± 886.01	27.45± 1.53	0.10± 0.00	0.58± 0.00	0.12± 0.03
	Week 5	11289.23± 216.44	11560.86 ± 434.16	1.07± 0.08	13122.28± 231.32	26.10± 0.62	0.12± 0.02	0.59± 0.01	0.08± 0.01
	Week 10	11807.16± 299.09	11944.67 ± 498.09	1.06± 0.09	11896.35± 958.81	24.99± 1.17	0.09± 0.00	0.59± 0.00	0.09± 0.02
R^2		**0.84**	**0.72**	**0.67**	**0.23**	**0.24**	**0.47**	**0.76**	**-**

Chapter 3

Imaging of myelin in mouse models of Alzheimer´s disease by multiparametric MRI

A. Egimendia *et al.* (Submitted)

1. Foreword

In the previous chapter, we have described a robust protocol for the assessment of myelin-related pathologies in a non-invasive manner, by means of MRI. It is largely known that magnetic resonance imaging parameters might be affected by several factors or pathological processes, such as oedema, inflammation, myelin loss, cell necrosis, microbleedings, permeation of the blood-brain barrier and many others.

In this chapter, we describe our studies to test the performance of the developed protocol in alternative animal models on which affectation of myelin might be only one of the potential events that concomitantly take place during the progression of the pathology. Conversely to the cuprizone model, where myelin pathology is much profound than any other pathological process, such as inflammation or axon loss, in models such as the ones studied in this chapter (namely the mouse model of amyloid precursor protein deposition and a mouse model of tauopathy), profound white and grey matter pathology is expected, while myelin pathology is uncertain.

Thus, on the one hand, we intend to see if the defined MRI parameters allow us to assess myelin content in a specific way and, on the other hand, to what extent this process takes place in Alzheimer disease.

1. Introduction

Alzheimer's disease is characterized by the deposition of β-amyloid protein (Aβ) and the formation of neurofibrillary tangles (NFT). Even though these are considered the hallmarks of AD's and the grey matter has been typically regarded as main affected tissue, the role that myelin plays in the development of the disease is a matter of discussion. *Post-mortem* studies have revealed white matter damage in Alzheimer's disease patients [372]. Myelin affectation is mainly mediated through the death of oligodendrocytes in this disease [109], [110], which are responsible for its production, maintenance and regeneration. Moreover, inflammation, Aβ accumulation and impaired neural activity can further damage white matter.

Deciphering the contribution of Aβ plaques and NFT in the onset and progression of the disease, and determining the effect that they exert in myelin would shed light in the pathogenesis of the disease, potentially enabling novel therapeutic approaches. In this task, MRI represents an invaluable tool to provide non-invasive insight of brain damage, not only allowing the evaluation of brain atrophy but also the detection of altered tissue microstructure in grey and white matter areas.

In this study two mouse models of Alzheimer's disease have been used, a mouse model that develops age dependent Aβ deposition and another transgenic mouse model of tauopathy, with three main goals: 1) Conduct a multiparametric MRI study to evaluate grey and white matter damage in both models; 2) Assess the impact of Aβ plaques and tau protein in myelin through Luxol fast blue histology, and 3) Evaluate the sensitivity of the different MRI parameters to determine myelin content in both animal models, for which white matter damage is expected.

2. Materials and methods

2.1. Animals and experimental protocol

Animal studies were conducted in our SPF facility under full accreditation from the Association for the Assessment and Accreditation of Laboratory Animal Care International (AAALAC). All animal procedures were approved by the Institutional animal care and use committee (IACUC), and local authorities (License PRO-AE-SS-101, Diputación Foral de Gipuzkoa, Spain).

Ad libitum access to food and water was provided to the animals under a controlled light environment (12 h light/dark). Seven B6SJL/J control mice and 5 B6SJLTg APP mice (APPSwFILon,PSEN1*M146L*L286V) (The Jackson Laboratory, Bar Harbor, Maine, USA) of 13 months of age have been used for the study. Additionally, 4 PS19 transgenic mice (B6;C3-Tg(Prnp-MAPT*P301S)PS19Vle/J) and 7 B6C3F1/J control mice (The Jackson Laboratory, Bar Harbor, Maine, USA) have been also scanned.

2.2. MRI

MR imaging was performed on an 11.7 Tesla horizontal bore Biospec 117/16 scanner (Bruker Biospin, Ettlingen, Germany) using a mouse brain surface coil for detection and a volumetric resonator for transmission. Anaesthesia was induced with 4% isofluorane and kept at 1.5-2% during the scanning session, carried by a 1-1.5 l/min current of N_2/O_2 (70/30) gas mixture. After tuning and matching of the RF-coil and setup of the system (i.e., adjustment of pulse power, shims, and resonance frequency) 3 scout images were acquired in axial, coronal and sagittal directions using a T1-Flash sequence, and used as a reference for the rest of the imaging session. Afterwards, a multiparametric imaging protocol was acquired (Fig 3.1.), including:

1) Susceptibility weighted imaging (SWI) was achieved with a gradient echo sequence with TR/TE=1200/6ms, FOV 12.75x12.75 mm^2, matrix size 170x170 (75 μm in-plane resolution), flip angle of 60º, Nav=3 averages and 24 consecutive slices of 500 μm thickness (FOV in z axis = 12 mm).

2) Magnetization transfer (MT) imaging was achieved acquiring 2 sets of 2 images (with different MT pulse strengths each image) using a FLASH (fast low angle single shot) pulse sequence using TR/TE=400/3 ms, FOV 25.6 mm x 25.6 mm, matrix size 256x256 (100μm in-plane resolution), a flip angle of 40º, Nav=6 averages and 2 sets of 12 consecutive slices of 500 μm thickness (covering the whole brain in a 2x6 mm field of view along z axis). MT contrast was generated by a pulse at irradiation offset of 4000 Hz, amplitude 7.8 μT and length 20ms (Msat) acquiring for reference a second image (M0) with identical parameters except for the irradiation offset of 30000 Hz.

3) T1-weighted images were acquired with a TurboRARE image sequence using a RARE factor of 2, TR/TE_{eff}=1200/6.0 ms, a FOV 12.75 mm x 12.75 mm and matrix size 170x170, giving an in-plane resolution of 75 μm, a flip angle 90º, Nav= 6 averages and 24 consecutive slices of 500 μm thickness (covering the whole brain in a 12 mm field of view along z axis).

4) T2-weighted images were achieved with a TurboRARE image sequence using a RARE factor of 8, TR/TE_{eff}=4938/40 ms, a FOV 12.75 mm x 12.75 mm and matrix size 170x170, giving an in-plane resolution of 75 μm, a flip angle 90º, Nav= 8 averages and 24 consecutive slices of 500 μm thickness (covering the whole brain in a 12 mm field of view along z axis).

5) Diffusion-related parameters were obtained with a spin-echo-DTI pulse

sequence acquired using TR/TE=1410/20 ms, FOV 12.8 mm x 9.6 mm and matrix size 128x96 (in-plane resolution = 100μm), flip angle of 90º, b value of 1000 $mm^{-2}s$ (using δ= 4 ms and Δ= 11 ms), 40 gradient directions, 5 b0 images and Nav=1 average. 24 consecutive slices of 500 μm thickness were acquired to cover the whole brain in a 12 mm field of view along z axis).

In this way, total scanning time of the complete imaging protocol was 2h 24m (5' 3 scout images + 30'40'' MTR + 10'12'' SWI + 12'34'' for T2w + 9'21'' for T1w + 76' for DTI), not considering the time required for the adjustments and animal positioning.

2.1. Image analysis

First, a set of preprocessing steps were performed for each image. Voxel dimension of all images was multiplied by 10 in order to improve the processing performance of FSL [FMRIB (Oxford Centre for Functional MRI of the Brain) Software Library; http://www.fmrib.ox.ac.uk/fsl, (Jenkinson et al., 2002; Smith, 2002)]. Additionally, Diffusion images were denoised using local PCA-based algorithm [351] implemented in Dipy library [352] for python.

Next, all the images were placed in the same space as a down-sampled in-house template. High resolution T2w images were used for achieving optimal brain extraction and registration to the template. T2-weighted images were skull stripped and bias corrected using FSL. Afterwards, registration to the in-house template was performed. Masks and transformation matrixes obtained for the T2w images were subsequently applied to each of the MR image modalities. Simultaneously, the publicly available AMBMC (Australian Mouse Brain Mapping Consortium, http://www.imaging.org.au/AMBMC/) mouse atlas was registered to the template for automatic regions of interest (ROIs) selection on images.

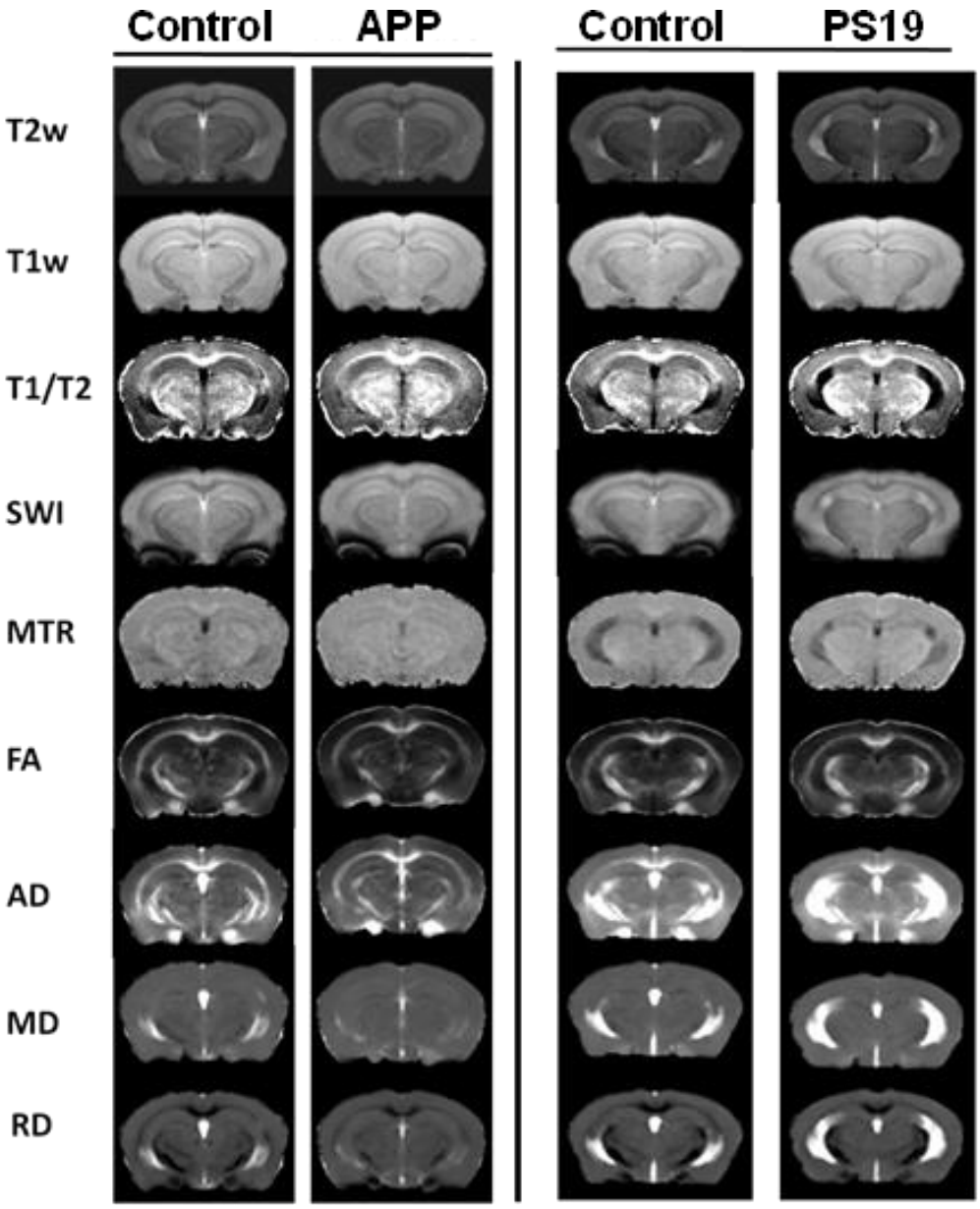

Figure 3.1. *Multiparametric MR imaging of APP and PS19 mice and their respective controls. T2-weighted imaging (T2w), T1-weighted imaging (T1), T1w/T2w ratio, susceptibility weighted imaging (SWI), magnetization transfer ratio (MTR), fractional anisotropy (FA), axial diffusivity (AD), mean diffusivity (MD) and radial diffusivity (RD).*

Once images were placed in the same space, T1-weighted and T2-weighted images were divided (T1w/T2w ratio) and Magnetization transfer ratio (MTR) was calculated using the formula MTR=100*(M0-Msat)/M0, where M0 is the signal intensity of the non-saturated image and Msat is the signal intensity of the off-resonance RF irradiation image.

Moreover, pixel signal intensities of T1-weighted, T2-weighted and SWI images were normalized for each image (taking brain mean value= 10000) in order to enable the inter-individual comparison of images.

A series of regions of interest (ROIs) were selected and extracted from the anatomical atlas, covering both gray matter and white matter regions including: the cerebellar peduncles (CP), the hippocampus (Hc), the thalamus (Th), the caudate putamen (CPu), the hypothalamus (Hyth) and the cortex (C), including somatosensory and auditory cortex. The CC was separated in the medial corpus callosum (med-CC) and the lateral corpus callosum (lat-CC), for image analysis.

Additionally, regional brain volumes (V) of grey matter areas were quantified by registration of the images to the AMBMC mouse brain atlas with 12 degrees of freedom.

2.2. Histology

After the MRI scanning session mice were sacrificed, brains were immediately removed and frozen in dry ice. Then, brains were stored at -80°C until processed. Twenty-five micrometre thick sections were cut on the microtome and stored mounted in glass at -20°C until stained. Samples were stained with Luxol fast blue (LFB) (Sigma, S3382) and analyzed on a cell observer microscope (Axio Observer, Carl Zeiss, Germany).

ImageJ software [353] was used for image processing. Then colour values were converted to optical density (OD) for myelin quantification. Evaluation of myelin content was performed on the genu of the corpus callosum (genu-CC), the medial corpus callosum (med-CC), the thalamus (Th), the striatum (CPu), the hippocampus (Hc), the motor cortex (MC) and a somatosensory cortex region (C).

2.3. Statistical analysis

Graphpad/Prism software was used for statistical analyses. Normality assessment was performed with quantile-quantile (Q-Q) plot [354]. For normally distributed data the statistical significance of the difference between groups was determined by a two-way analysis of variance (ANOVA). Afterwards, unpaired t-test was applied. If the sample did not follow normal distribution a Mann-Whitney test was applied. Statistical significances were set at $p>0.05$ (*).

3. Results

3.1. APP mouse model

Regional alterations respect to controls of different imaging parameters were observed at different ROIs of the brain of APP mice, (Fig. 3.2 and Suppl. Table 3.1). Most alterations were observed in water diffusion related parameters, entailing increased radial diffusivity (RD) values and reduced fractional anisotropy (FA) values, in several regions. Conversely, magnetization transfer ratios (MTR) and axial diffusivity (AD) did not reveal any significant difference between groups.

APP transgenic mice show abnormal values respect to controls in highly myelinated regions, like med-CC (ΔmSWI=5.5%, ΔmFA=-21.4%, ΔmRD=13%, $p<0.05$), the lat-CC (ΔmFA=-20.3%, $p<0.05$) and the CP (ΔmFA=-29%, ΔmRD=12.1%, ΔmMD=5.8%,

p<0.05). Among the subcortical regions, the Th (ΔmT2=-3.0%, ΔmT1=-2.1%, ΔmSWI=-4.1%, ΔmRD=3.5%, p<0.05), the CPu (ΔmT1w/T2wratio = -2.2, ΔmFA = -15.1%, ΔmMD=2.8%, ΔmRD=4.3%, p<0.05) and the Hyth (ΔmT2=-3.3%, p<0.05) exhibited alterations.

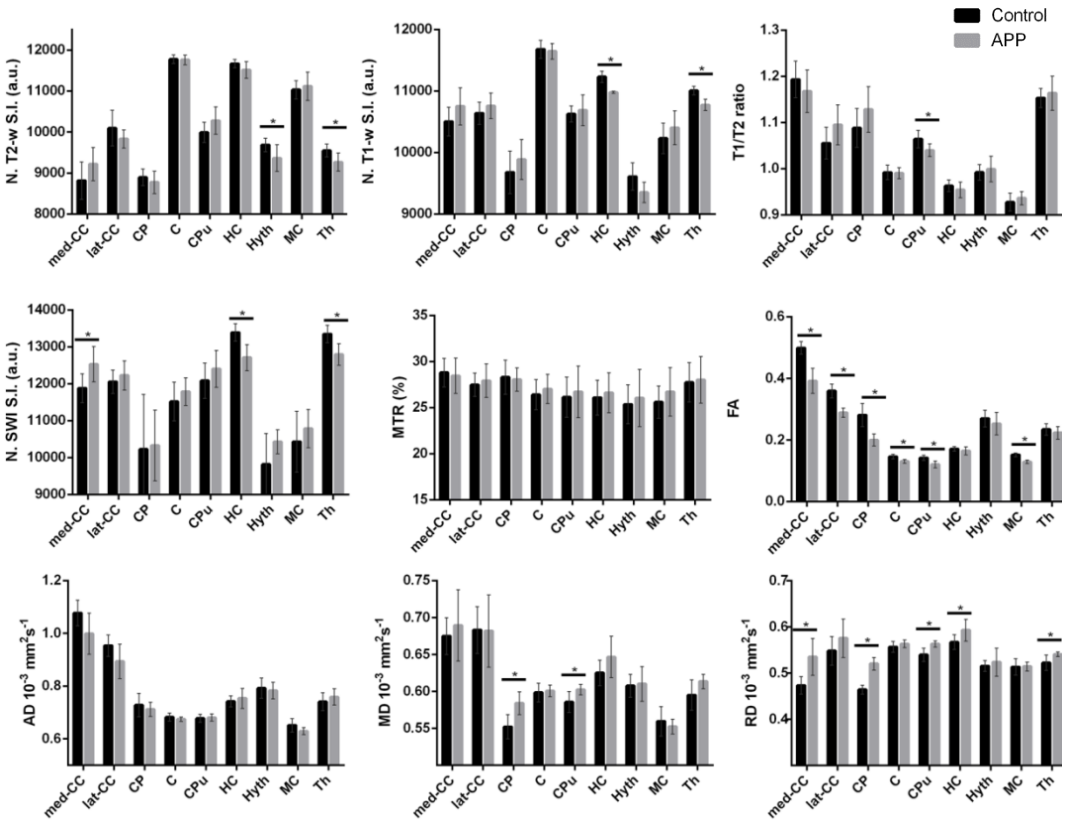

Figure 3.2. *Mean values of measured MRI parameters at different regions of interest in APP (grey bars) and control (black bars) mice. The medial corpus callosum (med-CC), lateral corpus callosum (lat-CC), cerebellar peduncles (CP), C (cortex), caudate putamen (CPu), hippocampus (HC), hypothalamus (Hyth), motor cortex (MC) and thalamus (Th) have been analyzed. * Represents p<0.05*

Cortical areas, in which Aβ plaques are presumably accumulated, also exhibit different values compared to controls, more precisely in the MC (ΔmT2=0.8%,

ΔmFA=-15%, p<0.05), C (ΔmFA=-10.4%,, p<0.05) and HC (ΔmT1=-2.2%, ΔmSWI=-5.1%, ΔmRD=4.6 p<0.05) regions. Moreover, taking the whole brain as an unique region of interest, the Aβ deposition transgenic mouse model showed 15.88% reduced mean FA values (Control = 0.23, APP-mouse = 0.19; p<0.05).

All in all, four different findings have been observed in grey matter, in this study: 1) Susceptibility weighted imaging, T1-weighted imaging and RD revealed abnormal values in the thalamus (also reduced T2w signal) and hippocampus; 2) FA revealed decreased values in the cortex (C and MC) in transgenic mice; 3) A rise in MD and RD and a decrease in FA, together with a decrease in the T1w/T2w ratio is observed in the CPu; 4) T2w imaging shows hypointensities in the hypothalamus. When it comes to highly myelinated white matter regions (CC and CP), the differences are mainly exhibited by DTI parameters, together with SWI.

Optical densities measured on Luxol fast blue staining images did not reveal any difference between the transgenic and control mice for the ROIs analyzed, as shown (Fig. 3.3). Numerical values are reported in supplementary data (Suppl. Table 3.2).

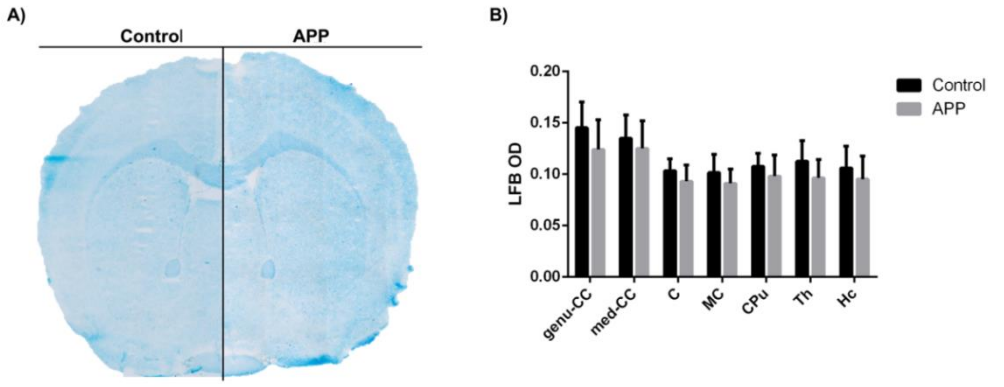

Figure 3.3. *Luxol fast blue (LFB) staining of APP mouse model. A) LFB staining of mouse control mice (left) and APP transgenic mice (right) B) Optical density measures of LFB at the genu of the corpus callosum (genu-CC), medial corpus callosum (med-CC), cortex (C), motor cortex (MC), caudate putamen (CPu), Hippocampus (Hc) and thalamus (Th).*

Volumetric changes in different ROIs of the brain were determined (Fig 3.4.). The analysis of this parameter revealed significantly reduced normalized volumes (respect to the whole brain volume) for APP mice respect to controls at the level of; C (V_{APP} = 13.56±0.45 %, $V_{Control}$ = 14.05±0.2 %, p<0.05), MC (V_{APP} = 7.67±0.15%, $V_{Control}$ = 8.10±0.24%, p<0.05), the HC (V_{APP} = 5.87±0.11%, $V_{Control}$= 6.04±0.11%, p<0.05) and the Th (V_{APP}= 2.79±0.07 $V_{Control}$ = 2.94±0.07, p<0.05). Whole brain volumes of the transgenic model were not significantly different from controls at the level of p<0.05 ($V_{Control}$ = 513 ± 5.54 mm^3; V_{APP} = 489 ± 11.19 mm^3).

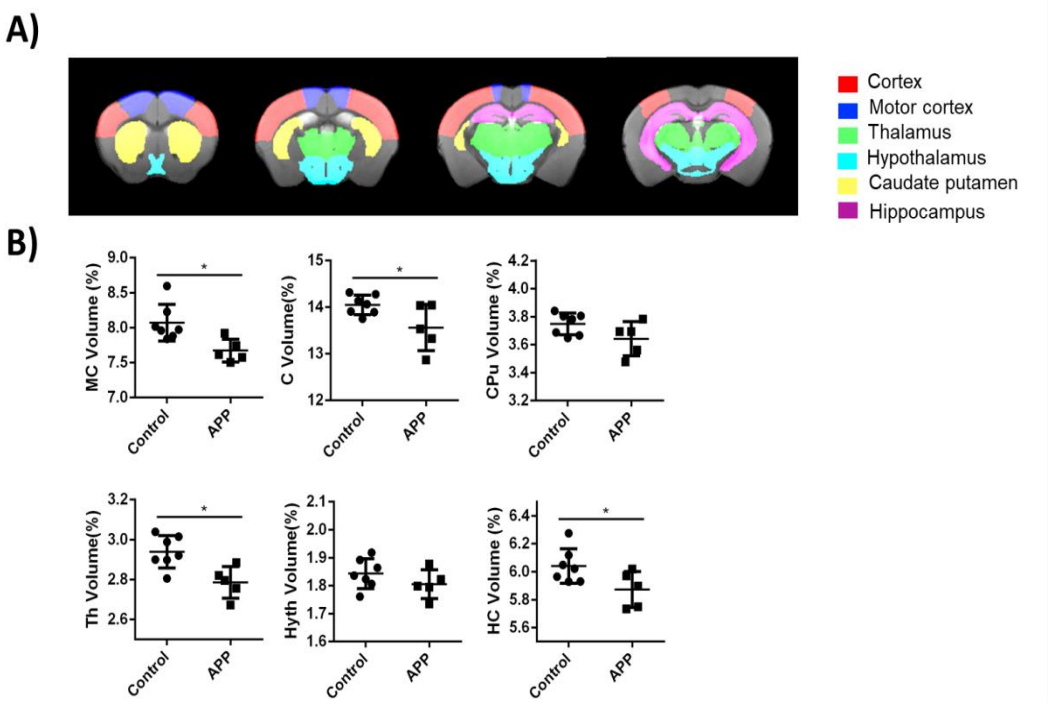

Figure 3.4. *Volume measurements of different regions of interest in APP and control mice. A) Regions of interest selected for analysis: Cortex (C), motor cortex (MC), thalamus (Th), hypothalamus (Hyth) and caudate putamen (Cpu). B) Mean values showing differences in the volume of the ROIs normalized for each animal as (%) of the total brain volume * Represents p<0.05.*

3.2. Mouse model of tauopathy

In the PS19 model of tauopathy most significant differences with respect to controls were observed for water diffusion related parameters and SWI signal intensities (Fig. 3.5, Suppl. Fig. 3.3). Mean values of the studied parameters with their standard deviation are reported in Suppl. Table S3.3. Parameters such as MTR, T1w/T2w ratio and T1-weighted signal intensity did not reveal any difference for any of the analyzed ROIs. Simultaneously, no significant differences were observed for any of the analyzed parameters for highly myelinated regions (i.e. med-CC, lat-CC, CP).

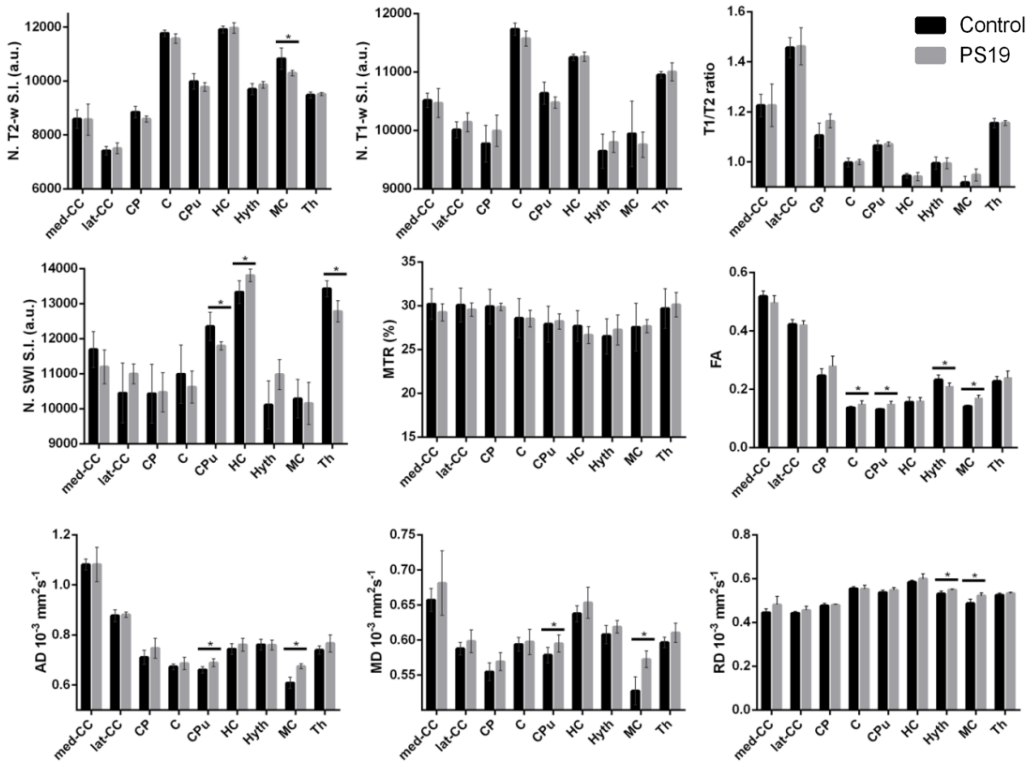

Figure 3.5. *Means of MRI parameters at different ROIs for PS19 mice (grey bars) vs. controls (black bars). Selected ROIs: corpus callosum (med-CC), lateral corpus callosum (lat-CC), cerebellar peduncles (CP), C (cortex), caudate putamen (CPu), hippocampus (HC), hypothalamus (Hyth), motor cortex (MC) and thalamus (Th). * Represents p<0.05.*

However, in regions where the presence of NFT was expected (i.e. HC, Th, C and MC), differences in MR parameters between PS19 mice and controls have been observed. FA was the only image parameter revealing differences between PS19 and control mice in the C (ΔmFA=8.4%). Similarly, SWI showed abnormally increased signal in the HC (ΔmSWI=3.8%), as well as a decreased signal in the Th (ΔmSWI=-4.8%) of PS19 mice, respect to controls. Differences were observed also for different parameters at the level of MC (ΔmT2=-5%, ΔmFA=20.5%, ΔmAD=10.9%, ΔmMD=8.6%, ΔmRD=7.2%), CPu (ΔmSWI=-4.5%, ΔmFA=13.9%, ΔmAD=4.3%, ΔmMD=2.9%,) and Hyth (ΔmSWI=8.6%, ΔmFA=-9.8%, ΔmRD=3.3%,). Taking the whole brain as a unique region of interest, PS19 mice exhibited 5.76% higher values of FA respect to the controls ($mFA_{control}$ = 0.215, FA_{PS19} = 0.228; $p<0.05$).

LFB staining did not reveal any significant difference in any region of interest between the PS19 mouse model and control mice (Fig. 3.6). Numerical values are reported in supplementary data (Suppl. Table 3.2).

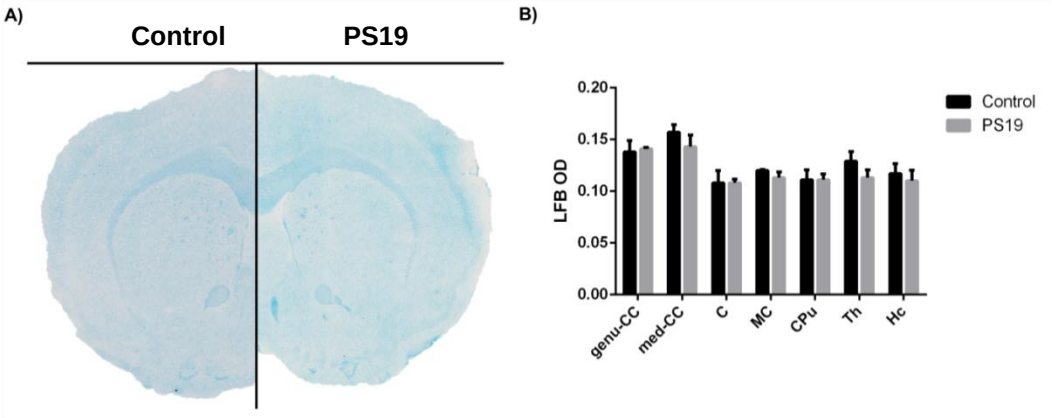

Figure 3.6. *Luxol fast blue (LFB) staining of PS19 mouse model of tauopathy. A) LFB staining of control mice (left) and PS19 transgenic mice (right) B) Optical density measures of LFB at the genu of the corpus callosum (genu-CC), medial corpus callosum (med-CC), cortex (C), motor cortex (MC), caudate putamen (CPu) and thalamus (Th).*

In terms of differences in volume, no regional differences have been observed between PS19 mice and controls at the level of Th, Hyth, C, MC and HC (Fig 3.7). Moreover, whole brain volume measurements have been performed ($V_{control}$ = 516 ± 27.75 mm^3; V_{PS19} = 514 ± 10.09 mm^3), resulting in no significant differences between groups.

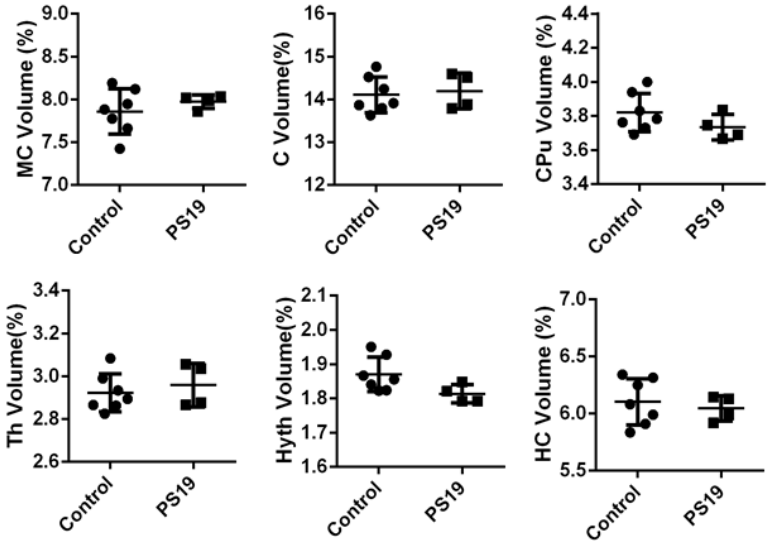

Figure 3.7. *Volume measurements of different regions of interest measured in PS19 and control mice. A) ROIs selected for analysis: Cortex (C), motor cortex (MC), thalamus (Th), hypothalamus (Hyth) and caudate putamen (Cpu). B) Mean values showing differences in volume of the ROIs normalized for each animal as (%) of the total brain volume * Represents p<0.05*

4. Discussion

4.1. APP mouse model

Due to the complexity of Alzheimer's disease, in which presence of Aβ plaques precede the accumulation of NFT, studies conducted before the onset of symptoms

provide a deep insight in the role that the Aβ might play in the progression of the disease and the occurrence of neurological deficits. However, the role that Aβ plaques have in the imaging and pathogenesis of Alzheimer's disease is inconclusive in the current state of the art [373].

The different scenario unfolded by the various parameters studied in this work might reflect the complexity of the model and the sensitivity of MRI to detect different pathological states, such as white matter damage. Signal arising from SWI might be a representative example of this situation. While SWI reveals hyperintense signal in a highly myelinated area of APP mice (the corpus callosum, CC), it exhibits hypointense signal in the Th and the HC, probably revealing a different pathological condition.

Multiparametric MRI has revealed different patterns in this study. Susceptibility weighted imaging, T1-weighted imaging and RD revealed abnormal values in the thalamus and hippocampus. Furthermore, FA revealed decreased values in the cortex in transgenic mice. In transgenic models of APP deposition, extensive accumulation of plaques has been reported in the thalamus, hippocampus and cortical regions [374]. Even though direct visualization of Aβ plaques calls for ultra-high resolution and large scanning times [374], [375], the presence of senile plaques might lie behind the abnormal values exhibited in T1w, RD and SWI in the Th and HC, or the decreased values of FA in C and MC. Of note, FA has been found to be the only parameter showing a difference in the C and MC, while no difference has been exhibited in the HC or Th. Thus, microstructural changes caused by Aβ deposition might be different in these regions.

Simultaneously, the CPu shows substantial alterations in diffusivity, with a rise in MD and RD and a decrease in FA, together with a decrease in the T1w/T2w ratio.

Concurrently, in a studied conducted by Müller and colleagues, decreased FA revealed abnormalities in this region [376]. The setting showed by the CPu might be similar to the one shown in highly myelinated areas, such as the CP or the CC. The reason behind such an altered diffusivity might be therefore related to axon atrophy, which is extensive in Alzheimer's disease [103]. Finally, T2w imaging has shown abnormalities in the Hyth and Th. Certainly, it is difficult to ascribe a particular pathological process to these abnormalities. More precisely, the Hyth has shown to be particularly metabolically altered in the APP transgenic mouse model [377], [378]. Additionally, a reduced amount of neurons and dendritic arborization have been described in Alzheimer's disease patients, even though, the number of plaques or tauopathy was minimal compared to other regions [379].

Thus, we have observed that multiparametric MRI reveals deep damage in the grey matter. The amyloid hypothesis bears that Aβ plaques cause neuronal death, leading to brain atrophy [102]. Deciphering the relationship between Aβ accumulation and brain atrophy is crucial for the understanding the pathological mechanism of the disease. Hippocampal atrophy is considered one of the most revealing features of AD patients [380], [381] as a key diagnostic characteristic in the early stages of the disease [382]. At this stage, not only volume changes but also abnormal diffusivity is detected by MRI in the HC [383]. Interestingly, multimodal studies performed in human Alzheimer's disease patients combining MRI and Positron emission tomography (PET) of Aβ deposition have demonstrated their correlation with atrophy in the brain [384], [385]. Additionally, growing evidence supports that mouse models expressing APP develop hippocampal atrophy [386]–[388]. According to this findings, we have observed brain atrophy in the HC, together with atrophy in the Th, C and MC which are some of the main atrophied regions of the brain in Alzheimer's disease patients [389]. Nevertheless, no significant difference

has been found for the total brain volume between APP mice and controls.

Even though Alzheimer's disease has been widely recognized as a grey matter disorder, in this study the implication of Aβ plaques in white matter damage and myelin loss has also been studied. *Post-mortem* studies have shown an elevated concentration of degraded myelin basic protein complex in human brains, as well as deposition of myelin basic protein (MBP) at the margins of Aβ plaques [106]. Certainly, growing evidence supports that white matter is extensively damaged in Alzheimer's disease [390]. In a study conducted in healthy adults, a decrease of FA in white matter tracts along with an increase of MD and RD was ascribed to increase on Aβ levels, resulting in loss of cognition [391]. Concurrently, Song et colleagues [279] described the same pattern in a transgenic mouse model of Aβ deposition at 15 months of age. In agreement with these findings, we showed that Aβ deposition leads to a reduction of FA values in the CC and CP together with an increase in RD and MD (MD only significantly in the CP). Precisely, the loss of integrity of myelin or demyelination has been attributed to a stable AD and an increased RD in white matter [270], [358], as demonstrated in the cuprizone mouse model of demyelination [267], [268]. Conversely, FA is considered highly sensitive to various pathological conditions and a nonspecific marker of microstructural damage and neuropathology [365]. A correlation of FA with axonal density has been found in *post-mortem* studies conducted in patients of Alzheimer's disease [392]. Of note, we have observed that the Aβ deposition transgenic model presents, on average, a 15.88% lower FA value for the whole brain, respect to controls.

Although abnormalities in white matter are evident in the Aβ transgenic mouse model, the underlying reason for this condition has not been deciphered so far. In this study, we have performed Luxol fast blue staining for the quantification of myelin content in this mouse model. LFB is considered a histological gold standard

for myelin [218]. Optical density values of LFB stained brain sections have revealed no significant differences for any region of interest analyzed between APP mice and controls. Thus, white matter damage might include damage beyond myelin pathology, such as axonal loss, without changes in net myelin content, which might be aggravated by the age of the mice (13 months). In fact, electron microscopy has revealed axonal damage in the APP/PS1 mouse model [393], as shown in Alzheimer's disease patients [394]. This pathological process might influence diffusion related MRI parameters such as FA, MD or RD.

Certainly, we have previously reported (Chapter 2) that radial diffusivity exhibits a good correlation with myelin pathology. Here we show that RD is also sensitive to pathological hallmarks not related to myelin content, as it exhibits significant difference between APP mice and controls in white matter regions such as the corpus callosum or the cerebellar peduncles, were myelin loss has not been detected (Fig 3.2.). Although RD has demonstrated its capacity to specifically monitor myelin content in several preclinical models [268], [270], [271], it might also be sensitive to extra-axonal water or inflammation [358], [362], [395], [396].

Conversely, in line with Luxol fast blue staining, T2-weighted imaging and T1-weighted imaging, which were validated in Chapter 2 as specific and sensitive markers of myelin, did not show any significant difference in major tracts of white matter (i.e. med-CC, lat-CC and CP) in the present study. Precisely, as aforementioned, diffusion-weighted imaging has revealed abnormalities in APP mice in these regions. These results might indicate that T2w and T1w imaging might be not sensitive to non myelin related pathological events happening at white matter tracts of the brain of our APP mouse model.

Thus, in a model where extensive degeneration was expected, and actually revealed

by multiparametric MRI, T2w and T1w imaging has shown robustness and low sensitivity to processes unrelated to myelin, while RD has been highly sensitive and efficient to detect further microstructural abnormalities. These results do not imply that other pathological events present in other models may also affect T1 and T2 imaging, only that those processes present in this model do not affect them.

Results from previous and current study reinforce the importance of the performance of multiparametric MRI studies, in order to avoid misleading conclusions and to get a deeper insight on tissue microstructure in different models of disease on which myelin plays either a minor or a major role.

4.2. PS19 mouse model of tauopathy

The advent of aggregates of hyperphosphorylated tau forming neurofibrillary tangles (NFTs) triggers the cognitive impairment in Alzheimer's disease. It is known that the appearance of Aβ plaques precedes the formation of NFT. Hence, it is challenging to evaluate the effect of the later in an isolated manner in the course of the disease in humans. In this context, transgenic mouse models of tauopathy have shed light into the role that NFTs might be playing, irrespective of APP accumulation. In this sense, it is important to highlight the difference between alternative murine models of tauopathy commonly used in literature.

The rTg4510 and PS19 mouse models are the most commonly used transgenic models of tauopathy. PS19 mouse model presents a circa 5-fold higher expression of tau transgene compared to control mice, while the rTg4510 express circa 13-fold levels. Additionally, the onset of tauopathy is exhibited at 6 months or 2-3 months in PS19 and rTg4510 models, respectively [397].

In this study, we have evaluated the behaviour of MRI parameters in PS19 mice. To

our knowledge, no DTI studies have been performed in this model so far, where hyperphosphorylated tau aggregation can be observed mainly in the hippocampus and cortex, and in a lesser extent in the thalamus and striatum [398]–[400].

DTI has shown to be the most sensitive and most widely used technique for the characterization of Alzheimer's disease mouse models. Most MRI studies in Alzheimer's disease models of tauopathy have been performed in the rTg4510 mouse. These studies agreed on the increase of MD and FA in grey matter regions [278], [401], [402]. In agreement with these authors, we have appreciated an increase of MD (in the CPu and MC) and of FA (C, MC and CPu) in grey matter regions. However, we have found that at the level of the Hyth FA values decrease, while RD and SWI values are increased, offering a different pattern to the one described by the previous parameters (MD and FA).

In line with studies conducted in Alzheimer's disease patients, the progression of the disease leads to higher MD values in grey matter regions [403]. Conversely, increased FA values in both PS19 and rTg4510 models contradict the diffusivity pattern observed in human patients, where FA is decreased in most regions [403]. The reduced values observed in the human brain might lie in the presence of Aβ plaques and damage triggered by them in Alzheimer's disease patients. This hypothesis is supported by the lower values of FA that we and others have observed in the mouse model of amyloid deposition. Additionally, AD increased values are found in the CPu and MC and increased values of RD in the MC in PS19 mice compared to controls. Thus, the presence of NFT might lead to increased directionality (higher FA) and diffusivity (higher MD).

It is should be born in mind that differences observed in diffusivity in mouse models of tauopathy have been observed in an advanced stage of the disease. In the study

conducted by Holmes and colleagues in the rTg4510 mouse model [402] they were only able to observe differences between the rTg4510 and the control groups at 7.5 months of age. Due to this fact they concluded that DTI parameters are not sensitive enough to detect abnormalities at an early stage of the pathology. This is of great interest when considering DTI as a potential marker for tauopathy.

Unlike cortical regions and CPu, the Th and the HC exhibit a different behaviour. These regions, in which accumulation of tau fibrils is expected, show no diffusion abnormalities for transgenic mice. Interestingly, while decreased SWI signal is observed in the Th (also observed for T2w signal) and CPu in PS19 mice, increased values are observed in the HC and Hyth. Interestingly, in the rTg4510 mouse model of tauopathy abnormal magnetic susceptibility was detected in the Th, CPu and HC, where NFT aggregation was observed (no results are exhibited Hyth-wise) [404]. Nevertheless, no correlation was observed between NFT burden and measured SWI signal. Although NFT may contribute to T2* effect, synaptic and neuronal densities or myelin content can also contribute to T2* [405]. Extent of neurodegeneration[406] and loss of microstructure, along with different NFT burden observed in different brain areas, might exert contrary effects in SWI signal.

Regarding white matter damage, DTI metrics show a different pattern in the PS19 respect to that reported for rTg4510 mouse models. The increased MD, RD and reduced FA values widely described in the rTg4510 model is in the line with the studies conducted in Alzheimer's disease patients [278], [401], [402]. Nevertheless, these differences have only been observed in an advanced phase of the disease, after month 7.5 [401], [402], and not in the early stages. Of note, no NFT has been observed in the CC at 8.5 months [278]. Considering the increased amount of tau overexpression in the rTg4510 (~13-fold) mouse model compared to the PS19 (~5-fold), absence of extensive white matter damage in this model might be reasonable.

These findings are supported by LFB staining, where no significant difference in myelin content were observed for any of the analyzed regions of interest.

Concerning volumetric measurements for the evaluation of potential brain atrophy, no differences have been observed between PS19 and control mice in any of the studied regions (C, MC, TH, CPu, Hyth). contrarily to previous studies that report volume loss in the HC [398] and neocortex [400] in this model. The use of more sensitive and accurate techniques for volume assessment might allow the identification of subtle differences, not detectable by atlas coregistration. Nevertheless, tauopathy has not shown to be a major factor contributing to brain volume loss compared to control mice at this age.

4.3. General considerations about Alzheimer's Disease models

Alzheimer's disease transgenic mouse models of β-amyloid deposition or tauopathy have provided knowledge to understand the physiopathology of the disease. However, in humans, both processes are concomitant, triggering extensive damage. In this study, we have studied the effect of APP deposition and NFT formation in a separate manner, in terms of myelin affectation, and we have evaluated the sensitivity of different MRI parameters to describe pathological hallmarks related with their presence. Main features of each model are summarized in Table 3.1.

Table 3.1. Summary of the alterations observed in animal models of Alzheimer's disease.

Model	White matter alterations	Demyelination	Grey matter alterations	Atrophy
APP-Aβ plaques	+	-	+	+
PS19- tauopathy	-	-	+	-

+ Represents existing phenomenon; - Represents absent phenomenon

Most differences are revealed by diffusion tensor imaging. In both models, MD and RD values are increased in some regions of the brain. However, we have observed that both animal models exhibit opposite behaviour in some situations. FA values in specific regions of grey matter, such as the C, MC and CPu are higher in the PS19 mouse model and lower in the APP mouse model. Interestingly, the mean FA value of the whole brain is 5.76% higher in PS19 mice, respect to their controls while it is 15.88% lower in APP mouse model, respect to their controls (Fig 3.8.).

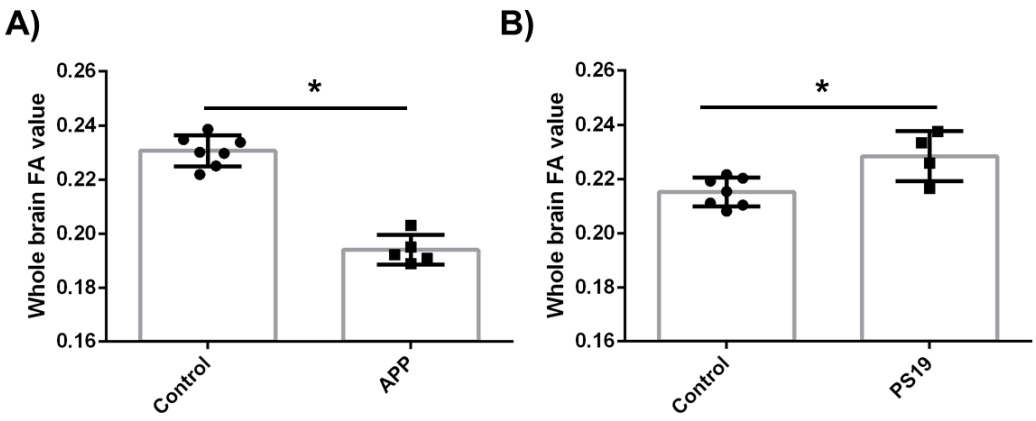

Figure 3.8. *Mean fractional anisotropy values (FA) in the whole brain for A) APP mouse model and B) PS19 tauopathy mouse model.*

At the same time, a similar phenomenon takes place in the HC, where PS19 mice exhibit higher values of normalized SWI image than their controls, while the APP mouse present decreased values in transgenic mice compared to controls. Hence, misleading interpretations might be taken when comparing transgenic mouse models with the human disease, where APP and NFT effects may compensate each other yielding no net changes. A more realistic view of the Alzheimer's disease may be provided by the triple-transgenic Alzheimer's disease mice model (3xTg mouse

model), where both NFT and Aβ plaques coexist. In this model, it has been described that FA and AD values were lower in the HC at 12-14 months of age [407]. Nevertheless, only increased radial diffusivity was exhibited in the APP mouse model in our study in this region.

Regarding myelin damage, our study shows that both the APP and the tauopathy mouse models exhibit no apparent myelin loss, judging by LFB staining of brain sections. While deposition of Aβ plaques seems to cause damage in the white matter, as revealed by diffusion MRI, tau protein fibrils do apparently lead to no significant white matter damage in the PS19 model. Conversely, as stated previously, tau protein aggregates result in white matter damage in the rTg4510d mouse model. The accumulation of NFT and Aβ plaques might provoke further damage that finally could cause extensive loss of myelin. Of note, in the triple-transgenic Alzheimer's disease mice (3xTg mouse model), damage of white matter is still controversial, and a matter of discussion [108], [408].

Finally, analysis of brain volumes has been performed, since atrophy is a particular feature of Alzheimer's disease patients [409]. We have observed that deposition of Aβ plaques results in atrophy of several regions of the brain. Conversely, the PS19 mouse model of tauopathy exhibits no regional atrophies, compared to controls. Interestingly, brain volume loss has been observed together with white matter extensive damage in APP mouse model. The correlation between both pathological features, however, is still inconclusive.

In this study, the previously described (chapter 2) correlation between T2-weighted and T1-weighted signal intensity and LFB-measured myelin content, found for the cuprizone mouse model, seems to hold well for the 2 studied models of Alzheimer's disease features. A different situation was observed for RD, which showed a high

correlation with myelin content in the cuprizone model but seems to be sensitive to non myelin related pathological events taking place in the white matter of APP mice. Therefore, a setting in which the presence of nonsignificant differences on T2w signal intensity values are shown together with decreased RD values, in a specific region of the brain, might reveal further non-myelin related pathological processes going on (e.g. axonal loss). Thus, the importance of performing multiparametric MR imaging to study brain-related pathologies is highlighted by these findings.

5. Conclusions

In this study the MRI hallmarks of two mouse models of Alzheimer's disease have been presented. We have observed through Luxol fast blue staining that myelin loss is not a relevant feature of the studied mouse models of Aβ deposition and of the studied mouse model of tauopathy (PS19). Nevertheless, multiparametric MRI has revealed extensive white matter alterations and regional atrophies triggered by Aβ deposition, while no white matter or atrophy has been observed in the mouse model of tauopathy. Multiparametric MRI has revealed alteration of different imaging parameters for several grey matter regions, probably as a consequence of the presence of NFT or senile plaques, or as a result of the damage triggered by them.

6. Supplementary data

Supplementary Table 3.1. *Mean (m) values ± Standard deviation (SD) for the different parameters studied at different regions of the brain. (All values are presented as m±SD, shadowed values indicate significant differences with p<0.05).*

Region		10^3 T2 (a.u.)	10^3 T1 (a.u.)	T1w/T2w (a.u.)	10^3 SWI (a.u.)	MTR (%)	FA	$10.^{-3}$ AD (mm^2s^{-1})	10^{-3} MD (mm^2s^{-1})	10^{-3} RD (mm^2s^{-1})
med-CC	**C**	9.2±0.5	10.7±0.3	1.53±0.06	12.5±0.4	28.4±1.7	0.39±0.04	1.00±0.07	0.69±0.04	0.53±0.04
	β	8.8±0.4	10.5±0.2	1.62±0.06	11.9±0.4	28.8±1.4	0.50±0.02	1.08±0.04	0.67±0.02	0.47±0.02
Lat-CC	**C**	9.8±0.2	10.8±0.2	1.41±0.05	12.2±0.3	27.9±1.6	0.29±0.01	0.89±0.06	0.68±0.04	0.58±0.04
	β	10.1±0.4	10.6±0.2	1.40±0.04	12.1±0.3	27.5±1.2	0.36±0.02	0.95±0.04	0.68±0.03	0.55±0.03
CP	**C**	8.8±0.2	9.89±0.3	1.37±0.07	10.3±0.9	28.0±1.1	0.20±0.02	0.71±0.02	0.58±0.01	0.52±0.01
	β	8.9±0.2	9.68±0.3	1.30±0.07	10.2±1.4	28.3±1.7	0.28±0.03	0.73±0.04	0.55±0.02	0.46±0.01
C	**C**	11.8±0.1	11.6±0.1	1.20±0.03	11.8±0.3	27.0±1.4	0.13±0.01	0.67±0.01	0.60±0.01	0.56±0.01
	β	11.8±0.1	11.7±0.1	1.20±0.03	11.5±0.5	26.4±1.5	0.15±0.01	0.68±0.01	0.60±0.01	0.56±0.01
CPu	**C**	10.3±0.3	10.7±0.2	1.24±0.03	12.4±0.4	26.7±2.5	0.12±0.01	0.68±0.01	0.60±0.01	0.56±0.01
	β	10.0±0.2	10.6±0.1	1.27±0.05	12.1±0.4	26.1±2.0	0.14±0.01	0.68±0.01	0.59±0.01	0.54±0.01
HC	**C**	11.5±0.2	11.0±0.2	1.15±0.04	12.7±0.3	26.6±1.9	0.16±0.01	0.75±0.03	0.65±0.03	0.59±0.02
	β	11.7±0.1	11.2±0.1	1.16±0.03	13.4±0.2	26.1±1.8	0.17±0.01	0.74±0.02	0.63±0.02	0.57±0.01
Hyth	**C**	9.4±0.3	9.35±0.1	1.22±0.03	10.4±0.3	26.1±2.8	0.25±0.03	0.78±0.03	0.61±0.02	0.52±0.03
	β	9.7±0.1	9.61±0.2	1.21±0.03	0.98±0.8	25.4±2.0	0.27±0.03	0.79±0.04	0.61±0.01	0.52±0.01
MC	**C**	11.1±0.3	10.4±0.2	1.16±0.04	10.8±0.5	25.6±1.6	0.13±0.00	0.63±0.01	0.55±0.01	0.51±0.01
	β	11.0±0.2	10.2±0.2	1.14±0.02	10.4±0.8	26.7±2.4	0.15±0.01	0.65±0.02	0.56±0.02	0.51±0.02
Th	**C**	9.27±0.2	10.8±0.1	1.40±0.11	12.8±0.3	28.0±2.3	0.22±0.02	0.76±0.03	0.61±0.01	0.54±0.00
	β	9.55±0.1	11.0±0.1	1.38±0.05	13.3±0.2	27.7±2.0	0.23±0.02	0.74±0.03	0.60±0.02	0.52±0.02

Supplementary Table 3.*2. Luxol fast blue optical density (OD) mean values ± Standard deviation (SD) for different regions of interest in the APP mouse model and the PS19 mouse model. (all values are presented as m±SD).*

Region	Group	APP LFB OD (a.u.)	PS19 LFB OD (a.u)
Genu-CC	**Control**	0.124±0.03	0.138±0.01
	Alzheimer's	0.145±0.02	0.141±0.01
Med-CC	**Control**	0.125±0.03	0.157±0.01
	Alzheimer's	0.135±0.02	0.143±0.01
C	**Control**	0.093±0.02	0.108±0.01
	Alzheimer's	0.103±0.01	0.108±0.01
MC	**Control**	0.091±0.01	0.120±0.01
	Alzheimer's	0.102±0.02	0.113±0.01
CPu	**Control**	0.098±0.02	0.111±0.01
	Alzheimer's	0.108±0.01	0.111±0.01
Th	**Control**	0.096±0.02	0.129±0.01
	Alzheimer's	0.113±0.02	0.113±0.01
Hc	**Control**	0.106±0.02	0.117±0.01
	Alzheimer's	0.095±0.02	0.11±0.01

Supplementary Table 3.3. *Mean (m) values ± Standard deviation (SD) for the different parameters studied at different regions of the brain in the PS19 mouse. (All values are presented as m±SD, shadowed values indicate significant differences with p<0.05*).

Region		10^3 T2 (a.u.)	10^3 T1 (a.u.)	T1w/T2w (a.u.)	10^3 SWI (a.u.)	MTR (%)	FA	10^{-3} AD (mm^2s^{-1})	10^{-3} MD (mm^2s^{-1})	10^{-3} RD (mm^2s^{-1})
med-CC	**C**	8.59±0.32	10.5±0.11	1.69±0.09	11.7±0.5	30.2±1.6	0.52±0.02	1.08±0.02	0.66±0.02	0.45±0.02
	β	8.57±0.50	10.5±0.21	1.66±0.10	11.2±0.4	29.2±0.8	0.50±0.02	1.08±0.06	0.68±0.04	0.48±0.03
Lat-CC	**C**	7.42±0.15	10.0±0.13	1.77±0.06	10.4±0.8	30.1±1.8	0.42±0.02	0.88±0.02	0.59±0.01	0.44±0.01
	β	7.50±0.18	10.1±0.14	1.75±0.08	11.0±0.2	29.5±0.6	0.42±0.01	0.88±0.01	0.60±0.01	0.46±0.02
CP	**C**	8.85±0.19	9.77±0.29	1.39±0.10	10.4±0.8	29.9±1.8	0.25±0.02	0.71±0.03	0.55±0.01	0.48±0.01
	β	8.58±0.10	9.99±0.23	1.43±0.04	10.5±0.5	29.9±0.3	0.28±0.03	0.75±0.03	0.57±0.01	0.48±0.00
C	**C**	11.7±0.11	11.7±0.10	1.26±0.06	11.0±0.8	28.6±2.1	0.14±0.00	0.67±0.01	0.59±0.01	0.55±0.01
	β	11.6±0.15	11.6±0.11	1.25±0.03	10.6±0.4	28.5±0.8	0.15±0.01	0.69±0.02	0.60±0.02	0.55±0.01
CPu	**C**	9.99±0.27	10.6±0.17	1.33±0.07	12.4±0.4	27.9±1.9	0.13±0.00	0.66±0.01	0.58±0.01	0.54±0.01
	β	9.78±0.14	10.5±0.08	1.32±0.04	11.8±0.1	28.2±0.7	0.15±0.01	0.69±0.01	0.60±0.01	0.55±0.01
HC	**C**	11.9±0.12	11.2±0.04	1.20±0.05	13.30.3	27.7±1.6	0.16±0.02	0.74±0.02	0.64±0.01	0.58±0.01
	β	12.0±0.17	11.3±0.07	1.18±0.04	13.8±0.2	26.6±0.8	0.16±0.01	0.76±0.02	0.65±0.02	0.60±0.02
Hyth	**C**	9.70±0.19	9.65±0.27	1.26±0.06	10.1±0.6	26.5±1.9	0.23±0.02	0.76±0.02	0.61±0.01	0.53±0.01
	β	9.86±11	9.80±0.15	1.23±0.02	11.0±0.4	27.2±1.4	0.21±0.01	0.76±0.02	0.62±0.01	0.55±0.00
MC	**C**	10.8±0.37	9.94±0.52	1.20±0.05	10.3±0.5	27.6±2.5	0.14±0.00	0.61±0.02	0.53±0.02	0.49±0.02
	β	10.3±0.09	9.76±0.19	1.20±0.04	10.2±0.5	27.7±0.6	0.17±0.01	0.67±0.01	0.57±0.01	0.52±0.01
Th	**C**	9.51±11	11.0±0.05	1.45±0.08	13.4±0.2	29.7±2.1	0.23±0.01	0.74±0.02	0.60±0.01	0.52±0.01
	β	9.52±0.05	11.0±0.13	1.42±0.04	12.8±0.3	30.1±1.1	0.24±0.02	0.77±0.03	0.61±0.01	0.53±0.01

Chapter 4

Longitudinal resting-state fMRI study of functional alterations during demyelination and spontaneous vs. clemastine enhanced remyelination in the cuprizone murine model

A. Egimendia *et al.* (Submitted)

1. Foreword

In the previous chapters the development of imaging strategies for the evaluation of myelin content along with the characterization of animal models of multiple sclerosis and Alzheimer‘s disease at an anatomical level have been accomplished. Although the recovery of lost myelin should be a priority for remyelinating therapies, it is clear that any potential therapeutic approach should aim to a functional recovery of the brain. In other words, a recovery of damage of anatomical structures might not ensure that affected functions could be recovered. In this chapter, the impact of myelin pathology at a functional level will be described by means of resting-state fMRI (rs-fMRI), further used to compare the processes of spontaneous vs. clemastine enhanced remyelination processes at a functional level.

Additionally, we do consider that the evaluation of a remyelination therapy, such as clemastine, in the cuprizone model by means of the established procedures for the assessment of myelin content would add evidence to the suitability of this approach. In this way a major priority would be accomplished, contributing to the development of remyelination therapies and providing further insight about the importance of these processes.

1. Introduction

Multiple sclerosis (MS) is a chronic demyelinating autoimmune disease of the central nervous system (CNS) characterized by the reaction of the immune system against myelin sheaths, resulting in the altered transmission of the electrical signal and in axonal loss. Although currently approved immune modulating therapies have shown to be effective in preventing the immune attacks, the disability of MS patients still increases in the progressive phase of the disease [50], and further actions are required to treat this condition. In this sense, remyelination, defined as the restoration of myelin sheaths conducted by myelinating oligodendrocytes, enables the functional recovery of neurons and may contribute to enhance the remission of clinical symptoms. However, even though migration of oligodendrocyte precursor cells (OPCs) into the lesion site has been reported in multiple sclerosis patients [39], [410], [411], spontaneous remyelination is frequently incomplete or absent, especially in advanced stages of the disease [412].

Hence, the therapeutic enhancement of remyelination has become a promising approach during the last decade [26]. Therapeutics such as the clemastine, a first generation antihistaminic, have shown efficacy in promoting OPC differentiation *in vitro* [147] and in stimulating remyelination in animal models, through the M1 muscarinic receptor [34], [144], [145]. Moreover, clemastine has also shown the capacity to shorten the P100 latency delay in visual evoked potentials in chronic demyelinating optic neuropathy in human patients [51].

Although the mechanisms underlying both demyelination and remyelination have been widely characterized in literature, their implications at a functional level, in particular in relation to alteration of brain connectivity, have not been fully assessed so far. Resting-state functional magnetic resonance imaging (rs-fMRI) focuses on

spontaneous low frequency brain fluctuations of the brain blood oxygen level dependent (BOLD) signal that occurs during resting conditions [330]. Anatomically organized resting-state networks (RSN) have been described across species and confirmed through several techniques such as optical imaging [413], positron emission tomography [414] or electroencephalography [415]. Moreover, this technique has revealed functional connectivity abnormalities in many different mouse models of disease [186], [310], [334].

In this sense, the characterization of the alteration of functional networks associated with demyelination and remyelination processes by means of rs-fMRI may represent an invaluable tool for the development of novel therapies against the disease. Thus, the aim of this study is to longitudinally study demyelination and remyelination phenomena, in terms of functional connectivity of the brain, and to establish whether rs-fMRI is capable to evaluate the potential therapeutic effects of clemastine, in the cuprizone mouse model of MS.

2. Materials and methods

2.1. Animals and experimental protocol

Animal experiments were performed in our Association for the Assessment and Accreditation of Laboratory Animal Care International (AAALAC) accredited animal facilities, and all animal procedures were approved by our Institutional Animal Care and Use Committee (IACUC), and local authorities (Diputación Foral de Gipuzkoa, Spain, Project N. PRO-AE-SS-127).

Toxic-induced mouse model of MS was used consisting on the use of the copper-chelating neurotoxicant cuprizone (N,N′-bis(cyclohexylideneamino)oxamide), which is one of the most widely used to study demyelination and remyelination in the

mouse [164]. Briefly, demyelination is triggered as a consequence of oligodendrocyte death, caused by the toxic, resulting in extensive demyelination mostly at the level of the corpus callosum (CC) and the cerebellum of the mouse brain, reaching maximal demyelination after 5 weeks of exposure to the toxic [196]. One of the main advantages of this model is that demyelination is reversible, and remyelination spontaneously takes place during the following weeks, after ceasing exposure to the toxic

Upon arrival at our facilities, mice were acclimated to their new environment for ten days prior to the first manipulation. *Ad libitum* access to standard food pellets and autoclaved tap water was provided to the animals under a controlled light environment (12/12 h light/dark cycle) in SPF rooms. Eighteen C57BL/6J male mice (n=18) of eight weeks of age (Charles River Laboratories, Barcelona, Spain) were used for this study. No single animal died spontaneously or by consequence of manipulation, and no one has to be sacrificed by the application of humanitarian endpoints. At the beginning of the study (week 0), the diet of twelve mice (n=12) was switched to 0.2% (w/w) cuprizone-doped food pellets (Envigo TD.140800, Envigo Research Model Services, Barcelona, Spain), for a period of 5 weeks. Food was replaced every 3 days and animals were weighed on a weekly basis. At week (W) 5, the diet was switched back to a standard one until the end of the study (week 10). In parallel, 6 control animals (n=6) received the standard diet during the 10 weeks study period. Half of the animals (n=6) submitted to cuprizone diet received a 10 mg/kg/day dose of clemastine (ID. SML0445, Sigma-Aldrich, St Luis, MO, USA) diluted in water containing 0.25% DMSO (ID. M81802, Sigma-Aldrich, St Luis, MO, USA) by oral gavage during 14 days, starting at week 5 of the study (same day of interruption of cuprizone diet). Mice that did not receive clemastine, were administered with water containing 0.25% of DMSO (oral gavage) as a control

group. The decision about the dose, the frequency and duration of this treatment (daily dose of 10 mg/kg for 2 weeks) was based on previous literature [145]. A schematic representation of the experimental design is presented in Fig. 4.1.

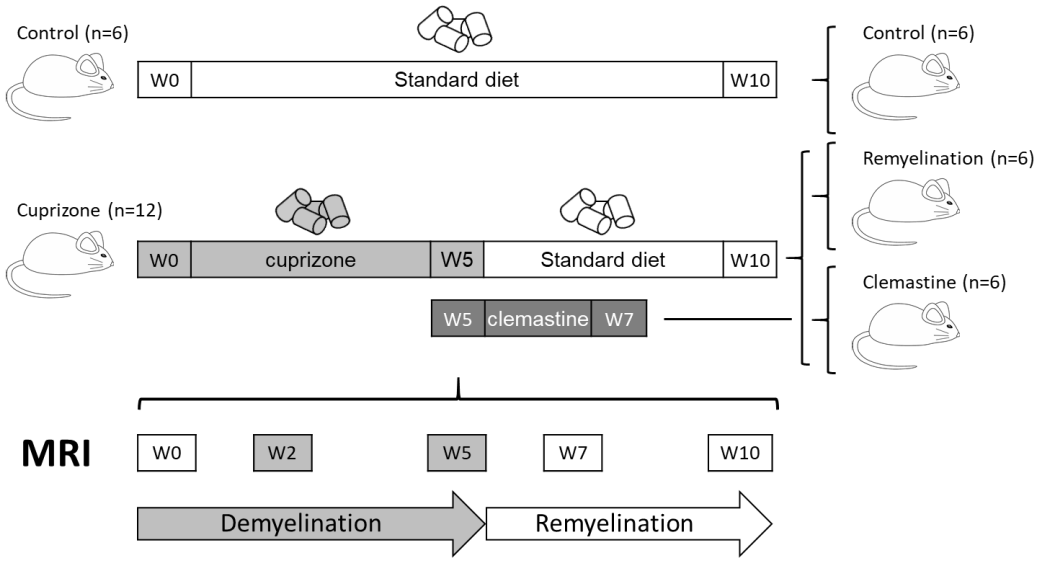

Figure 4.1. *Experimental design of the study. Twelve mice (n=12) were treated with cuprizone in the diet (0.2 % w/w) for 5 weeks. Next, the diet was switched to a standard one, splitting this group in 2: Clemastine treated group (n=6) using a 10 mg/kg daily dose from W5 to W7, and spontaneous recovery group (n=6). Control mice were fed with a standard diet throughout the whole study period. Functional and T2w anatomical imaging studies were conducted at weeks 0, 2, 5, 7 and 10*

2.1. MRI

MRI measurements were performed on an 11.7 Tesla horizontal bore Biospec 117/16 USR scanner (Bruker, Ettlingen, Germany), using ^{1}H mouse brain surface coil for reception and a volumetric coil for transmission. Animals were scanned

prior to (W0), and at weeks 2 (W2) and 5 (W5), after exposure to cuprizone. Afterwards, remyelination and potential effects of clemastine were evaluated by scanning the mice at week 7 (W7) and week 10 (W10). (i.e., 2 and 5 weeks after withdrawal from cuprizone).

T2-weighted (T2w) high-resolution anatomical imaging was conducted under isoflurane anaesthesia (3.5% for induction, ~2% for maintenance) in a gas mixture of N_2/O_2 (70/30) at 1-1.5 l/min. A TurboRARE sequence was acquired covering the full brain with the following parameters: repetition time, TR=5550 ms; RARE = 8; effective echo time TE=26 ms; FOV =17.5 mm x 17.5 mm; Image matrix 175 x 175; 48 slices with a thickness of 0.3 mm without a gap.

For fMRI studies, anaesthesia was induced with 3.5% isoflurane and was kept at 1.5-1.8% for maintenance. A single bolus of 0.06 mg/kg dexmedetomidine (Dexdomitor, Elanco-Lilly, Madrid, Spain) suspended in 250 µl of NaCl was subcutaneously administered 15-20 minutes before functional imaging acquisition, followed by a decrease of isoflurane levels to 0-0.5% within the following 5 minutes, with continuous adjustments to maintain respiration rate of the animals at 100-120 breaths per minute during the whole functional imaging data acquisition.

During fMRI sessions, an anatomical T2-weighted image was acquired for image registration purposes, with the same geometrical parameters (same coordinates origin, spatial resolution and slice orientation, thickness and gap) as functional imaging sets. Imaging parameters were: RARE sequence with a RARE factor of 8, TR =2500 ms; Effective echo time =30 ms; FOV = 17.5 mm x 17.5 mm; image matrix = 96 x 96; 9 slices of 0.5 mm thickness with 0.1 mm inter-slice gap (covering a total length of 5.3 mm).

For functional imaging, a 2D multi-slice gradient echo-planar imaging (GE-EPI)

protocol (adapted from (Grandjean et al., 2014)) was used with the following parameters: TR/TE=2840 ms/13 ms; FOV = 17.5 mm x 17.5 mm; image matrix = 96 x 96; 9 slices of 0.5 mm with 0.1 mm inter-slice gap; Number of repetitions n= 115 (for a total scanning time of 5 min 26 s). After finishing functional imaging sessions animals were recovered, reverting dexmedetomidine by an i.p. injection of 1mg/kg Atipamezol (Antisedan, Pfizer, Madrid, Spain), suspended in 100 mL of NaCl.

2.2. Image analysis

Processing of anatomical and functional NIFTI [416] images was performed with FSL [FMRIB (Oxford Centre for Functional MRI of the Brain) Software Library; http://www.fmrib.ox.ac.uk/fsl, (Jenkinson et al., 2002; Smith, 2002)]. Single-session probabilistic Independent Component Analysis (pICA) was conducted using Melodic interface of FSL (http://fsl.fmrib.ox.ac.uk/fsl/fslwiki/MELODIC), including motion correction (MCFLIRT) and high-pass temporal filtering (< 0.01 Hz). Independent components were classified following the approach put forward by Griffanti and colleagues [417]. After the regression of noise components, group Independent component analysis was performed with MELODIC, applying a 0.3 mm full-width half maximum (FWHM) Gaussian kernel for smoothing [418]. Functional images were first registered to anatomical images and then to the publicly available AMBMC (Australian Mouse Brain Mapping Consortium, http://www.imaging.org.au /AMBMC/) C57BL/6J mouse atlas. Spatial maps generated from the group ICA were thoroughly inspected to select networks of interest based on previous studies [330], [336].

Concerning group-spatial maps, dual regression was used to generate subject-specific versions of the spatial maps and associated time series. [419], [420]. Finally, FSL's randomize permutation-testing tool was used to look for group differences

and significant networks, at $p<0.001$ corrected p values. For group comparisons, the threshold of the corrected p-value was set at $p<0.05$.

Simultaneously, 13 regions of interest (ROIs) were extracted from the anatomical atlas and grouped in three main networks: 1) The Cortical Network (CN), encompassing the primary (M1) and secondary (M2) motor cortex and the primary (S1) and secondary (S2) somatosensory cortex. 2) The Subcortical Network (SN), involving the thalamus (Th) and the caudate putamen (CPu). 3) The Default Mode Network (DMN), composed by the prelimbic cingulate (Cg), the piriform cortex (Pir), the rostral dorsal prelimbic cortex (PrL), the retrosplenial granular and dysgranular cortex (RSG/RSD), the hypothalamus (Hyth), dentate gyrus of the hippocampus (Hc/dg) and the hippocampal commissure (Hc). All these regions were selected separately in each of the brain hemispheres (we have used prefix "l" for left and "r" for right hemispheres, when presenting results of each ROI). To facilitate interpretation of results, regions involved in the DMN and the hippocampus have been grouped (grouping the Hc and the Hc/dg), which has shown to be altered in the cuprizone model [186]. Particular attention has also been set for the cortico-thalamic network, due to its importance in sensory processing, comprising interactions between the thalamus and cortical regions [421].

Finally, Seed-based Correlation analysis was conducted. Group level full correlation analysis was carried out between pairs of ROIs with a personalized version of FSLNets (v0.6; www.fmrib.ox.ac.uk/fsl). Correlation matrices were constructed with a customized script.

T2w anatomical images have been used to compare myelin content between groups. Global intensity normalization (mean=10000) of skull stripped high-resolution anatomical images were performed and signal intensity values were measured in

the medial corpus callosum (med-CC) of the brain, where demyelination is more evident in cuprizone exposed mice [196]. To avoid user-dependent ROI selection biases, high resolution anatomical images were registered to a down-sampled anatomical atlas, and the CC region was automatically extracted.

2.3. Statistical analysis

Graphpad/Prism (Graphpad Software, San Diego, CA, USA) and Biovinci (BioTuring Inc., San Diego, CA, USA) software were used for statistical analyses. For functional data, all the cross-correlations involved in each of the studied networks were averaged and the total standard deviation was calculated, assuming the independence of each interaction within each mouse. Both for functional and anatomical data D'agostino-Pearson normality test was performed to assess the distribution of data. When data were normally distributed for all groups, a two-tailed unpaired t-test was performed. Otherwise, groups were tested with the non-parametric Mann-Whitney test.

For statistical significance we need to consider that despite groups are formed by n=6 animals, the analyzed networks contain a much higher number of experimental units. For the calculation of the mean±SD values of z-score of a particular network, this number of n=6 has to be multiplied by the number of individual interactions between pairs of ROIs that form part of the considered network (each interaction has its own z-score value and is an experimental unit). Thus the number of experimental units for the comparison of z-scores of the Default Mode Network is n_{eu}=6x91=546, being 6 the number of animals and 91 the number of interactions between regions of interest forming part of the DMN for each animal (91 z-scores for each animal), for the thalamic interactions n_{eu}=6x25=150, the same as for

hypothalamic interactions (n_{eu}=6x25=150), for thalamocortical interactions n_{eu}=6x16=96 and for homotopic interactions n_{eu}=6x13=78.

Using the software G*Power3.1.9.2 (University Düsseldorf) we have calculated the minimum effect size or Cohen's d value required to achieve a value of α=0.05 and (1-β)=0.95 in a one-tail t-test with two samples of independent means and equal size, resulting in (d≥0.2) for n=546, (d≥0.381) for n=150, (d≥0.477) for n=96 and (d≥0.53) and for n=78 experimental units per group, respectively.

Now, using the equation of Cohen's d value, given by:

$$(Cohen's)d = \frac{M_2 - M_1}{\sqrt{\left({SD_1}^2 + {SD_2}^2\right)/2}}$$

Where M_1 and M_2 are the mean values of the variable for groups 1 and 2 and SD_1 andSD_2 are their standard deviations, and considering that SD_1 = SD_2 = 0.5 M_1 (i.e. that SD is the same for both groups and equal the 50% of the mean of group 1, which is in the order of magnitude of those values observed in our experiments and others reported in literature), and expressing M_2 as a percentage of change from M_1 (i.e. M_2 = (1+x) M_1, or M_2 is M_1 incremented by a 100 x %) the equation simplifies to:

$$x \geq d/2$$

Under these plausible conditions for our experimental design and setup, changes equal or higher to 10% in the mean z-score of the DMN ($x \geq (d_{DMN}/2)=(0.2/2)=0.1$) will be significant at the level of $p<0.05$, using an n=6 animals (546 experimental units). In the same way, changes in mean z-score equal or higher than 19% for thalamic and for hypothalamic interactions, equal or higher than 24% for thalamo-cortical interactions, or equal or higher than 26% for homotopic interactions,

differences will be significant at the level of $p<0.05$, under our experimental design (n=6 animals per group) and under our experimental conditions ($SD_1 \sim SD_2 \sim 0.5$ M_1).

3. Results

3.1. Effects of demyelination and remyelination at an anatomical level

The sustained administration of 0.2% (w/w) cuprizone in the diet to mice induces a loss of myelin that can be visualized as an increase of signal intensity on T2w anatomical MRI images (Fig. 4.2A). In this figure it is noticeable how the contrast between white matter (hypointense on T2w images) and grey matter vanishes upon loss of myelin, concomitant to the poisoning with cuprizone. Such loss of contrast is highly pronounced in large white matter tracts (such as the central section of the corpus callosum, ROI magnified under each brain image in Fig. 4.2A) but it is barely distinguishable by the naked eye on other regions of the brain. Cuprizone withdrawal induces a progressive increase of contrast in these regions, suggesting remyelination (Fig. 4.2).

Fig. 4.2B presents the relative changes on signal intensity on T2w images for the three study groups during the follow-up period, for two different regions of interest (medial corpus callosum and caudate putamen). Demyelination in the med-CC progresses during the administration of cuprizone, peaking at week 5. Thus, compared to controls, these animals present a significant increase in normalized T2w signal intensity (ΔN.T2wSI = 4.1%, $p<0.05$) at the med-cc, after two weeks of exposure to cuprizone. Such difference reaches a value of 12% at week 5, which is maintained until week 7 (ΔN.T2wSI =13.2 %).

Next, the progressive restoration of myelin sheaths in the CC by spontaneous remyelination reduces the difference between these two groups to 9.5% at week 10. Thus, according to T2w MRI, only partial remyelination is observed in this animal model, since values do not reach original levels. Conversely, at the hypothalamus, were no extensive demyelination was expected, no changes were observed on T2w signal intensity all through the study (Fig. 4.2B).

On the same plots, we also present the normalized T2w signal intensity for the group of animals treated with clemastine during the remyelination period, observing a significant reduction of this parameter at week 7 (ΔN.T2wSI = -3.5%, $p<0.05$) respect to the cuprizone group. At this point, the clemastine treated group showed however higher values of signal intensity than the control group (ΔN.T2wSI = 10%, $p<0.05$). Interestingly, at week 10, there was no significant difference in the normalized signal intensity at the med-CC between both groups exposed to cuprizone (spontaneous recovery vs. clemastine treated animals).

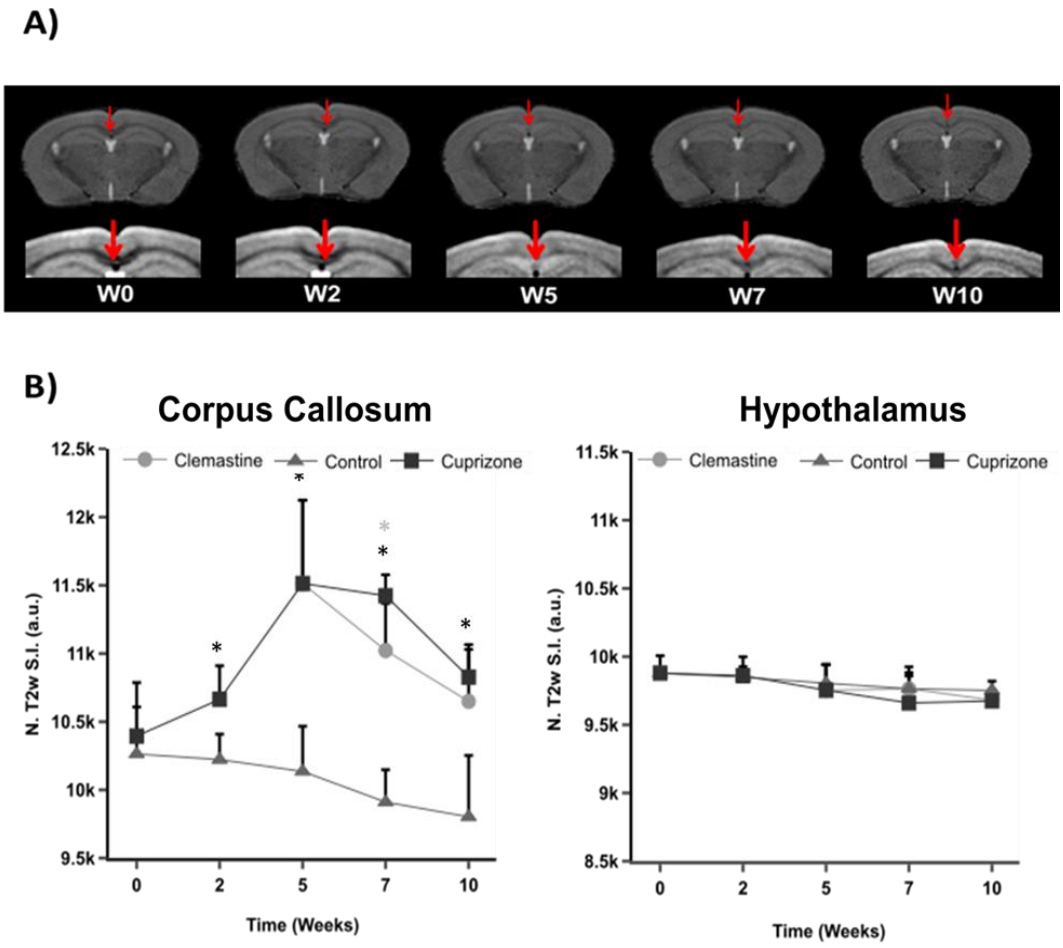

Figure 4.2. *Effects of demyelination-remyelination on T2w signal intensity. Poisoning with cuprizone (demyelination, weeks W0 to W5) induces T2w signal intensity increase in regions with a high density of myelin (such as the corpus callosum), leaving invariant the signal on regions with lower myelin density (such as the hypothalamus). Returning to a standard diet (remyelination, weeks W5 to W10) renormalizes T2w signal to a certain extent.* ***A)*** *Representative MR images of the brain of a mouse at different periods of the study, with a magnification of the central zone of the corpus callosum.* ***B)*** *Quantitative representation of longitudinal changes on signal intensity observed for the three studied groups, at two regions of interest representative of considerable (corpus callosum) and not-significant (hypothalamus) alterations on myelin content (black *: p<0.05 between control and cuprizone, grey *: p<0.05 between Clemastine and cuprizone).*

Signal intensity levels of these two groups were significantly higher than the (healthy) controls (ΔN.T2wSI = 8% for clemastine and 9.5% for cuprizone groups, both at $p<0.05$).

Finally, a trend to lower signal intensity values (higher myelin content) with aging was observed for the med-CC in healthy controls (Fig. 4.2B), with no significant differences from week to week, but with a cumulative effect of 4.5% (not significant at $p<0.05$ level, probably due to the high standard deviations observed) from week 0 to week 10 (8 to 18 weeks of age). No significant variations on signal intensities were observed for controls at the Hyth (grey matter, therefore low myelin content) through the whole study (Fig. 4.2B).

3.2. Cuprizone poisoning alters functional networks

To assess the level of brain activity in the animals, z-score cross-correlations matrices were constructed (Fig. 4.3). In these matrixes, 13 regions of the left (prefix "l", framed in blue) and 13 of the right (prefix "r", framed in red) brain hemispheres were correlated by pairs (see methods section and Fig. 4.3 legend for the list of analyzed regions), generating a total of 325 z-score values (actually 676, but matrixes are symmetric about their diagonal). The strongest correlations seem to correspond to inter- and intra-hemispheric cortical and cortical-subcortical interactions, and between specific regions inside the DMN. Cross-correlation z-score matrixes were constructed for each group of animals at all studied time-points. Fig. 4.4 compares the matrixes for the group cuprizone vs. controls, at weeks W0, W2, W5, W7 and W10, while Fig. 4.5 presents the matrixes for the group cuprizone vs. group clemastine at weeks W7 and W10. (X and Y axes, i.e. ROI legends, are the same as for Fig. 4.4 in all matrixes presented in both figures).

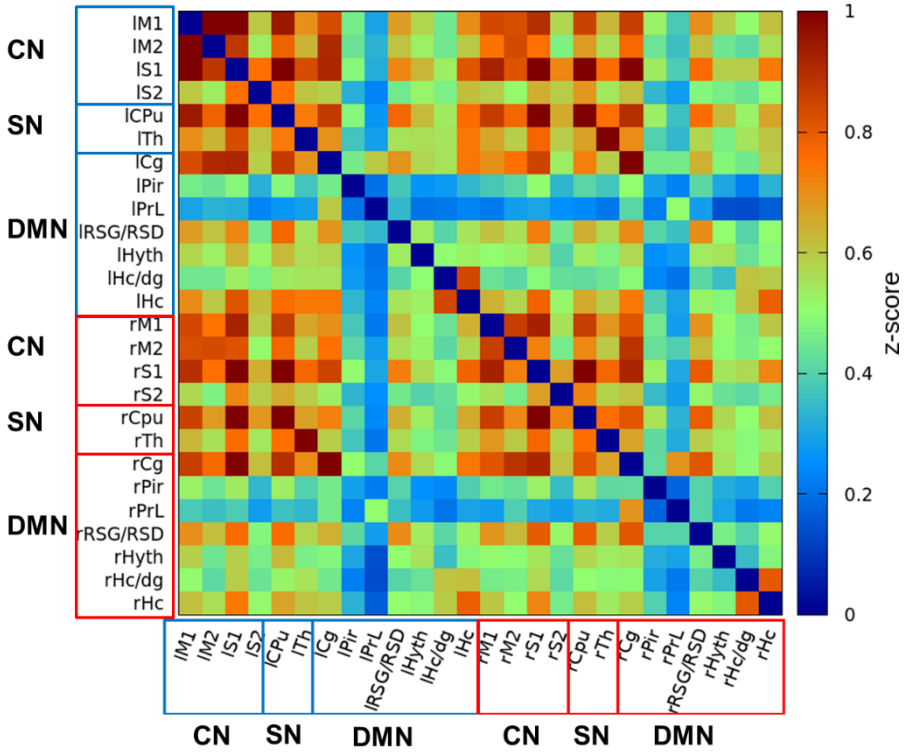

Figure 4.3. *Representative full cross-correlation matrix obtained from the seed-based functional connectivity analysis. Colours represent the degree of correlation (z-scores with a scale bar on the side) observed between multiple pairs of regions of the brain, corresponding to the cortical network (CN), subcortical network (SN) and default mode network (DMN). Analyzed ROIs: (l and r prefixes stand for left and right brain hemispheres) M1, M2 (primary and secondary motor cortex); S1, S2 (primary and secondary somatosensory cortex); Cpu (caudate-putamen); Th (thalamus); Cg (prelimbic cingulate); Pir (piriform cortex); PrL (rostral dorsal prelimbic cortex); RSG/RSD (retrosplenial granular and dysgranular cortex); Hyth (hypothalamus); Hc/dg (dentate gyrus of the hippocampus); Hc (hippocampal commissure).*

Figure 4.4. *On the right page, full cross-correlation matrices of control vs. cuprizone treated animals at the different time-points of the study including periods of demyelination (weeks W2 and W5) and remyelination (weeks W7 and W10). No significant changes were observed between groups prior to starting the treatment (W0). X and Y axes (ROI labels) and colour scale (z-score) are the same as presented in figure 4.3 but obviated here to facilitate visualization.*

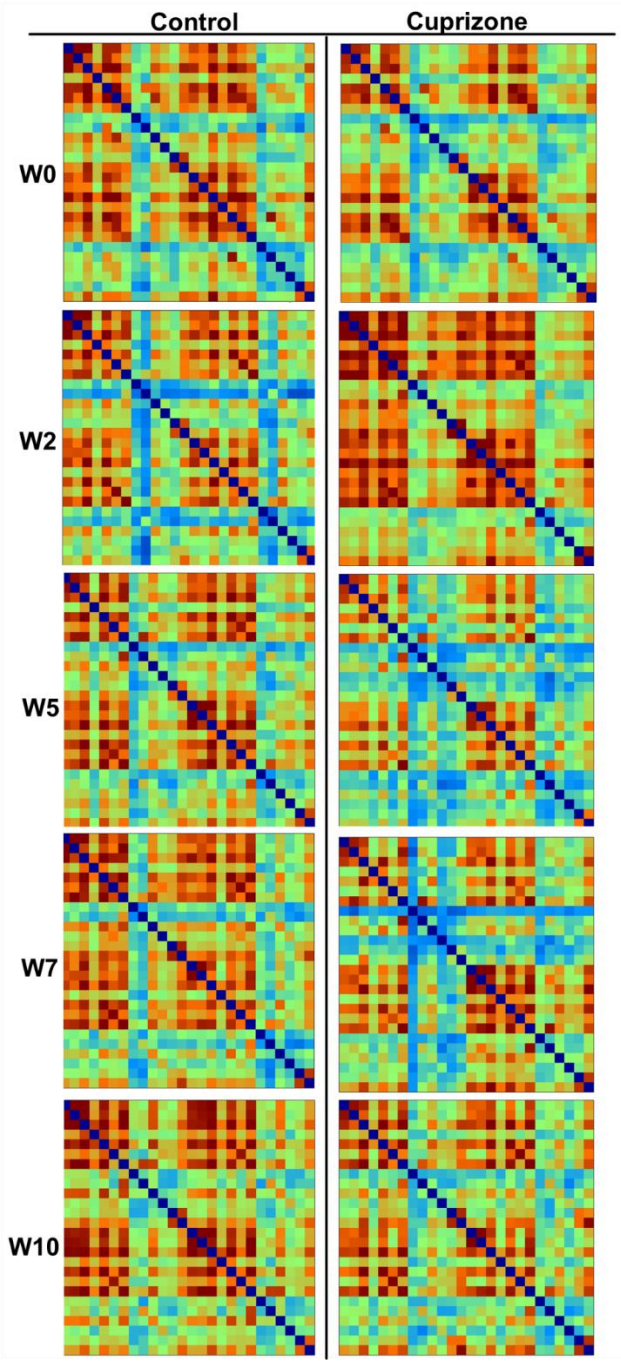
Control
Cuprizone
W0
W2
W5
W7
W10

The analysis of individual correlations from these matrixes could be rather complex, considering the large number of regions of interest included. For this reason, we further processed the data to provide simpler parameters that reflect brain functionality with fewer variables.

Thus, for each set of data presented in Fig. 4.4 and 4.5, we defined; a) the mean functional connectivity (mFC) of all homotopic correlations (e.g. lM1-rM1, lTh-rTh, etc.), b) the mFC of all thalamo-cortical correlations, and c) the mFC of the DMN (Cg, Pir, PrL, RSG/RSD, Hyth, Hc/dg, Hc). Plots of variation with time of these 3 parameters (mFC ± SD) are presented in Fig. 4.6. When this analysis is performed, up to 3 different temporal profile patterns of change in mFC were detected:

1) For the homotopic interactions (h-mFC) no significant differences between controls and cuprizone groups were observed until week 5 (W5), where the cuprizone exposed mice show a reduced strength in homotopic correlations compared to controls (h-mFC: control = 0.76±0.30 vs. cuprizone = 0.65±0.3, $p<0.05$). Such hypoactivity is still significant at week 7 (h-mFC: control = 0.82±0.33 vs. cuprizone = 0.68±0.36, $p<0.05$), but reverted at week 10 of experiment.

2) For thalamo-cortical network (tc-mFC), no significant difference is observed at the beginning of experiment between controls (tc-mFC = 0.70±0.33) and cuprizone treated mice (tc-mFC = 0.65±0.26). The administration of cuprizone for 2 weeks resulted in an increase of connectivity in the thalamo-cortical network compared to control mice (tc-mFC: control = 0.65±0.14 vs. cuprizone = 0.79±0.21, $p<0.05$). This condition is reverted after 5 weeks of administration of cuprizone, were the intoxicated mice exhibited a reduced strength of connectivity in this network (tc-mFC: control = 0.65±0.20 vs.

cuprizone = 0.54±0.22, $p<0.05$). Contrary to the recovery observed for homotopic interactions, the difference between cuprizone exposed and control mice is maintained until the end of the study (tc-mFC: $control_{(W7)}$ = 0.71±0.24 vs. $cuprizone_{(W7)}$ = 0.62±0.21, $p<0.05$; $control_{(W10)}$ = 0.67±0.30 vs. $cuprizone_{(W10)}$ =0.57±0.37, $p<0.05$).

3) The DMN show a similar trend like the thalamo-cortical network until week 5, and then a progressive recovery as the one showed by homotopic interactions. Briefly, no significant difference is observed at the beginning of the experiment between control mice and cuprizone exposed mice (DMN-mFC: control = 0.65±0.20 vs. cuprizone =0.54±0.22, $p<0.05$). At week 2 an increase in DMN connectivity is observed in the cuprizone exposed mice compared to control mice (DMN-mFC: control = 0.44±0.23 vs. cuprizone =0.56±0.28, $p<0.05$).

The exposure to cuprizone for 5 weeks cause a substantial reduction of connectivity of cuprizone exposed mice (DMN-mFC = 0.41±0.25) compared to control group (DMN-mFC = 0.50±0.23). The withdrawal of cuprizone from diet enables a progressive restoration of the DMN. At week 7, cuprizone exposed mice still exhibit reduced connectivity (DMN-mFC: control = 0.51±0.26 vs. cuprizone =0.44±0.26, $p<0.05$) compared to control mice, while at week 10 of study no significant alteration is observed.

In addition, a fast inspection of individual ROIs at the maximum point of demyelination (W5) reveals the highest differences between cuprizone and controls at the level of the Hyth and the Th. Plots of the change of z-score vs. time for these two regions are included in Fig. 4.6. After suffering an increase in connectivity strength at week 2 ($p<0.05$), a decay in correlation was observed in the Hyth (z-

Score: control = 0.53±0.20 vs. cuprizone = 0.36±0.18, Δz-score = 32%, p<0.05) and Th (z-Score: control = 0.64±0.21 vs. cuprizone = 0.48±0.25, Δz-score = 25%, p<0.05) (Fig. 4.6B). For both groups the difference with controls was gradually reduced until week 10 of the experiment, showing still a significant difference at week 7 of the experiment (z-Score: control = 0.66±0.26 vs. cuprizone = 0.56±0.25, p<0.05).

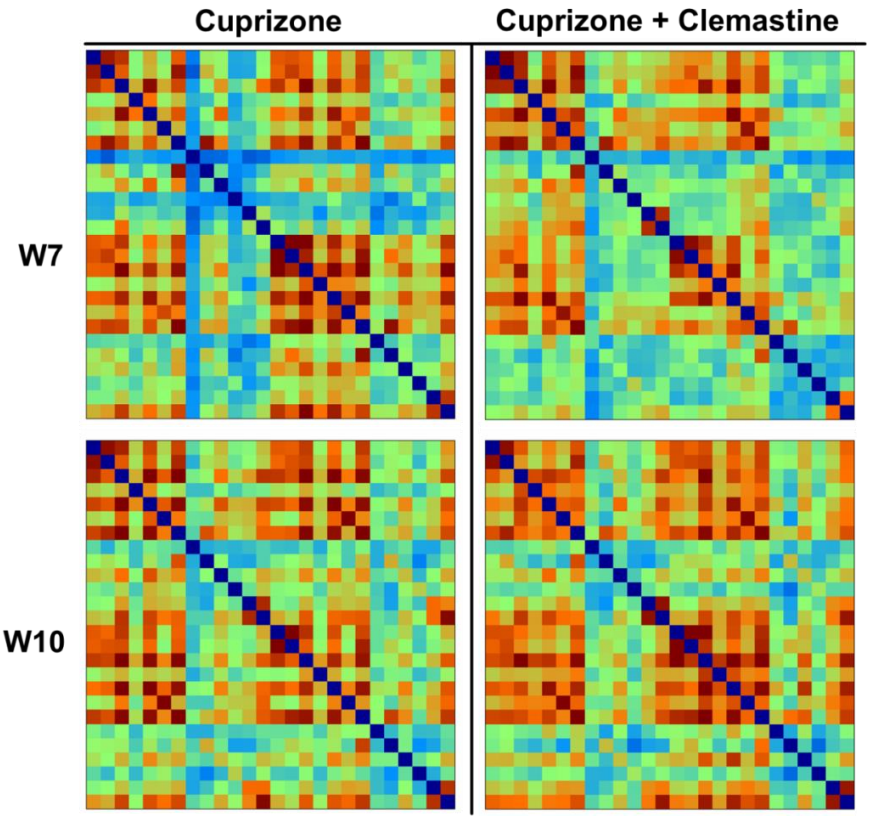

Figure 4.5. *Full cross-correlation matrices showing changes on functional patterns of mice during remyelination (weeks W7 and W10) of cuprizone poisoned mice and untreated (spontaneous recovery) vs. treated with Clemastine form weeks W5 to W7. X and Y axes (ROI labels) and colour scale (z-score) are the same as presented in figure 4.3 but obviated here to facilitate visualization.*

3.3. MRI is sensitive to clemastine enhanced remyelination

The administration of clemastine enabled the recovery of the thalamo-cortical network in intoxicated mice, which unlike the homotopic interactions and the DMN, was not spontaneously recovered after the retrieval of cuprizone. The treatment of clemastine lead to an increase of the connectivity of the thalamo-cortical network, both at week 7 (z-score, clemastine = 0.73±0.26; cuprizone =0.62±0.21) and at week 10 of study (z-score, clemastine = 0.68±0.22; cuprizone =0.57±0.37) (Fig. 4.6A). Concerning homotopic interactions and DMN, no significant differences were found between both groups all along the study.

With respect to the administration of clemastine, the recovery of the mice back to a healthy pattern was accelerated, especially in the most affected regions. Two weeks after the withdrawal of cuprizone from diet (W7 of the study), when the cuprizone-exposed mice present a partial remyelination in the main affected regions, clemastine-treated mice showed higher correlation levels at the Th (z-score at clemastine-treated = 0.69±0.25, at W2= 0.56±0.25, ΔmFC=19%, $p<0.05$) and Hyth (z-score at W0 = 0.46±0.24, at W2= 0.40±0.23, ΔmFC=13%, $p<0.05$), compared to the untreated cuprizone-exposed group. Importantly, these were the regions highly altered by cuprizone exposure at the maximum point of demyelination (week 5). Once the remyelination is completed after 5 weeks of the withdrawal from cuprizone, the connectivity of clemastine-treated and non-treated groups was notably similar (Fig. 4.6).

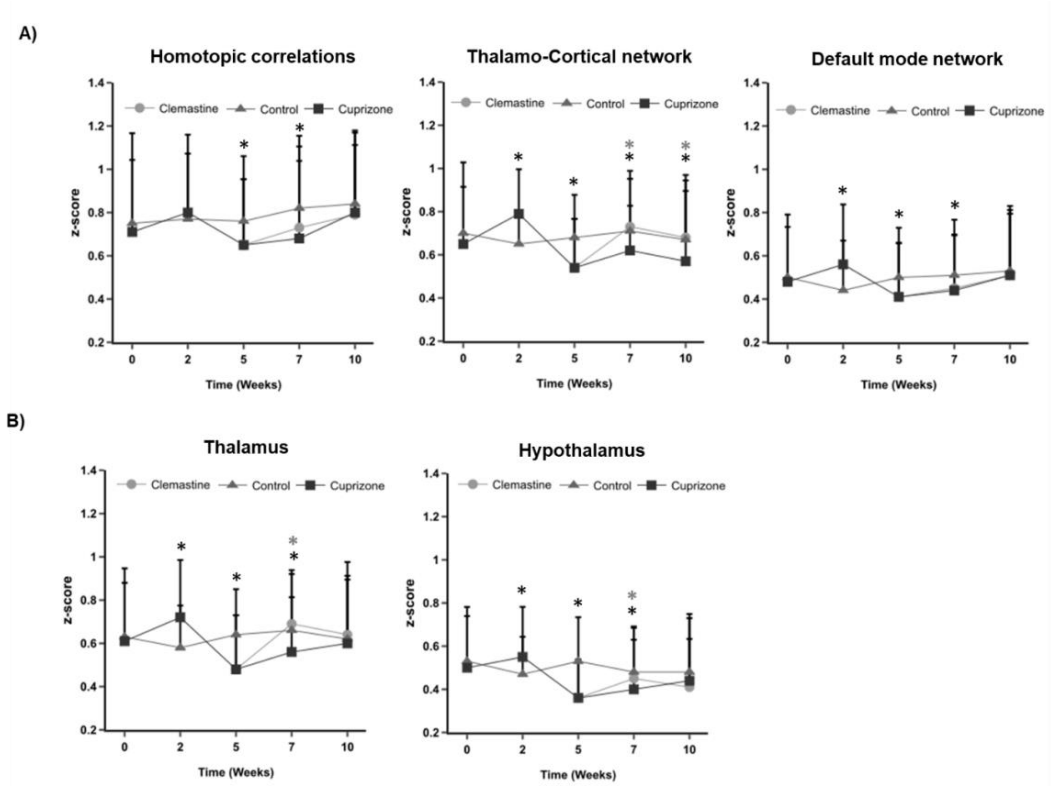

Figure 4.6. *Plots of the average z-scores (mean ± SD) over time for control, cuprizone exposed and clemastine treated mice.* ***A)*** *Homotopic (left vs. right) correlations, thalamo-cortical network and default mode network.* ***B)*** *Thalamus and hypothalamus. "For different ROIs, as indicated in the title of each plot". (black *: p<0.05 between control and cuprizone, grey *: p<0.05 between Clemastine and cuprizone).*

3.4. Functional networks of the brain

In the previous sections, an analysis of brain activity was reported on the base of interactions between *ad hoc* selected regions of interest (seed-based analysis). Alternatively, we also performed a (seed-free) group Independent Component Analysis (gICA) of each group of animals at each time point of the study. The

performance of this approach leads to functional maps of the brain, describing different active regions for each group of animals. In figure 4.7 we present a representative output of the analysis (with a level of significance of $p<0.001$) for one group of animals at one specific time point. Detected active regions corresponded to clearly identifiable components (at both brain hemispheres) of the SN, CN and DMN networks (Fig. 4.7).

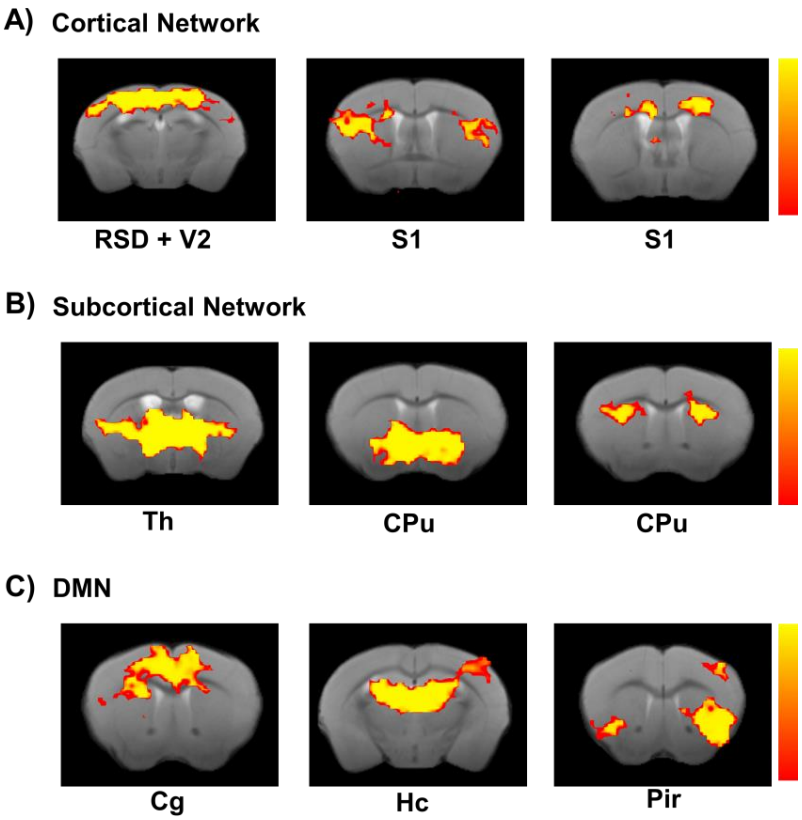

Figure 4.7. *Representative functional hubs derived from the group Independent Component Analysis (gICA). Regions corresponding to A) cortical networks, B) subcortical network and C) default mode network are represented. Significance of each pixel for each network on the dual regression analysis is represented overlaid in colour, from red ($p<0.05$) to yellow ($p<0.001$).*

Functional connectivity analysis revealed higher connectivity in control mice in the motor cortex (specifically at the M2 region) comparing to cuprizone treated groups after 5 weeks of exposure to cuprizone ($p<0.05$) (Fig. 4.8A). In fact, if we compare anatomical T2w images of mice at this time point (Fig. 4.8B), we could observe a change in contrast on the fibres of the motor area. However, the mean of the signal intensity for these two groups was not significantly different at $p<0.05$ level (normalized mean signal intensity: control = 17847±506 vs. cuprizone = 18006±330). gICA analysis showed no other significant differences between groups and any other time point.

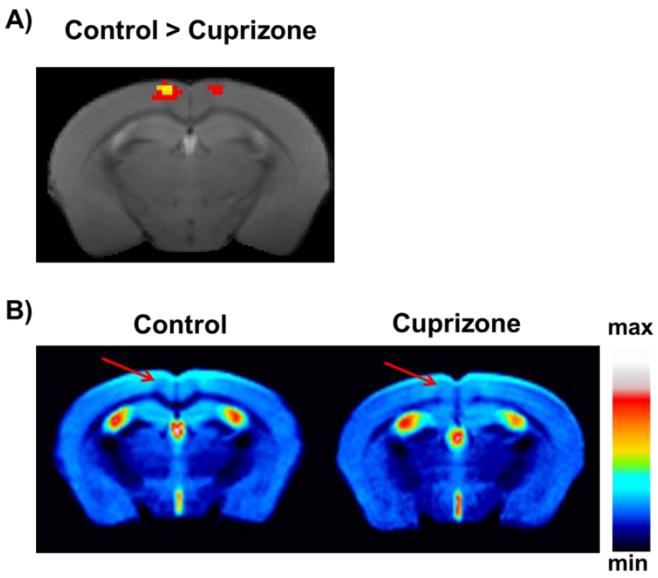

Figure 4.8. *Group-level comparison by means of dual-regression of cuprizone treated vs. control mice.* ***A)*** *At week W5, control mice show a significantly higher activation at the secondary motor cortex (in both hemispheres), compared to cuprizone treated mice. Colour overlay indicates the significance level from red ($p<0.4$) to yellow ($p<0.05$).* ***B)*** *Colour-coded (with scale bar in arbitrary units) T2w MRI images of two animals showing lower signal intensity (representative of higher myelin content) on the M2 region (arrow) for the control group respect to the cuprizone treated animals.*

4. Discussion

4.1. Demyelination effects on functional connectivity

Myelin-related disorders include an important amount of neurological pathologies that range from rare genetic conditions to common demyelinating diseases, such as multiple sclerosis [422]. Myelin loss *per se* results in alteration of electrical conduction along affected axons, whose accumulated effects result on axonal dysfunction and loss, and on clinical deficits and functional disability. Concurrently, and in response to most demyelinating conditions, remyelination, the regenerative process by which myelin sheaths are restored, takes place in a spontaneous manner [423].

However, the potential extension of the damage together with the fact that pathological conditions and aging may affect the capacity of individuals to repair myelin has triggered a growing interest in therapeutic approaches to enhance remyelination for the treatment of demyelinating conditions [423].

In this sense, the use of animal models of de- and re-myelination, such as the cuprizone murine model, [424] is boosting our understanding of these processes, and represents a highly valuable tool for the development of remyelinating therapies.

Though an important body of research has been published about the molecular [425], anatomical [426], metabolic [427] and behavioral changes [428] associated to the loss of myelin in mice intoxicated with cuprizone, the use of functional imaging techniques to characterize how neuronal networks and brain function are altered during the processes of de- and remyelination are very scarce for this model. In fact, to our knowledge, there is only one work that has used functional MRI to study

alterations of functional networks in cuprizone treated mice [186]. In this work, Hübner *et al.* perform an extensive study of the whole brain functional and structural connectivity of mice at a chronic state of demyelination (chronic exposition to cuprizone), demonstrating the capacity of resting-state fMRI studies to provide invaluable information about the effects of demyelination on the brain, at a functional level.

In this work, we have applied resting-state functional MR imaging (rs-fMRI) to further deep into the knowledge of the functional changes associated to cuprizone intoxication in the murine model, including not chronic, but acute changes in brain connectivity that include periods of demyelination and spontaneous remyelination (after withdrawal from the toxicant). Thus, our study has been designed in a longitudinal manner, including up to 5 rs-fMRI sessions per animal within 10 weeks (5 weeks of demyelination and 5 weeks of remyelination), to provide information about the fast and partially reversible functional reorganization of brain networks associated with the loss and regain of myelin, complementing previous findings on this model by Hübner *et al.*

Furthermore, we aimed to study if the use of established therapeutics that promote remyelination, such as clemastine [144], have an impact on brain functional reorganization during the remyelinating processes, in comparison to animals that undergo a spontaneous recovery from the demyelinating insult.

In this sense, our results confirm the existence of significant changes in the mouse brain, both at anatomical and functional level, concomitant to the processes of demyelination and remyelination in the murine cuprizone model of multiple sclerosis. At an early stage (week 2 after cuprizone exposure), while demyelination progresses in the brain of intoxicated animals (as revealed by anatomical T2w MRI),

a state of increased functional connectivity (hyperactivity) is detected for these animals respect to healthy controls as revealed by Fig. 4.4. This phenomenon has already been described for several neurological pathologies or conditions, including multiple sclerosis [429], [430], and both in rodents [431], [432] and humans [335], [433]. Indeed, such hyper-connectivity has been associated with the first state of neurodegenerative diseases [434], [435]. Gorges and colleagues [321] suggest that during the first stage of the disease, a compensatory response (overcompensation) is given, finally yielding in a connectivity and cognitive decline at later stages, when the brain cannot endure further damage. Furthermore, behavioural tests conducted in cuprizone intoxicated mice have revealed hyperactivity and reduced anxiety after three weeks of cuprizone treatment (when still demyelination is not extensive) and motor dysfunction after 5 weeks of treatment, when extensive demyelination is patent [436]. Our results fully support these observations, since the early increase in brain activity is later transformed in a decreased connectivity at week 5, the peak of demyelination in this animal model.

An alternative interpretation of this finding can be provided from a metabolic point of view. At the CNS, myelin provides the insulation required for the fast saltatory conduction of electrical impulse throughout the internodes up to the nodes of Ranvier. In this way, the metabolic requirement of neurons for impulse transmission is minimized since it avoids the continuous regeneration of the action potential [437]. Hence, for demyelinating diseases such as MS, before a total failure to transmit electrical impulses happens in severely affected axons, there is a transient state during which impulse transmission is still feasible but at a cost of high metabolic demand, required by partially denuded axons to function. Such increased metabolic demand could call for higher oxygen and nutrient need, [438], [439] affecting (actually increasing) the BOLD effect, on which functional MRI is based.

Herein the observation of a hyperactive state, before falling into hypoactivation or neuronal networks at more developed stages of demyelination.

While the connectivity at week 2 suffers a global increase for cuprizone treated animals, reflected in an increase of z-scores in practically all the analyzed correlations between pairs of nodes (see Fig. 4.4), at the point of maximal demyelination (week 5). Such an increase is neutralized and actual several correlations suffer a significant drop in z-score respect to healthy controls. This drop is especially noticeable for cross-correlations that involve the thalamus (Th) and the hypothalamus (Hyth), affecting the thalamo-cortical network and the DMN. This result is in total agreement with those reported by Hübner *et al.* for chronic demyelination, [186] confirming that functional alterations on both networks already take place at acute phases of demyelination, and remain permanently if remyelination does not occur (like in the experiment performed by those authors).

Our data also reveals that homotopic correlations (i.e. transcallosal interactions, those taking place between nodes located at different brain hemisphere) are also decreased at week 5. It is logical to consider that the CC might play a key role in this interactions, since it is the largest neural pathway between both hemispheres of the brain [440], enabling the connection between homologous nodes. We (Fig. 4.2) and others [425], [426] have clearly seen a reduction on white matter content at the mid-section of the CC at week 5 post cuprizone. Reduction of homotopic correlations in relation to reduced mid-CC section is not exclusive for this model of MS and they have also been described in schizophrenia [441], where an abnormal CC size has been reported [442]. Interestingly, the cuprizone mouse model has also been put forward as a model for schizophrenia since it mimics some of its symptoms, including spatial working memory and social interaction [443], [444].

Further functional alterations associated with cuprizone triggered demyelination have been revealed in our group Independent Component Analysis, which shows a higher level of functionality at the secondary motor cortex (M2) in control mice, compared to cuprizone exposed mice, as reported by other authors [428], [436], [445].

4.2. Spontaneous remyelination effects on functional connectivity

The withdrawal of cuprizone from the diet led to a progressive increase of functional connectivity of poisoned mice towards normal values observed in healthy controls, showing a complete recovery of brain function at week 10 (5 weeks post withdrawal), with no significant differences between controls and cuprizone treated mice. This result suggests that spontaneous remyelination, reflected in a partial renormalization of T2w signal in MRI images (Fig. 4.1), might be a plausible explanation for the return to normal functional patterns in the brain of intoxicated animals, as it happens in other animal models [446], [447]. Regardless of the role that myelin plays, providing insulation and promoting fast impulse propagation [35], oligodendrocyte proliferation and the remyelination carried out by them can allow the trophic support of this cells to the axon [448], which might also benefit functional recovery. The recovery of brain function is not immediate to the withdrawal of cuprizone, but progressive over time, since we observed that at week 7 of the study (week 2 after withdrawal from cuprizone) the mean cross-correlation values of cross-correlations involving the most affected nuclei, i.e. Th and the Hyth, are still lower for cuprizone treated mice, respect to the healthy controls. These rules out the possibility that cuprizone ingestion is, *per se,* the origin of alterations observed in the connectivity of the brain (sudden recovery after withdrawal would be expected in this case).

Taking overall all the results for the whole studied period (demyelination + remyelination periods) it is interesting to notice that up to 3 different patterns of changes in functional connectivity have been detected, depending on the type of interactions considered for analysis (see Fig. 4.6). Looking at homotopic interactions, still, normal activity is detected at week W2 (no hyperactivity), dropping to abnormally reduced levels of activity at week W5 (peak of demyelination). Significantly reduced levels of activity are still detected at week W7, when spontaneous remyelination has been occurring for already 2 weeks, and only revert to normal levels of activity at week W10. The third pattern of network reorganization has been detected for the thalamo-cortical network that shows hyperactivity at week 2 and reduced activity at week 5 for cuprizone treated mice, but functional deficits are maintained through the duration of the whole study, never reaching normal values despite spontaneous remyelination takes place. This result is actually very interesting because is in total agreement with the observations of Hübner et al. that find that the thalamo-cortical networks is one of the affected ones after chronic demyelination induced by prolonged exposition to cuprizone [186]. Finally, for the default mode network (DMN) the pattern is very similar to the one observed for the thalamo-cortical network, except for the fact that in this case, normal levels of activity are detected at week 10.

The importance of this finding, reporting up to 3 different patterns of functional networks reorganization over time, is that it may explain the differences and discrepancies observed in the studies of behavioural tests performed in cuprizone treated mice, reported in the literature (see [449], for a recent review on the subject). The different nature of the different behavioural tests implies that they may be focusing on the use of particular networks, and therefore one could expect different behaviour of animals during the demyelination and remyelination periods,

depending on the characteristic network reorganization pattern that corresponds.

4.3. Clemastine enhances remyelination and functional recovery

Clemastine, a widely available H1-antihistamine that targets the M1 muscarinic receptor, is claimed to be one of the most robustly validated compounds with remyelinating capacity, whose effects have been demonstrated in multiple independent laboratories, with a wide variety of *in vitro* and *in vivo* models [450]. This compound has previously shown to promote behavioural recovery in the cuprizone model, [145] and studies conducted in humans demonstrated a more efficient remyelination capacity and reduction of clinical disability in patients treated with this drug [295], [451]. Thus, a group of cuprizone intoxicated animals have been treated with clemastine, with the aim to compare the potential benefits of therapeutically-enhanced remyelination, in comparison to spontaneous remyelination, both at an anatomical and functional level. Interestingly, literature describing the beneficial effects of clemastine in animal models of demyelinating disorders has mostly been based on histopathological observations, and behavioural testing, but no imaging studies have yet been reported, to our knowledge.

Data presented in Fig. 4.2 shows that clemastine-treated animals present a faster axonal recovery than spontaneously recovering animals, with a significantly lower signal intensity on T2w images at large white matter tracts (such as the middle section of the corpus callosum) at week 7 (2 weeks of treatment), although at the end of the study (week 10) no significant differences were found between both cuprizone groups. In any case, T2w signal never drops to the level of controls, indicating that remyelination takes place only partially, after intoxication with cuprizone. It is interesting to notice that the difference on T2w signal between clemastine treated and non-treated animals is maintained from weeks 5 to 7 (when

treatment is interrupted) and disappears towards week 10. From this result, one could speculate if prolonged treatment with clemastine would have a further effect on remyelination. This is a limitation of our study since we have tested only one dose and treatment period (based on previous literature Liu, 2016, although other authors have used longer treatment periods; Li et al, 2015) and further work on this direction would have to be performed in the future, to see if clemastine is able to promote further remyelination or at less shortens the recovery time if no further effect is observed, in comparison with spontaneous remyelinating mechanisms. For other brain regions with lower axonal density, such as the hypothalamus, no differences were found between groups (controls, cuprizone and cuprizone+clemastine) at any time-point (Fig. 4.2) but this may be indicative of a lack of sensitivity of the MRI technique to detect minor changes on myelin in these areas, rather than the absence of differences at all.

Thus, our *in vivo*, non-invasive and longitudinal MR imaging studies show, in agreement with previous histopathological analysis (Li, 2015; Liu, 2016, and others) that clemastine has an impact on the remyelinating process, at anatomical level, and speeds up recovery, though final endpoints seem to be similar to those achieved by spontaneous remyelination, once the treatment is interrupted. The question that remains now is how the use of clemastine impacts on the functional organization of the brain after demyelination and during remyelination.

Accordingly, with anatomical data, our functional MRI studies also show that clemastine enhances recovery from the cuprizone insult, reflected mainly in higher connectivity of the cortico-thalamic network and the mean connectivity of the thalamus and hypothalamus for the group of animals treated with clemastine, respect to the untreated cuprizone group. These differences are already significant at week 7, after 2 weeks of treatment with clemastine, reaching these animals the

same level of connectivity than controls (total recovery, in terms of strength of correlations of functional networks). At the end of the study, there are no significant differences in mean functional connectivity among groups (controls vs. cuprizone vs. cuprizone+clemastine) at the level of the DMN, Th and Hyth, but there are significant differences between the cuprizone group and the other two groups at the level of the thalamo-cortical network (the one in which Hübner et al found differences after chronic demyelination, Hübner, 2017). In this sense we can claim that clemastine actually enhances functional recovery of demyelinating animals, favouring the regaining the normal functionality of the thalamo-cortical network, which presents persistent alterations (damage) in non-treated cuprizone animals.

For the rest of affected networks, it is important to argue that, regardless of the fact that there were no differences in the degree of recovery at the end of the study, between clemastine treated and non-treated cuprizone animals, the faster functional recovery promoted by clemastine (functional recovery already present at week 7) may be an advantage. Prompt remyelination could not only enable functional recovery, but it also prevents axonal degeneration and progression of the disease, which is at the final term the responsible of the main disability seen in MS patients [27].

It is uncertain which implications may have the functional differences observed in our 10-weeks study on the long term. In fact, Manrique and colleagues have reported that animals submitted to cuprizone recover normal motor functions shortly after discontinuing the use of toxic, but 6 months later they present again some degree of locomotor dysfunction, with axonal loss at the CC [195]. It is plausible to believe that early recovery of the thalamo-cortical connectivity observed in clemastine treated mice might lead to a reduction or even a total correction of such locomotor dysfunction, observed in untreated cuprizone mice.

Finally, it is interesting to comment that functional connectivity shows an increasing trend for healthy controls, which actually correlates with the lower levels of signal intensity in T2w MRI anatomical images (Fig. 4.2) observed in the corpus callosum of these animals (indicative of higher axonal density in this portion of white matter). This phenomenon can be explained as the regular changes observed in young animals along maturation, since animals are young (8 weeks) at the beginning of our study and mature 2.5 months after. This result is in line with previously published works that report both, a progressive increase of myelin content in the brain of mice during their first 6 months of age [452], and an increase on functional connectivity at different brain networks between months 2 and 8 of age, when young mice mature (Egimendia, 2019).

5. Conclusions

In conclusion, our work shows that resting-state fMRI is a valuable tool for the longitudinal and non-invasive follow up of changes in functional networks organization in the brain during demyelination and remyelination processes. Functional studies correlated well with anatomical MRI studies performed by us and others, showing loss and subsequent increase of myelin in key areas of the brain, such as the corpus callosum.

During demyelination, cuprizone poisoned mice undergo a reduction in the mean functional connectivity on their brain, revealed by cross-correlations between homotopic nodes and the thalamo-cortical axis, as well as reduced activity on the default mode network. When remyelination (either spontaneous or enhanced by therapeutic intervention) takes place, most networks return to normal levels of activity with time, except for the thalamo-cortical network, which is only recovered upon treatment of the animals with clemastine. In fact, we could confirm that the use

of clemastine speeds up the process of recovery upon remyelination (both at an anatomical and functional level), although the level of recovery is not higher respect to spontaneously recovering animals at the end of the study, except for the aforementioned thalamo-cortical network. This difference, in fact, may have important consequences at chronic stages.

Using this longitudinal approach, we have been able to identify up to 3 different temporal patterns of functional reorganization in the processes of demyelination-remyelination, which could help to better understand those processes and potential differences on behavioural testing outcomes, depending on the network implicated in the development of the observed task.

Further functional studies should provide evidence to evaluate the potential effects of clemastine treatment for longer periods of time that the ones used here, and for potential chronic functional differences between spontaneously *vs*. therapeutically-enhanced remyelination processes.

Chapter 5

Aging Reduces the Functional Brain Networks Strength - a Resting State fMRI Study of Healthy Mouse Brain

A. Egimendia *et al.* Front. Aging Neurosci. (2019) 11:277. doi: 10.3389/fnagi.2019.00277

1. Foreword

In the second chapter, we have interestingly described how low dose cuprizone exposure during 5 weeks can cause MRI detectable abnormalities in white matter tracts even 6 months after the administration of the toxic. During regeneration studies, such as the ones conducted with remyelination therapies, testing the long-lasting effects of therapies is highly advisable. These long periods involving the monitorization of functional deficits during disease evolution as well as the functional recoveries during therapeutic interventions represent a substantial fraction of the lifespan of the experimental animals.

Furthermore, in the previous chapter, we observed an increasing trend in brain connectivity in control (healthy) mice, in parallel to an increase in myelination, as suggested by our anatomical MRI studies. This evidence suggests that aging, including the brain maturation and degeneration processes involving myelin, might be a considerable contributing effect on the description of brain connectivity.

In this chapter we describe the modulation of the brain connectome during the maturation and aging of healthy mice, depicted by the resting-state functional MRI protocol developed in previous chapters. The description of this natural evolution of the brain should be helpful for the interpretation of results and experimental design.

1. Introduction

Mouse models have become the cornerstone of research for neurodegenerative diseases such as multiple sclerosis [453], [454], Alzheimer's disease [455], Parkinson`s disease [456] or amyotrophic lateral sclerosis [457]. This has been achieved due to the opportunities that mice offer to be genetically manipulated along with the continuous discovery of gene mutations related to many neurodegenerative pathologies [458].

In this context, functional magnetic resonance imaging (fMRI) has become a crucial tool for the study of functional deficits in brain diseases and of functional improvements due to therapeutic intervention, respectively [459]. Resting-state fMRI (rsfMRI) is noninvasive and measures at high spatial resolution blood oxygen level dependent (BOLD) patterns at low frequencies in the absence of external stimuli [301]. From such data, the functional connectivity between different anatomical nuclei in the brain is constructed, and the functional neuronal networks are determined. Thus, rsfMRI permits to unravel the disturbances of the functional neuronal networks during the development of cerebral diseases and their functional improvements after therapeutic interventions.

The study of many cerebral diseases and brain lesions such as e.g. neurodegenerative diseases or stroke and the exploration of effective therapeutic strategies requires long-term monitoring, often of several months [334], [459], [460]. A factor that is, however, often overlooked in rsfMRI studies of mice is the progressing age of the individuals during the required longitudinal studies. Here we present a rsfMRI study on the effects of aging on functional connectivity in the healthy mouse brain in the range of 2-13 months of age. For the analysis of brain connectivity, we have combined Independent Component Analysis (ICA) to denoise

rsfMRI data and Seed-based Correlation Analysis (SCA) to study the correlation between various cortical and subcortical regions of interest (ROIs) while focusing on the sensorimotor networks and the default mode network. For the first time, we describe changes of the mouse brain connectome during healthy aging, defining an inverse U-shape curve for the functional connectivity that peaks at the age of 8-9 months followed by a substantial continuous decrease during progressing aging.

2. Materials and methods

2.1. Animals and experimental protocol

All animal experiments were performed in accordance with the guidelines of the German Animal Welfare Act and approved by the local authorities (Landesamt für Naturschutz, Umwelt und Verbraucherschutz NRW). Ad libitum access to food and water was provided to the animals under a controlled light environment (12 h light/dark).

Twenty-four C57BL/6J male mice (Janvier, Le Genest-St Isle, France) were studied, subdivided into 4 groups of age: 2 months (n=6), 5 months (n=6), 8 months (n=6) and 12 months (n=6). Each group was scanned twice with a one month gap between both acquisitions. Thus, eight time points in total were covered in the study: 2, 3, 5, 6, 8, 9, 12 and 13 months.

2.2. MRI

MRI measurements were carried out on a dedicated animal MRI scanner (Bruker BioSpec, Ettlingen, Germany) operating with a horizontal magnet at 9.4T. Radio frequency (RF) excitation and signal reception were performed with a cryogenic 1H quadrature surface coil (CryoProbe, Bruker BioSpin, Ettlingen, Germany).

Monitoring of physiological parameters was achieved with a 1025T System (SA Instruments, Stony Brook, New York) and recorded with DASYlab Software (National Instruments, Austin, TX). Body temperature was measured with a fibre optic rectal probe (SA Instruments, Stony Brook, New York) and kept at 37±1 °C by a water circulating system (Medres, Cologne, Germany). Anesthesia was induced in all mice with isoflurane (3.5%) in air mixture of N2 (70%) and O2 (30%), and was reduced to 2% isoflurane in the scanner, where the animal's head was fixed with ear bars and a tooth holder in a dedicated MR compatible animal cradle.

MRI experiments were conducted using Paravision 6.01 (Bruker BioSpin, Ettlingen, Germany). Isoflurane was kept at 1.5-1.8%, thoroughly adjusted throughout the duration of the experiments, for keeping the breathing rate stable (100-120 bpm). A single bolus of 0.1 mg/kg medetomidine (Domitor, Elanco) was subcutaneously administered suspended in 250 μL of NaCl, 15-20 minutes before functional imaging acquisition. Within 5 minutes following the medetomidine injection, isoflurane was decreased to 0.5-0%, maintaining a maximum of 100-120 breaths per minute during the complete functional imaging data acquisition.

An anatomical reference TurboRARE scan was acquired with the following parameters: TR/TE= 5,500ms/32.5ms, matrix 256 x 256, field of view (FOV) 17.5 mm x 17.5 mm, 48 consecutive (no gap) slices of 0.3 mm, RARE factor of 8, and 2 averages. Then, an adapted gradient echo echo-planar imaging protocol [338] was used for functional image acquisition TR/TE=2,840 ms/18 ms, FOV 17.5 mm x 17.5 mm, matrix 96 x 96, in-plane resolution 182 μm x 182 μm, 16 slices of 0.5 mm with 0.1 mm inter-slice gap. Once the scanning protocol was completed, a 1mg/kg Atipamezol (Antisedan, Pfizer), suspended in 100 μL of NaCl, was subcutaneously administered to reverse the effects of medetomidine.

2.3. Data processing

All datasets were brain extracted using FSL [FMRIB (Oxford Centre for Functional MRI of the Brain) Software Library; http://www.fmrib.ox.ac.uk/fsl, [461], [462]]. Preprocessing of rsfMRI data was performed with single-session pICA (Probabilistic Independent Component Analysis) with the MELODIC interface of FSL (http://fsl.fmrib.ox.ac.uk/fsl/fslwiki/MELODIC), following an adapted procedure of Bajic and colleagues [316]. This preprocessing consisted of motion correction with MCFLIRT [461], high-pass temporal filtering (> 0.01 Hz) and registration to the anatomical reference image set (TurboRARE images) which was registered to an in-house mouse brain template. A threshold of $p<0.05$ was applied to the z-scores spatial maps of the independent components provided by MELODIC, before being manually classified into signal or noise, based on information offered by independent component spatial maps, power spectra and time series [327]. In order to achieve the cleaning of data, the components classified as noise were regressed. Following data denoising, a 0.3 mm full-width half maximum (FWHM) Gaussian kernel was applied for spatial smoothing.

Several brain ROIs were selected for functional connectivity analysis. Cortical regions include the primary somatosensory cortex (S1), the secondary somatosensory cortex (S2), primary and secondary motor cortex (M1/2), the visual cortex (VC) and the auditory cortex (AC). Subcortical nodes are the caudate putamen (CPu) and the thalamus (Th). Moreover, several regions of the default mode network (DMN) were extracted: the entorhinal cortex (EntC), prelimbic cingulate (Cg), the rostral dorsal prelimbic cortex (PrL), the retrosplenial granular and dysgranular cortex (RSG/RSD), the globus pallidus (GP), the hypothalamus (Hyth) and the

hippocampus (Hp). The DMN is regarded as the basal activity network of the brain [463].

Group analysis was conducted by using a customized version of FSLNets (v0.6; www.fmrib.ox.ac.uk/fsl) in five main steps: 1) Averaging of time series in each ROI; 2) Calculate full Pearson correlation between pairs of ROIs 3) Transformation of Pearson correlation r values to z-score by applying Fisher transformation to normalize data 4) Calculate group mean values for each correlation 5) Build matrices representing z-score values between pairs of nodes (i.e. regions).

2.4. Analysis of age profile of functional connectivity

To construct the age profile of the functional connectivity, we followed two strategies. As the first approach, we plotted the mean correlation coefficients versus time for each single measured temporal point (2, 3, 5, 6, 8, 9, 12 and 13 months of age). Alternatively, we plotted the mean correlation coefficients versus time, averaging the two temporal data sets for each group of animals studied (each group was scanned twice in consecutive months), thus resulting in 4 temporal points at 2.5 (averaging month 2 and 3 for animal group 1), 5.5 (averaging month 5 and 6 for animal group 2), 8.5 (averaging month 8 and 9 for animal group 3) and 12.5 (averaging month 12 and 13 for animal group 4) months.

2.5. Statistical analysis

Prism X.0 (Graphpad Software, San Diego, CA) was used for the statistical analyses. D'agostino-Pearson normality test was performed to assess the distribution of data for each network or cross-correlation of interest. In case data was normally distributed for all groups, an analysis of the variance for repeated measures

(ANOVA) was performed, followed by a two-tailed unpaired t-test. Otherwise, the non-parametric Kruskal-Wallis test was first conducted followed by Mann Whitney test for pairs of groups. Statistical significances were set at $p<0.05$ (*), $p<0.01$(**) and $p<0.001$(***).

3. Results

3.1. Whole-brain networks

Color-coded matrices from months 2 to 13, showing the z-scores corresponding to interactions between different brain regions, separately analyzed for the left and right hemisphere, are presented in Fig. 5.1. In a first visual inspection, the overall correlation is found to increase from month 2 to month 8 as indicated by the color change in the matrices. After month 8, the connectivity strength decreased again progressively until the last time point at 13 months. Nevertheless, temporal changes are not completely linear and fluctuations of z-scores from one time point to the next are considerable when separately analyzing different nodes. To distinguish potential patterns for individual networks, we followed two approaches. First, we decided to group the connectivities in four groups: 1) all intra-hemispheric connectivities of the left hemisphere, 2) all intra-hemispheric connectivities of the right hemisphere, 3) all inter-hemispheric connectivities, and 4) all connectivities within the whole brain (grouping all 2268 calculated connections together). The averaged z-scores of each of these network groups were plotted versus time (Fig. 5.2A). In addition, we considered that the temporal gap of 1 month between some experimental points is too narrow to attribute changes in correlation to an aging effect, and that variability observed in such short periods could be due to many

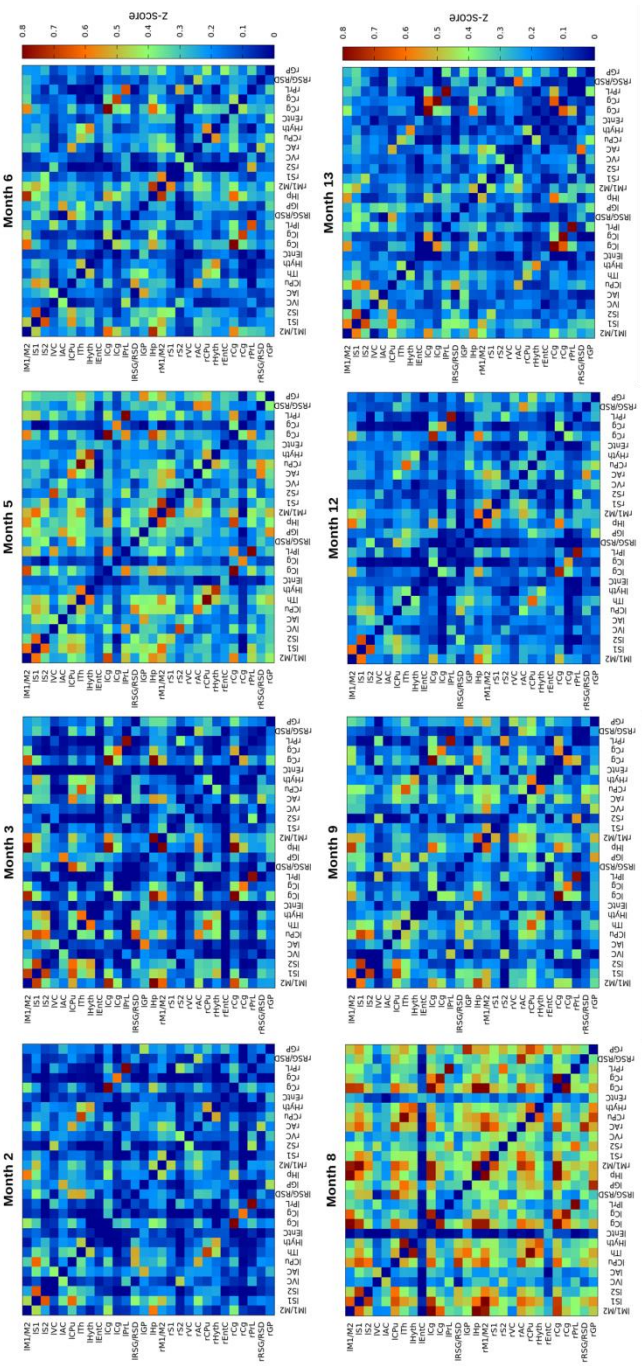

Figure 5.1. *Resting state fMRI full correlation matrices of the inter- and intra-hemispheric connectivities for 15 ROIs of the brain. Z-score values of cross-correlations are plotted. The 8 matrices correspond to 2, 3, 5, 6, 8, 9, 12 and 13 months of age of healthy C57BL/6J mice. There is an overall continuous increase of the power of correlation until month 8, indicated by the color change in the LUT. The correlation power decreases again from month 8 until month 13 (p<0.001). The 15 regions of interest are: S1, primary somatosensory cortex; S2, secondary somatosensory cortex; M1/2, primary and secondary motor cortex; VC, visual cortex; AC, auditory cortex; CPu, caudate putamen; Th, thalamus; EntC, entorhinal cortex; Cg, prelimbic cingulate; PrL, rostral dorsal prelimbic cortex; RSG/RSD, retrosplenial granular and dysgranular cortex; GP, globus pallidus; Hyth, hypothalamus; Hp, hippocampus. "l" prefix indicates left hemisphere, "r" prefix indicates right hemisphere.*

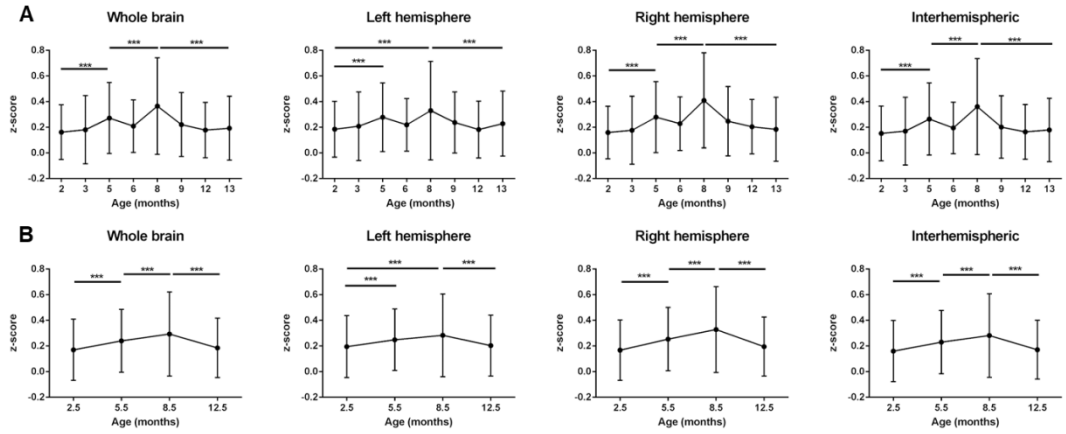

Figure 5.2. *Averaged z-score values of left and right intra-hemispheric, inter-hemispheric and whole-brain connectivities. A) z-score values, analyzed at the 8 experimental time points (2, 3, 5, 6, 8, 9, 12 and 13 months). The power of correlation increases up to month 8 and then decreases again until month 13 in a fluctuating way. B) z-scores of equally spaced pairs of time points (averaged z-scores for 2-3, 5-6, 8-9, 12-13 months, see Methods section). Smoothed temporal trends show an inverse-U shape curve peaking at month 8.5. Error bars indicate SD. p<0.001(***).*

other experimental or biological factors. Thus, a smoothing of the temporal series was achieved by averaging data with temporal gaps of 1 month (i.e. the pair of scans for each group of animals), resulting in a reduction of the eight measured time points into 4 evenly spaced time points (3-4 months of temporal resolution, see methods section. In this way, better interpretable, smoother trends for aging effects were obtained (Fig. 5.2B). As shown in Fig. 5.2B, the mean z-score of both, right and left intra-hemispheric groups of correlations, as well as inter-hemispheric and whole-brain connectivities become increasingly stronger from month 2.5 to month 8.5. The increase of the power of correlation from one time point to the next is highly significant for all these periods ($p<0.001$). After peaking at month 8.5, there is

a highly significant decrease in connectivity until the month 12.5 ($p<0.001$ in all cases).

3.2. Grouping the whole brain into connectivity subsets

In a further analysis, the brain nuclei were grouped in 3 regions encompassing 1) the cortical network (CN) consisting of M1/2, S1, S2, AC, and VC, 2) the subcortical network (SN) consisting of CPu and Th, and 3) the Default Mode Network (DMN) (Hyth, EntC, Cg, PrL, RSG/RSD, GP, and Hp). Then, the interactions among these three different networks were studied.

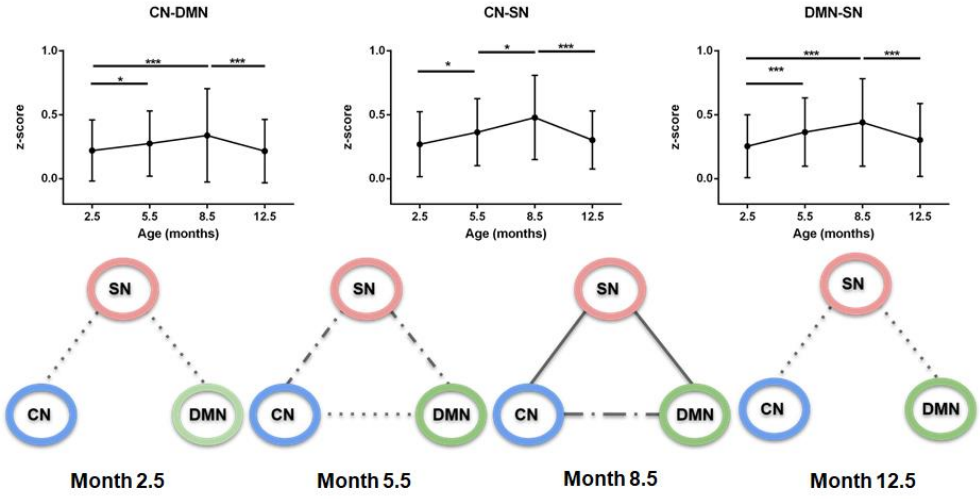

***Figure 5.3**. Inter-network connectivities. Upper row: z-scores of connections between cortical network (CN), subcortical network (SN) and default mode network (DMN). There is a significant increase of connectivity until 8.5 months, followed by a decrease until month 12.5 in all cases. Lower row: Schematic representation of the strength of correlations over time. Each graph, from left to right, represents a specified age (2.5, 5.5, 8.8 and 12.5 months). Solid line, z-score>0.41; Dash-dotted line, z-score>0.33; Dotted line, z-score>0.25; No line, z-score<0.25. CN-SN and SN-DMN connections show a higher correlation over time than the CN-DMN connection ($p<0.001$). Error bars indicate SD. $p<0.05$ (*) and $p<0.001$(***)*

The connectivity significantly increased for all three inter-network connections: CN-DMN, CN-SN, DMN-SN networks from month 2.5 to 8.5 ($p<0.001$ CN-DMN, $p<0.001$ CN-SN, $p<0.001$ DMN-SN), as presented in Fig. 5.3. From the age of 8.5 months, a continuous decrease of the inter-network correlations was seen between month 8.5 and month 12.5. Interestingly, the connectivity strength reached at month 8.5 for CN-SN and DMN-SN networks was stronger than that for the CN-DMN ($p<0.001$ at month 8.5).

3.3. Analysis of sensorimotor and default mode networks

In the final step, we assessed the individual patterns of connectivities between individual nuclei within the sensorimotor network and the DMN, respectively. A set of the stronger connections within the sensorimotor network is presented in Fig. 5.4.

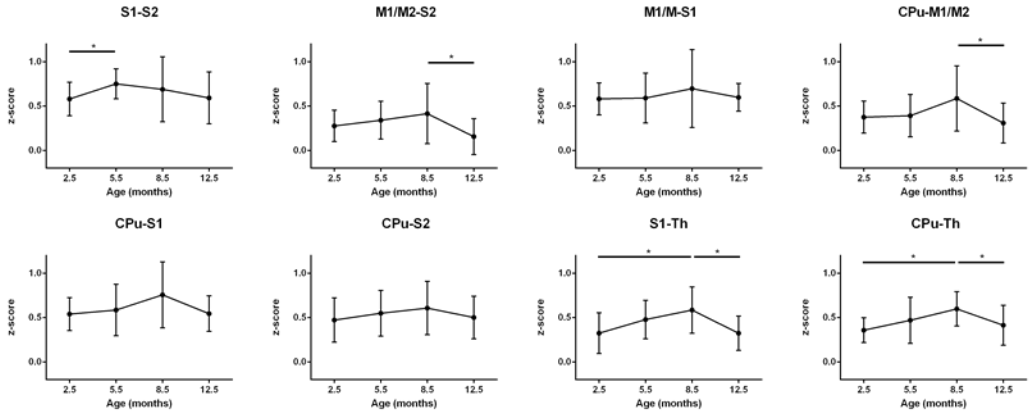

Figure 5.4. *Mean z-score values of cross-correlations of pairs of ROIs of the sensorimotor network over the life span period (2.5 months, 5.5 months, 8.5 months and 12.5 months). A significant increase in connectivity was seen from month 2.5 to month 8.5 in S1-Th and CPu-Th connections. The CPu-M1/2, CPu-Th and S1-Th correlations undergo a decrease from month 8.5 to month 12.5. Error bars indicate SD. p<0.05 (*).*

All connectivities share the pattern of the largest z-score values at 8.5 months except the interaction between S1 and S2 which reaches its maximal strength already at 5.5 months. This inverse U-shape pattern is most pronounced for the connections M1/2-S2, S1-Th, and CPu-Th. In contrast, the connections M1/2-S1, S1-CPu, S2-CPu have only a very weak, non-significant inverse U-shape during the whole aging process. Interestingly, the z-score values at 12.5 months reach low connectivity strength well comparable to those at 2.5 months.

Plotting the mean correlation of all interactions of the DMN over time leads to a clear inverse U-shape curve, significantly increasing step-wise from month 2.5 to month 5.5 and month 8.5 followed by a significant decrease to month 12.5 ($p<0.001$;$p<0.05$; $p<0.001$ respectively) (Fig. 5.5, top left). Performing an analysis of connections between the individual nodes of the DMN, temporal trends show mostly the same pattern, but are more variable than for the sensorimotor network (Fig. 5.5). Most DMN-internal interactions present the strongest correlation at month 8.5, being significantly different from month 2.5 (GP-Hp, $p<0.05$; Cg-Hyth, $p<0.005$; Hyth-Hp $p<0.05$) and show a decline from month 8.5 to month 12.5 (Cg-Hyth, Hyth-GP and the PrL-Hp; $p<0.05$). A highly significant U-shape pattern of the thalamus (Th) was seen with both Hyth and Hp. Both correlations undergo an increase until month 8.5 ($p<0.05$), but, while the Hp-Th connection is somehow sustained after month 8.5, the Hyth-Th connection undergoes a considerable decline from that point until month 12.5. The Cg-PrL interaction remained constant over time with strong connectivity (z-score mean = 0.50). Contrary to the sensorimotor network curves, some DMN-internal connectivities do not decrease at 12.5 months to the low z-score values at 2.5 months, but stagnate at higher values, although clearly lower than at 8.5 months. This is most pronounced for some connections of the hippocampus: GP-Hp, Hyth-Hp, Hp-Th.

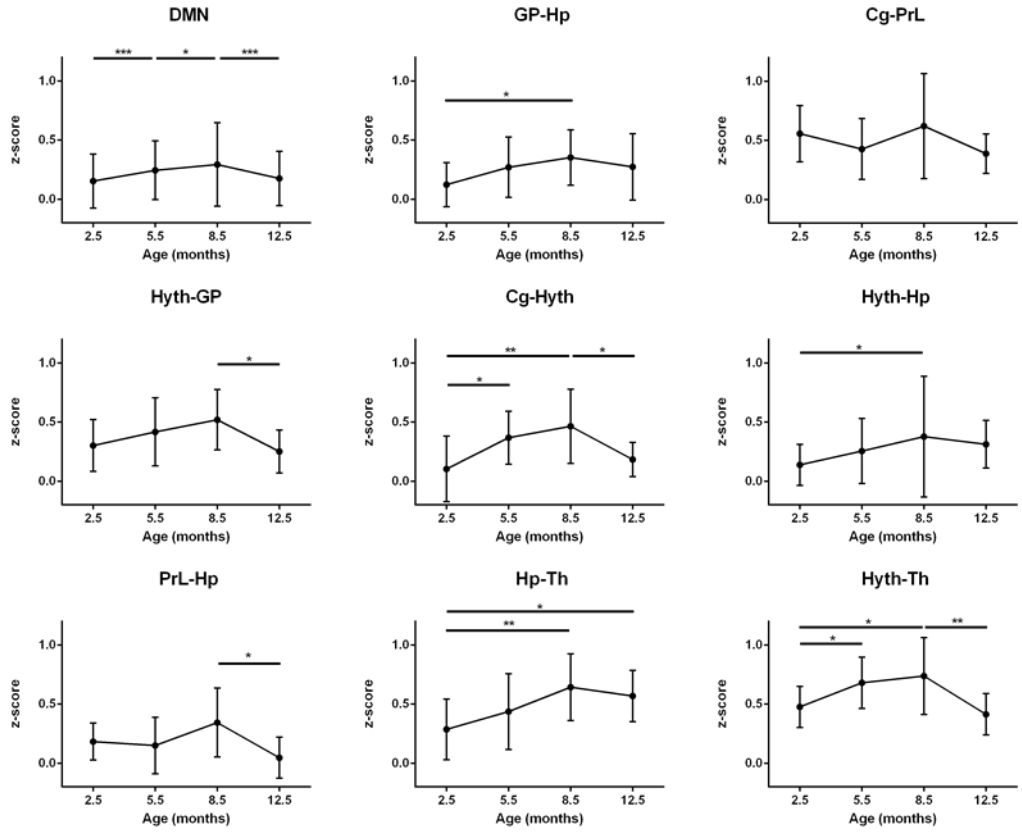

Figure 5.5. *Default-mode network connectivity. Top left: mean z-score value of all interactions between DMN regions is represented. All other diagrams: Cross-correlation of pairs of ROIs of the DMN is represented. An increasingly strong interaction is seen in month 8.5 comparing to 2.5 in GP-Hp, Cg-Hyth, Hyth-Hp, Hp-Th and Hyth-Th correlations. There is also a decrease of correlation from month 8.5 to month 12.5 in Hyth-GP, Cg-Hyth, PrL-Hp and Hyth-Th. An inverse U-shape curve is typically seen. Error bars indicate SD. p<0.05 (*), p<0.01(**) and p<0.001(***).*

3.4. Condensed aging effects of the functional networks

Finally, we have studied the average correlation of a selected node with all other nodes across the brain, reflecting the average connectivity strength of this particular

node over time. In Fig. 5.6, this behaviour pattern is presented for all cortical nodes (Fig. 5.6, left), both subcortical nodes (thalamus and caudate putamen; Fig. 5.6, centre) and for all nodes of the DMN (Fig. 5.6, right). In all three groups, the average connectivity strength shows an almost identical U-shape pattern with the maximal values at 8.5 months of age. Only the entorhinal cortex in the DMN group (Fig. 5.6, right) deviates from this pattern and shows an irregular pattern. From these curves, the prominent change in functional connectivity strength across progressing aging is clearly seen. Thus, the subcortical functional connectivity strength loses 36% of its maximal value at 12-13 months of age in thalamus and caudate putamen.

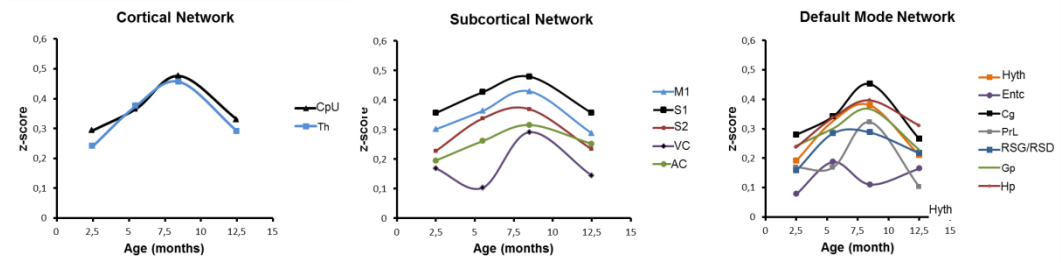

Figure 5.6. *Aging effects of functional connectivity for individual cortical, subcortical and DMN nodes. Mean z-score values of correlations of each ROI are represented. All nodes show an inverse U-shape behaviour with a pronounced maximum of z-scores at 8.5 months of age, followed by a substantial drop to low values at 12.5 months of age. Only the entorhinal cortex (right diagram; DMN) shows a deviating behaviour with an early maximum at 5.5 months.*

In the cortical node group, the loss of functional connectivity strength at 12-13 months varies between 20% for the auditory cortex (AC) and 50% for the visual cortex (VC). The other cortical nodes have a drop of 33%. In the DMN, the drop of functional connectivity is also strongly expressed. While RSG/RSD and Hp show a 24% and 22% drop respectively, GP, Cg and Hyth experience a much stronger loss of

38% (GP), 40% (Cg), and 45% (Hyth). The strongest effect is noted for the rostral dorsal prelimbic cortex (PrL) with a massive 70% loss in functional connectivity strength at 12-13 months of age.

4. Discussion

In the present study we have carefully investigated the age dependence of functional networks by systematic analysis of the resting state fMRI data. The age between 2 and 13 months of age was studied, thus covering the most relevant life span phase typically used in chronic long-term experimental mouse models on cerebral diseases and lesions. We have particularly focused on the sensorimotor networks and the default mode network (DMN) as these are most often the relevant functional networks investigated for functional deficits during brain diseases and for functional improvements during therapeutic strategies. Thus, we have unraveled an inverse U-shape behaviour of the functional network strength with aging, reaching the maximal strength at 8-9 months of age for both, the sensorimotor networks and the DMN.

The age dependence curve shows similar functional network values shortly after weaning of 2 months of age and at progressed aging at 13 months of age, crossing the maximum strength at 8-9 months. Cortical and subcortical groups presented an overall drop of approximately 33% in network strength when going from 8 to 13 months, with the exception of only a few correlations such as the M1/2-S1 or the Cg-PrL connections which remained rather constant along the whole temporal series. It should be also highlighted that the S1-S2 connection peaked already at month 5.5, unlike the rest of all the studied interactions. In the DMN, the variability in network strength was more pronounced, varying from 24% for RSG/RSD, GP, and Hp to 70% for the rostral dorsal prelimbic cortex (PrL).

Two earlier studies dealing with mouse models of Alzheimer's disease and focusing on the age dependence of the disease reflected in functional networks changes had also included WT litter mates in their age dependence studies [338], [464]. Although the age dependence of the healthy litter mates in those studies was not discussed explicitly in both reports and their focus was primarily on the AD models, information about the age dependence of the resting state fMRI data can be derived from their data presentation. Grandjean et al. [338] had included an age range from 1 to 21 months at variable step sizes, including an age range similar to ours. Careful analysis of the functional networks of the healthy litter mates was limited to the early life phase and data had been recorded in isoflurane anesthesia, different from the present medetomidine-isoflurane mixture, which may affect the functional network results. But from the examples listed in the report of Grandjean and colleagues, maximum connectivity strength appears to occur between 5 to 8 months of age for the healthy litter mates which agrees well with our present results. In the report by Shah et al. [464], quantitative analysis of the hippocampus showed a slight increase in connectivity till month 8, and for the prefrontal network a similar increase was reported from 3 to 7 months. Considering the rather low level information of the age dependence of the healthy litter mates in these two studies, the agreement with our inverse U-shape curve peaking at 8-9 months is very good.

A few recent studies on aging dependence of functional networks in healthy human subjects [465], [466] point also to a general inverse U-shape of functional network strength. These authors typically compared two or three age groups, defining them as adolescent, adult and aged healthy human subjects where the age span within one group was rather widely defined. These studies confirm our findings in mice that the functional connectivity strength increases from early life, reaches a maximum to descend again during progressed aging. Thus, Bo and colleagues [465] focusing on

the cognitive and motor networks, found an equivalent inverse U-shape behavior for both networks, peaking at the young adult group, aged 18-33 years in their investigation.

Our study shows how functional connectivity (FC) increases continuously from the second month of life until month 8-9 in the life span of mice, from where a continuous decrease in FC takes place until month 12.5. Although the strength of the FC is variable, the inverse-U shape is robust throughout the whole brain. Underlying reasons for this age dependent behavior of the functional networks are not understood but a relationship with structural network changes has been considered. During the whole life span, a change of the integrity of white and gray matter content has been reported. Thus, in a study focusing on the structural brain development of young mice, we recently reported a continuous myelination increase in healthy mouse brain up to six months of age with parallel cortical thinning, clearly indicating an ongoing morphological change during this period of mouse brain adolescence [467]. In a study on structural brain networks with 484 healthy subjects aging between 5 and 85 years old, Douaud and colleagues described an inverse U-shape pattern [468]. In their study, they revealed how certain regions of the brain thrive in a late stage of adolescence till structural connectivity peaked at approximately 40 years of age, followed by a decrease during aging. With the combined protocol of diffusion spectrum imaging (DSI) and resting state fMRI, Green et al. [334] could show dramatic functional changes without structural changes in mouse models of tauopathy. The same authors moreover reported that the parallel decreases of structural and functional networks strength after stroke were decoupled when a stem cell treatment to the stroke was included in the experimental protocol [469]. Thus, it will be of particular interest in future studies to coregister structural and functional networks using a combined protocol of

diffusion spectrum imaging (DSI) and resting state state fMRI to unravel whether structural and functional network changes develop in parallel with healthy aging or whether they may also become decoupled at a certain point. Parallel to structural alterations, hemodynamic parameters may also contribute to the observed age dependence decrease of functional connectivity. Thus, Balbi and colleagues studied the age dependent changes of microcirculation in mouse brain [470]. Their most important finding was that neurovascular coupling becomes impaired after eight months already – where also the maximal functional connectivity, observed by us, started to decline - while no change of cellular composition of the neurovascular coupling or impaired Ca2+ reactivity was found.

We believe that our studies have an important consequence for the design, performance and analysis of future longitudinal rsfMRI studies in mice. As we have seen, there is a strong effect of aging in mouse connectome, even for temporal periods as short as a few months. Establishing 8-9 months as the age at which connectivity starts to decline and taking into account the progression with age, will benefit to avoid confounds of aging effects underlying the particular aspects of disease-caused functional alterations of slow, long-term functional regeneration processes. In particular, it is between the 8th and 12th month of life where the mouse begins to show signs of deterioration. The first senescent changes take place presumably between 10 and 15 months of age, at 15 months approximately the mouse loses its fertility, and at 18 months aging biomarkers are considered evident [471]. On the other hand, during the early life span till 8-9 months of age, a continuously increasing strength of the functional networks may partly cover decreases caused by cerebral diseases and may lead to overestimation of therapeutic effects during apparent “recovery” of functional networks. Thus, we have planned to extend the study on stroke induction at variable age in mice to

clarify stroke induced functional connectivity alterations as a function of age and to decipher whether functional network derangements after stroke are more severe in aged or young mice.

5. Conclusions

Functional connectivity strength of the sensorimotor and default mode networks in the mouse increases from month 2, continuously reaching the maximum at 8 to 9 months of age. The decrease of the functional network strength after 8-9 months reflects the progressing aging and reaches low values at 12-13 months of age equivalent to those in the early adolescent phase at 2-3 months. In summary, the functional network strength follows a clear inverse U-shape curve during adolescence to maximum at adulthood and progressed aging.

General discussion

In this work different applications of ultra-high field magnetic resonance imaging have been explored for the study of neurodegenerative diseases. Starting by the innovative imaging of organotypic cultures, we followed with multiparametric anatomical studies of *in vivo* mouse models of different neurological disorders, to finish with the application of the promising field of resting-state functional MRI. Two main objectives were set at the beginning of the work, namely: 1) to develop imaging protocols to evaluate imaging parameters for the non-invasive assessment of myelin content in models for the study of remyelination; 2) to understand the impact of demyelination and remyelination in the CNS at a functional and anatomical level.

It is undoubted that myelin has been the cornerstone of this work. Even though myelin pathology takes place in several disorders, as reviewed in the introduction section, multiple sclerosis is the quintessential demyelinating disease, due to the fact that myelin damage triggers a countless number of pathological processes and due to its social and economic impact. After performing substantial advances by means of immunomodulating therapies, scientific research is targeting at remyelination as a neuroprotective approach for this pathology. This strategy has shown promising results in preclinical models, giving rise to a bunch of drugs as potential remyelination therapeutics that so far, have not yet been approved for human use.

The inaccurate evaluation of therapies or the poor current understanding of demyelinating and remyelinating processes might be responsible in part for such lack of translation. Thus, in this work, we addressed these issues by using first organotypic cultures and then the cuprizone murine model of myelin-related pathology. Tough conceptually feasible, we have encountered several practical obstacles in our endeavour to image organotypic cultures. Currently, quantification of myelin in organotypic cultures is far from being simple and straightforward,

making highly difficult its establishment as a robust in vitro model for non-invasive studies. At this moment, our approach to quantify myelin content through MRI has not succeeded, although progress has been made and work continues in this direction. In this context, it is our belief that the future of organotypic culture as a model for the longitudinal evaluation of remyelination therapies highly depends on the development of robust and reproducible molecular imaging techniques, either by MRI or by any other imaging technique, which implies the development of molecular imaging probes specific and sensitive to myelin. Further work is in progress in this regard in our laboratory.

Moving into *in vivo* studies, the cuprizone model is maybe the most widely used model for the evaluation of remyelinating therapies, owing to its reproducibility, simplicity and the predictive fashion in which myelin pathology takes place. Moreover, while myelin pathology is extensive in this model, other pathological processes (e.g. axonal loss) take place in a lower extent, enabling the evaluation of specific therapies to myelin in complex scenarios. In this way, we have revealed the high sensitivity and specificity of T2-weighted imaging, T1-weighted imaging and radial diffusivity to myelin pathology in the cuprizone mouse model at high fields. Particularly interesting has been the sensitivity and specificity offered by T2-weighted imaging, even able to detect mild remyelination after the demyelinating insult. Of note, these parameters show different temporal patterns of evolution, which might indicate that they are affected in a different extent by other phenomena rather than myelin contribution, and therefore can be sensitive to other pathological events taking place in the cuprizone model.

Testing these parameters in other preclinical models of neurodegenerative diseases might provide further evidence of the suitability of the parameters to monitor myelin in complex scenarios where multiple pathological processes take place

concomitantly. To achieve this goal, we have made use of a mouse model of amyloid deposition and a model of tauopathy. In these models, neurodegeneration, axonal loss and all in all, profound damage in the microstructure of the brain is expected, as reported in the literature. In this setting, radial diffusivity has shown sensitivity to non-myelin related pathology in the white matter tracts of the brain, for which T2w and T1w imaging have shown to be insensitive. Analysing retrospectively the results of the cuprizone model study, with this fact in mind, we found a plausible explanation for the fact that RD showed poor sensitivity for remyelination (which in turn was observable by T1w and T2w imaging) following the peak of demyelination (week 5), indicating that further damage to tissue may occur apart from myelin loss in this model.

Therefore, the multiparametric studies conducted might indicate that in absence of substantial pathological events apart from demyelination T2w imaging, T1w imaging and RD show a good specificity and sensitivity for the detection and quantification of this phenomenon. Nevertheless, when further pathological processes are present in the brain, RD might lose sensitivity for it. For this reason, we do believe that the conduction of multiparametric studies, rather than studies based on a unique parameter, can provide further insight into the state of the white matter tracts of the brain beyond myelin pathology, as exhibited in Table 6.1.

It is our belief that T2w imaging is highly robust for the evaluation of myelin in the cuprizone mouse model at high magnetic fields, at which, in the end, remyelination therapies are usually tested. The excellent performance of T2w imaging has been confirmed when the effect of the potential remyelinating therapeutic clemastine was evaluated, being able to reveal the remyelinating effect of the drug. Therefore, a pragmatic approach as the one carried out in that study could only consist on T2w imaging to assess myelin content in the cuprizone mouse model. However, a more

robust conclusion or even the evaluation of further tissue damage might be achieved in case T1w and RD are also registered together with T2W, mainly in other models different to the cuprizone mouse model.

Table 6,1. *Multiparametric MRI as a tool for characterization of white matter tracts.*

Condition	ΔT2w	ΔT1w	ΔRD
Healthy tissue	-	-	-
Demyelination	↑	↑	↑
Further damage	-	-	↑

Before moving forward, we would like to point out that T2w, T1w and RD might not be useful to evaluate the efficiency of a given therapy in clinical trials or other preclinical models. Indeed, they have shown to be sensitive to non-myelin related pathology observed in demyelinating plaques of patients, not providing an accurate measure of the myelin content. However, we cannot discard that in absence of a certain pathological event, such as inflammation, mainly the normalization of T2w signal can provide a semiquantitative measure of myelin. Thus, being aware of the sensitivity of these parameters to other pathological events, the robustness of their applicability in other pathologies is still a matter of study. Of note, it is highly advisable that specific staining of myelin with Luxol fast blue or other techniques is carried out in preclinical models before assuming the validity of these parameters to evaluate myelin. In other words, we are well aware that T2w imaging is a powerful tool for the study of myelin in the cuprizone mouse model, but that its full validity is

not readily translatable to human multiple sclerosis. Still, it is a very powerful tool for the development of novel therapies in animal models of the disease, which is not a minor issue.

On the other hand, regarding myelin content on grey matter, it has to be considered that grey matter is a low myelinated tissue, and pathology in it might be highly variable and too complex to specifically quantify myelin. As observed in the mouse models of Alzheimer's disease, abnormalities in the grey matter are extensive and probably, poorly correlated with myelin, due to the accumulation of neurofibrillary tangles, amyloid plaques or cell loss.

It is also worth pointing out that diffusion-weighted imaging has shown a great sensitivity to detect microstructural abnormalities both in grey and white matter in Alzheimer's disease models. As discussed in previous chapters, although the poor specificity of DTI parameters has been widely reported in the literature, the use of DTI as a first approach to detect abnormalities might be highly considered.

Nevertheless, we do considerer that developing specific imaging markers, not only to myelin but also different pathological events such as β-amyloid plaques, will be of utmost importance to monitor diseases and evaluate therapies in humans and preclinical models. In fact, to us, the use of MRI in preclinical imaging should be oriented towards the substitution of histological studies and performance of longitudinal studies, entailing a substantial reduction in the use of animals and a deeper understanding of pathological processes. Moreover, the contribution of machine learning approaches for imaging analysis should not be underestimated for the diagnosis and detection of subtle abnormalities in humans and preclinical models.

In this context, the use of higher magnetic fields in humans (e.g. 7 Tesla) might give a boost to the imaging sensitivity and give rise to a better understanding of diseases. Nevertheless, we do believe that a vast progression would be needed to tackle the complexity and challenges that using such a high magnetic field involve and achieve the implementation of the system for clinical use on a daily basis. Additionally, even the side-effects of being exposed at ultra-high field are still unresolved so far.

Parallel to brain anatomy related studies and, as aforementioned, understanding of the impact of demyelination and remyelination at a functional level can provide a further insight into these processes, for which reason functional imaging of animal models of myelin pathology has been set as an important objective in our work. After setting up a protocol for the performance of resting-state functional MRI (rs-fMRI) at our laboratory, we conducted a longitudinal study in which an evident trend throughout the study was observed: increased connectivity at the onset of demyelination, followed by reduced connectivity at the peak of demyelination, and a recovery of connectivity strengths during the following weeks, a process that was boosted when treating animals with clemastine. Interesting findings of these studies were, on the one hand, the coincidence of observed trends with those reported for other pathologies and on the other hand, the degree of correlation of functional imaging with the reported behavioural test conducted in this animal model. In brief, periods of hyperactivity are followed early after the onset of the pathology, later followed by a reduction in the activity as the disease progresses. Moreover, the observation that spontaneous or therapeutically enhanced remyelination triggers the recovery of connectivity supports the importance of developing therapies that promote remyelination. It has to be taken into consideration that even though demyelination is the most evident pathological process going on in the cuprizone model, the administration of toxic compound might also alter different aspects of the

organism (of the brain) that finally could also contribute to a different resting-state condition.

It is our belief that the capacity observed for rs-fMRI at high-field to detect this temporal pattern of evolution in the cuprizone mouse model is of great interest for the evaluation of therapies, further supported when combining functional with anatomical (T2w, T1w and RD) imaging. By carrying out an experimental strategy that includes the acquisition of longitudinal multiparametric anatomical imaging along with functional imaging we have been able to provide a full characterization of the effects of demyelination and remyelination and to highlight the potential benefits of the remyelinating therapy based on the use of clemastine.

Interestingly, we have been able to observe that healthy mice show an increasing connectivity during the duration of the study, revealing increased myelination of healthy individuals with maturation revealing, on the one hand, the high sensitivity of this approach to detect small changes in myelin naturally occurring in maturing healthy individuals, and on the other hand, calling for the study of myelin changing in aging individuals including both maturing from youth to adulthood, and decline form adulthood to seniority. This study was indeed performed as part of our research.

Certainly resting-state fMRI has also been sensitive to detect the effect of aging in mouse brain. In Chapter 5 of this work, we report an inverse U-shape curve in connectivity observed in mice aging from 2 months to 13 months of life, peaking at month 8. This natural trend is very important and should be taken into account for a complete study of disease-related or therapeutic-related effects on connectivity, to avoid false assignation of temporal trends to what it is normal in healthy subjects that undergo natural processes concomitant to aging.

Despite resting-state functional MRI has been revealed as a powerful tool for the study of brain function, results obtained with this technique should be taken carefully. In the cuprizone mouse model, the hyperconnectivity observed at the onset of the disease might be a compensatory effect to the produced damage in the brain. Nevertheless, the interpretation of the peak observed at month 8 in the aging study might be more difficult to understand. At this point there are two possible situations: 1) The brain is making an effort to maintain existing function, as observed in the cuprizone model; 2) The brain is fully mature and functionally optimal, and declines from this point on. Certainly, it is difficult to answer this question. Nevertheless, it seems reasonable to attribute the drop in connectivity observed after month 8 to an impaired function, as observed in the cuprizone model from week 2 to week 5. Hence, resting-state results are sometimes hard to interpret. BOLD response might be affected by several factors that under pathology are not considered or predicted. For this reason, we do consider that extensive research in healthy mice and characterization of mouse brain function could substantially improve the interpretation of data.

However, it is notorious the contribution that resting-stage fMRI has done in clinical and preclinical models, mainly due to its capacity to detect abnormalities under pathological conditions. During the last years, great progress has been made in preclinical models, by developing tools for analysis and characterizing resting-state networks mainly in rodents. The achievement of the standardization of data analysis approaches, acquisition and anaesthetic protocols would be of utmost importance for reproducibility of the technique, and a very recently published work stress these points in deep [472]. Actually, the analytical approach carried out can influence the obtained results and interpretation of data.

Even though we have made a contribution to develop imaging protocols and characterize demyelination and remyelination, it is interesting to highlight that apart from making progress in the understanding of the cuprizone model, it would be also interesting to develop novel animal models that could better mimic human multiple sclerosis hallmarks, and improve the translation of diagnostic and therapeutic tools into the clinics. We consider that the cuprizone model is a model of great use for the evaluation of therapies and understanding of myelin pathology. Nevertheless, the complexity of multiple sclerosis and the role that the immune system plays in this disease should not be underestimated. The EAE model, whose pathology might be more similar to the human MS, is not predictable and reproducible enough and the evaluation of therapies is challenging. Indeed, the lack of more complete animal models might be among the potential explanations for the poor efficiency that treatments show in clinical trials.

Therefore, in this work started in October 2016 we have provided further evidence for the interest of multiparametric MRI for the detection of pathological processes and assessment of myelin content that, combined by rs-fMRI, would result in a deep and complete view of the brain state in these pathologies. We hope that this work can contribute to the development of remyelinating therapies, not only in multiple sclerosis but also in other pathologies were demyelination causes damage.

Conclusions

1. Quantification of myelin in organotypic cultures by means of MRI might be challenging and might require the development of a thoroughly designed set up.

2. T2-weighted imaging, T1-weighted imaging and radial diffusivity have shown a high specificity in the cuprizone mouse model at high magnetic field.

3. T2-weighted imaging has exhibited the highest capacity to accurately monitor demyelination and remyelination processes in the cuprizone mouse model.

4. Radial diffusivity has shown to be sensitive to non-myelin related pathology in the APP mouse model of Alzheimer's disease, while T1-weighted and T2-weighted have not.

5. Diffusion-weighted imaging has shown to be highly sensitive for the detection of abnormalities in the mouse models used.

6. Amyloid plaques lead to volume loss and white matter and grey matter abnormalities in mouse brain, but not to myelin loss.

7. Tau protein might not cause white matter damage and atrophy in the mouse brain, while grey matter damage might take place.

8. Cuprizone administration to mice results in connectivity and function abnormalities during demyelination, which are reversed with remyelination.

9. Clemastine enhances remyelination and leads to the recovery of functional connectivity in the cuprizone mouse model

10. Brain connectivity shows an inverse U-shape curve pattern throughout mouse life, peaking at month 8 of life.

11. Combination of functional and multiparametric anatomical imaging for the evaluation of myelin pathology might be of interest for the evaluation of remyelination therapies.

Bibliography

[1] J. J. Harris and D. Attwell, "The Energetics of CNS White Matter," *J. Neurosci.*, vol. 32, no. 1, pp. 356–371, Jan. 2012.

[2] F. A. C. Azevedo *et al.*, "Equal numbers of neuronal and nonneuronal cells make the human brain an isometrically scaled-up primate brain," *J. Comp. Neurol.*, vol. 513, no. 5, pp. 532–541, 2009.

[3] A. Verkhratsky and A. Butt, *Glial Neurobiology*. Chichester, UK: John Wiley & Sons, Ltd, 2007.

[4] V. Parpura and P. G. Haydon, "Physiological astrocytic calcium levels stimulate glutamate release to modulate adjacent neurons," *Proc. Natl. Acad. Sci.*, vol. 97, no. 15, pp. 8629–8634, Jul. 2000.

[5] J. J. LoTurco, "Neural circuits in the 21st century: synaptic networks of neurons and glia.," *Proc. Natl. Acad. Sci. U. S. A.*, vol. 97, no. 15, pp. 8196–7, Jul. 2000.

[6] K. K. Bercury and W. B. Macklin, "Dynamics and Mechanisms of CNS Myelination," *Dev. Cell*, vol. 32, no. 4, pp. 447–458, Feb. 2015.

[7] J. I. Alvarez, T. Katayama, and A. Prat, "Glial influence on the blood brain barrier," *Glia*, vol. 61, no. 12, pp. 1939–1958, Dec. 2013.

[8] C. J. Jensen, A. Massie, and J. De Keyser, "Immune Players in the CNS: The Astrocyte," *J. Neuroimmune Pharmacol.*, vol. 8, no. 4, pp. 824–839, Sep. 2013.

[9] S. D. Skaper, L. Facci, and P. Giusti, "Mast cells, glia and neuroinflammation: partners in crime?," *Immunology*, vol. 141, no. 3, pp. 314–327, Mar. 2014.

[10] L. Xiao, R. Ide, and C. Saiki, "Stem cell therapy for central nerve system injuries: glial cells hold the key," *Neural Regen. Res.*, vol. 9, no. 13, p. 1253, 2014.

[11] H. Lodish, A. Berk, S. L. Zipursky, P. Matsudaira, D. Baltimore, and J. Darnell, "The Action Potential and Conduction of Electric Impulses," *Molecular Cell Biology. 4th edition.* 2000.

[12] C. Xu, X. Wang, and S. Wang, "[Effect of soybean protein and high calcium intake on the concentration of serum lipids in hypercholesterolemic rats].," *Zhonghua Yu Fang Yi Xue Za Zhi*, vol. 35, no. 5, pp. 318–21, Sep. 2001.

[13] K.-A. Nave and H. B. Werner, "Myelination of the Nervous System: Mechanisms and Functions," *Annu. Rev. Cell Dev. Biol.*, vol. 30, no. 1, pp. 503–533, Oct. 2014.

[14] S. PFEIFFER, A. WARRINGTON, and R. BANSAL, "The oligodendrocyte and its many cellular processes," *Trends Cell Biol.*, vol. 3, no. 6, pp. 191–197, Jun. 1993.

[15] H. Inouye and D. A. Kirschner, "Membrane interactions in nerve myelin. I.

Determination of surface charge from effects of pH and ionic strength on period," *Biophys. J.*, vol. 53, no. 2, pp. 235–245, Feb. 1988.

[16] F. I. Gruenenfelder, G. Thomson, J. Penderis, and J. M. Edgar, "Axon-glial interaction in the CNS: what we have learned from mouse models of Pelizaeus-Merzbacher disease," *J. Anat.*, vol. 219, no. 1, pp. 33–43, Jul. 2011.

[17] C. Lappe-Siefke *et al.*, "Disruption of Cnp1 uncouples oligodendroglial functions in axonal support and myelination," *Nat. Genet.*, vol. 33, no. 3, pp. 366–374, Mar. 2003.

[18] I. Griffiths, "Axonal Swellings and Degeneration in Mice Lacking the Major Proteolipid of Myelin," *Science (80-.).*, vol. 280, no. 5369, pp. 1610–1613, Jun. 1998.

[19] M. Baraban, S. Mensch, and D. A. Lyons, "Adaptive myelination from fish to man," *Brain Res.*, vol. 1641, pp. 149–161, Jun. 2016.

[20] T. Chomiak and B. Hu, "What Is the Optimal Value of the g-Ratio for Myelinated Fibers in the Rat CNS? A Theoretical Approach," *PLoS One*, vol. 4, no. 11, p. e7754, Nov. 2009.

[21] H. O. B. Gautier *et al.*, "Neuronal activity regulates remyelination via glutamate signalling to oligodendrocyte progenitors," *Nat. Commun.*, vol. 6, no. 1, p. 8518, Dec. 2015.

[22] I. A. McKenzie *et al.*, "Motor skill learning requires active central myelination," *Science (80-.).*, vol. 346, no. 6207, pp. 318–322, Oct. 2014.

[23] Y. Lee *et al.*, "Oligodendroglia metabolically support axons and contribute to neurodegeneration," *Nature*, vol. 487, no. 7408, pp. 443–448, Jul. 2012.

[24] A. S. Saab *et al.*, "Oligodendroglial NMDA Receptors Regulate Glucose Import and Axonal Energy Metabolism," *Neuron*, vol. 91, no. 1, pp. 119–132, Jul. 2016.

[25] I. Micu *et al.*, "The molecular physiology of the axo-myelinic synapse," *Exp. Neurol.*, vol. 276, pp. 41–50, Feb. 2016.

[26] J. R. Plemel, W. Liu, and V. W. Yong, "Remyelination therapies: multiple sclerosis," *Nat. Rev. Drug Discov.*, vol. 16, pp. 1–18, 2017.

[27] K. A. Irvine and W. F. Blakemore, "Remyelination protects axons from demyelination-associated axon degeneration," *Brain*, vol. 131, no. 6, pp. 1464–1477, 2008.

[28] S. G. Waxman, M. J. Craner, and J. A. Black, "Na+ channel expression along axons in multiple sclerosis and its models," *Trends Pharmacol. Sci.*, vol. 25, no. 11, pp. 584–591, Nov. 2004.

[29] A. M. Brown, R. Wender, and B. R. Ransom, "Ionic Mechanisms of Aglycemic Axon Injury in Mammalian Central White Matter," *J. Cereb. Blood Flow Metab.*, vol. 21, no. 4,

pp. 385–395, Apr. 2001.

[30] N. Kessaris, M. Fogarty, P. Iannarelli, M. Grist, M. Wegner, and W. D. Richardson, "Competing waves of oligodendrocytes in the forebrain and postnatal elimination of an embryonic lineage," *Nat. Neurosci.*, vol. 9, no. 2, pp. 173–179, 2006.

[31] H.-H. Tsai *et al.*, "Oligodendrocyte precursors migrate along vasculature in the developing nervous system," *Science (80-.).*, vol. 351, no. 6271, pp. 379–384, Jan. 2016.

[32] E. Dejana and C. Betsholtz, "Oligodendrocytes follow blood vessel trails in the brain," *Science (80-.).*, vol. 351, no. 6271, pp. 341–342, Jan. 2016.

[33] J. R. Patel and R. S. Klein, "Mediators of oligodendrocyte differentiation during remyelination," *FEBS Lett.*, vol. 585, no. 23, pp. 3730–3737, Dec. 2011.

[34] F. Mei *et al.*, "Accelerated remyelination during inflammatory demyelination prevents axonal loss and improves functional recovery," *Elife*, vol. 5, Sep. 2016.

[35] R. J. M. Franklin and C. Ffrench-Constant, "Remyelination in the CNS: from biology to therapy," *Nat. Rev. Neurosci.*, vol. 9, no. 11, pp. 839–855, Nov. 2008.

[36] R. J. M. Franklin, "Why does remyelination fail in multiple sclerosis?," *Nature Reviews Neuroscience*, vol. 3, no. 9. pp. 705–714, 2002.

[37] V. E. Miron, T. Kuhlmann, and J. P. Antel Jack P., "Cells of the oligodendroglial lineage, myelination, and remyelination," *Biochim. Biophys. Acta - Mol. Basis Dis.*, vol. 1812, no. 2, pp. 184–193, 2011.

[38] A. Alizadeh, S. M. Dyck, and S. Karimi-Abdolrezaee, "Myelin damage and repair in pathologic CNS: challenges and prospects.," *Front. Mol. Neurosci.*, vol. 8, no. July, p. 35, 2015.

[39] G. Wolswijk, "Chronic stage multiple sclerosis lesions contain a relatively quiescent population of oligodendrocyte precursor cells.," *J. Neurosci.*, vol. 18, no. 2, pp. 601–9, Jan. 1998.

[40] T. Kuhlmann, V. Miron, Q. Cuo, C. Wegner, J. Antel, and W. Bruck, "Differentiation block of oligodendroglial progenitor cells as a cause for remyelination failure in chronic multiple sclerosis," *Brain*, vol. 131, no. 7, pp. 1749–1758, Jul. 2008.

[41] R. H. Woodruff, M. Fruttiger, W. D. Richardson, and R. J. M. Franklin, "Platelet-derived growth factor regulates oligodendrocyte progenitor numbers in adult CNS and their response following CNS demyelination," *Mol. Cell. Neurosci.*, vol. 25, no. 2, pp. 252–262, 2004.

[42] M. S. Y. Yeung *et al.*, "Dynamics of oligodendrocyte generation and myelination in the human brain," *Cell*, vol. 159, no. 4, pp. 766–774, 2014.

[43] B. H. Toyama *et al.*, "Identification of Long-Lived Proteins Reveals Exceptional Stability of Essential Cellular Structures," *Cell*, vol. 154, no. 5, pp. 971–982, Aug. 2013.

[44] P. Villoslada, "Neuroprotective therapies for multiple sclerosis and other demyelinating diseases," *Mult. Scler. Demyelinating Disord.*, vol. 1, no. 1, p. 1, Dec. 2016.

[45] P. Patrikios *et al.*, "Remyelination is extensive in a subset of multiple sclerosis patients," *Brain*, vol. 129, no. 12, pp. 3165–3172, Jun. 2006.

[46] C. Confavreux and S. Vukusic, "Age at disability milestones in multiple sclerosis," *Brain*, vol. 129, no. 3, pp. 595–605, Mar. 2006.

[47] S. K. Ludwin, "Chronic demyelination inhibits remyelination in the central nervous system. An analysis of contributing factors," *Lab. Investig.*, 1980.

[48] E. S. Aliaga and F. Barkhof, "MRI mimics of multiple sclerosis," in *Handbook of Clinical Neurology*, vol. 122, 2014, pp. 291–316.

[49] C. Confavreux and S. Vukusic, "Non-specific immunosuppressants in the treatment of multiple sclerosis," *Clin. Neurol. Neurosurg.*, vol. 106, no. 3, pp. 263–269, Jun. 2004.

[50] B. A. C. Cree *et al.*, "Long-term evolution of multiple sclerosis disability in the treatment era," *Ann. Neurol.*, vol. 80, no. 4, pp. 499–510, Oct. 2016.

[51] A. J. Green *et al.*, "Clemastine fumarate as a remyelinating therapy for multiple sclerosis (ReBUILD): a randomised, controlled, double-blind, crossover trial," *Lancet*, vol. 390, no. 10111, pp. 2481–2489, Dec. 2017.

[52] D. Kremer *et al.*, "pHERV-W envelope protein fuels microglial cell-dependent damage of myelinated axons in multiple sclerosis," *Proc. Natl. Acad. Sci.*, vol. 116, no. 30, pp. 15216–15225, Jul. 2019.

[53] S. J. Jackson, G. Giovannoni, and D. Baker, "Fingolimod modulates microglial activation to augment markers of remyelination," *J. Neuroinflammation*, vol. 8, no. 1, p. 76, 2011.

[54] M. N. Alme *et al.*, "Fingolimod does not enhance cerebellar remyelination in the cuprizone model," *J. Neuroimmunol.*, vol. 285, pp. 180–186, Aug. 2015.

[55] E. Voss, P. Raab, C. Trebst, and M. Stangel, "Clinical approach to optic neuritis: pitfalls, red flags and differential diagnosis," *Ther. Adv. Neurol. Disord.*, vol. 4, no. 2, pp. 123–134, 2011.

[56] A. T. Toosy, D. F. Mason, and D. H. Miller, "Optic neuritis," *Lancet Neurol.*, vol. 13, no. 1, pp. 83–99, 2014.

[57] H. Roed, J. Frederiksen, A. Langkilde, T. L. Sørensen, M. Lauritzen, and F. Sellebjerg, "Systemic T-cell activation in acute clinically isolated optic neuritis," *J. Neuroimmunol.*, vol. 162, no. 1–2, pp. 165–172, May 2005.

[58] T. Jenkins, "New developments in the treatment of optic neuritis," *Eye Brain*, p. 83, Jun. 2010.

[59] A. Brusa, S. J. Jones, and G. T. Plant, "Long-term remyelination after optic neuritis," *Brain*, vol. 124, no. 3, pp. 468–479, Mar. 2001.

[60] S. J. Jones, "Visual evoked potentials after optic neuritis," *J. Neurol.*, vol. 240, no. 8, pp. 489–494, 1993.

[61] A. Brusa, S. J. Jones, R. Kapoor, D. H. Miller, and G. T. Plant, "Long-term recovery and fellow eye deterioration after optic neuritis, determined by serial visual evoked potentials," *J. Neurol.*, vol. 246, no. 9, pp. 776–782, Sep. 1999.

[62] S. J. Jones and A. Brusa, "Neurophysiological evidence for long-term repair of MS lesions: implications for axon protection," *J. Neurol. Sci.*, vol. 206, no. 2, pp. 193–198, Feb. 2003.

[63] M. S. Van Der Knaap, N. I. Wolf, and V. M. Heine, "Clinical Practice Leukodystrophies Five new things," *Neurol Clin Pr.*, vol. 6, no. October, pp. 506–514, 2016.

[64] N. Cartier *et al.*, "Hematopoietic Stem Cell Gene Therapy with a Lentiviral Vector in X-Linked Adrenoleukodystrophy," *Science (80-.).*, vol. 326, no. 5954, pp. 818–823, Nov. 2009.

[65] A. Biffi *et al.*, "Lentiviral Hematopoietic Stem Cell Gene Therapy Benefits Metachromatic Leukodystrophy," *Science (80-.).*, vol. 341, no. 6148, pp. 1233158–1233158, Aug. 2013.

[66] P. Leone *et al.*, "Long-Term Follow-Up After Gene Therapy for Canavan Disease," *Sci. Transl. Med.*, vol. 4, no. 165, p. 165ra163-165ra163, Dec. 2012.

[67] A. A. Boucher *et al.*, "Long-term outcomes after allogeneic hematopoietic stem cell transplantation for metachromatic leukodystrophy: the largest single-institution cohort report," *Orphanet J. Rare Dis.*, vol. 10, no. 1, p. 94, Dec. 2015.

[68] M. S. van der Knaap and M. Bugiani, "Leukodystrophies — much more than just diseases of myelin," *Nat. Rev. Neurol.*, vol. 14, no. 12, pp. 747–748, Dec. 2018.

[69] C. López-Otín, M. A. Blasco, L. Partridge, M. Serrano, and G. Kroemer, "The Hallmarks

of Aging," *Cell*, vol. 153, no. 6, pp. 1194–1217, Jun. 2013.

[70] M. L. Feldman and A. Peters, "Ballooning of myelin sheaths in normally aged macaques," *J. Neurocytol.*, vol. 27, no. 8, pp. 805–814, 1998.

[71] A. Peters and A. Peters, "The Effects of Normal Aging on Nerve Fibers and Neuroglia in the Central Nervous System," *Aging (Albany. NY).*, vol. 593, no. 2002, pp. 1–26, 2009.

[72] A. J. Mierzwa, C. M. Marion, G. M. Sullivan, D. P. McDaniel, and R. C. Armstrong, "Components of myelin damage and repair in the progression of white matter pathology after mild traumatic brain injury," *J. Neuropathol. Exp. Neurol.*, vol. 74, no. 3, pp. 218–232, 2015.

[73] A. Peters, M. B. Moss, and C. Sethares, "Effects of aging on myelinated nerve fibers in monkey primary visual cortex," *J. Comp. Neurol.*, vol. 419, no. 3, pp. 364–376, Apr. 2000.

[74] G. Bartzokis, "Age-related myelin breakdown: A developmental model of cognitive decline and Alzheimer's disease," *Neurobiol. Aging*, vol. 25, no. 1, pp. 5–18, 2004.

[75] A. S. Dekaban and D. Sadowsky, "Changes in brain weights during the span of human life: Relation of brain weights to body heights and body weights," *Ann. Neurol.*, vol. 4, no. 4, pp. 345–356, Oct. 1978.

[76] E. Kövari *et al.*, "Cortical Microinfarcts and Demyelination Significantly Affect Cognition in Brain Aging," *Stroke*, vol. 35, no. 2, pp. 410–414, Feb. 2004.

[77] R. J. M. Franklin, C. Zhao, and F. J. Sim, "Ageing and CNS remyelination," *Neuroreport*, vol. 13, no. 7, pp. 923–928, May 2002.

[78] S. Shen *et al.*, "Age-dependent epigenetic control of differentiation inhibitors is critical for remyelination efficiency," *Nat. Neurosci.*, vol. 11, no. 9, pp. 1024–1034, Sep. 2008.

[79] G. L. Hinks and R. J. M. Franklin, "Delayed Changes in Growth Factor Gene Expression during Slow Remyelination in the CNS of Aged Rats," *Mol. Cell. Neurosci.*, vol. 16, no. 5, pp. 542–556, Nov. 2000.

[80] S. A. Shields, J. M. Gilson, W. F. Blakemore, and R. J. M. Franklin, "Remyelination occurs as extensively but more slowly in old rats compared to young rats following gliotoxin-induced CNS demyelination," *Glia*, vol. 28, no. 1, pp. 77–83, Oct. 1999.

[81] L. Cantuti-Castelvetri *et al.*, "Defective cholesterol clearance limits remyelination in the aged central nervous system," *Science (80-.).*, vol. 359, no. 6376, pp. 684–688, Feb. 2018.

[82] J. M. Ruckh *et al.*, "Rejuvenation of regeneration in the aging central nervous system," *Cell Stem Cell*, vol. 10, no. 1, pp. 96–103, 2012.

[83] D. T. Lackland *et al.*, "Factors Influencing the Decline in Stroke Mortality," *Stroke*, vol. 45, no. 1, pp. 315–353, Jan. 2014.

[84] I. Ünal-Çevik, M. Kılınç, A. Can, Y. Gürsoy-Özdemir, and T. Dalkara, "Apoptotic and Necrotic Death Mechanisms Are Concomitantly Activated in the Same Cell After Cerebral Ischemia," *Stroke*, vol. 35, no. 9, pp. 2189–2194, Sep. 2004.

[85] B. A. Sutherland, J. Minnerup, J. S. Balami, F. Arba, A. M. Buchan, and C. Kleinschnitz, "Neuroprotection for Ischaemic Stroke: Translation from the Bench to the Bedside," *Int. J. Stroke*, vol. 7, no. 5, pp. 407–418, Jul. 2012.

[86] L. Catanese, J. Tarsia, and M. Fisher, "Acute Ischemic Stroke Therapy Overview," *Circ. Res.*, vol. 120, no. 3, pp. 541–558, Feb. 2017.

[87] J. Zhou *et al.*, "Long-Term Post-Stroke Changes Include Myelin Loss, Specific Deficits in Sensory and Motor Behaviors and Complex Cognitive Impairment Detected Using Active Place Avoidance," *PLoS One*, vol. 8, no. 3, p. e57503, Mar. 2013.

[88] H. Shi *et al.*, "Demyelination as a rational therapeutic target for ischemic or traumatic brain injury," *Exp. Neurol.*, vol. 272, pp. 17–25, Oct. 2015.

[89] L. E. Wang *et al.*, "Degeneration of corpus callosum and recovery of motor function after stroke: A multimodal magnetic resonance imaging study," *Hum. Brain Mapp.*, vol. 33, no. 12, pp. 2941–2956, 2012.

[90] R. Zhang, M. Chopp, and Z. G. Zhang, "Oligodendrogenesis after cerebral ischemia," *Frontiers in Cellular Neuroscience*, vol. 7, no. OCT. pp. 1–7, 2013.

[91] E. G. Hughes, S. H. Kang, M. Fukaya, and D. E. Bergles, "Oligodendrocyte progenitors balance growth with self-repulsion to achieve homeostasis in the adult brain," *Nat. Neurosci.*, vol. 16, no. 6, pp. 668–676, Jun. 2013.

[92] S. Wang *et al.*, "Notch Receptor Activation Inhibits Oligodendrocyte Differentiation," *Neuron*, vol. 21, no. 1, pp. 63–75, Jul. 1998.

[93] S. P. J. Fancy *et al.*, "Axin2 as regulatory and therapeutic target in newborn brain injury and remyelination," *Nat. Neurosci.*, vol. 14, no. 8, pp. 1009–1016, Aug. 2011.

[94] E. G. Sozmen *et al.*, "Nogo receptor blockade overcomes remyelination failure after white matter stroke and stimulates functional recovery in aged mice," *Proc. Natl. Acad. Sci.*, vol. 113, no. 52, pp. E8453–E8462, Dec. 2016.

[95] N. Miyamoto *et al.*, "Phosphodiesterase III Inhibition Promotes Differentiation and

Survival of Oligodendrocyte Progenitors and Enhances Regeneration of Ischemic White Matter Lesions in the Adult Mammalian Brain," *J. Cereb. Blood Flow Metab.*, vol. 30, no. 2, pp. 299–310, Feb. 2010.

[96] J. Sun *et al.*, "WIN55, 212-2 promotes differentiation of oligodendrocyte precursor cells and improve remyelination through regulation of the phosphorylation level of the ERK 1/2 via cannabinoid receptor 1 after stroke-induced demyelination," *Brain Res.*, vol. 1491, pp. 225–235, Jan. 2013.

[97] J. Nair and V. Kumar, "Current and Emerging Therapies in the Management of Hypoxic Ischemic Encephalopathy in Neonates," *Children*, vol. 5, no. 7, p. 99, Jul. 2018.

[98] J. Zhang *et al.*, "Bone Marrow Stromal Cells Increase Oligodendrogenesis after Stroke," *J. Cereb. Blood Flow Metab.*, vol. 29, no. 6, pp. 1166–1174, Jun. 2009.

[99] L. Otero-Ortega *et al.*, "White Matter Repair After Extracellular Vesicles Administration in an Experimental Animal Model of Subcortical Stroke," *Sci. Rep.*, vol. 7, no. 1, p. 44433, Apr. 2017.

[100] B. H. Chen *et al.*, "Melatonin improves vascular cognitive impairment induced by ischemic stroke by remyelination via activation of ERK1/2 signaling and restoration of glutamatergic synapses in the gerbil hippocampus," *Biomed. Pharmacother.*, vol. 108, no. August, pp. 687–697, Dec. 2018.

[101] A. Serrano-Pozo, M. P. Frosch, E. Masliah, and B. T. Hyman, "Neuropathological Alterations in Alzheimer Disease," *Cold Spring Harb. Perspect. Med.*, vol. 1, no. 1, pp. a006189–a006189, Sep. 2011.

[102] D. J. Selkoe and J. Hardy, "The amyloid hypothesis of Alzheimer's disease at 25 years," *EMBO Mol. Med.*, vol. 8, no. 6, pp. 595–608, Jun. 2016.

[103] S. E. Nasrabady, B. Rizvi, J. E. Goldman, and A. M. Brickman, "White matter changes in Alzheimer's disease: a focus on myelin and oligodendrocytes," *Acta Neuropathol. Commun.*, vol. 6, no. 1, p. 22, Dec. 2018.

[104] K. Mullane and M. Williams, "Alzheimer's therapeutics: Continued clinical failures question the validity of the amyloid hypothesis—but what lies beyond?," *Biochem. Pharmacol.*, vol. 85, no. 3, pp. 289–305, Feb. 2013.

[105] D. J. Selkoe, "Resolving controversies on the path to Alzheimer's therapeutics," *Nature Medicine*. 2011.

[106] X. Zhan *et al.*, "Myelin Basic Protein Associates with AβPP, Aβ1-42, and Amyloid Plaques in Cortex of Alzheimer's Disease Brain," *J. Alzheimer's Dis.*, vol. 44, no. 4, pp. 1213–1229, Feb. 2015.

[107] A. E. Roher *et al.*, "Increased Aβ Peptides and Reduced Cholesterol and Myelin Proteins Characterize White Matter Degeneration in Alzheimer's Disease †," *Biochemistry*, vol. 41, no. 37, pp. 11080–11090, Sep. 2002.

[108] M. K. Desai, K. L. Sudol, M. C. Janelsins, M. A. Mastrangelo, M. E. Frazer, and W. J. Bowers, "Triple-transgenic Alzheimer's disease mice exhibit region-specific abnormalities in brain myelination patterns prior to appearance of amyloid and tau pathology," *Glia*, vol. 57, no. 1, pp. 54–65, 2009.

[109] H. Lassmann *et al.*, "Cell death in Alzheimer's disease evaluated by DNA fragmentation in situ," *Acta Neuropathol.*, vol. 89, no. 1, pp. 35–41, Jan. 1995.

[110] D. J. Selkoe, "Resolving controversies on the path to Alzheimer's therapeutics," *Nat. Med.*, vol. 17, no. 9, pp. 1060–1065, Sep. 2011.

[111] J.-T. Lee *et al.*, "Amyloid-β peptide induces oligodendrocyte death by activating the neutral sphingomyelinase–ceramide pathway," *J. Cell Biol.*, vol. 164, no. 1, pp. 123–131, Jan. 2004.

[112] J. Xu *et al.*, "Amyloid-beta peptides are cytotoxic to oligodendrocytes.," *J. Neurosci.*, vol. 21, no. 1, p. 118, Jan. 2001.

[113] N. Jantaratnotai, J. K. Ryu, S. U. Kim, and J. G. McLarnon, "Amyloid β peptide-induced corpus callosum damage and glial activation in vivo," *Neuroreport*, vol. 14, no. 11, pp. 1429–1433, Aug. 2003.

[114] X. Cui *et al.*, "Donepezil, a drug for Alzheimer's disease, promotes oligodendrocyte generation and remyelination," *Acta Pharmacol. Sin.*, vol. 40, no. 11, pp. 1386–1393, Nov. 2019.

[115] N. Aggarwal, R. Shah, and D. Bennett, "Alzheimer's disease: Unique markers for diagnosis & new treatment modalities," *Indian J. Med. Res.*, vol. 142, no. 4, p. 369, 2015.

[116] B. T. Gold, N. F. Johnson, D. K. Powell, and C. D. Smith, "White matter integrity and vulnerability to Alzheimer's disease: Preliminary findings and future directions," *Biochim. Biophys. Acta - Mol. Basis Dis.*, vol. 1822, no. 3, pp. 416–422, Mar. 2012.

[117] D. Wu *et al.*, "LINGO-1 antibody ameliorates myelin impairment and spatial memory deficits in the early stage of 5XFAD mice," *CNS Neurosci. Ther.*, vol. 24, no. 5, pp. 381–393, May 2018.

[118] D. Cadavid *et al.*, "Safety and efficacy of opicinumab in patients with relapsing multiple sclerosis (SYNERGY): a randomised, placebo-controlled, phase 2 trial," *Lancet Neurol.*, vol. 18, no. 9, pp. 845–856, Sep. 2019.

[119] E. Golding, “Sequelae following traumatic brain injury The cerebrovascular perspective,” *Brain Res. Rev.*, vol. 38, no. 3, pp. 377–388, Feb. 2002.

[120] G. Spitz, J. J. Maller, R. O’Sullivan, and J. L. Ponsford, “White Matter Integrity Following Traumatic Brain Injury: The Association with Severity of Injury and Cognitive Functioning,” *Brain Topogr.*, vol. 26, no. 4, pp. 648–660, Oct. 2013.

[121] P. Perel, I. Roberts, O. Bouamra, M. Woodford, J. Mooney, and F. Lecky, “Intracranial bleeding in patients with traumatic brain injury: A prognostic study,” *BMC Emerg. Med.*, vol. 9, no. 1, p. 15, Dec. 2009.

[122] H. Takase *et al.*, “Oligodendrogenesis after traumatic brain injury,” *Behavioural Brain Research*, vol. 340. Elsevier B.V., pp. 205–211, 2018.

[123] J. Flygt, A. Djupsjö, F. Lenne, and N. Marklund, “Myelin loss and oligodendrocyte pathology in white matter tracts following traumatic brain injury in the rat,” *Eur. J. Neurosci.*, vol. 38, no. 1, pp. 2153–2165, 2013.

[124] M. Haber *et al.*, “Minocycline plus N-acteylcysteine induces remyelination, synergistically protects oligodendrocytes and modifies neuroinflammation in a rat model of mild traumatic brain injury,” *J. Cereb. Blood Flow Metab.*, vol. 38, no. 8, pp. 1312–1326, 2018.

[125] J. Flygt *et al.*, “Neutralization of Interleukin-1β following Diffuse Traumatic Brain Injury in the Mouse Attenuates the Loss of Mature Oligodendrocytes,” *J. Neurotrauma*, vol. 35, no. 23, pp. 2837–2849, Dec. 2018.

[126] D. A. Shear *et al.*, “Neural progenitor cell transplants promote long-term functional recovery after traumatic brain injury,” *Brain Res.*, vol. 1026, no. 1, pp. 11–22, 2004.

[127] F. Wu *et al.*, “Vitamin B12 Enhances Nerve Repair and Improves Functional Recovery After Traumatic Brain Injury by Inhibiting ER Stress-Induced Neuron Injury,” *Front. Pharmacol.*, vol. 10, no. April, pp. 1–12, Apr. 2019.

[128] B. Fehily and M. Fitzgerald, “Repeated Mild Traumatic Brain Injury,” *Cell Transplant.*, vol. 26, no. 7, pp. 1131–1155, Jul. 2017.

[129] J. J. Bazarian *et al.*, “Persistent, Long-term Cerebral White Matter Changes after Sports-Related Repetitive Head Impacts,” *PLoS One*, vol. 9, no. 4, p. e94734, Apr. 2014.

[130] J. D. Guest, E. D. Hiester, and R. P. Bunge, “Demyelination and Schwann cell responses adjacent to injury epicenter cavities following chronic human spinal cord injury,” *Exp. Neurol.*, vol. 192, no. 2, pp. 384–393, 2005.

[131] X. Z. Liu *et al.*, “Neuronal and glial apoptosis after traumatic spinal cord injury.,” *J. Neurosci.*, vol. 17, no. 14, pp. 5395–406, Jul. 1997.

[132] M. J. Crowe, J. C. Bresnahan, S. L. Shuman, J. N. Masters, and M. S. Beattie, "Apoptosis and delayed degeneration after spinal cord injury in rats and monkeys," *Nat. Med.*, vol. 3, no. 1, pp. 73–76, Jan. 1997.

[133] Z. C. Hesp, E. A. Goldstein, C. J. Miranda, B. K. Kaspar, and D. M. McTigue, "Chronic oligodendrogenesis and remyelination after spinal cord injury in mice and rats," *J. Neurosci.*, vol. 35, no. 3, pp. 1274–1290, 2015.

[134] K. A. Dent *et al.*, "Oligodendrocyte birth and death following traumatic brain injury in adult mice," *PLoS One*, vol. 10, no. 3, pp. 1–17, 2015.

[135] J. Lasiene, L. Shupe, S. Perlmutter, and P. Horner, "No Evidence for Chronic Demyelination in Spared Axons after Spinal Cord Injury in a Mouse," *J. Neurosci.*, vol. 28, no. 15, pp. 3887–3896, Apr. 2008.

[136] H. Takase *et al.*, "Oligodendrogenesis after traumatic brain injury," *Behav. Brain Res.*, vol. 340, pp. 205–211, Mar. 2018.

[137] M. O. Totoiu and H. S. Keirstead, "Spinal cord injury is accompanied by chronic progressive demyelination," *J. Comp. Neurol.*, vol. 486, no. 4, pp. 373–383, Jun. 2005.

[138] M. Mekhail, G. Almazan, and M. Tabrizian, "Oligodendrocyte-protection and remyelination post-spinal cord injuries : A review," *Prog. Neurobiol.*, vol. 96, no. 3, pp. 322–339, 2012.

[139] K. S. Straley, C. W. P. Foo, and S. C. Heilshorn, "Biomaterial Design Strategies for the Treatment of Spinal Cord Injuries," *J. Neurotrauma*, vol. 27, no. 1, pp. 1–19, Jan. 2010.

[140] Y.-X. Zhou, R. Pannu, T. Q. Le, and R. C. Armstrong, "Fibroblast growth factor 1 (FGFR1) modulation regulates repair capacity of oligodendrocyte progenitor cells following chronic demyelination," *Neurobiol. Dis.*, vol. 45, no. 1, pp. 196–205, Jan. 2012.

[141] F. M. Bareyre, M. Kerschensteiner, O. Raineteau, T. C. Mettenleiter, O. Weinmann, and M. E. Schwab, "The injured spinal cord spontaneously forms a new intraspinal circuit in adult rats," *Nat. Neurosci.*, vol. 7, no. 3, pp. 269–277, Mar. 2004.

[142] A. S. Wahl *et al.*, "Asynchronous therapy restores motor control by rewiring of the rat corticospinal tract after stroke," *Science (80-.).*, vol. 344, no. 6189, pp. 1250–1255, Jun. 2014.

[143] B. V. Ineichen, P. S. Plattner, N. Good, R. Martin, M. Linnebank, and M. E. Schwab, "Nogo-A Antibodies for Progressive Multiple Sclerosis," *CNS Drugs*, vol. 31, no. 3, pp. 187–198, 2017.

[144] Z. Li, Y. He, S. Fan, and B. Sun, "Clemastine rescues behavioral changes and enhances

remyelination in the cuprizone mouse model of demyelination," *Neurosci. Bull.*, vol. 31, no. 5, pp. 617–625, 2015.

[145] J. Liu *et al.*, "Clemastine Enhances Myelination in the Prefrontal Cortex and Rescues Behavioral Changes in Socially Isolated Mice," *J. Neurosci.*, vol. 36, no. 3, pp. 957–962, Jan. 2016.

[146] B. A. C. Cree *et al.*, "Clemastine rescues myelination defects and promotes functional recovery in hypoxic brain injury," *Brain*, vol. 141, no. 1, pp. 85–98, 2018.

[147] F. Mei *et al.*, "Micropillar arrays as a high-throughput screening platform for therapeutics in multiple sclerosis," *Nat. Med.*, vol. 20, no. 8, pp. 954–960, 2014.

[148] M. Haber *et al.*, "Minocycline plus N-acteylcysteine induces remyelination, synergistically protects oligodendrocytes and modifies neuroinflammation in a rat model of mild traumatic brain injury," *J. Cereb. Blood Flow Metab.*, vol. 38, no. 8, pp. 1312–1326, Aug. 2018.

[149] C. W. N. S. S. J. R. B. Usselman, "乳鼠心肌提取 HHS Public Access," *Physiol. Behav.*, vol. 176, no. 3, pp. 139–148, 2017.

[150] J. C. Dugas, Y. C. Tai, T. P. Speed, J. Ngai, and B. A. Barres, "Functional Genomic Analysis of Oligodendrocyte Differentiation," *J. Neurosci.*, vol. 26, no. 43, pp. 10967–10983, Oct. 2006.

[151] A. P. Robinson, J. M. Rodgers, G. E. Goings, and S. D. Miller, "Characterization of Oligodendroglial Populations in Mouse Demyelinating Disease Using Flow Cytometry: Clues for MS Pathogenesis," *PLoS One*, vol. 9, no. 9, p. e107649, Sep. 2014.

[152] J. Newville, L. Jantzie, and L. Cunningham, "Embracing oligodendrocyte diversity in the context of perinatal injury," *Neural Regen. Res.*, vol. 12, no. 10, p. 1575, 2017.

[153] Z. Chen *et al.*, "Oligodendrocyte–spinal cord explant co-culture: An in vitro model for the study of myelination," *Brain Res.*, vol. 1309, pp. 9–18, Jan. 2010.

[154] S. Lee *et al.*, "A culture system to study oligodendrocyte myelination processes using engineered nanofibers," *Nat. Methods*, vol. 9, no. 9, pp. 917–922, Sep. 2012.

[155] N. Daviaud, E. Garbayo, P. C. Schiller, M. Perez-Pinzon, and C. N. Montero-Menei, "Organotypic cultures as tools for optimizing central nervous system cell therapies," *Exp. Neurol.*, vol. 248, pp. 429–440, 2013.

[156] H. Zhang, A. A. Jarjour, A. Boyd, and A. Williams, "Central nervous system remyelination in culture - A tool for multiple sclerosis research," *Exp. Neurol.*, vol. 230, no. 1, pp. 138–148, 2011.

[157] E. Birgbauer, T. S. Rao, and M. Webb, "Lysolecithin induces demyelination in vitro in a cerebellar slice culture system," *J. Neurosci. Res.*, vol. 78, no. 2, pp. 157–166, 2004.

[158] G. A. Tan, K. L. Furber, M. P. Thangaraj, L. R. Sobchishin, J. R. Doucette, and A. J. Nazarali, "Organotypic Cultures from the Adult CNS: A Novel Model to Study Demyelination and Remyelination Ex Vivo," *Cell. Mol. Neurobiol.*, vol. 38, no. 1, pp. 317–328, 2018.

[159] R. N. Nishimura, N. K. Blank, K. L. Tiekotter, R. Cole, and J. De Vellis, "Myelination of mouse cerebellar explants by rat cultured oligodendrocytes," *Brain Res.*, vol. 337, no. 1, pp. 159–162, 1985.

[160] C. Humpel, "Organotypic brain slice cultures: A review," *Neuroscience*, vol. 305, pp. 86–98, Oct. 2015.

[161] K. Rambani, J. Vukasinovic, A. Glezer, and S. M. Potter, "Culturing thick brain slices: An interstitial 3D microperfusion system for enhanced viability," *J. Neurosci. Methods*, vol. 180, no. 2, pp. 243–254, Jun. 2009.

[162] Y. Pang, B. Zheng, S. L. Kimberly, Z. Cai, P. G. Rhodes, and R. C. S. Lin, "Neuron-oligodendrocyte myelination co-culture derived from embryonic rat spinal cord and cerebral cortex," *Brain Behav.*, vol. 2, no. 1, pp. 53–67, Jan. 2012.

[163] N. Gogolla, I. Galimberti, V. DePaola, and P. Caroni, "Long-term live imaging of neuronal circuits in organotypic hippocampal slice cultures," *Nat. Protoc.*, vol. 1, no. 3, pp. 1223–1226, Aug. 2006.

[164] I. Osorio-Querejeta, M. Sáenz-Cuesta, M. Muñoz-Culla, and D. Otaegui, "Models for Studying Myelination, Demyelination and Remyelination," *NeuroMolecular Med.*, vol. 19, no. 2–3, pp. 181–192, 2017.

[165] D. A. Lyons *et al.*, "erbb3 and erbb2 Are Essential for Schwann Cell Migration and Myelination in Zebrafish," *Curr. Biol.*, vol. 15, no. 6, pp. 513–524, Mar. 2005.

[166] Q. Bai, M. Sun, D. B. Stolz, and E. A. Burton, "Major isoform of zebrafish P0 is a 23.5 kDa myelin glycoprotein expressed in selected white matter tracts of the central nervous system," *J. Comp. Neurol.*, vol. 519, no. 8, pp. 1580–1596, Jun. 2011.

[167] D. J. Burrows *et al.*, "Animal models of multiple sclerosis: From rodents to zebrafish," *Mult. Scler. J.*, vol. 25, no. 3, pp. 306–324, 2019.

[168] B. B. Kirby *et al.*, "In vivo time-lapse imaging shows dynamic oligodendrocyte progenitor behavior during zebrafish development," *Nat. Neurosci.*, vol. 9, no. 12, pp. 1506–1511, Dec. 2006.

[169] P. Kulkarni, S. Yellanki, R. Medishetti, D. Sriram, U. Saxena, and P. Yogeeswari, "Novel

Zebrafish EAE model: A quick in vivo screen for multiple sclerosis," *Mult. Scler. Relat. Disord.*, vol. 11, pp. 32–39, Jan. 2017.

[170] A. A. Jarjour, H. Zhang, N. Bauer, C. ffrench-Constant, and A. Williams, "In vitro modeling of central nervous system myelination and remyelination," *Glia*, vol. 60, no. 1, pp. 1–12, 2012.

[171] S. Heimerl *et al.*, "Alterations of Plasma Lysophosphatidylcholine Species in Obesity and Weight Loss," *PLoS One*, vol. 9, no. 10, p. e111348, Oct. 2014.

[172] J. Y. Park, S.-H. Lee, M.-J. Shin, and G.-S. Hwang, "Alteration in Metabolic Signature and Lipid Metabolism in Patients with Angina Pectoris and Myocardial Infarction," *PLoS One*, vol. 10, no. 8, p. e0135228, Aug. 2015.

[173] S. Ma *et al.*, "Cell culture-based profiling across mammals reveals DNA repair and metabolism as determinants of species longevity," *Elife*, vol. 5, Nov. 2016.

[174] J. R. Plemel *et al.*, "Mechanisms of lysophosphatidylcholine-induced demyelination: A primary lipid disrupting myelinopathy," *Glia*, vol. 66, no. 2, pp. 327–347, Feb. 2018.

[175] J. Yoo and Q. Cui, "Curvature Generation and Pressure Profile Modulation in Membrane by Lysolipids: Insights from Coarse-Grained Simulations," *Biophys. J.*, vol. 97, no. 8, pp. 2267–2276, Oct. 2009.

[176] B. Nait-Oumesmar, L. Decker, F. Lachapelle, V. Avellana-Adalid, C. Bachelin, and A. B.-. Van Evercooren, "Progenitor cells of the adult mouse subventricular zone proliferate, migrate and differentiate into oligodendrocytes after demyelination," *Eur. J. Neurosci.*, vol. 11, no. 12, pp. 4357–4366, Dec. 1999.

[177] R. H. Woodruff and R. J. M. Franklin, "Demyelination and remyelination of the caudal cerebellar peduncle of adult rats following stereotaxic injections of lysolecithin, ethidium bromide, and complement/anti-galactocerebroside: A comparative study," *Glia*, vol. 25, no. 3, pp. 216–228, Feb. 1999.

[178] N. D. Jeffery and W. F. Blakemore, "Remyelination of mouse spinal cord axons demyelinated by local injection of lysolecithin.," *J. Neurocytol.*, vol. 24, no. 10, pp. 775–81, Oct. 1995.

[179] C. Wang and M. R. Kotter, "Experimental Demyelination and Remyelination of Murine Spinal Cord by Focal Injection of Lysolecithin," in *Methods in Molecular Biology*, vol. 1791, no. March, 2018, pp. 233–241.

[180] L. J. Lehto *et al.*, "Lysophosphatidyl Choline Induced Demyelination in Rat Probed by Relaxation along a Fictitious Field in High Rank Rotating Frame," *Front. Neurosci.*, vol. 11, Aug. 2017.

[181] W. F. Blakemore, “Ethidium bromide induced demyelination in the spinal cord of the cat,” *Neuropathol. Appl. Neurobiol.*, vol. 8, pp. 365–375, 1982.

[182] W. F. Blakemore, “The case for a central nervous system (CNS) origin for the Schwann cells that remyelinate CNS axons following concurrent loss of oligodendrocytes and astrocytes,” *Neuropathol. Appl. Neurobiol.*, vol. 31, no. 1, pp. 1–10, Feb. 2005.

[183] M. Lindner *et al.*, “Sequential myelin protein expression during remyelination reveals fast and efficient repair after central nervous system demyelination,” *Neuropathol. Appl. Neurobiol.*, p. 071026235340007–???, Oct. 2007.

[184] T. Skripuletz, V. Gudi, D. Hackstette, and M. Stangel, “De- and remyelination in the CNS white and grey matter induced by cuprizone: The old, the new, and the unexpected,” *Histol. Histopathol.*, vol. 26, no. 12, pp. 1585–1597, 2011.

[185] M. Lindner, J. Fokuhl, F. Linsmeier, C. Trebst, and M. Stangel, “Chronic toxic demyelination in the central nervous system leads to axonal damage despite remyelination,” *Neurosci. Lett.*, vol. 453, no. 2, pp. 120–125, Apr. 2009.

[186] N. S. Hübner *et al.*, “The connectomics of brain demyelination: Functional and structural patterns in the cuprizone mouse model,” *Neuroimage*, vol. 146, pp. 1–18, Feb. 2017.

[187] A. Petiet, M.-S. Aigrot, and B. Stankoff, “Gray and White Matter Demyelination and Remyelination Detected with Multimodal Quantitative MRI Analysis at 11.7T in a Chronic Mouse Model of Multiple Sclerosis,” *Front. Neurosci.*, vol. 10, no. OCT, pp. 1–10, Oct. 2016.

[188] S. A. Berghoff *et al.*, “Blood-brain barrier hyperpermeability precedes demyelination in the cuprizone model,” *Acta Neuropathol. Commun.*, vol. 5, no. 1, p. 94, 2017.

[189] E. J. McMahon, K. Suzuki, and G. K. Matsushima, “Peripheral macrophage recruitment in cuprizone-induced CNS demyelination despite an intact blood-brain barrier,” *J. Neuroimmunol.*, vol. 130, no. 1–2, pp. 32–45, 2002.

[190] W. Xu, T. Barrientos, and N. C. Andrews, “Iron and Copper in Mitochondrial Diseases,” *Cell Metab.*, vol. 17, no. 3, pp. 319–328, Mar. 2013.

[191] A. Nack *et al.*, “Expression of Translocator Protein and [18F]-GE180 Ligand Uptake in Multiple Sclerosis Animal Models,” *Cells*, vol. 8, no. 2, p. 94, Jan. 2019.

[192] B. D. Butts, C. Houde, and H. Mehmet, “Maturation-dependent sensitivity of oligodendrocyte lineage cells to apoptosis: implications for normal development and disease,” *Cell Death Differ.*, vol. 15, no. 7, pp. 1178–1186, Jul. 2008.

[193] M. M. Hiremath, Y. Saito, G. W. Knapp, J. P.-Y. Ting, K. Suzuki, and G. K. Matsushima,

"Microglial/macrophage accumulation during cuprizone-induced demyelination in C57BL/6 mice," *J. Neuroimmunol.*, vol. 92, no. 1–2, pp. 38–49, Dec. 1998.

[194] V. Gudi, S. Gingele, T. Skripuletz, and M. Stangel, "Glial response during cuprizone-induced de- and remyelination in the CNS: lessons learned.," *Front. Cell. Neurosci.*, vol. 8, no. March, p. 73, 2014.

[195] N. Manrique-Hoyos *et al.*, "Late motor decline after accomplished remyelination: Impact for progressive multiple sclerosis," *Ann. Neurol.*, vol. 71, no. 2, pp. 227–244, 2012.

[196] I. Tagge *et al.*, "Spatio-temporal patterns of demyelination and remyelination in the cuprizone mouse model," *PLoS One*, vol. 11, no. 4, pp. 1–24, 2016.

[197] A. Hagiwara *et al.*, "Myelin Measurement: Comparison between Simultaneous Tissue Relaxometry, Magnetization Transfer Saturation Index, and T1w/T2w Ratio Methods," *Sci. Rep.*, vol. 8, no. 1, pp. 1–12, 2018.

[198] J. D. Thiessen *et al.*, "Quantitative MRI and ultrastructural examination of the cuprizone mouse model of demyelination," *NMR Biomed.*, vol. 26, no. 11, pp. 1562–1581, 2013.

[199] S. Fjær *et al.*, "Deep gray matter demyelination detected by magnetization transfer ratio in the cuprizone model," *PLoS One*, vol. 8, no. 12, 2013.

[200] V. Schultz *et al.*, "Acutely damaged axons are remyelinated in multiple sclerosis and experimental models of demyelination," *Glia*, vol. 65, no. 8, pp. 1350–1360, Aug. 2017.

[201] B. M. Krauspe *et al.*, "Short-Term Cuprizone Feeding Verifies N-Acetylaspartate Quantification as a Marker of Neurodegeneration," *J. Mol. Neurosci.*, vol. 55, no. 3, pp. 733–748, Mar. 2015.

[202] T. C. Wood *et al.*, "Whole-brain ex-vivo quantitative MRI of the cuprizone mouse model," *PeerJ*, vol. 4, p. e2632, 2016.

[203] E. van Tilborg, C. M. van Kammen, C. G. M. de Theije, M. P. A. van Meer, R. M. Dijkhuizen, and C. H. Nijboer, "A quantitative method for microstructural analysis of myelinated axons in the injured rodent brain," *Sci. Rep.*, vol. 7, no. 1, p. 16492, Dec. 2017.

[204] C. S. Constantinescu, N. Farooqi, K. O'Brien, and B. Gran, "Experimental autoimmune encephalomyelitis (EAE) as a model for multiple sclerosis (MS)," *Br. J. Pharmacol.*, vol. 164, no. 4, pp. 1079–1106, Oct. 2011.

[205] S. KUERTEN *et al.*, "MP4- and MOG:35–55-induced EAE in C57BL/6 mice

differentially targets brain, spinal cord and cerebellum☆," *J. Neuroimmunol.*, vol. 189, no. 1–2, pp. 31–40, Sep. 2007.

[206] A. P. Robinson, C. T. Harp, A. Noronha, and S. D. Miller, "The experimental autoimmune encephalomyelitis (EAE) model of MS," in *Handbook of Clinical Neurology*, 2014, pp. 173–189.

[207] M. Peiris, G. R. Monteith, S. J. Roberts-Thomson, and P. J. Cabot, "A model of experimental autoimmune encephalomyelitis (EAE) in C57BL/6 mice for the characterisation of intervention therapies," *J. Neurosci. Methods*, vol. 163, no. 2, pp. 245–254, 2007.

[208] J. F. Kurtzke, "Epidemiologic contributions to multiple sclerosis: An overview," *Neurology*, vol. 30, no. Issue 7, Part 2, pp. 61–79, Jul. 1980.

[209] A. J. Bieber, D. R. Ure, and M. Rodriguez, "Genetically Dominant Spinal Cord Repair in a Murine Model of Chronic Progressive Multiple Sclerosis," *J. Neuropathol. Exp. Neurol.*, vol. 64, no. 1, pp. 46–57, Jan. 2005.

[210] I. Pirko, J. Gamez, A. J. Johnson, S. I. Macura, and M. Rodriguez, "Dynamics of MRI lesion development in an animal model of viral-induced acute progressive CNS demyelination," *Neuroimage*, vol. 21, no. 2, pp. 576–582, Feb. 2004.

[211] I. PIRKO *et al.*, "A human antibody that promotes remyelination enters the CNS and decreases lesion load as detected by T2-weighted spinal cord MRI in a virus-induced murine model of MS," *FASEB J.*, vol. 18, no. 13, pp. 1577–1579, Oct. 2004.

[212] I. Pirko, T. K. Nolan, S. K. Holland, and A. J. Johnson, "Multiple Sclerosis: Pathogenesis and MR Imaging Features of T1 Hypointensities in Murine Model," *Radiology*, vol. 246, no. 3, pp. 790–795, Mar. 2008.

[213] I. Pirko, A. J. Johnson, A. K. Lohrey, Y. Chen, and J. Ying, "Deep gray matter T2 hypointensity correlates with disability in a murine model of MS," *J. Neurol. Sci.*, vol. 282, no. 1–2, pp. 34–38, Jul. 2009.

[214] M. M. Paz Soldán *et al.*, "Correlation of Brain Atrophy, Disability, and Spinal Cord Atrophy in a Murine Model of Multiple Sclerosis," *J. Neuroimaging*, vol. 25, no. 4, pp. 595–599, Jul. 2015.

[215] C. Laule *et al.*, "Magnetic resonance imaging of myelin," *Neurotherapeutics*, vol. 4, no. 3, pp. 460–484, Jul. 2007.

[216] J. Kiernan, "Histochemistry of Staining Methods for Normal and Degenerating Myelin in the Central and Peripheral Nervous Systems," *J. Histotechnol.*, vol. 30, no. 2, pp. 87–106, 2007.

[217] P. Prentø, "A contribution to the theory of biological staining based on the principles for structural organization of biological macromolecules," *Biotech. Histochem.*, vol. 76, no. 3, pp. 137–161, Jan. 2001.

[218] H. Klüver and E. Barrera, "A Method for the Combined Staining of Cells and Fibers in the Nervous System," *J. Neuropathol. Exp. Neurol.*, vol. 12, no. 4, pp. 400–403, Oct. 1953.

[219] J. K. F. Van Staden, "Application of phthalocyanines in flow- and sequential-injection analysis and microfluidics systems: A review," *Talanta*, vol. 139, pp. 75–88, 2015.

[220] V. Carriel, I. Garzón, M. Alaminos, and A. Campos, "Evaluation of myelin sheath and collagen reorganization pattern in a model of peripheral nerve regeneration using an integrated histochemical approach," *Histochem. Cell Biol.*, vol. 136, no. 6, pp. 709–717, Dec. 2011.

[221] V. Carriel, A. Campos, M. Alaminos, S. Raimondo, and S. Geuna, *Histochemistry of Single Molecules*, vol. 1560. New York, NY: Springer New York, 2017.

[222] J. B. M. Warntjes, A. Persson, J. Berge, and W. Zech, "Myelin detection using rapid quantitative MR imaging correlated to macroscopically registered luxol fast blue-stained brain specimens," *Am. J. Neuroradiol.*, vol. 38, no. 6, pp. 1096–1102, 2017.

[223] M. Y. Khodanovich *et al.*, "Histological validation of fast macromolecular proton fraction mapping as a quantitative myelin imaging method in the cuprizone demyelination model," *Sci. Rep.*, vol. 7, no. October 2016, pp. 1–12, 2017.

[224] R. CHOLEWIAK, L. BUTCHER, and N. KETTLEWELL, "Oil red O and hematoxylin: A rapid histologic technic," *Physiol. Behav.*, vol. 3, no. 4, pp. 585-IN6, Jul. 1968.

[225] L. Schmued, J. Bowyer, M. Cozart, D. Heard, Z. Binienda, and M. Paule, "Introducing Black-Gold II, a highly soluble gold phosphate complex with several unique advantages for the histochemical localization of myelin," *Brain Res.*, vol. 1229, pp. 210–217, Sep. 2008.

[226] F. A. Mithen, P. M. Wood, H. C. Agrawal, and R. P. Bunge, "Immunohistochemical study of myelin sheaths formed by oligodendrocytes interacting with dissociated dorsal root ganglion neurons in culture," *Brain Res.*, vol. 262, no. 1, pp. 63–69, Feb. 1983.

[227] C. Puckett *et al.*, "Myelin-specific proteolipid protein is expressed in myelinating schwann cells but is not incorporated into myelin sheaths," *J. Neurosci. Res.*, vol. 18, no. 4, pp. 511–518, 1987.

[228] F. Di Scipio, S. Raimondo, P. Tos, and S. Geuna, "A simple protocol for paraffin-embedded myelin sheath staining with osmium tetroxide for light microscope observation," *Microsc. Res. Tech.*, vol. 71, no. 7, pp. 497–502, Jul. 2008.

[229] D. Purger, E. M. Gibson, and M. Monje, "Myelin plasticity in the central nervous system," *Neuropharmacology*, vol. 110, pp. 563–573, 2016.

[230] M. F. Stidworthy, S. Genoud, U. Suter, N. Mantei, and R. J. M. Franklin, "Quantifying the early stages of remyelination following cuprizone-induced demyelination.," *Brain Pathol.*, vol. 13, no. 3, pp. 329–39, Jul. 2003.

[231] R. Aharoni *et al.*, "Assessing remyelination - metabolic labeling of myelin in an animal model of multiple sclerosis," *J. Neuroimmunol.*, vol. 301, pp. 7–11, Dec. 2016.

[232] C. Y. Jao, M. Roth, R. Welti, and A. Salic, "Metabolic labeling and direct imaging of choline phospholipids in vivo," *Proc. Natl. Acad. Sci.*, vol. 106, no. 36, pp. 15332–15337, Sep. 2009.

[233] R. A. de Graaf, *In Vivo NMR Spectroscopy*. Chichester, UK: John Wiley & Sons, Ltd, 2007.

[234] M. A. Bernstein, K. F. King, and X. J. Zhou, *Handbook of MRI Pulse Sequences*. Elsevier, 2004.

[235] R. W. Brown, Y. C. N. Cheng, E. M. Haacke, M. R. Thompson, and R. Venkatesan, *Magnetic Resonance Imaging*. Chichester, UK: John Wiley & Sons Ltd, 2014.

[236] H.-L. Margaret Cheng, N. Stikov, N. R. Ghugre, and G. A. Wright, "Practical medical applications of quantitative MR relaxometry," *J. Magn. Reson. Imaging*, vol. 36, no. 4, pp. 805–824, Oct. 2012.

[237] M. W. Hayt, "MRI in practice," *Dentomaxillofacial Radiol.*, vol. 28, no. 1, pp. 66–66, Jan. 1999.

[238] S. H. Koenig, R. D. Brown, M. Spiller, and N. Lundbom, "Relaxometry of brain: Why white matter appears bright in MRI," *Magn. Reson. Med.*, vol. 14, no. 3, pp. 482–495, Jun. 1990.

[239] W. Kucharczyk, P. M. Macdonald, G. J. Stanisz, and R. M. Henkelman, "Relaxivity and magnetization transfer of white matter lipids at MR imaging: importance of cerebrosides and pH.," *Radiology*, vol. 192, no. 2, pp. 521–529, Aug. 1994.

[240] A. J. Barkovich, "Concepts of myelin and myelination in neuroradiology," *American Journal of Neuroradiology*. pp. 1099–1109, 2000.

[241] R. B. Dietrich *et al.*, "MR evaluation of early myelination patterns in normal and developmentally delayed infants," *Am. J. Neuroradiol.*, vol. 150, pp. 889–896, 1988.

[242] I. O. Jelescu *et al.*, "In vivo quantification of demyelination and recovery using compartment-specific diffusion MRI metrics validated by electron microscopy,"

Neuroimage, vol. 132, pp. 104–114, May 2016.

[243] D. Merkler *et al.*, "Multicontrast MRI of remyelination in the central nervous system," *NMR Biomed.*, vol. 18, no. 6, pp. 395–403, 2005.

[244] B. D. Trapp, R. Ransohoff, and R. Rudick, "Axonal pathology in multiple sclerosis: relationship to neurologic disability," *Curr. Opin. Neurol.*, vol. 12, no. 3, pp. 295–302, Jun. 1999.

[245] N. De Stefano *et al.*, "Evidence of Axonal Damage in the Early Stages of Multiple Sclerosis and Its Relevance to Disability," *Arch. Neurol.*, vol. 58, no. 1, Jan. 2001.

[246] K. Nakamura, J. T. Chen, D. Ontaneda, R. J. Fox, and B. D. Trapp, "T1-/T2-weighted ratio differs in demyelinated cortex in multiple sclerosis," *Ann. Neurol.*, vol. 82, no. 4, pp. 635–639, Oct. 2017.

[247] J. Iwatani *et al.*, "Use of T1-weighted/T2-weighted magnetic resonance ratio images to elucidate changes in the schizophrenic brain," *Brain Behav.*, vol. 5, no. 10, p. n/a-n/a, Oct. 2015.

[248] K. Shmueli, J. A. de Zwart, P. van Gelderen, T.-Q. Li, S. J. Dodd, and J. H. Duyn, "Magnetic susceptibility mapping of brain tissue in vivo using MRI phase data," *Magn. Reson. Med.*, vol. 62, no. 6, pp. 1510–1522, Dec. 2009.

[249] C. Wiggins, V. Gudmundsdottir, D. Le Bihan, V. Lebon, and M. Chaumeil, "Orientation Dependence of White Matter T2* Contrast at 7 T : A Direct Demonstration," in *Proceedings 16th Scientific Meeting, International Society for Magnetic Resonance in Medicine, Toronto*, 2008.

[250] J. Lee *et al.*, "The contribution of myelin to magnetic susceptibility-weighted contrasts in high-field MRI of the brain," *Neuroimage*, vol. 59, no. 4, pp. 3967–3975, 2012.

[251] N. Nathoo *et al.*, "Susceptibility-weighted imaging in the experimental autoimmune encephalomyelitis model of multiple sclerosis indicates elevated deoxyhemoglobin, iron deposition and demyelination," *Mult. Scler. J.*, vol. 19, no. 6, pp. 721–731, May 2013.

[252] I. Argyridis, W. Li, G. A. Johnson, and C. Liu, "Quantitative magnetic susceptibility of the developing mouse brain reveals microstructural changes in the white matter," *Neuroimage*, vol. 88, pp. 134–142, Mar. 2014.

[253] C. Liu, W. Li, G. A. Johnson, and B. Wu, "High-field (9.4T) MRI of brain dysmyelination by quantitative mapping of magnetic susceptibility," *Neuroimage*, vol. 56, no. 3, pp. 930–938, Jun. 2011.

[254] E. M. Haacke *et al.*, "Characterizing iron deposition in multiple sclerosis lesions using

susceptibility weighted imaging," *J. Magn. Reson. Imaging*, vol. 29, no. 3, pp. 537–544, Feb. 2009.

[255] B. Yao *et al.*, "Chronic Multiple Sclerosis Lesions: Characterization with High-Field-Strength MR Imaging," *Radiology*, vol. 262, no. 1, pp. 206–215, Jan. 2012.

[256] F. Bagnato *et al.*, "Tracking iron in multiple sclerosis: a combined imaging and histopathological study at 7 Tesla," *Brain*, vol. 134, no. 12, pp. 3602–3615, Dec. 2011.

[257] K. Deh *et al.*, "Magnetic susceptibility increases as diamagnetic molecules breakdown: Myelin digestion during multiple sclerosis lesion formation contributes to increase on QSM," *J. Magn. Reson. Imaging*, vol. 48, no. 5, pp. 1281–1287, Nov. 2018.

[258] R. M. Henkelman, G. J. Stanisz, and S. J. Graham, "Magnetization transfer in MRI: a review.," *NMR Biomed.*, vol. 14, no. 2, pp. 57–64, Apr. 2001.

[259] W. Zaaraoui *et al.*, "Monitoring demyelination and remyelination by magnetization transfer imaging in the mouse brain at 9.4 T," *Magn. Reson. Mater. Physics, Biol. Med.*, 2008.

[260] M. S. A. Deloire-Grassin *et al.*, "In vivo evaluation of remyelination in rat brain by magnetization transfer imaging," *J. Neurol. Sci.*, vol. 178, no. 1, pp. 10–16, 2000.

[261] R. Aharoni *et al.*, "Magnetic resonance imaging characterization of different experimental autoimmune encephalomyelitis models and the therapeutic effect of glatiramer acetate," *Exp. Neurol.*, vol. 240, pp. 130–144, Feb. 2013.

[262] E. L. A. Blezer, J. Bauer, H. P. M. Brok, K. Nicolay, and B. A. 't Hart, "Quantitative MRI-pathology correlations of brain white matter lesions developing in a non-human primate model of multiple sclerosis," *NMR Biomed.*, vol. 20, no. 2, pp. 90–103, Apr. 2007.

[263] K. Schmierer, F. Scaravilli, D. R. Altmann, G. J. Barker, and D. H. Miller, "Magnetization transfer ratio and myelin in postmortem multiple sclerosis brain," *Ann. Neurol.*, vol. 56, no. 3, pp. 407–415, Sep. 2004.

[264] P. J. Gareau, B. K. Rutt, S. J. Karlik, and J. R. Mitchell, "Magnetization transfer and multicomponent T2 relaxation measurements with histopathologic correlation in an experimental model of MS," *J. Magn. Reson. Imaging*, vol. 11, no. 6, pp. 586–595, Jun. 2000.

[265] E. Sbardella, F. Tona, N. Petsas, and P. Pantano, "DTI Measurements in Multiple Sclerosis: Evaluation of Brain Damage and Clinical Implications," vol. 2013, pp. 1–12, 2015.

[266] Y. Assaf and O. Pasternak, "Diffusion tensor imaging (DTI)-based white matter

mapping in brain research: A review," *J. Mol. Neurosci.*, vol. 34, no. 1, pp. 51–61, 2008.

[267] S.-W. Sun, H.-F. Liang, K. Trinkaus, A. H. Cross, R. C. Armstrong, and S.-K. Song, "Noninvasive detection of cuprizone induced axonal damage and demyelination in the mouse corpus callosum," *Magn. Reson. Med.*, vol. 55, no. 2, pp. 302–308, Feb. 2006.

[268] S.-K. Song *et al.*, "Demyelination increases radial diffusivity in corpus callosum of mouse brain," *Neuroimage*, vol. 26, no. 1, pp. 132–140, May 2005.

[269] M. Xie *et al.*, "Rostrocaudal Analysis of Corpus Callosum Demyelination and Axon Damage Across Disease Stages Refines Diffusion Tensor Imaging Correlations With Pathological Features," *J. Neuropathol. Exp. Neurol.*, vol. 69, no. 7, pp. 704–716, Jul. 2010.

[270] S.-K. Song, S.-W. Sun, M. J. Ramsbottom, C. Chang, J. Russell, and A. H. Cross, "Dysmyelination Revealed through MRI as Increased Radial (but Unchanged Axial) Diffusion of Water," *Neuroimage*, vol. 17, no. 3, pp. 1429–1436, Nov. 2002.

[271] S.-K. Song, S.-W. Sun, W.-K. Ju, S.-J. Lin, A. H. Cross, and A. H. Neufeld, "Diffusion tensor imaging detects and differentiates axon and myelin degeneration in mouse optic nerve after retinal ischemia.," *Neuroimage*, vol. 20, no. 3, pp. 1714–22, Nov. 2003.

[272] W. Y. Aung, S. Mar, and T. L. Benzinger, "Diffusion tensor MRI as a biomarker in axonal and myelin damage.," *Imaging Med.*, vol. 5, no. 5, pp. 427–440, 2013.

[273] M. D. Budde, J. H. Kim, H. Liang, J. H. Russell, A. H. Cross, and S. Song, "Axonal injury detected by in vivo diffusion tensor imaging correlates with neurological disability in a mouse model of multiple sclerosis," *NMR Biomed.*, vol. 21, no. 6, pp. 589–597, Jul. 2008.

[274] S.-W. Sun, H.-F. Liang, R. E. Schmidt, A. H. Cross, and S.-K. Song, "Selective vulnerability of cerebral white matter in a murine model of multiple sclerosis detected using diffusion tensor imaging," *Neurobiol. Dis.*, vol. 28, no. 1, pp. 30–38, Oct. 2007.

[275] F. Fink *et al.*, "Comparison of Diffusion Tensor-Based Tractography and Quantified Brain Atrophy for Analyzing Demyelination and Axonal Loss in MS," *J. Neuroimaging*, vol. 20, no. 4, pp. 334–344, Oct. 2010.

[276] J. L. and I. P. JM Tillema, "White matter changes in paediatric multiple sclerosis and monophasic demyelinating disorders," *Brain*, vol. 140, no. 5, pp. 1300–1315, 2017.

[277] S.-W. Sun, H.-F. Liang, T. Q. Le, R. C. Armstrong, A. H. Cross, and S.-K. Song, "Differential sensitivity of in vivo and ex vivo diffusion tensor imaging to evolving optic nerve injury in mice with retinal ischemia," *Neuroimage*, vol. 32, no. 3, pp. 1195–1204, Sep. 2006.

[278] J. A. Wells *et al.*, "In vivo imaging of tau pathology using multi-parametric quantitative MRI," *Neuroimage*, vol. 111, pp. 369–378, May 2015.

[279] S. K. Song, J. H. Kim, S. J. Lin, R. P. Brendza, and D. M. Holtzman, "Diffusion tensor imaging detects age-dependent white matter changes in a transgenic mouse model with amyloid deposition," *Neurobiol. Dis.*, vol. 15, no. 3, pp. 640–647, 2004.

[280] A. Mackay, K. Whittall, J. Adler, D. Li, D. Paty, and D. Graeb, "In vivo visualization of myelin water in brain by magnetic resonance," *Magn. Reson. Med.*, vol. 31, no. 6, pp. 673–677, Jun. 1994.

[281] M. D. Does and J. C. Gore, "Compartmental study ofT1 andT2 in rat brain and trigeminal nerve in vivo," *Magn. Reson. Med.*, vol. 47, no. 2, pp. 274–283, Feb. 2002.

[282] E. Alonso-Ortiz, I. R. Levesque, and G. B. Pike, "MRI-based myelin water imaging: A technical review," *Magn. Reson. Med.*, vol. 73, no. 1, pp. 70–81, Jan. 2015.

[283] I. M. Vavasour, K. P. Whittall, A. L. Mackay, D. K. B. Li, G. Vorobeychik, and D. W. Paty, "A comparison between magnetization transfer ratios and myelin water percentages in normals and multiple sclerosis patients," *Magn. Reson. Med.*, vol. 40, no. 5, pp. 763–768, Nov. 1998.

[284] C. Birkl *et al.*, "The influence of brain iron on myelin water imaging," *Neuroimage*, vol. 199, pp. 545–552, Oct. 2019.

[285] J. P. Wansapura, S. K. Holland, R. S. Dunn, and W. S. Ball, "NMR relaxation times in the human brain at 3.0 tesla," *J. Magn. Reson. Imaging*, vol. 9, no. 4, pp. 531–538, Apr. 1999.

[286] S. Webb, C. A. Munro, R. Midha, and G. J. Stanisz, "Is multicomponent T2 a good measure of myelin content in peripheral nerve?," *Magn. Reson. Med.*, vol. 49, no. 4, pp. 638–645, 2003.

[287] H. FERNANDEZ-MORAN and J. B. FINEAN, "Electron microscope and low-angle x-ray diffraction studies of the nerve myelin sheath.," *J. Biophys. Biochem. Cytol.*, vol. 3, no. 5, pp. 725–48, Sep. 1957.

[288] V. Sheth *et al.*, "Magnetic resonance imaging of myelin using ultrashort Echo time (UTE) pulse sequences: Phantom, specimen, volunteer and multiple sclerosis patient studies," *Neuroimage*, vol. 136, pp. 37–44, Aug. 2016.

[289] Q. He *et al.*, "Direct magnitude and phase imaging of myelin using ultrashort echo time (UTE) pulse sequences: A feasibility study," *Magn. Reson. Imaging*, vol. 39, pp. 194–199, Jun. 2017.

[290] M. J. Wilhelm *et al.*, "Direct magnetic resonance detection of myelin and prospects for

quantitative imaging of myelin density," *Proc. Natl. Acad. Sci.*, vol. 109, no. 24, pp. 9605–9610, Jun. 2012.

[291] B. Stankoff *et al.*, "Imaging of CNS myelin by positron-emission tomography," *Proc. Natl. Acad. Sci.*, vol. 103, no. 24, pp. 9304–9309, Jun. 2006.

[292] B. Stankoff *et al.*, "Imaging central nervous system myelin by positron emission tomography in multiple sclerosis using [methyl-11C]-2-(4′-methylaminophenyl)- 6-hydroxybenzothiazole," *Ann. Neurol.*, vol. 69, no. 4, pp. 673–680, Apr. 2011.

[293] Y. Wang *et al.*, "In Vivo Quantification of Myelin Changes in the Vertebrate Nervous System," *J. Neurosci.*, vol. 29, no. 46, pp. 14663–14669, Nov. 2009.

[294] C. Wu *et al.*, "A novel PET marker for in vivo quantification of myelination," *Bioorg. Med. Chem.*, vol. 18, no. 24, pp. 8592–8599, Dec. 2010.

[295] B. Bodini *et al.*, "Dynamic Imaging of Individual Remyelination Profiles in Multiple Sclerosis," *Ann. Neurol.*, vol. 79, no. 5, pp. 726–738, May 2016.

[296] P. Brugarolas, D. S. Reich, and B. Popko, "Detecting Demyelination by PET: The Lesion as Imaging Target," *Mol. Imaging*, vol. 17, p. 153601211878547, Jan. 2018.

[297] M. Veronese *et al.*, "Quantification of [11C]PIB PET for imaging myelin in the human brain: A test-retest reproducibility study in high-resolution research tomography," *J. Cereb. Blood Flow Metab.*, vol. 35, no. 11, pp. 1771–1782, 2015.

[298] M. Zhang *et al.*, "Evaluation of Myelin Radiotracers in the Lysolecithin Rat Model of Focal Demyelination: Beware of Pitfalls!," *Contrast Media Mol. Imaging*, vol. 2019, pp. 1–10, May 2019.

[299] H. Lv *et al.*, "Resting-state functional MRI: Everything that nonexperts have always wanted to know," *Am. J. Neuroradiol.*, vol. 39, no. 8, pp. 1390–1399, 2018.

[300] S. Ogawa, T. M. Lee, A. R. Kay, and D. W. Tank, "Brain magnetic resonance imaging with contrast dependent on blood oxygenation.," *Proc. Natl. Acad. Sci.*, vol. 87, no. 24, pp. 9868–9872, Dec. 1990.

[301] B. Biswal, F. Zerrin Yetkin, V. M. Haughton, and J. S. Hyde, "Functional connectivity in the motor cortex of resting human brain using echo-planar mri," *Magn. Reson. Med.*, vol. 34, no. 4, pp. 537–541, Oct. 1995.

[302] Y. Ma *et al.*, "Resting-state hemodynamics are spatiotemporally coupled to synchronized and symmetric neural activity in excitatory neurons," *Proc. Natl. Acad. Sci.*, vol. 113, no. 52, pp. E8463–E8471, Dec. 2016.

[303] Z. Shehzad *et al.*, "The Resting Brain: Unconstrained yet Reliable," *Cereb. Cortex*, vol.

19, no. 10, pp. 2209–2229, Oct. 2009.

[304] H. Lu, Q. Zou, H. Gu, M. E. Raichle, E. A. Stein, and Y. Yang, "Rat brains also have a default mode network," *Proc. Natl. Acad. Sci.*, vol. 109, no. 10, pp. 3979–3984, Mar. 2012.

[305] J. L. Vincent *et al.*, "Intrinsic functional architecture in the anaesthetized monkey brain," *Nature*, vol. 447, no. 7140, pp. 83–86, May 2007.

[306] B. R. White, A. Q. Bauer, A. Z. Snyder, B. L. Schlaggar, J.-M. Lee, and J. P. Culver, "Imaging of Functional Connectivity in the Mouse Brain," *PLoS One*, vol. 6, no. 1, p. e16322, Jan. 2011.

[307] J. Aoe *et al.*, "Evaluation of the default-mode network by quantitative 15O-PET: comparative study between cerebral blood flow and oxygen consumption," *Ann. Nucl. Med.*, vol. 32, no. 7, pp. 485–491, Aug. 2018.

[308] S. A. R. B. Rombouts, F. Barkhof, R. Goekoop, C. J. Stam, and P. Scheltens, "Altered resting state networks in mild cognitive impairment and mild Alzheimer's disease: An fMRI study," *Hum. Brain Mapp.*, vol. 26, no. 4, pp. 231–239, Dec. 2005.

[309] D. Vidal-PiÃ±eiro *et al.*, "Decreased Default Mode Network connectivity correlates with age-associated structural and cognitive changes," *Front. Aging Neurosci.*, vol. 6, Sep. 2014.

[310] C. J. Werner *et al.*, "Altered resting-state connectivity in Huntington's Disease," *Hum. Brain Mapp.*, vol. 35, no. 6, pp. 2582–2593, 2014.

[311] J. Klohs *et al.*, "Longitudinal Assessment of Amyloid Pathology in Transgenic ArcAβ Mice Using Multi-Parametric Magnetic Resonance Imaging," *PLoS One*, vol. 8, no. 6, p. e66097, Jun. 2013.

[312] J. Grandjean *et al.*, "Early Alterations in Functional Connectivity and White Matter Structure in a Transgenic Mouse Model of Cerebral Amyloidosis," *J. Neurosci.*, vol. 34, no. 41, pp. 13780–13789, Oct. 2014.

[313] D. Kalthoff, C. Po, D. Wiedermann, and M. Hoehn, "Reliability and spatial specificity of rat brain sensorimotor functional connectivity networks are superior under sedation compared with general anesthesia," *NMR Biomed.*, Jan. 2013.

[314] D. Kalthoff, J. U. Seehafer, C. Po, D. Wiedermann, and M. Hoehn, "Functional connectivity in the rat at 11.7T: Impact of physiological noise in resting state fMRI," *Neuroimage*, vol. 54, no. 4, pp. 2828–2839, Feb. 2011.

[315] V. Zerbi, J. Grandjean, M. Rudin, and N. Wenderoth, "Mapping the mouse brain with rs-fMRI: An optimized pipeline for functional network identification," *Neuroimage*,

vol. 123, pp. 11–21, Dec. 2015.

[316] D. Bajic, M. M. Craig, C. R. L. Mongerson, D. Borsook, and L. Becerra, "Identifying Rodent Resting-State Brain Networks with Independent Component Analysis," *Front. Neurosci.*, vol. 11, Dec. 2017.

[317] C. P. Pawela *et al.*, "Resting-state functional connectivity of the rat brain," *Magn. Reson. Med.*, vol. 59, no. 5, pp. 1021–1029, May 2008.

[318] R. M. Hutchison, S. M. Mirsattari, C. K. Jones, J. S. Gati, and L. S. Leung, "Functional Networks in the Anesthetized Rat Brain Revealed by Independent Component Analysis of Resting-State fMRI," *J. Neurophysiol.*, vol. 103, no. 6, pp. 3398–3406, Jun. 2010.

[319] E. Jonckers, J. Van Audekerke, G. De Visscher, A. Van der Linden, and M. Verhoye, "Functional Connectivity fMRI of the Rodent Brain: Comparison of Functional Connectivity Networks in Rat and Mouse," *PLoS One*, vol. 6, no. 4, p. e18876, Apr. 2011.

[320] D. C. Van Essen *et al.*, "The Human Connectome Project: A data acquisition perspective," *Neuroimage*, vol. 62, no. 4, pp. 2222–2231, Oct. 2012.

[321] M. Gorges, F. Roselli, H.-P. Müller, A. C. Ludolph, V. Rasche, and J. Kassubek, "Functional Connectivity Mapping in the Animal Model: Principles and Applications of Resting-State fMRI," *Front. Neurol.*, vol. 8, May 2017.

[322] K. Murphy, R. M. Birn, and P. A. Bandettini, "Resting-state fMRI confounds and cleanup," *Neuroimage*, vol. 80, pp. 349–359, Oct. 2013.

[323] C. F. Beckmann, "Modelling with independent components," *Neuroimage*, vol. 62, no. 2, pp. 891–901, 2012.

[324] M. J. Mckeown *et al.*, "Analysis of fMRI data by blind separation into independent spatial components," *Hum. Brain Mapp.*, vol. 6, no. 3, pp. 160–188, 1998.

[325] M. De Luca, C. F. Beckmann, N. De Stefano, P. M. Matthews, and S. M. Smith, "fMRI resting state networks define distinct modes of long-distance interactions in the human brain," *Neuroimage*, vol. 29, no. 4, pp. 1359–1367, Feb. 2006.

[326] C. F. Beckmann, M. DeLuca, J. T. Devlin, and S. M. Smith, "Investigations into resting-state connectivity using independent component analysis," *Philos. Trans. R. Soc. B Biol. Sci.*, vol. 360, no. 1457, pp. 1001–1013, May 2005.

[327] L. Griffanti *et al.*, "Hand classification of fMRI ICA noise components," *Neuroimage*, vol. 154, pp. 188–205, 2017.

[328] G. Salimi-Khorshidi, G. Douaud, C. F. Beckmann, M. F. Glasser, L. Griffanti, and S. M. Smith, "Automatic denoising of functional MRI data: Combining independent component analysis and hierarchical fusion of classifiers," *Neuroimage*, vol. 90, pp. 449–468, Apr. 2014.

[329] L. Griffanti *et al.*, "ICA-based artefact removal and accelerated fMRI acquisition for improved resting state network imaging," *Neuroimage*, vol. 95, pp. 232–247, Jul. 2014.

[330] V. Zerbi, J. Grandjean, M. Rudin, and N. Wenderoth, "Mapping the mouse brain with rs-fMRI: An optimized pipeline for functional network identification," *Neuroimage*, vol. 123, pp. 11–21, 2015.

[331] G. Tononi, O. Sporns, and G. M. Edelman, "A measure for brain complexity: relating functional segregation and integration in the nervous system.," *Proc. Natl. Acad. Sci.*, vol. 91, no. 11, pp. 5033–5037, May 1994.

[332] Y. Liu, J.-H. Gao, M. Liotti, Y. Pu, and P. T. Fox, "Temporal dissociation of parallel processing in the human subcortical outputs," *Nature*, vol. 400, no. 6742, pp. 364–367, Jul. 1999.

[333] V. Zerbi *et al.*, "Resting-State Functional Connectivity Changes in Aging apoE4 and apoE-KO Mice," *J. Neurosci.*, vol. 34, no. 42, pp. 13963–13975, Oct. 2014.

[334] C. Green *et al.*, "Functional networks are impaired by elevated tau-protein but reversible in a regulatable Alzheimer's disease mouse model," *Mol. Neurodegener.*, vol. 14, no. 1, pp. 1–13, 2019.

[335] S. Arnold Anteraper, C. Triantafyllou, A. T. Sawyer, S. G. Hofmann, J. D. Gabrieli, and S. Whitfield-Gabrieli, "Hyper-Connectivity of Subcortical Resting-State Networks in Social Anxiety Disorder," *Brain Connect.*, vol. 4, no. 2, pp. 81–90, Mar. 2014.

[336] Q. Bukhari, A. Schroeter, D. M. Cole, and M. Rudin, "Resting State fMRI in Mice Reveals Anesthesia Specific Signatures of Brain Functional Networks and Their Interactions," *Front. Neural Circuits*, vol. 11, Feb. 2017.

[337] R. Weber, P. Ramos-Cabrer, D. Wiedermann, N. van Camp, and M. Hoehn, "A fully noninvasive and robust experimental protocol for longitudinal fMRI studies in the rat," *Neuroimage*, vol. 29, no. 4, pp. 1303–1310, Feb. 2006.

[338] J. Grandjean, A. Schroeter, I. Batata, and M. Rudin, "Optimization of anesthesia protocol for resting-state fMRI in mice based on differential effects of anesthetics on functional connectivity patterns," *Neuroimage*, vol. 102, pp. 838–847, Nov. 2014.

[339] A. A. Jarjour, H. Zhang, N. Bauer, C. Ffrench-Constant, and A. Williams, "In vitro modeling of central nervous system myelination and remyelination," *Glia*, vol. 60, no.

1, pp. 1–12, Jan. 2012.

[340] J. Agulla *et al.*, "In Vivo Theranostics at the Peri-Infarct Region in Cerebral Ischemia," *Theranostics*, vol. 4, no. 1, pp. 90–105, 2014.

[341] G. Rouser, S. Fleischer, and A. Yamamoto, "Two dimensional thin layer chromatographic separation of polar lipids and determination of phospholipids by phosphorus analysis of spots," *Lipids*, vol. 5, no. 5, pp. 494–496, May 1970.

[342] F. L. Goerner and G. D. Clarke, "Measuring signal-to-noise ratio in partially parallel imaging MRI," *Med. Phys.*, vol. 38, no. 9, pp. 5049–5057, Aug. 2011.

[343] J. Agulla *et al.*, "Quick adjustment of imaging tracer payload, for in vivo applications of theranostic nanostructures in the brain," *Nanomedicine Nanotechnology, Biol. Med.*, vol. 10, no. 4, pp. 851–858, May 2014.

[344] A. Akbarzadeh *et al.*, "Liposome: classification, preparation, and applications," *Nanoscale Res. Lett.*, vol. 8, no. 1, p. 102, Dec. 2013.

[345] J. M. Vega-Riquer, G. Mendez-Victoriano, R. A. Morales-Luckie, and O. Gonzalez-Perez, "Five Decades of Cuprizone, an Updated Model to Replicate Demyelinating Diseases," *Curr. Neuropharmacol.*, vol. 17, no. 2, pp. 129–141, Jan. 2019.

[346] C. Laule *et al.*, "Myelin water imaging in multiple sclerosis: quantitative correlations with histopathology," *Mult. Scler.*, vol. 12, no. 6, pp. 747–753, 2006.

[347] M. Ganzetti, N. Wenderoth, and D. Mantini, "Whole brain myelin mapping using T1- and T2-weighted MR imaging data.," *Front. Hum. Neurosci.*, vol. 8, no. September, p. 671, 2014.

[348] M. J. Wilhelm *et al.*, "Direct magnetic resonance detection of myelin and prospects for quantitative imaging of myelin density," *Proc. Natl. Acad. Sci.*, vol. 109, no. 15, pp. 9605–9610, 2012.

[349] L. Turati *et al.*, "In vivo quantitative magnetization transfer imaging correlates with histology during de- and remyelination in cuprizone-treated mice," *NMR Biomed.*, vol. 28, no. 3, pp. 327–337, 2015.

[350] C. Laule *et al.*, "Magnetic Resonance Imaging of Myelin," *Neurotherapeutics*, vol. 4, no. 3, pp. 460–484, 2007.

[351] J. V. Manjón, P. Coupé, L. Concha, A. Buades, D. L. Collins, and M. Robles, "Diffusion Weighted Image Denoising Using Overcomplete Local PCA," *PLoS One*, vol. 8, no. 9, p. e73021, Sep. 2013.

[352] E. Garyfallidis *et al.*, "Dipy, a library for the analysis of diffusion MRI data," *Front.*

Neuroinform., vol. 8, Feb. 2014.

[353] C. A. Schneider, W. S. Rasband, and K. W. Eliceiri, "NIH Image to ImageJ: 25 years of image analysis," *Nat. Methods*, vol. 9, no. 7, pp. 671–675, Jul. 2012.

[354] A. Loy, L. Follett, and H. Hofmann, "Variations of Q – Q Plots: The Power of Our Eyes!," *Am. Stat.*, vol. 70, no. 2, pp. 202–214, Apr. 2016.

[355] Torkildsen, L. A. Brunborg, K. M. Myhr, and L. Bø, "The cuprizone model for demyelination," *Acta Neurol. Scand.*, vol. 117, no. SUPPL. 188, pp. 72–76, 2008.

[356] N. Nathoo, V. W. Yong, and J. F. Dunn, "Understanding disease processes in multiple sclerosis through magnetic resonance imaging studies in animal models," *NeuroImage Clin.*, vol. 4, pp. 743–756, 2014.

[357] J. Orije *et al.*, "Longitudinal monitoring of metabolic alterations in cuprizone mouse model of multiple sclerosis using 1H-magnetic resonance spectroscopy," *Neuroimage*, vol. 114, pp. 128–135, Jul. 2015.

[358] P. J. Winklewski, A. Sabisz, P. Naumczyk, K. Jodzio, E. Szurowska, and A. Szarmach, "Understanding the Physiopathology Behind Axial and Radial Diffusivity Changes—What Do We Know?," *Front. Neurol.*, vol. 9, no. FEB, Feb. 2018.

[359] A. H. Cross and L. Piccio, "Immunopathogenesis of Multiple Sclerosis," in *Multiple Sclerosis and CNS Inflammatory Disorders*, Chichester, UK: John Wiley & Sons, Ltd., 2014, pp. 10–17.

[360] K. M. Höflich *et al.*, "Acute axonal damage in three different murine models of multiple sclerosis: A comparative approach," *Brain Res.*, vol. 1650, pp. 125–133, 2016.

[361] K. Schmierer, H. G. Parkes, and P.-W. So, "Direct visualization of remyelination in multiple sclerosis using T2-weighted high-field MRI," *Neurology*, vol. 72, no. 5, pp. 472–472, Feb. 2009.

[362] Y. Wang *et al.*, "Quantification of increased cellularity during inflammatory demyelination," *Brain*, vol. 134, no. 12, pp. 3590–3601, Dec. 2011.

[363] K. Schmierer *et al.*, "Quantitative magnetic resonance of postmortem multiple sclerosis brain before and after fixation," *Magn. Reson. Med.*, vol. 59, no. 2, pp. 268–277, Feb. 2008.

[364] K. Schmierer *et al.*, "Diffusion tensor imaging of post mortem multiple sclerosis brain," *Neuroimage*, vol. 35, no. 2, pp. 467–477, Apr. 2007.

[365] A. L. Alexander, J. E. Lee, M. Lazar, and A. S. Field, "Diffusion Tensor Imaging of the Brain," *Neurotherapeutics*, vol. 4, no. 3, pp. 316–329, 2007.

[366] L. T. Remington, A. A. Babcock, S. P. Zehntner, and T. Owens, "Microglial Recruitment, Activation, and Proliferation in Response to Primary Demyelination," *Am. J. Pathol.*, vol. 170, no. 5, pp. 1713–1724, May 2007.

[367] S. Pfeifenbring, S. Nessler, C. Wegner, C. Stadelmann, and W. Brück, "Remyelination After Cuprizone-Induced Demyelination Is Accelerated in Juvenile Mice.," *J. Neuropathol. Exp. Neurol.*, vol. 74, no. 8, pp. 756–66, 2015.

[368] N. H. Stricker *et al.*, "Decreased white matter integrity in late-myelinating fiber pathways in Alzheimer's disease supports retrogenesis," *Neuroimage*, vol. 45, no. 1, pp. 10–16, Mar. 2009.

[369] M. Ota *et al.*, "Age-related degeneration of corpus callosum measured with diffusion tensor imaging," *Neuroimage*, vol. 31, no. 4, pp. 1445–1452, Jul. 2006.

[370] R. C. Armstrong, T. Q. Le, N. C. Flint, A. C. Vana, and Y.-X. Zhou, "Endogenous Cell Repair of Chronic Demyelination," *J. Neuropathol. Exp. Neurol.*, vol. 65, no. 3, pp. 245–256, Mar. 2006.

[371] M. Kipp, T. Clarner, J. Dang, S. Copray, and C. Beyer, "The cuprizone animal model: New insights into an old story," *Acta Neuropathol.*, vol. 118, no. 6, pp. 723–736, 2009.

[372] J.-J. Sun, Q.-G. Ren, L. Xu, and Z.-J. Zhang, "LINGO-1 antibody ameliorates myelin impairment and spatial memory deficits in experimental autoimmune encephalomyelitis mice," *Sci. Rep.*, vol. 5, no. 1, p. 14235, Nov. 2015.

[373] F. Kametani and M. Hasegawa, "Reconsideration of Amyloid Hypothesis and Tau Hypothesis in Alzheimer's Disease," *Front. Neurosci.*, vol. 12, Jan. 2018.

[374] S. P. Lee, M. F. Falangola, R. A. Nixon, K. Duff, and J. A. Helpern, "Visualization of β-amyloid plaques in a transgenic mouse model of Alzheimer's disease using MR microscopy without contrast reagents," *Magn. Reson. Med.*, vol. 52, no. 3, pp. 538–544, 2004.

[375] C. Dudeffant *et al.*, "Contrast-enhanced MR microscopy of amyloid plaques in five mouse models of amyloidosis and in human Alzheimer's disease brains," *Sci. Rep.*, vol. 7, no. 1, p. 4955, Dec. 2017.

[376] H.-P. Müller, J. Kassubek, I. Vernikouskaya, A. C. Ludolph, D. Stiller, and V. Rasche, "Diffusion Tensor Magnetic Resonance Imaging of the Brain in APP Transgenic Mice: A Cohort Study," *PLoS One*, vol. 8, no. 6, p. e67630, Jun. 2013.

[377] H. Zheng *et al.*, "The hypothalamus as the primary brain region of metabolic abnormalities in APP/PS1 transgenic mouse model of Alzheimer's disease," *Biochim. Biophys. Acta - Mol. Basis Dis.*, vol. 1864, no. 1, pp. 263–273, Jan. 2018.

[378] M. Ishii, G. Wang, G. Racchumi, J. P. Dyke, and C. Iadecola, "Transgenic Mice Overexpressing Amyloid Precursor Protein Exhibit Early Metabolic Deficits and a Pathologically Low Leptin State Associated with Hypothalamic Dysfunction in Arcuate Neuropeptide Y Neurons," *J. Neurosci.*, vol. 34, no. 27, pp. 9096–9106, Jul. 2014.

[379] S. J. Baloyannis, I. Mavroudis, D. Mitilineos, I. S. Baloyannis, and V. G. Costa, "The Hypothalamus in Alzheimer's Disease," *Am. J. Alzheimer's Dis. Other Dementiasr*, vol. 30, no. 5, pp. 478–487, Aug. 2015.

[380] T. R. Stoub, L. DeToledo-Morrell, G. T. Stebbins, S. Leurgans, D. A. Bennett, and R. C. Shah, "Hippocampal disconnection contributes to memory dysfunction in individuals at risk for Alzheimer's disease," *Proc. Natl. Acad. Sci.*, vol. 103, no. 26, pp. 10041–10045, Jun. 2006.

[381] X. Guo, Y. Han, K. Chen, Y. Wang, and L. Yao, "Mapping joint grey and white matter reductions in Alzheimer's disease using joint independent component analysis," *Neurosci. Lett.*, vol. 531, no. 2, pp. 136–141, Dec. 2012.

[382] W. J. P. Henneman *et al.*, "Hippocampal atrophy rates in Alzheimer disease: Added value over whole brain volume measures," *Neurology*, vol. 72, no. 11, pp. 999–1007, Mar. 2009.

[383] G. Douaud *et al.*, "Brain Microstructure Reveals Early Abnormalities more than Two Years prior to Clinical Progression from Mild Cognitive Impairment to Alzheimer's Disease," *J. Neurosci.*, vol. 33, no. 5, pp. 2147–2155, Jan. 2013.

[384] G. B. Frisoni, M. Lorenzi, A. Caroli, N. Kemppainen, K. Nagren, and J. O. Rinne, "In vivo mapping of amyloid toxicity in Alzheimer disease," *Neurology*, vol. 72, no. 17, pp. 1504–1511, Apr. 2009.

[385] G. ChÃ©telat *et al.*, "Relationship between atrophy and Î²-amyloid deposition in Alzheimer's disease," *Ann. Neurol.*, p. NA-NA, 2009.

[386] J.-C. Dodart, C. Mathis, J. Saura, K. R. Bales, S. M. Paul, and A. Ungerer, "Neuroanatomical Abnormalities in Behaviorally Characterized APPV717F Transgenic Mice," *Neurobiol. Dis.*, vol. 7, no. 2, pp. 71–85, Apr. 2000.

[387] M. H. Donovan, U. Yazdani, R. D. Norris, D. Games, D. C. German, and A. J. Eisch, "Decreased adult hippocampal neurogenesis in the PDAPP mouse model of Alzheimer's disease," *J. Comp. Neurol.*, vol. 495, no. 1, pp. 70–83, Mar. 2006.

[388] F. Gonzalez-Lima, J. D. Berndt, J. E. Valla, D. Games, and E. M. Reiman, "Reduced corpus callosum, fornix and hippocampus in PDAPP transgenic mouse model of Alzheimer's disease," *Neuroreport*, vol. 12, no. 11, pp. 2375–2379, Aug. 2001.

[389] I. Stepan-Buksakowska *et al.*, "Cortical and subcortical atrophy in alzheimer disease: Parallel atrophy of thalamus and hippocampus," *Alzheimer Dis. Assoc. Disord.*, vol. 28, no. 1, pp. 65–72, 2014.

[390] J. Sun, H. Zhou, F. Bai, Z. Zhang, and Q. Ren, "Remyelination: A Potential Therapeutic Strategy for Alzheimer's Disease?," *J. Alzheimer's Dis.*, vol. 58, no. 3, pp. 597–612, Jun. 2017.

[391] D. Wolf, F. U. Fischer, A. Scheurich, and A. Fellgiebel, "Non-Linear Association between Cerebral Amyloid Deposition and White Matter Microstructure in Cognitively Healthy Older Adults," *J. Alzheimer's Dis.*, vol. 47, no. 1, pp. 117–127, Jul. 2015.

[392] A. A. Gouw *et al.*, "Heterogeneity of white matter hyperintensities in Alzheimer's disease: post-mortem quantitative MRI and neuropathology," *Brain*, vol. 131, no. 12, pp. 3286–3298, Dec. 2008.

[393] K. Dikranian, "Electron microscopist's view of the Alzheimer's plaque," *Biomed. Rev.*, vol. 23, p. 9, Dec. 2012.

[394] F. M. Benes, P. A. Farol, R. E. Majocha, C. A. Marotta, and E. D. Bird, "Evidence for axonal loss in regions occupied by senile plaques in Alzheimer cortex," *Neuroscience*, vol. 42, no. 3, pp. 651–660, Jan. 1991.

[395] C.-W. Chiang *et al.*, "Quantifying white matter tract diffusion parameters in the presence of increased extra-fiber cellularity and vasogenic edema," *Neuroimage*, vol. 101, pp. 310–319, Nov. 2014.

[396] X. Wang *et al.*, "Diffusion basis spectrum imaging detects and distinguishes coexisting subclinical inflammation, demyelination and axonal injury in experimental autoimmune encephalomyelitis mice," *NMR Biomed.*, vol. 27, no. 7, pp. 843–852, Jul. 2014.

[397] J. L. Jankowsky and H. Zheng, "Practical considerations for choosing a mouse model of Alzheimer's disease," *Mol. Neurodegener.*, vol. 12, no. 1, p. 89, Dec. 2017.

[398] R. Crescenzi *et al.*, "Longitudinal imaging reveals subhippocampal dynamics in glutamate levels associated with histopathologic events in a mouse model of tauopathy and healthy mice," *Hippocampus*, vol. 27, no. 3, pp. 285–302, Mar. 2017.

[399] D. E. Hurtado *et al.*, "Aβ Accelerates the Spatiotemporal Progression of Tau Pathology and Augments Tau Amyloidosis in an Alzheimer Mouse Model," *Am. J. Pathol.*, vol. 177, no. 4, pp. 1977–1988, Oct. 2010.

[400] Y. Yoshiyama *et al.*, "Synapse Loss and Microglial Activation Precede Tangles in a P301S Tauopathy Mouse Model," *Neuron*, vol. 53, no. 3, pp. 337–351, Feb. 2007.

[401] N. Sahara *et al.*, "In Vivo Tau Imaging for a Diagnostic Platform of Tauopathy Using the rTg4510 Mouse Line," *Front. Neurol.*, vol. 8, Dec. 2017.

[402] H. E. Holmes *et al.*, "Imaging the accumulation and suppression of tau pathology using multiparametric MRI," *Neurobiol. Aging*, vol. 39, pp. 184–194, Mar. 2016.

[403] S. E. Rose, A. L. Janke PhD, and J. B. Chalk, "Gray and white matter changes in Alzheimer's disease: A diffusion tensor imaging study," *J. Magn. Reson. Imaging*, vol. 27, no. 1, pp. 20–26, Jan. 2008.

[404] J. O'Callaghan *et al.*, "Tissue magnetic susceptibility mapping as a marker of tau pathology in Alzheimer's disease," *Neuroimage*, vol. 159, pp. 334–345, Oct. 2017.

[405] Y. Zhao *et al.*, "In vivo detection of microstructural correlates of brain pathology in preclinical and early Alzheimer Disease with magnetic resonance imaging," *Neuroimage*, vol. 148, pp. 296–304, Mar. 2017.

[406] K. Kopeikina, B. Hyman, and T. Spires-Jones, "Soluble forms of tau are toxic in Alzheimer's disease," *Transl. Neurosci.*, vol. 3, no. 3, Jan. 2012.

[407] W. M. Snow *et al.*, "In Vivo Detection of Gray Matter Neuropathology in the 3xTg Mouse Model of Alzheimer's Disease with Diffusion Tensor Imaging," *J. Alzheimer's Dis.*, vol. 58, no. 3, pp. 841–853, 2017.

[408] M. Z. Kastyak-Ibrahim *et al.*, "Neurofibrillary tangles and plaques are not accompanied by white matter pathology in aged triple transgenic-Alzheimer disease mice," *Magn. Reson. Imaging*, vol. 31, no. 9, pp. 1515–1521, 2013.

[409] C. Bernard *et al.*, "Time course of brain volume changes in the preclinical phase of Alzheimer's disease," *Alzheimer's Dement.*, vol. 10, no. 2, p. 143–151.e1, Mar. 2014.

[410] N. Scolding, R. Franklin, S. Stevens, C. H. Heldin, A. Compston, and J. Newcombe, "Oligodendrocyte progenitors are present in the normal adult human CNS and in the lesions of multiple sclerosis.," *Brain*, vol. 121 (Pt 1, pp. 2221–8, Dec. 1998.

[411] A. Chang, W. W. Tourtellotte, R. Rudick, and B. D. Trapp, "Premyelinating Oligodendrocytes in Chronic Lesions of Multiple Sclerosis," *N. Engl. J. Med.*, vol. 346, no. 3, pp. 165–173, Jan. 2002.

[412] J. M. Frischer *et al.*, "Clinical and pathological insights into the dynamic nature of the white matter multiple sclerosis plaque," *Ann. Neurol.*, vol. 78, no. 5, pp. 710–721, Nov. 2015.

[413] E. Guevara, N. Sadekova, H. Girouard, and F. Lesage, "Optical imaging of resting-state functional connectivity in a novel arterial stiffness model," *Biomed. Opt. Express*, vol. 4, no. 11, p. 2332, Nov. 2013.

[414] R. Bai *et al.*, "Simultaneous calcium fluorescence imaging and MR of ex vivo organotypic cortical cultures: a new test bed for functional MRI," *NMR Biomed.*, vol. 28, no. 12, pp. 1726–1738, Dec. 2015.

[415] M. Dyrba, M. Grothe, T. Kirste, and S. J. Teipel, "Multimodal analysis of functional and structural disconnection in Alzheimer's disease using multiple kernel SVM," *Hum. Brain Mapp.*, vol. 36, no. 6, pp. 2118–2131, 2015.

[416] S. Ferraris, D. Ismail Shakir, J. Van Der Merwe, W. Gsell, J. Deprest, and T. Vercauteren, "Bruker2nifti: Magnetic Resonance Images converter from Bruker ParaVision to Nifti format," *J. Open Source Softw.*, vol. 2, no. 16, p. 354, Aug. 2017.

[417] L. Griffanti *et al.*, "Hand classification of fMRI ICA noise components," *Neuroimage*, vol. 154, pp. 188–205, Jul. 2017.

[418] A. Astrom, R. Forchheimer, and J.-E. Eklund, "Global feature extraction operations for near-sensor image processing," *IEEE Trans. Image Process.*, vol. 5, no. 1, pp. 102–110, Jan. 1996.

[419] L. D. Nickerson, S. M. Smith, D. Öngür, and C. F. Beckmann, "Using Dual Regression to Investigate Network Shape and Amplitude in Functional Connectivity Analyses," *Front. Neurosci.*, vol. 11, Mar. 2017.

[420] C. Beckmann, C. Mackay, N. Filippini, and S. Smith, "Group comparison of resting-state FMRI data using multi-subject ICA and dual regression," *Neuroimage*, vol. 47, p. S148, Jul. 2009.

[421] F. Briggs and W. M. Usrey, "Emerging views of corticothalamic function," *Curr. Opin. Neurobiol.*, vol. 18, no. 4, pp. 403–407, 2008.

[422] I. D. Duncan and A. B. Radcliff, "Inherited and acquired disorders of myelin: The underlying myelin pathology," *Exp. Neurol.*, vol. 283, pp. 452–475, Sep. 2016.

[423] M. Abu-Rub and R. Miller, "Emerging Cellular and Molecular Strategies for Enhancing Central Nervous System (CNS) Remyelination," *Brain Sci.*, vol. 8, no. 6, p. 111, Jun. 2018.

[424] G. K. Matsushima and P. Morell, "The neurotoxicant, cuprizone, as a model to study demyelination and remyelination in the central nervous system.," *Brain Pathol.*, vol. 11, pp. 107–116, 2001.

[425] J. Praet, C. Guglielmetti, Z. Berneman, A. Van der Linden, and P. Ponsaerts, "Cellular and molecular neuropathology of the cuprizone mouse model: Clinical relevance for multiple sclerosis," *Neurosci. Biobehav. Rev.*, vol. 47, pp. 485–505, 2014.

[426] T. Skripuletz, V. Gudi, D. Hackstette, and M. Stangel, "De- and remyelination in the

CNS white and grey matter induced by cuprizone: The old, the new, and the unexpected," *Histol. Histopathol.*, vol. 26, no. 12, pp. 1585–1597, 2011.

[427] J. Praet *et al.*, "Cuprizone-induced demyelination and demyelination-associated inflammation result in different proton magnetic resonance metabolite spectra," *NMR Biomed.*, vol. 28, no. 4, pp. 505–513, Apr. 2015.

[428] J. Tomas-Roig, M. Torrente, M. Cabré, E. Vilella, and M. T. Colomina, "Long lasting behavioural effects on cuprizone fed mice after neurotoxicant withdrawal," *Behav. Brain Res.*, vol. 363, pp. 38–44, May 2019.

[429] M. V. Au Duong *et al.*, "Modulation of effective connectivity inside the working memory network in patients at the earliest stage of multiple sclerosis," *Neuroimage*, vol. 24, no. 2, pp. 533–538, 2005.

[430] V. M. Leavitt, G. R. Wylie, P. A. Girgis, J. DeLuca, and N. D. Chiaravalloti, "Increased functional connectivity within memory networks following memory rehabilitation in multiple sclerosis," *Brain Imaging Behav.*, vol. 8, no. 3, pp. 394–402, Sep. 2014.

[431] F. K. Johnson *et al.*, "Amygdala hyper-connectivity in a mouse model of unpredictable early life stress," *Transl. Psychiatry*, vol. 8, no. 1, p. 49, Dec. 2018.

[432] T. Tsurugizawa, B. Djemai, and A. Zalesky, "The impact of fasting on resting state brain networks in mice," *Sci. Rep.*, vol. 9, no. 1, pp. 1–12, 2019.

[433] S. R. Das *et al.*, "Increased functional connectivity within medial temporal lobe in mild cognitive impairment," *Hippocampus*, vol. 23, no. 1, pp. 1–6, Jan. 2013.

[434] M. Gorges, H. P. Müller, D. Lulé, E. H. Pinkhardt, A. C. Ludolph, and J. Kassubek, "To rise and to fall: Functional connectivity in cognitively normal and cognitively impaired patients with Parkinson's disease," *Neurobiol. Aging*, vol. 36, no. 4, pp. 1727–1735, 2015.

[435] F. G. Hillary, C. A. Roman, U. Venkatesan, S. M. Rajtmajer, R. Bajo, and N. D. Castellanos, "Hyperconnectivity is a Fundamental Response to Neurological Disruption Introduction : Disconnecting the Brain," *Neuropsychology*, vol. 29, no. 1, pp. 59–75, 2015.

[436] N. Franco-Pons, M. Torrente, M. T. Colomina, and E. Vilella, "Behavioral deficits in the cuprizone-induced murine model of demyelination/remyelination," *Toxicol. Lett.*, vol. 169, no. 3, pp. 205–213, 2007.

[437] S. Poliak and E. Peles, "The local differentiation of myelinated axons at nodes of Ranvier," *Nat. Rev. Neurosci.*, vol. 4, no. 12, pp. 968–980, Dec. 2003.

[438] M. J. Craner, J. Newcombe, J. A. Black, C. Hartle, M. L. Cuzner, and S. G. Waxman,

"Molecular changes in neurons in multiple sclerosis: Altered axonal expression of Nav1.2 and Nav1.6 sodium channels and Na+/Ca2+ exchanger," *Proc. Natl. Acad. Sci.*, vol. 101, no. 21, pp. 8168–8173, May 2004.

[439] S. G. Waxman, "Ions, energy and axonal injury: towards a molecular neurology of multiple sclerosis," *Trends Mol. Med.*, vol. 12, no. 5, pp. 192–195, May 2006.

[440] J. S. Bloom and G. W. Hynd, "The role of the corpus callosum in interhemispheric transfer of information: Excitation or inhibition?," *Neuropsychol. Rev.*, vol. 15, no. 2, pp. 59–71, 2005.

[441] C. Knöchel *et al.*, "Interhemispheric hypoconnectivity in schizophrenia: Fiber integrity and volume differences of the corpus callosum in patients and unaffected relatives," *Neuroimage*, vol. 59, no. 2, pp. 926–934, Jan. 2012.

[442] J. E. Downhill *et al.*, "Shape and size of the corpus callosum in schizophrenia and schizotypal personality disorder," *Schizophr. Res.*, vol. 42, no. 3, pp. 193–208, May 2000.

[443] H. J. Yang *et al.*, "Region-specific susceptibilities to cuprizone-induced lesions in the mouse forebrain: Implications for the pathophysiology of schizophrenia," *Brain Res.*, vol. 1270, pp. 121–130, 2009.

[444] N. R. Herring and C. Konradi, "Myelin, copper, and the cuprizone model of schizophrenia.," *Front. Biosci. (Schol. Ed).*, vol. 3, pp. 23–40, 2011.

[445] N. Hibbits, R. Pannu, T. J. Wu, and R. C. Armstrong, "Cuprizone Demyelination of the Corpus Callosum in Mice Correlates with Altered Social Interaction and Impaired Bilateral Sensorimotor Coordination," *ASN Neuro*, vol. 1, no. 3, p. AN20090032, May 2009.

[446] D. LIEBETANZ and D. MERKLER, "Effects of commissural de- and remyelination on motor skill behaviour in the cuprizone mouse model of multiple sclerosis," *Exp. Neurol.*, vol. 202, no. 1, pp. 217–224, Nov. 2006.

[447] P. D. Murray, "Spontaneous remyelination following extensive demyelination is associated with improved neurological function in a viral model of multiple sclerosis," *Brain*, vol. 124, no. 7, pp. 1403–1416, Jul. 2001.

[448] K.-A. Nave, "Myelination and the trophic support of long axons," *Nat. Rev. Neurosci.*, vol. 11, no. 4, pp. 275–283, Apr. 2010.

[449] M. K. Sen, D. A. Mahns, J. R. Coorssen, and P. J. Shortland, "Behavioural phenotypes in the cuprizone model of central nervous system demyelination," *Neurosci. Biobehav. Rev.*, vol. 107, pp. 23–46, Dec. 2019.

[450] R. M. Bove and A. J. Green, "Remyelinating Pharmacotherapies in Multiple Sclerosis," *Neurotherapeutics*, vol. 14, no. 4, pp. 894–904, Oct. 2017.

[451] S. Bramow *et al.*, "Demyelination versus remyelination in progressive multiple sclerosis," *Brain*, vol. 133, no. 10, pp. 2983–2998, Oct. 2010.

[452] L. Hammelrath *et al.*, "Morphological maturation of the mouse brain: An in vivo MRI and histology investigation," *Neuroimage*, vol. 125, pp. 144–152, 2016.

[453] M. A. A. Binnewijzend *et al.*, "Resting-state fMRI changes in Alzheimer's disease and mild cognitive impairment," *Neurobiol. Aging*, vol. 33, no. 9, pp. 2018–2028, Sep. 2012.

[454] R. M. Ransohoff, "Animal models of multiple sclerosis: the good, the bad and the bottom line," *Nat. Neurosci.*, vol. 15, no. 8, pp. 1074–1077, Aug. 2012.

[455] M. A. Busche *et al.*, "Clusters of Hyperactive Neurons Near Amyloid Plaques in a Mouse Model of Alzheimer's Disease," *Science (80-.).*, vol. 321, no. 5896, pp. 1686–1689, Sep. 2008.

[456] P. M. A. Antony, N. J. Diederich, and R. Balling, "Parkinson's disease mouse models in translational research," *Mamm. Genome*, vol. 22, no. 7–8, pp. 401–419, Aug. 2011.

[457] C. Lutz, "Mouse models of ALS: Past, present and future," *Brain Res.*, vol. 1693, pp. 1–10, Aug. 2018.

[458] G. Huang, C. Ashton, D. S. Kumbhani, and Q.-L. Ying, "Genetic manipulations in the rat: progress and prospects," *Curr. Opin. Nephrol. Hypertens.*, vol. 20, no. 4, pp. 391–399, Jul. 2011.

[459] P. Ramos-Cabrer, C. Justicia, D. Wiedermann, and M. Hoehn, "Stem Cell Mediation of Functional Recovery after Stroke in the Rat," *PLoS One*, vol. 5, no. 9, p. e12779, Sep. 2010.

[460] M. Wiesmann *et al.*, "A specific dietary intervention to restore brain structure and function after ischemic stroke," *Theranostics*, vol. 7, no. 2, pp. 493–512, 2017.

[461] M. Jenkinson, "Improved Optimization for the Robust and Accurate Linear Registration and Motion Correction of Brain Images," *Neuroimage*, vol. 17, no. 2, pp. 825–841, Oct. 2002.

[462] S. M. Smith, "Fast robust automated brain extraction," *Hum. Brain Mapp.*, vol. 17, no. 3, pp. 143–155, Nov. 2002.

[463] J. M. Stafford *et al.*, "Large-scale topology and the default mode network in the mouse connectome," *Proc. Natl. Acad. Sci.*, vol. 111, no. 52, pp. 18745–18750, Dec. 2014.

[464] D. Shah *et al.*, "Early pathologic amyloid induces hypersynchrony of BOLD resting-state networks in transgenic mice and provides an early therapeutic window before amyloid plaque deposition," *Alzheimer's Dement.*, vol. 12, no. 9, pp. 964–976, Sep. 2016.

[465] J. Bo *et al.*, "Lifespan Differences in Cortico-Striatal Resting State Connectivity," *Brain Connect.*, vol. 4, no. 3, pp. 166–180, Apr. 2014.

[466] D. D. Jolles, M. A. van Buchem, E. A. Crone, and S. A. R. B. Rombouts, "A Comprehensive Study of Whole-Brain Functional Connectivity in Children and Young Adults," *Cereb. Cortex*, vol. 21, no. 2, pp. 385–391, Feb. 2011.

[467] L. Hammelrath *et al.*, "Morphological maturation of the mouse brain: An in vivo MRI and histology investigation," *Neuroimage*, vol. 125, pp. 144–152, Jan. 2016.

[468] G. Douaud *et al.*, "A common brain network links development, aging, and vulnerability to disease," *Proc. Natl. Acad. Sci.*, vol. 111, no. 49, pp. 17648–17653, Dec. 2014.

[469] C. Green *et al.*, "Sensorimotor Functional and Structural Networks after Intracerebral Stem Cell Grafts in the Ischemic Mouse Brain," *J. Neurosci.*, vol. 38, no. 7, pp. 1648–1661, Feb. 2018.

[470] M. Balbi *et al.*, "Dysfunction of Mouse Cerebral Arteries during Early Aging," *J. Cereb. Blood Flow Metab.*, vol. 35, no. 9, pp. 1445–1453, Sep. 2015.

[471] K. FLURKEY, J. MCURRER, and D. HARRISON, "Mouse Models in Aging Research," in *The Mouse in Biomedical Research*, Elsevier, 2007, pp. 637–672.

[472] J. Grandjean *et al.*, "Common functional networks in the mouse brain revealed by multi-centre resting-state fMRI analysis," *Neuroimage*, vol. 205, p. 116278, Jan. 2020.